Novel Growth Methods of Organic-Inorganic Lead Tri-Halide Perovskite Material for Photovoltaic Applications

HANAA OMER ALMAGHAMSI

January 2020

A THESIS SUBMITTED TO DE MONTRORT UNIVERISTY IN THE

PARTIAL FULFILMENT OF THE REQUIREMENT FOR THE

DEGREE OF

DOCTOR OF PHILOSOPHY (PhD)

Emerging Technologies Research Centre. School of Engineering and Sustainable

Development, De Montfort University, The Gateway, Leicester, United Kingdom, LE1 9BH

Novel Growth Methods of Organic-Inorganic Lead Tri-Halide Perovskite Material for Photovoltaic Applications

HANAA OMER ALMAGHAMSI

PhD supervisors:

Prof. Shashi Paul – 1st supervisor

Dr. Iulia Salaoru – 2nd supervisor

Dr. Krishna Nama Manjunatha – 2nd supervisor

Examinations:

Dr. Mohammed Mabrook – External Examiner

Dr. Adam Moroz – Internal Examiner

Emerging Technologies Research Centre. School of Engineering and Sustainable

Development, De Montfort University, The Gateway, Leicester, United Kingdom, LE1 9BH

Author's declaration

I declare that no part of the results in this thesis has been submitted for any degree or qualification at De Montfort University, or any other academic institutions. All the presented work in this thesis is the result of research undertaken by me at the Emerging Technologies Research Centre (EMTERC), De Montfort University (DMU), unless explicit acknowledgement is given.

Permission to copy or use whole or part of the work contained herein must be solicited except for the purpose of private study or academic purposes in which case the author must be explicitly acknowledged.

Hanaa Omer AlMaghamsi

Leicester, UK

October 2019

Acknowledgement

Firstly, my very special acknowledgement goes to God Almighty “Allah”.

I would also like to express my deepest gratitude to my mother for her great support, without whom I would not have reached this level. Since my childhood, she has been encouraging me to be unique and independent. Surely, she has belief in me and seen this coming before I have even reached.

My special thanks are also extended to my supervisor Prof. Paul, Head of Emerging Technologies Research Centre, without his valuable constructive suggestions, guidance, and encouraging words, I would not have been this confident to move forward and accomplish the research goals. I am also so grateful to Dr. Salaoru and Dr. Manjunatha for their support and advice. Great thanks to my supervisors (Prof. Paul and Dr. Manjunatha) for their assisting to make samples using the PECVD and CVD systems. Many thanks are expressed to Mr. Paul Taylor, the EMTERC Senior Technician, for assisting in ordering the required materials and ensuring all equipment in laboratory in a good state of functionality during my research period.

I gratefully acknowledge the health and life science department at DMU for granting me access to use the X-ray diffraction spectroscopy, the data from which has been presented in this thesis.

My heartfelt and deep appreciation goes to my soul, my daughter, Leen, who has been by my side throughout this hard-working period, my brothers and sister for their emotional support and motivation to study abroad.

My sincere thanks go to the soul of my father whom did not live to see me undertake this degree.

I would sincerely like to thank my PhD colleagues for support and encouragement.

Last but not least, I would especially like to thank King Abdul-Aziz University for granting me this opportunity to pursue my dream to achieve my PhD.

Abstract

Whilst different methodologies have been used to grow perovskite materials, still, there are demands to develop commercial approach techniques that could alleviate the problem associated with the various phases formed within the perovskite material, which may cause of its crystallographic instability. Therefore, the research study was aimed to assist in moving towards this objective by developing novel methods for the deposition of perovskite thin films ($CH_3NH_3PbI_3$ = $MAPbI_3$) that are scalable and industry-acceptable. It was also aimed to focus, along with the scalable process, on an atomic scale of processing to deposit materials with ATM (Atom to Matter), where the defect density within the films are minimised. In view of that, different CVD deposition methods to deposit $MAPbI_3$ thin films were proposed in this study, including Radio Frequency-Plasma Enhanced Chemical Vapour Deposition (RF-PECVD) and Atmospheric-Pressure Chemical Vapour Deposition (APCVD).

The first proof-of-concept was demonstrated to obtain perovskite films with a tetragonal crystal structure by a PECVD process that was not reported till date. This achievement is encouraging as the PECVD process is fully scalable and already available technology in the industries. The growth was subsequently successfully achieved by using carbon, nitrogen and hydrogen radicals that were contained a gas such as methane (CH_4) and ammonia (NH_3). A prior deposition of PbI_2 thin films by either spin-coating or thermal evaporating was implemented previously before they were exposed to the organic molecules in the plasma state that was formed by RF power via a PECVD technique. The effect of the variation of PECVD growth parameters (such as substrate temperature, RF power density and chamber pressure) on the properties of the films deposited was critically analysed. The conditions that yielded the best quality material achieved from this study were at substrate temperature of 100 °C and under low power density (22 mW/cm^2) and high chamber pressure (1000 mtorr). An attempt was made to understand the properties of the resultant films, in terms of the physical, optical and electrical properties, which led to develop and provide appropriate explanations of the possible growth mechanisms.

Considering the cost with the use of the scalable process that any an industrial technique would prefer, a modified non-vacuum CVD system was additionally demonstrated in this work to deposit $MAPbI_3$ films at atmospheric pressure, hence the name APCVD. The growth of the $MAPbI_3$ films was controlled based on the concentration of the precursor and the temperature. The lower concentration of the molecules passing over the substrate enhanced the crystallographic stability, where the *in-situ* cubic structure was achieved. With the use of this novel design of the reactor specifically for the deposition of $MAPbI_3$ perovskite films; excellent stability of these films at room temperature without care of storage for more than two months in an open atmosphere provided an alternative approach to obtain the stable $MAPbI_3$ perovskite film. In addition to the low temperature and lower concentration

of the precursor used for the fabrication of a novel design of the reactor to grow films with the bottom-up approach (i.e. atom by atom or molecules), this study was successful in fabricating a proof-of-concept solar cell using this method for the first time. The obtained perovskite material has significantly contributed to understanding of the crystallographic stability issues reported in the photovoltaics which are incorporated with the perovskite materials over the last recent years.

Table of Contents

Table of Figures

List of tables

List of Abbreviations

A	**Ampere**
Å	**Angstrom**
AACVD	**Aerosol-Assisted Chemical Vapour Deposition**
AC	**Alternating Current**
AFM	**Atomic Force Microscope**
AM1.5	**The air mass 1.5**
Ar	**Argon**
AR	**Adsorption Rate**
BSE	**Backscattered Electron**
CB	**Conduction Band**
CB	**Chlorobenzene**
CBM	**Conduction Band Minimal**
CH4	**Methane**
CR	**Chemical Reaction**
CSVT	**Close Space Vapour Transport**
CVD	**Chemical Vapour Deposition**
D	**Diffusion**
DC	**Direct Current**
DCM	**Dichloromethane**
DMF	**Dimethylformamide**

DMSO	**Dimethyl Sulfoxide**
DR	**Deposition Rate**
e-h	**Electron- hole pair**
E_a	**Activation Energy**
EB	**Binding Energy**
Eg	**Energy band gap**
E_i	**Ion Energy**
ETL	**Electron Transport Layer**
eV	**Electronvolt**
FF	**Fill Factor**
GBL	**Gamma-butyrolactone**
GHz	**Giga Hertz**
HCVD	**Hybrid Chemical Vapour Deposition**
HPCVD	**Hybrid Physical Chemical Vapour Deposition**
HTL	**Hole Transport Layer**
I	**Iodine**
IPA	**Isopropyl Alcohol**
ITCVD	**In-situ Tubular Chemical Vapour Deposition**
ITU	**International Telecommunications Union**
KB	**Boltzmann Constant**
kHz	**Kilo Hertz**

kWh	**Kilo Watt for one hour**
LPCVD	**Low-Pressure Chemical Vapour Deposition**
MA= CH3NH3	**Methyl Ammonium**
MAPbI3	**Methyl Ammonium Lead tri-Iodide**
MFC	**Mean Flow Controller**
MFP	**Mean Free Path**
MOSFET	**Metal-Oxide-Semiconductor Field-Effect Transistor**
MW	**Microwave**
n-type	**Negatively doped semiconductor**
N_2	**Nitrogen**
NH_3	**Ammonia**
NIR	**Near-Infrared Radiation (λ= 700 nm- 2500 nm)**
NMP	**N-Methyl-2-pyrrolidone**
O_2	**Oxygen**
°C	**Degree Celsius**
P	**Chamber Pressure**
p-type	**Positively doped semiconductor**
Pb	**Lead**
PbI_2	**Lead Iodide**
PCE	**Power Conversion Efficiency**
PECVD	**Plasma-Enhanced Chemical Vapour Deposition**

PL	**Photoluminescence**
P_{rf}	**Radio Frequency Power**
PSCs	**Perovskite Solar Cells**
PV	**Photovoltaic**
PVD	**Physical Vapour Deposition**
PWh	**Pico Watt for one hour**
RF	**Radio Frequency**
rpm	**Rotation per minutes**
sccm	**Standard Cubic Centimetres per Minutes (gas flow unit)**
SCs	**Solar Cells**
SE	**Secondary Electron**
SEM	**Scanning Electron Microscope**
SSE	**Solvent-Solvent Extraction**
STC	**Standard Test Conditions**
T	**Temperature**
TEM	**Transmittance Electron Microscope**
TFT	**Thin-Film Transistor**
TGA	**Thermogravimetric analysis**
TL	**Toluene**
UV	**Ultra-Violet**
UV-Vis-IR	**Ultra-Violet-Visible-Infrared spectroscopy**

VASP	**Vapour-Assisted-Solution-Process**
VB	**Valence Band**
V_b	**Self-bias Voltage**
VBM	**Valence Band Maximal**
V_f	**Floating Potential**
V_p	**Plasma Potential**
XRD	**X-Ray Diffraction**

List of Symbols

A	**Absorption**
α	**Absorption coefficient**
c	**Velocity of light**
m	**Charged mass**
q	**Charged particle**
σ	**Collision cross section**
J-V	**Current density-voltage**
$\mathbf{e^-}$	**Electron**
k	**Extinction coefficient**
εi	**Imaginary dielectric constant**
ν	**Light frequency**
λ	**Mean Free Path**
$\mathbf{V_{oc}}$	**Open Circuit Voltage**
n	**Particle Density**
hν	**Photon Energy**
h	**Plank's constant**
h	**Plank's constant**
η	**Power Conversion Efficiency**
εr	**Real dielectric constant**

R	**Reflectance**
n	**Refractive index**
Isc	**Short Circuit Voltage**
T%	**Transmittance**

"Difficulties in your life do not come to destroy you but to help you realise your hidden potential and power."

-Avul Pacir Zainulabidin Abdul Kalam
Atomic Scientist and President of India
(1931-2015)

"Success isn't just about what you accomplish in your life; it's about what you inspire others to do."

— Mohsin Jameel

List of attended conferences during PhD study

1. Hanaa Al-Maghamsi, Iulia Salaoru, Shashi Paul "*Evaluation of the structural, optical and electrical behaviour of c-oriented Lead iodide (PbI2) thin films grown via spin-coating technique for perovskite solar cell application"* ICPAM conference-2016 in Romania.
2. Hanaa Al-Maghamsi, Iulia Salaoru, Krishna Nama Manjunatha, Shashi Paul "*Forming Lead Iodide Perovskite Thin-Films in Seconds*" MRS Fall Meeting-2017 in USA.
3. Hanaa Al-Maghamsi "*Study of morphology and optical properties of c-oriented Lead iodide (PbI2) thin films grown via spin-coating technique to obtain stable perovskite films"* One Day Student Led Research Workshop-2018 in UK.

List of journal articles submitted and suggested for review

1. Hanaa Al-Maghamsi, Krishna Nama Manjunatha, Shashi Paul "Evaluation of the structural, optical and electrical behaviour of c-oriented Lead iodide (PbI2) thin films grown via spin-coating technique for perovskite solar cell application", submitted in applied surface science, 2018.

List of journal articles to be submitted

1. Hanaa Al-Maghamsi, Krishna Nama Manjunatha, Shashi Paul "Demonstration of industrial PECVD process to deposit a stable perovskite thin films", to be submitted in Small, 2020.

2. Hanaa Al-Maghamsi, Krishna Nama Manjunatha, Shashi Paul "Deposition of stable Cubic structure perovskite thin films using novel CVD process", to be submitted in Nature, 2020.

3. Hanaa Al-Maghamsi, Krishna Nama Manjunatha, Shashi Paul "Exploitation of Pizeo Transducer atomision for efficient transport of precursor to obtain stoichiometric, efficient and stable perovskite films in the photovoltaic applications", to be submitted in Nature, 2020.

Chapter 1 Thesis Synopsis

"The modern age is already fossilized at heart, built on discards and relics. It has no real future. We a living in a fossil economy."

Hermann Scheer, The Solar Economy (2002)

1.1 Introduction

The demand for energy is significantly increasing with the soaring global population and the strong economic growth, especially in some countries such as India and China [1]. Moreover, the energy consumption is estimated to increase from 169 PWh in 2015 to 216 PWh in 2040 [1]. Despite the fact that renewable energy is considered to be the fastest growth energy source, a high percentage (77%) of energy is still estimated to be produced by the conventional methods; fossil fuel based until 2040 [1]. These conventional energy sources tend to vanish in a near future and a major source of the emission of carbon dioxide, which is seriously affecting the environment and the planet, so the search for alternative sources to produce sufficient energy has become a paramount concern for all nations.

Renewable energy is a tropical research subject for the scientific community. The solar energy is one of the available renewable energy choices, owing to the possibility to obtain a long-term, sustainable and reliable source of carbon-free energy from the sun. The amount of solar radiation received by our planet in a year is 1.5×10^{18} kWh while the rate of energy consumed is about 10,000 times smaller [2], [3]. This means that the solar energy is the perfect alternative because it is much higher than the consumed conventional energy in the entire world, therefore, it can fulfil the world demand for energy [4].

Photovoltaic solar cells are effectively used to convert the solar energy to electricity. The development of solar cells has shown a great deal of attention by many scientific researchers to improve conversion efficiency, stability, reduce the cost, in addition to ease of fabrication of the cells.

1.2 Evolution and Market Evaluation of Photovoltaic (PV) Technology

The first PV device was discovered in 1839 by Edmond Becquerel; when he covered two electrodes (platinum) with silver bromide in a conductive acidic solution (electrolyte), an electrical current was generated by exposing these electrodes to light [5]. The word 'photovoltaic' was first used in 1883 when Charles Fritts developed a solar cell using selenium sandwiched between two gold metal sheets [6]. The photovoltaic effect as a method of generating electricity had not immediately become widespread until the selenium was replaced by alternative materials. In the modern age, the usage of the photovoltaic effect re-emerged in 1941. When Russell Ohl was investigating diode technologies, he unexpectedly found that the connection of p-type and n-type semiconductor materials led to the voltage produced across the p-n junction when exposed to light [7]. In 1954, the first silicon p-n junction photovoltaic cell was demonstrated at Bell laboratories by Chapin, Fuller and Pearson which had an efficiency of 6% [8]. Then, a further 4% had been achieved [9]. In the early 1960s, the major use of the application of photovoltaic cells was in space for satellites that led to significant interest by the governments [10]. This resulted in motivating technological improvements and efficiency, and as a result, crystalline silicon solar cells (c-Si-SCs) performances increased by more than 26% [11]. Such interest and motivation also promoted the development of new types of devices called thin film photovoltaics such as the Gallium Arsenide (GaAs), Cadmium Telluride (CdTe) and Copper Indium Gallium Selenide (CIGS) heterojunction thin film photovoltaic cells. Other technologies which included the utilisation of polycrystalline silicon and amorphous silicon had emerged in the 1980s [9], [12]. Although these had the advantage of cheaper manufacturing costs, their performance was inferior to that of the single crystal silicon device which is still commonly used till today.

The present record efficiencies of single-junction solar cells from different technologies can be depicted in **Table 1-1**. These are evaluated and measured under standard test conditions (STC), which allows a better comparison among various PV systems. This comparison is dependent on the efficiency variation which has been characterised on the basis of the device area.

Table 1-1: The highest confirmed efficiencies with regard to single-junction solar cells for different absorber materials measured under the global AM1.5 spectrum (1000 Wm^{-2}) at 25°C. Abbreviations: aperture area (ap), designated illumination area (da), total area (t), Fraunhfer-Institut für solare Energiesysteme (FhG-ISE), Institute for Solar Energy Research, Hamelin (ISFH), National Renewable Energy Laboratory (NREL), Japanese National Institute of Advanced Industrial Science and Technology (AIST).

Classification	*Efficiency (%)*	*Area (cm^2)*	*Test centre*	*Date*	*Ref.*
GaAs (thin film)	29.1± 0.6	0.998 (ap)	FhG-ISE	(10/18)	[13]
CdTe (thin film)	22.1± 0.5	0.4798 (da)	Newport	(11/15)	[13]
ClGs (thin film)	22.9± 0.5	1.041 (da)	AIST	(11/17)	[14]
Si (crystalline cell)	26.1± 0.3	3.0857 (da)	ISFH	(02/18)	[11]
Si (multi-crystalline cell)	22.0± 0.4	245.83 (t)	FhG-ISE	(09/17)	[15]
Perovskite (thin film)	24.2± 0.8	0.0955 (ap)	Newport	(01/19)	[16]
Organic (thin film)	16.4± 0.2	0.0413 (da)	NREL	(05/19)	[17]
Organic (thin film)	16.4± 0.4	0.0394 (da)	Newport	(03/18)	[18]

Although GaAs solar cells have gained the highest efficiency as exhibited in Table 1.1, they were exclusively used in space applications due to expensive production costs. The crystalline silicon (c-Si) based PV technologies, on the other hand, have been predominantly and generally used as shown in **Figure 1-1**. In 2018, the total consumed energy from PV technologies exceeded 100GW [19]. 97% of the modules installed in 2018 were manufactured of c-Si due to its stability, non-toxicity and abundance, while thin film modules covered only 3% of the total solar cell market. The used materials in the manufacture of these thin film solar cells are mainly dominated by cadmium telluride (CdTe) and copper indium selenium (CIS) [19]. Moreover, from the 97% of c-Si solar cell coverage, 92% was fabricated using p-type c-Si while the remaining (5%) was covered by n-type c-Si.

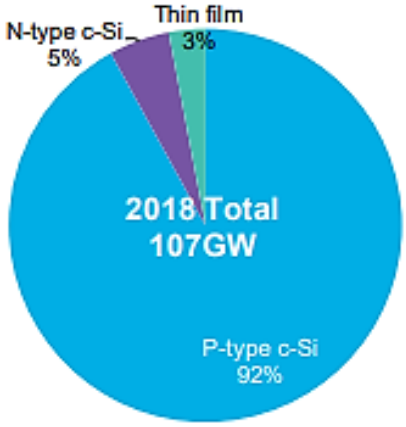

Figure 1-1: The total global shipment of PV modules in 2018 [19].

The current issues in silicon technology regarding the production costs have significantly limited the manufacture of c-Si based solar cells. Hence, the potential now is to produce low cost alternatives with competitive efficiency to the conventional solar cells. This has motivated a large number of researches. Some laboratory-based work demonstrated solar cells with comparable efficiency to the silicon solar cells, however, the stability of their performance and efficiency has not yet achieved which have made them commercially unsuccessful. Therefore, more attention towards thin film photovoltaic solar cells is required to enhance and optimise their stability.

1.3 The Motivation for the Choice of Perovskite Solar Cells (PSCs)

As a new family within the third-generation solar cells, methylammonium lead tri-halide perovskites cells are considered to be one of the most rapidly growing sectors in the development of the solar cell technology. **Figure 1-2** presents the word record device efficiencies for different PV technologies during the period from the mid of 1970s until 2019s. The most efficient solar cells are held by a multi-junction device built from several III-V semiconductors; as high as 47.1% [20]. Due to the fact that single junction PSCs have been only developed recently, their assessment has been undergone for few years; since 2012. Moreover, despite their recent invention, the PSCs efficiency has been rapidly increased to 24.2± 0.8 % by 2019 comparing to their original efficiency which was 3.8% [16]. The current PSCs efficiency is comparable to the efficiency of silicon single junction solar cells, which typically reached an efficiency of 26.1± 0.3% after 60 years of research, as shown in **Table 1-1** and Figure 1-2 [16], [21], [22]. Additionally, PSCs are easier and cheaper to fabricate on a laboratory scale. However, they may encounter some challenges when are produced on an industrial scale. These issues requires the use of tailored engineering to commercial manufacturing [23].

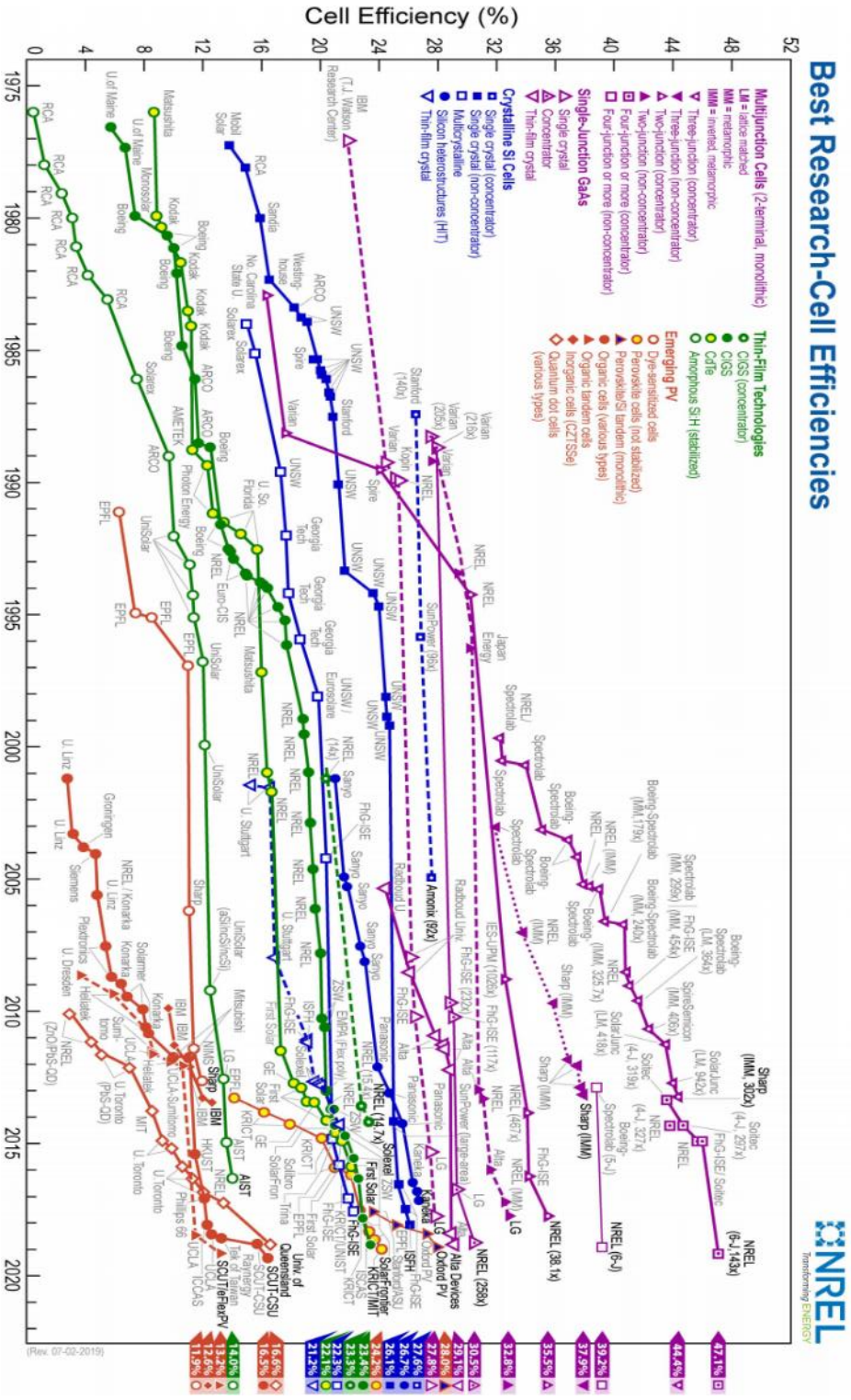

Figure 1-2: National Renewable Energy Laboratory (NREL) chart showing the efficiencies of currently researched solar cells versus the year [20]. Perovskite solar cells (yellow circle with red boundary) have increased efficiencies by a substantial amount in a relatively short space of time, and now have a certified efficiency of 24.2% (as of July 2019).

Despite the high efficiency, the working principles of PSCs are still to be entirely understood. As some progress has been made over time regarding understanding the mechanism of PSCs, the stability of their operation should be improved. The relatively poor stability has to be addressed to enhance the PSCs lifetime for several years [24]. Indeed, there are two sources of stability issues; **(1)** extrinsic factors which affect the perovskite stability when exposed to the environment consisting of humidity, elevated temperature and E-M radiation degradation radiation, and **(2)** intrinsic sources which influence the stability of crystallographic structure of perovskite thin film which could be formed as a consequence of manufacturing techniques that led to changes in the material crystallinity and morphology. A number of fabrication techniques may render some amorphous structures or inhomogeneity in the material which results in high defect density, leading to such stability issues. Currently, in the published literature, the perovskite films have been mostly deposited by spin coating, doctor blade, wire wound, inkjet printing, thermal evaporation, dip coating, and chemical vapour deposition (CVD). However, in most of these processes, a lot of materials are squirted/printed/dropped/spreaded/pressed which do not provide an adequate amount of time for the atoms and/or molecules to organise and bond with other atoms with minimal or no defects causing imperfect crystals. Additionally, few of these processes require a further annealing process to improve the crystallinity and minimise the defects. Is it really required to add more steps (process, etc) to obtain a film with larger defects by using such techniques? Moreover, it is believed that the existence of defects (e.g. point, line, plane defects and/or mixture of cubic and tetragonal phases) within the structure of perovskite material are more likely to be the elementary source of the intrinsic instability for this material, in which the crystallographic structure is significantly degraded when exposed to the environment. In addition, the aforementioned issues would strongly have a bad impact on the grain's shape and size as well as the surface area of the perovskite crystal, as a result, the material's key properties; such as carrier lifetime and the diffusion length, would be affected. Hence, the PV device's efficiency and stability are also influenced. Such a solar cell stability issue; particularly that of crystallographic instability, in perovskite material provides a clear direction as to the original assessment of solar cells and efforts to overcome these limitations are ongoing in this ever-growing research field. Hence, it is required to design thin film deposition techniques to obtain a film with a minimal defect density that may result in a more stable material which would be an ideal step towards the commercialisation of perovskite solar cells. In a nutshell, it can be seen that the field is still in its infancy stages and there are a number of issues to be understood before these materials can really be considered by the manufacturing industries.

1.4 Research Aim and Objectives

This research is aimed to develop novel methods for the deposition of perovskite thin films ($CH_3NH_3PbI_3$ = $MAPbI_3$) by utilising scalable and industry-accepted techniques. It is believed that if a process is designed to provide an adequate amount of time and energy required for the atoms and/or molecules to be bonded in a perfect structure, a stable crystal lattice with a minimum defect-density (ideally zero; which is not possible) would be formed. Therefore, this work was also aimed to focus, along with scalable process, on an atomic scale of processing to deposit material with ATM (Atom to Matter). In such process, it is always required to deposit films or grow any material with the control of precursor with one atom resolution to contribute in enhancing the crystallographic stability of as-deposited perovskite films. This process is similar to ALD (Atomic Layer Deposition), where the materials are obtained with the least defect in the films. In view of that, different CVD deposition methods to deposit $MAPbI_3$ thin films were proposed in this research, including Radio Frequency-Plasma Enhanced Chemical Vapour Deposition (RF-PECVD) and Atmospheric-Pressure Chemical Vapour Deposition (APCVD). As the obtained perovskite material ($CH_3NH_3PbI_3$) has a significant contribution to the understanding of the stability issues reported in the next generation photovoltaics that incorporates perovskite materials over the recent years.

The first synthesis approach is achieved by two-step depositions; **(1)** the deposition of the inorganic part "lead iodide (PbI_2)", using two different techniques, and **(2)** a novel conversion process by utilising an industrial PECVD technique to deposit the organic part "methyl-ammonium (CH_3NH_3 = MA)" into PbI_2 coated thin films to establish the high-quality light absorber layer ($MAPbI_3$).

Since the PbI_2 thin film would be one of the main parts in the final material, its structural, morphological and optical properties were optimised. **Firstly**, two techniques were used to deposit PbI_2 thin films; the spin coating and the thermal evaporation methods. The spin-coated films required a post-annealing step in order to evaporate the solvent accommodated within the lattice, where a variable parameter of annealing duration was studied. The structure, morphology and optical properties of annealed PbI_2 films were investigated by X-ray diffraction (XRD), scanning electron microscope (SEM), atomic force microscope (AFM) and ultraviolet-visible-infrared (UV-VIS-IR) spectroscopy. The evaporated films were also characterised to investigate their crystallinity, morphology and optical properties. **Secondly**, the PbI_2 layers were exposed into a gaseous mixture of methane and ammonia by means of RF-PECVD process. The emphasis is to investigate in detail and explain the growth dynamics and how the variation of PECVD growth parameters affect the structural, optical and electrical properties of the resultant films "perovskite" in a better and simple approach, which has not been established until now to the best of our knowledge.

PECVD process is an existing technique already in use by many PV research labs and commercial companies for the fabrication of various semiconductor devices including amorphous thin film silicon solar cells, polycrystalline silicon solar cells, and nanostructure solar cells as well as other semiconductor devices such as MOSFET, TFT, and memory. Subsequently, this can be easily utilised without the need of a new fabrication process and an expensive equipment to obtain the material withe high stability that can be achieved by reducing the bulk defects and shunting.

In contrast to the non-plasma CVD methods, the PECVD approach is generally used to deposit a material at low-temperature (< 400℃). Basically, applying radio-frequency radiation can lead to the creation of unstable ion-molecules and passive-molecules of methane gas (CH_3^+, H, $C_2H_5^+$, $C_nH_{2n+1}^+$, e^-) and ammonia gas (NH_2^+, H^+, H, e^-) [25]. It is worth mentioning that PECVD requires a thermal energy for PbI_2 thin film. Therefore, under a certain temperature less than 400℃ these induced ions will diffuse into PbI_2 thin film resulting in a quick chemical reaction. It is critical to select the appropriate temperature, as PbI_2 will dissociate at that temperature. Heating the PbI_2 thin film during the reaction could significantly influence the properties of the perovskite film such as its morphology and mechanical stresses (both tensile and compressive) within the film. It may also result in reducing the pinholes and defects which can lead to the improvement of the quality and stability of the perovskite layers. Moreover, the other benefits of PECVD technique include the control over stoichiometry (the compounds involved in a chemical reaction) and conformal substrate coverage. Hence, compared to other techniques that use more stable precursors including solid and liquid sources, the PECVD process could produce higher stability of perovskite layer.

The second CVD deposition approach is motivated by the need to qualify one of the tents of CVD process which is the use of an infinite source to precisely control over the film thickness with providing a desirable stoichiometry. Considering the cost with the use of a scalable process, a non-vacuum CVD process used to deposit perovskite material at atmospheric pressure (APCVD) is another motivation of selecting such deposition method. A built-in-house atomiser has to be designed to work efficiently with the perovskite solution, in term of atomisation PbI_2, MAI molecules along with molecules of the selected solvent simultaneously into the reactor. All precursors will interact with the surface of substrates inside the CVD reactor that are kept at an elevated temperature, where more energy is gained by the atom and further leading towards more controlled growth/deposition of the film. More attention paid in the deposition process/growth dynamic by controlling many parameters including the solution concentration, the growth temperatures, the molar concentration of the precursor, the surface of the substrate, the flow rate of a carrier gas. Due to this growth based on a fine droplet (mist) generation, two atomised methods were conducted in this thesis; bubbler and piezoelectric transducer. The objectives of using these atomisers are to:

- Study of two different physical mechanisms for the atomisation of liquid to form a mist of solvent (DMF) with the compound (PbI_2 and MAI) dissolved in DMF.
- Examine the factors that influence the generation of the droplets in both systems.
- Develop a method to determine the optimal conditions at which the micro-droplets contains a desirable material.
- Determine the necessary deposition conditions for the formation of $CH_3NH_3PbI_3$ thin films.

1.5 Organisation of Thesis

This research was comprised of nine chapters, describing the historic development of perovskite materials and their relatively photovoltaic devices after which the theory of solar cells was presented. In addition, fabrication and characterisation methods as well as the critical analysis of the methods and results were discussed.

Chapter 1 explained the aims and objectives of this research with a brief evolution and market evaluation of PV market. The motivation to select the perovskite material for the PV applications was also provided.

Chapter 2 presented the historical background of perovskite materials. The evolution of the underlying structure of perovskite materials and phase transition were discussed. In addition, the outstanding optical and electrical properties of perovskite materials were introduced for understanding their ability to be an efficient absorber layer of photovoltaic devices. The intrinsic perovskite stability affected by either crystallography structure or environmental conditions was also discussed.

In **Chapter 3**, theoretical basic definitions of photovoltaic cell components, operation and working principle were explained in detail, while a particular emphasis was placed on perovskite solar cells (PSCs). Furthermore, the instability in PSC rising from their relative layers was discussed.

In **Chapter 4**, the fabrication methods used for the synthesis $CH_3NH_3PbI_3$ thin films in this work were explained including: spin-coating, thermal evaporation, plasma enhanced chemical vapour deposition (PECVD) and the two delivery systems used in an atmospheric- pressure chemical vapour deposition process (APCVD); bubbler and piezoelectric transducer.

Chapter 5 explained the characterisation techniques used to investigate the crystallinity, morphology, optical and electrical properties of the prepared thin films.

Chapter 6 devoted to discuss the initial deposition step of perovskite material where PbI_2 thin films deposited by two different methods; spin-coating and thermal evaporation techniques. The spin-coated films were subjected to a different annealing treatment. The attributes of these films were investigated and compared with the attributes of the evaporated film.

In **Chapter 7**, the influence of the growth parameters of the PECVD process on the conversion of PbI_2 into perovskite phase was critically discussed. These varied parameters involve substrate temperature, RF-power and chamber pressure.

In **Chapter 8,** a single-step deposition process APCVD was examined, which based on the atomisation concept of a liquid precursor into a droplet generation "mist". A considerable emphasis was placed on the used atomiser systems. Two atomisers were studied in which different sources of energy applied to the liquid to compromise its stability, hence droplet would generate.

Finally, in **Chapter 9,** the conclusion of this research was expressed concisely. Along with the conclusion; suggestions for the exploration and development of this work in future were mentioned.

References

[1] U.S. Energy Information Administration, "International energy outlook 2018",

https://www.eia.gov/outlooks/ieo/ (accessed 29 July, 2019).

[2] G. Demésy and S. John, "Solar energy trapping with modulated silicon nanowire photonic crystals," *Journal of applied physics*, vol 112, no 7, pp. 074326, 2012.

[3] T. C. Sum and N. Mathews, "Advancements in perovskite solar cells: Photophysics behind the photovoltaics," *Energy & environmental science*, vol 7, no 8, pp. 2518-2534, 2014.

[4] M. A. Green, "Silicon photovoltaic modules: A brief history of the first 50 years," *Progress in photovoltaics: Research and applications*, vol 13, no 5, pp. 447-455, 2005.

[5] A. Becquerel, "Recherches sur les effets de la radiation chimique de la lumière solaire au moyen des courants électriques," *Comptes rendus de LAcadémie des sciences*, vol 9, pp. 145-149, 1839.

[6] C. E. Fritts, "On a new form of selenium cell, and some electrical discoveries made by its use," *American journal of science*, no 156, pp. 465-472, 1883.

[7] R.S. Ohl, *Light-sensitive electric device*, 1941.

[8] D. M. Chapin, C. Fuller and G. Pearson, "A new silicon p-n junction photocell for converting solar radiation into electrical power," *Journal of applied physics*, vol 25, no 5, pp. 676-677, 1954.

[9] A. Goetzberger and C. Hebling, "Photovoltaic materials, past, present, future," *Solar energy materials and solar cells*, vol 62, no 1, pp. 1-19, 2000.

[10] H. A. Zahl and H. K. Ziegler, "Power sources for satellites and space vehicles," *Solar energy*, vol 4, no 1, pp. 32-38, 1960.

[11] F. Haase, C. Hollemann, S. Schaefer, A. Merkle, M. Rienaecker, J. Krügener, R. Brendel and R. Peibst, "Laser contact openings for local poly-si-metal contacts enabling 26.1%-efficient POLO-IBC solar cells," *Solar energy materials and solar cells*, vol 186, pp. 184-193, 2018.

[12] J. Nelson, "The physics of solar cells." 2003.

[13] M. A. Green, Y. Hishikawa, E. D. Dunlop, D. H. Levi, J. Hohl-Ebinger and A. W. Ho-Baillie, "Solar cell efficiency tables (version 52)," *Progress in photovoltaics: Research and applications*, vol 26, no 7, pp. 427-436, 2018.

[14] J. Wu, Y. Hirai, T. Kato, H. Sugimoto and V. Bermudez, , "New world record efficiency up to 22.9% for cu (in, ga)(se, S) 2 thin-film solar cells," In *7th world conference on photovoltaic energy conversion (WCPEC-7)*, 2018, pp. 10-15.

[15] F. Schindler, B. Michl, P. Krenckel, S. Riepe, J. Benick, R. Müller, A. Richter, S. W. Glunz and M. C. Schubert, "Optimized multicrystalline silicon for solar cells enabling conversion efficiencies of 22%," *Solar energy materials and solar cells*, vol 171, pp. 180-186, 2017.

[16] E. H. Jung, N. J. Jeon, E. Y. Park, C. S. Moon, T. J. Shin, T. Yang, J. H. Noh and J. Seo, "Efficient, stable and scalable perovskite solar cells using poly (3-hexylthiophene)," *Nature*, vol 567, no 7749, pp. 511, 2019.

[17] S. Dong, K. Zhang, B. Xie, J. Xiao, H. Yip, H. Yan, F. Huang and Y. Cao, "High-performance large-area organic solar cells enabled by sequential bilayer processing via nonhalogenated solvents," *Advanced energy materials*, vol 9, no 1, pp. 1802832, 2019.

[18] G. Zhang, J. Zhao, P. C. Chow, K. Jiang, J. Zhang, Z. Zhu, J. Zhang, F. Huang and H. Yan, "Nonfullerene acceptor molecules for bulk heterojunction organic solar cells," *Chemical reviews*, vol 118, no 7, pp. 3447-3507, 2018.

[19] X. Wang and A. Barnett, "The evolving value of photovoltaic module efficiency," *Applied sciences*, vol 9, no 6, pp. 1227, 2019.

[20] NREL - National Center For Photovoltaics, "“Research cell efficiency records” https://www.nrel.gov/pv/cell-efficiency.html (accessed 29 July, 2019).

[21] M. A. Green, K. Emery, Y. Hishikawa, W. Warta and E. D. Dunlop, "Solar cell efficiency tables (version 45)," *Progress in photovoltaics: Research and applications*, vol 23, no 1, pp. 1-9, 2015.

[22] Q. Wali, N. K. Elumalai, Y. Iqbal, A. Uddin and R. Jose, "Tandem perovskite solar cells," *Renewable and sustainable energy reviews*, vol 84, pp. 89-110, 2018.

[23] R. F. Service, "Turning up the light," *Science (new york, N.Y.)*, vol 342, no 6160, pp. 794-5, 797, Nov 15 2013.

[24] M. A. Green, A. Ho-Baillie and H. J. Snaith, "The emergence of perovskite solar cells," *Nature photonics*, vol 8, no 7, pp. 506-514, 2014.

[25] A. Fridman, *Plasma chemistry*, Cambridge university press, 2008.

Chapter 2 Structure, Optical and Electrical Properties of Perovskite

In this chapter, the status of perovskite materials since its discovery has been presented in section 2.1. In section 2.2, the underlying structure evolution of perovskite material and phase transition has discussed. The formation of energy levels of the electronic configuration of perovskite materials is introduced before going on to their outstanding optical and electrical properties which make it suitable to be an efficient absorber layer for photovoltaic devices. Section 2.3 then describes the various deposition methods to obtain perovskite materials including advantages and disadvantages. Finally, section 2.4 focuses in greater details on the perovskite stability issues due to the intrinsic (crystal structure) and extrinsic (environmental conditions) factors.

2.1 Perovskite Material History:

The name "perovskite" was originally used to describe a mineral composed of calcium titanate ($CaTiO_3$). This mineral was discovered in the Ural Mountains of Russia by the German mineralogist Gustav Rose in 1839 and Rose named the mineral 'perovskite' in honour of the Russian mineralogist Lev Perovskite [1]. Researchers now use the name "perovskite" to describe any crystals with a structure similar to that of $CaTiO_3$; with typical structure of ABX_3, where A and B represent monovalent and divalent metal cations respectively, while X is an anion (**Figure 2-1**).

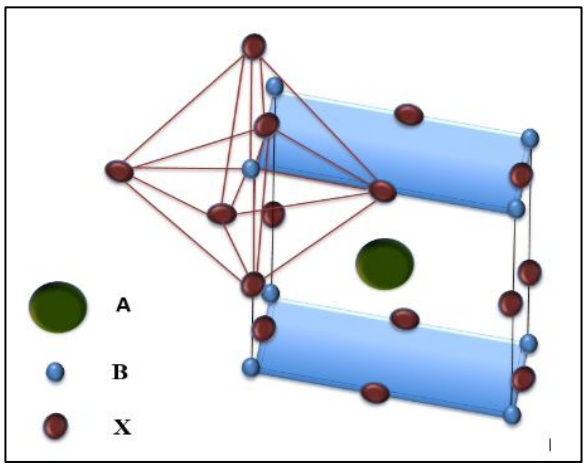

Figure 2-1: ABX_3 perovskite structure with X bonded to the A- ion and B-ion, thereby creating a three-dimensional cubic lattice.

Figure 2-1 illustrates the cubic structure of a conventional perovskite with ABX_3 structure, where the A cation is placed in the cuboctahedral interstices with a corner-sharing octahedral BX_6 unit [2]. A well-investigated class of perovskite materials are based on oxides (ABO_3), which a exhibit variety of properties such as ferroelectric, dielectric and piezoelectric behaviours [3]. Halide perovskites are another sub-class of perovskite family that have attracted the attention of the PV community. In halide perovskite, A can be an organic or an inorganic cation, B is commonly lead (Pb) or tin (Sn), and X is a halide anion (X= iodide (I), bromide (Br), chloride (Cl)). In this thesis, more attention will be given to halide perovskite materials.

Caesium lead trihalides ($CsPbCl_3$, $CsPbBr_3$ and $CsPbI_3$) were the first known types of halide perovskite material that were synthesised from aqueous solution in 1893 by Wells [4]. The investigation of these materials ($CsPbX_3$, X=I, Br, Cl) using X-ray crystallography was carried out by Moller in order to determine the arrangement of the atoms and confirmed the presence of the perovskite structure [5]. It was further discovered that $CsPbCl_3$ exhibited a maximum spectral sensitivity in the violet region of visible spectrum (EM), while $CsPbBr_3$ in the blue-to-green region and $CsPbI_3$ in the red region [6]. After successful work on $CsPbX_3$, Moller further carried out work on caesium tin trihalides ($CsSnX_3$, where X = Cl, Br and I) [7]. Although $CsSnX_3$ was earlier discovered in the 1920s, but it had not been experimentally investigated on the structural and phase equilibrium until the late 1950s [8]. Synthesis method for $CsSnX_3$ via aqueous solution obtained from the melts of anhydrous halides was developed by Scaife et al. [9], as this material was not affected by both oxygen and water. It was further reported that $CsSbBr_3$ and $CsSnI_3$ exhibited a tetragonal structure and orthorhombic structure when synthesised at low temperatures (12 ºC) respectively.

Besides all-inorganic perovskites, a series of perovskite-materials were investigated, in which the A-site cation is occupied by organic molecules to form an organic-inorganic perovskite family. The most basic organic cation used at the A site in perovskite structure is CH_4^+. In the early of 1960s, the organic cation was incorporated into the perovskite structure, in which methane CH_4^+ ion formed the A cation of the structure (CH_4CdCl_3) as reported by Wyckoff [10]. In view of this, formamidinium ($NH_2CH{=}NH_2^+$) [11] and tris (dimethylammonium) $(NH_2(CH_3)_2)^+$ cations [12] were utilised at the A site of perovskite material.

The organic group methylammonium ($CH_3NH_3^+$, MA) was identified by Weber, which occupied the A site cation in the Sn based trihalide ($CH_3NH_3SnX_3$) perovskites [13]. It was discovered that, the $CH_3NH_3SnBr_xI_{3-x}$ (x = 0-3) possessed a cubic structure with unit cell parameters of a = 5.89Å (x=3), a = 6.01Å (x=2) and a = 6.24Å (x=0). Weber further discovered the organic Pb-based trihalide perovskites as promising materials for use in PV application. This material's ($CH_3NH_3PbX_3$ (X=Cl, Br and I)) unit cell parameters were identified to be a = 5.68Å (X = Cl), a = 5.92Å (X = Br) and a =

6.27Å (X = I) in its cubic form [14]. This material was earlier used in Light Emitting Diodes (LED) and Thin Film Transistors (TFT) by David Mitzi and his co-workers between 1990s to early 2000s [15]. In 2009, Myasaka reported for the first time their application in PV devices, fabricated using two perovskite compounds ($CH_3NH_3PbI_3$ and $CH_3NH_3PbBr_3$) [16].

2.2 Material Properties of Methylammonium lead tri-iodide ($CH_3NH_3PbI_3$) perovskite

2.2.1 Phase Transformations in the Crystal Structure

Since the organic-inorganic halide-based perovskite material is more complicated than the inorganic semiconductor absorber materials such as silicon (Si), CdTe, and CIGS, understanding its crystal structure and the phase transitions due to the static and dynamic disorder are essential. This helps to understand the origin of their behaviour in PV performance. The distortions/rotation in the perovskite structure is strongly dependent on the inorganic components, i.e. the lead and halide atoms forming the 'BX_6' octahedral cage that serves as the dominant component. However, these components can cause a disorder orientation of the $CH_3NH_3^+$ cation in the crystal structure as it resides in the interstitial site of the 'BX_6' octahedral framework/network [17]. Four solid phases of $CH_3NH_3PbI_3$ have been reported as a function of temperature, three of them perovskite-like (named as α, β, and γ) and the fourth one is δ-phase that refers to the non-perovskite structure [18]. The possible tilted perovskite structures can undergo a phase transition to a cubic-phase (α) at temperatures above 327 K [19]. For T < 327 K, a non-centrosymmetric tetragonal β-phase is formed with lattice parameters of a = 8.855 Å and c = 12.659 Å [16]. **Figure 2-2** shows the cubic (α) and tetragonal (β) phase of the $CH_3NH_3PbI_3$ lattice; the transition from α- to β-phase shown in this Figure 2-2, occurs at 293 K with a PbI_6 tilting angle of 16.4°. As a consequence of this tilting of the octahedral framework, the length of the unit cell is doubled [20]. The re-orientation of the $CH_3NH_3^+$ cation, which is noticed in the α- and β-phase, could be the source of the ferroelectric phenomenon. Under an external electric field, a hysteresis behaviour seen in the current/voltage curves is corresponding to the organic cation re-orientation and the inorganic Pb-I lattice resistance [20, 21]. For T < 162 K, the phase transition of the perovskite structure to orthorhombic phase (γ) could be achieved. In this phase, the $CH_3NH_3^+$ cations are ordered. As the phase transition from α to β and γ with decreasing temperatures, leads to an increase in the tilting angle as well as deformation effects [22]. Aforementioned transition phases occur in the solid form; however, the fourth phase transition (δ) can be formed in the presence of solvents [20].

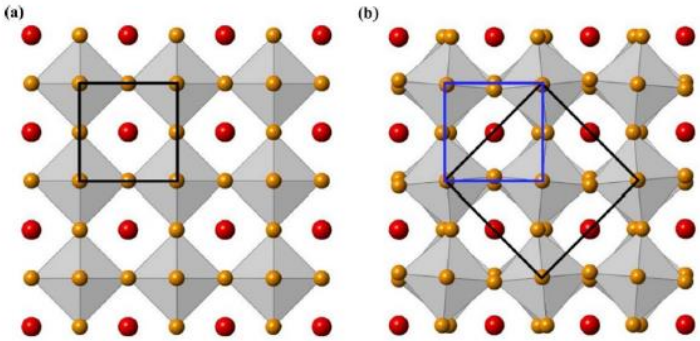

Figure 2-2: Lead halide perovskite lattice; (a) cubic-phase and (b) tetragonal-phase. A cations (CH_3NH_3) are red, X halide atoms are yellow and the M cation is located in the core of the grey octahedra (reprinted with permission [18]).

2.2.2 Optical Energy Bandgap

The cationic and anionic components of the common organometal halide perovskite ($CH_3NH_3PbI_3$) are $CH_3NH_3^+$ (MA), Pb^+ and I_3^-. The configuration of electrons in the outer orbitals of natural Lead (Pb) atom is $5d^{10}6s^26p^2$, which shows four valence electrons; while two valence electrons are present in Pb^+ ion that is in perovskite material according to its outer orbital ($5d^{10}6s^26p^0$). Similarly, natural Iodine (I) has seven valence electrons in the outer orbital ($4d^{10}5s^25p^5$), while an extra valence electron is present in the I^- ion (anionic compound present in perovskite material) according to the configuration of electrons in its outer orbitals ($4d^{10}5s^25p^6$). Thus, the conduction band minimum (CBM) of $CH_3NH_3PbI_3$ is composed of s-antibonding state of empty Pb 6p and I 5s orbitals, and the valence band maximum (VBM) is formed by the s-antibonding states of Pb 6s and I 5p [23-25]. As a result, direct band gap with an estimated value of energy ~1.5 eV is formed (**Figure 2-3 a**) [25- 27]. Therefore, perovskite material has a semiconducting property and is suitable for PV application [24], [28]. Due to its band gap of 1.55eV, semiconductor $MAPbI_3$ should generate a photocurrent up to 27 mA/cm^2 [29].

There are numbers of simulated studies of the electronic structure of $CH_3NH_3PbI_3$. It was discovered by Borriello et al. [30] that the organic cation's function ($MA=CH_3NH_3^+$) in defining the band structure, and in particular, the conduction and valence band orbitals was not significant, although it is important in establishing charge balancing within the lattice [23, 24, 31]. The outcomes from calculations demonstrated that the stability of the perovskite cage against distortion depended significantly on the embedded cation. Its electronic properties may be altered by affecting the B-X bond length, a feature that has been shown to be crucial in determining the bandgap [32]. However, the crystal lattice geometry can be affected by the organic cation size and its orientation that causes strain on the PbI_6 octahedra, hence altering the band structure [33, 34]. As a consequence of a rapid

rotation of MA^+ cation at room temperature [25, 35], a dynamic variation in the bandgap has been noticed. These resulted in the creation of an indirect transition positioned slightly below the direct band gap (**Figure 2-3 b**) [25]. Furthermore, in this diagram, strong absorption and long diffusion length can be linked to the existence of both direct and indirect bandgaps. Existence of indirect band gap, in the case of oriented MA^+, has a benefit in having longer lifetimes since the exciton's recombination will thermalise to the band edge. Meanwhile, the slightly higher energy of the direct band gap, in this case, will keep the strong absorption of the perovskite materials.

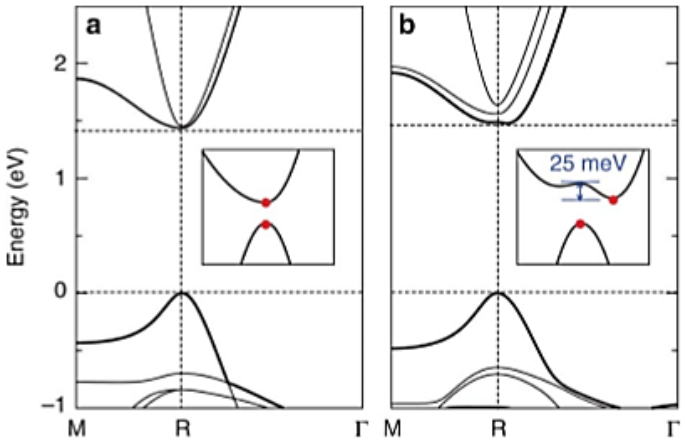

Figure 2-3: The $CH_3NH_3PbI_3$ band structure calculated by density functional theory for varied orientation of the $CH_3NH_3^+$ cation along (a) [111] direction forming direct band gap and (b) [011] direction forming indirect band gap (reprinted with permission [25]).

Tuning the bandgap to increase the absorption wavelengths region is essential in order to enhance the performance of solar cells. Recent studies have revealed that halide perovskites (AMX_3) offer the possibility of tuning the bandgap by varying the combination of all of the cationic and anionic components [36, 37]. Two ways were proposed by researchers to alter the perovskite bandgap. Geng et al. [38] showed that the organic cation can control the bandgap of the inorganic cage M-X-M by changing their bond lengths and bond angles. For instance, by using formamidinium $HC(NH_2)_2^+$, a noticeable reduction in the bandgap of about 0.07 eV was observed [39]. The other way is to directly modify the dimensions of the inorganic cage that modifies the M – X bond length [40]. This process can be understood as aforementioned, that the CBM and the VBM) is formed by PbI_6 cage, in case of $CH_3NH_3PbI_3$. Therefore, the replacement of the big Pb^{2+} atoms with small Sn^{2+} atoms leads to a reduction in the bandgap from 1.55 eV to 1.17 eV by changing the VBM and CBM positions [41]. Moreover, a reduction of band gap value can be obtained by manipulating the halide as Eperon et al. reported [42]. They compared the bandgap values between a mixture of halides ($FAPbI_X\ Br_{3-x}$) and $FAPbI_3$ and found that a change in value from 2.23 eV ($FAPbI_3$) to 1.48 eV ($FAPbI_X\ Br_{3-x}$) observed [42]. The schematic energy level diagram for different perovskite materials is shown in **Figure 2-4**.

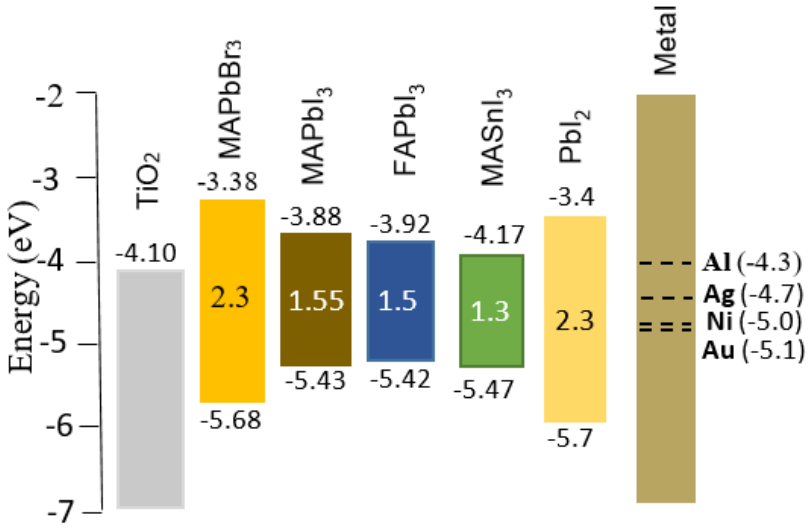

Figure 2-4: Comparing the VB and CB of perovskite materials, titania and various metals.

2.2.3 Balanced charge-generating, transporting and collection behaviour

Justifying the organic-inorganic halide perovskite materials' optical and electrical properties are essential, to determine their suitability as candidates for fabrication of high efficiency PV devices. Although the perovskite film has absorption coefficient lower than many polymers (fullerene blends used in organic solar cells [43]), it is significantly higher than traditional inorganic semiconductors in the visible light region such as crystalline silicon [44] and GaAs [45] (**Figure 2-5**). Therefore, ultrathin layer of organic-inorganic halide perovskite material (~500-600 nm) is sufficient to effectively absorb the incident photons, leading to the reduction in used material and low-cost of production.

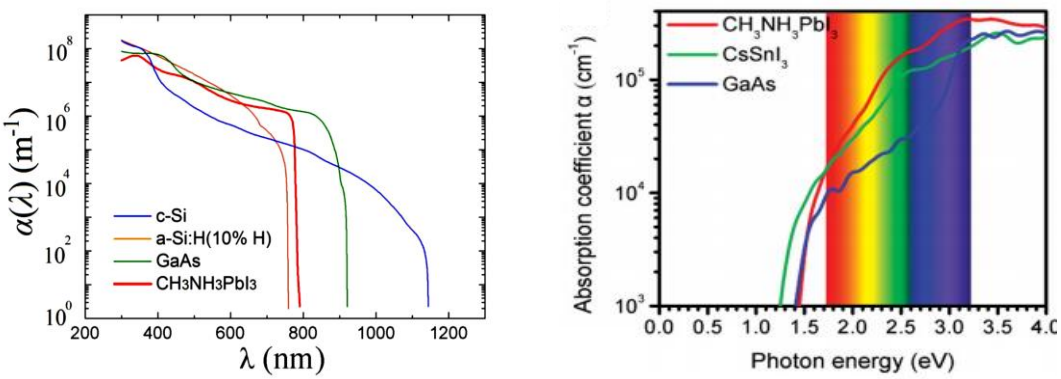

Figure 2-5: Absorption coefficient of different PV materials at rang of wavelengths (reprinted with permission from [44], [45]).

Strong optical absorption of $CH_3NH_3PbI_3$ is one of perovskite's outstanding properties [46]. Thus, the photoexcitation may lead to the generation of exciton (electrons and holes pair (e-h)) under illumination that are electrostatically bonded with an estimated value of binding energy (E_B < 5 meV) for tetragonal phase and is about ~15 meV for orthorhombic phase at room temperature [47], [48]. Since the thermal energy (26 meV) at room temperature is higher than the exciton binding energy (E_B) in perovskite materials, excitonic nature/type in $CH_3NH_3PbI_3$ is classified to be Wannier-Mott mechanism with a large exciton radius [47, 48]. This small binding energy of the excitons can be expected to free charges in picoseconds when exposed to light [49, 50].

Once the generation of electrons and holes has taken place under ambient sunlight, they have ability to move along the perovskite thickness because of the extremely low non-radiative recombination rates, which is in tens of micro-second timescales [51]. This property contributes to the high open circuit voltage (V_{OC}) measured in perovskite solar cells [52]. However, in the case of radiative recombination of the excitons, carriers can be led to emitting photons causing Photoluminescence (PL) of the perovskite material. The PL peak emission of $CH_3NH_3PbI_3$ has been found to be at ~770 nm [46].

Carrier mobility is another important parameter for electrical performance of PV device. Such perovskites ($CH_3NH_3PbI_3$ and $CH_3NH_3PbI_{3-x}Cl_x$) have free charge carrier mobilities in the range of 10-20 $cm^2V^{-1}s^{-1}$ [50, 53], which is several times (3-4 orders of magnitude) higher compared to typical organic semiconductors (fullerene derivative [6,6]-phenyl-C_{61}-butyric acid methyl ester (PCBM)), where the mobility is of the order of 10^{-3} $cm^2V^{-1}s^{-1}$ [54, 55]. Thus, long electron-hole diffusion lengths have been measured of the order of 1 micrometer in the mixed halide perovskite ($CH_3NH_3PbI_{(3-x)}Cl_{(x)}$), and hundreds of nanometers in iodide based perovskites [46, 56- 58]. This increased diffusion lengths in the mixed halide perovskites may be attributed to changes in the film morphology. Likewise, single crystal $CH_3NH_3PbI_3$ grows with good long-range ordering compared to polycrystalline $CH_3NH_3PbI_3$ films. Therefore, single-crystal $CH_3NH_3PbI_3$ possesses sharp band-edge absorption, high carrier mobility, longer lifetimes and long diffusion lengths (> 175 um) that is higher than that of polycrystalline films, as a result of lower density of trap states [59, 60]. In the case of the polycrystalline form, it mostly contains point defects (these determine n-type or p-type behaviour) or grain boundary defects (trap states, recombination centres) [59].

In addition to the properties of perovskite materials mentioned above, they also exhibit ambipolar carrier transport characteristics, meaning that the material behaves as light harvesting and transporting layer for both electrons and holes [61]. High ambipolar performance of perovskite was clearly observed when it was exposed to light, demonstrating balanced electron and hole mobilities and diffusion lengths [46, 50, 62, 63]. As a result, the degradation in fill factor (FF) and PCE would be

significantly minimized/reduced [43]. Due to this unique intrinsic property of perovskite, it can be used in all types of PSCs architectures (see section 3.2.3) [64, 65].

However, the deposition process of perovskite materials is critical to their electrical, optical and physical properties, since carrier separation, transport and recombination rates depend on the morphology, thickness, crystallinity and crystallite size of the perovskite layer, in order to obtain high PV performance [66, 67]. Different deposition methods can produce different quality of perovskite materials as explained in the following section.

2.3 Preparation methods of perovskite material

To date, there are number of deposition techniques established (**Figure 2-6**) by which the quality and properties of perovskite thin films were altered in order to produce a highly crystalline and uniform films. The film thickness has to be thick enough to maximise the absorption of incident photons and thin enough for the fast collection of the generated charges with less trap-defects and large grain size. Solution-based deposition methods and vapour-based deposition methods are considered and details of these methods, their advantages and disadvantages are summarised in the next sections.

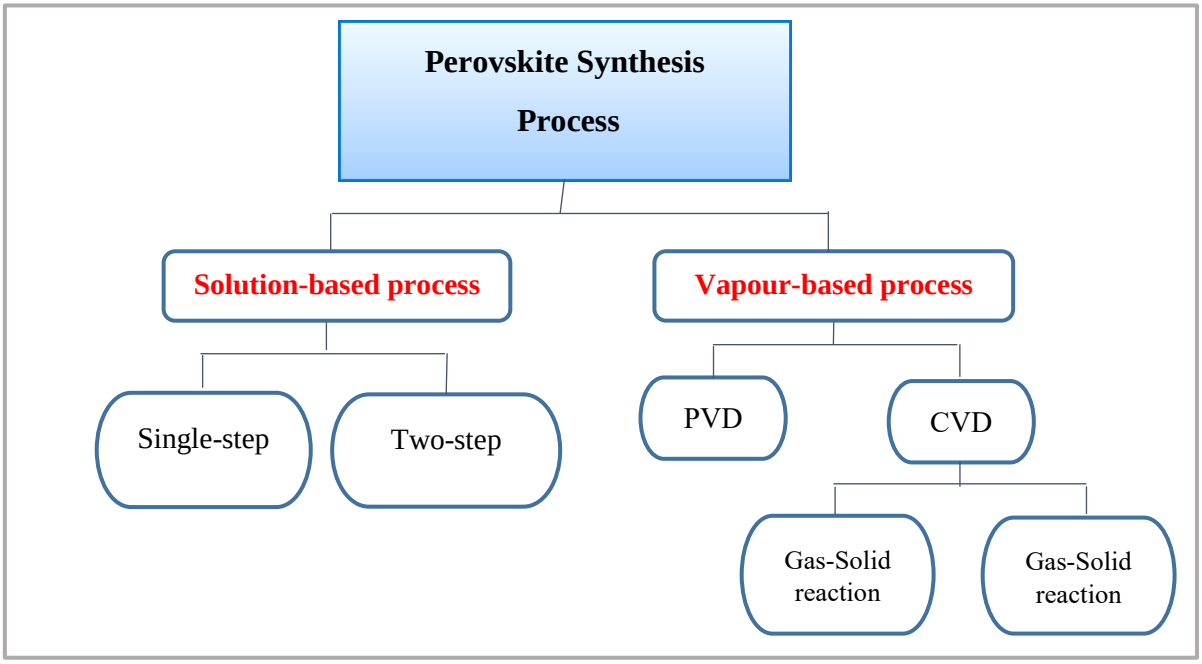

Figure 2-6: Different methods of synthesis techniques for perovskite materials.

2.3.1 Solution-based deposition techniques

Among various approaches, solution-based methods are widely used for the deposition of perovskite thin films because of its cost-effectiveness and simplicity. However, it is difficult to produce thin film

in the large scale using this method. In addition, the partial surface coverage of coated films leads to the existence of defects in the film. As a result, the formation of pinholes within the film facilitates the connection between HTL and ETL that could lead to high charge recombination. Therefore, a significant reduction in the device performance is observed because of decrease in fill factor and open-circuit voltage [68].

A number of solution processing techniques have been developed for the deposition of halide perovskites, such as doctor-blade coating [69], slot-die coating [70], spraying [71], spin coating [66], and inkjet printing [72].

2.3.1.1 Conventional Solution Techniques

Spin coating is a commonly used solution technique at laboratory scale, which can be mainly divided into two broad categories: one-step and two-step depositions. In one-step deposition, the precursor solution is prepared by blending the organic and inorganic solute materials and dissolving them in polar aprotic solvent such as N,N-dimethylformamide (DMF) [73], gamma-butyrolactone (GBL) [74], or dimethyl sulfoxide (DMSO) [75]. After the film is coated on the substrate, annealing step is required for inducing the crystallisation of the film and evaporation of the residual solvent. This step is usually done under N_2 atmosphere at 70-110 ºC and the duration ranges from minutes to a few hours. However, it can be reduced to few seconds by utilising NIR radiation [76] and to a fraction of second via photonic flash-annealing [77]. Conversely, deposition of PbX_2 and MAX has been suggested in a two-step process obtained by the following procedure: initially, PbI_2 thin film is deposited after dissolving in DMF solution, followed by deposition of a 2-propanol solution of CH_3NH_3I over the PbI_2 film. The second step is usually performed by various methods: dipping the PbI_2 thin film into IPA solution of MAI [78], spin-coating the MAI solution on top of the PbI_2 thin film [79], or exposing the PbI_2 thin film to MAI vapour [80]. The prepared perovskite layers by different thin film methodologies results in different thin film morphologies as shown in **Figure 2-7**.

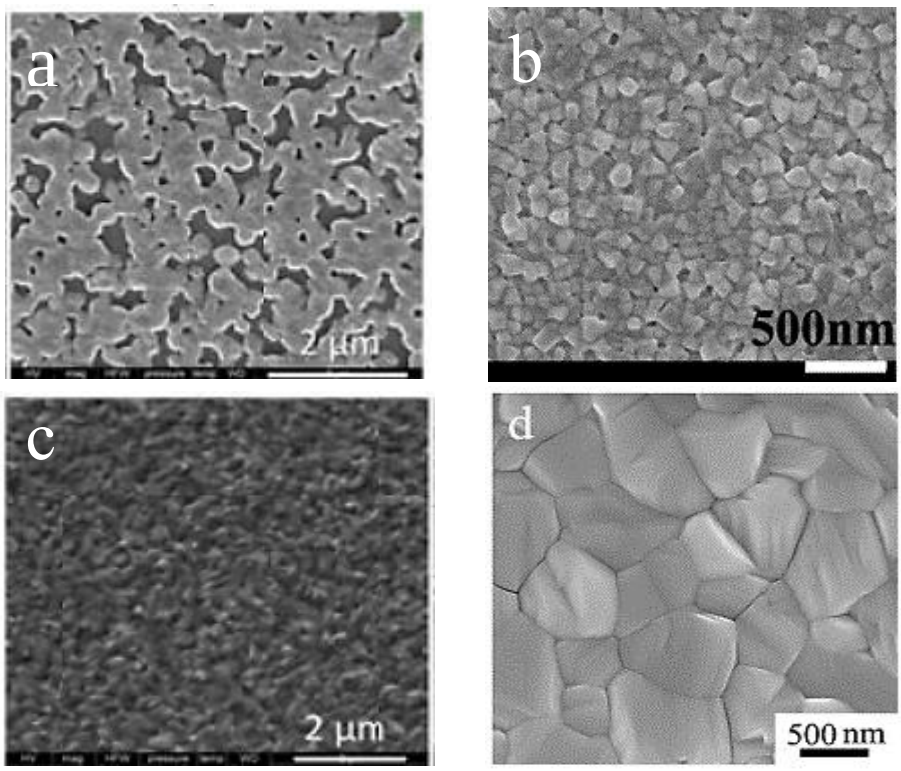

Figure 2-7: Top-view of prepared perovskite film deposited by different methods: a) one-step deposition, b) two-step deposition by dipping technique, c) two-step deposition by spin-coating technique, d) two-step deposition by vapour assisted (reprinted with permission from [81], [82], [83]).

Despite the simplicity of the aforementioned deposition methods, it is hard to control the crystallization process that leads to inhomogeneity in the material, surface roughness and partial conversion to perovskite. Hence, reproducibility is difficult, and the device performance decreases. Therefore, numerous modifications on solution processing techniques have been proposed to control the crystallisation kinetics.

2.3.1.2 Solvent-Engineering methods

In order to enhance the perovskite crystallinity, two solvent-engineering methods have been reported, including: (1) additive-containing perovskite precursor solution and (2) anti-solvent additive treatment. Number of chemical additives have been adopted to control film morphology such as hydroiodic acid (HI) [84], hydrochloric acid (HCl) [85], 1,8-diiodooctane (DIO) [86], 5-ammoniumvaleric iodide (5-AVA) [87], N-cyclohexyl-2 pyrrolidone (CHP) [88], and deionized water (DI-H_2O) [89- 91]. These additives resulted in improving the uniformity of films since they enhance the material solubility in the solvent [84].

In another approach, to control the perovskite crystallisation rate, an anti-solvent treatment step is employed. The function of the anti-solvent additive is to remove the residual solvent during the formation of an intermediate phase leading to improvement in the film uniformity and the solar cell performance [92]. In this study, $CH_3NH_3Pb(I_{3-x}Br_x)$ was formed by dissolving the precursors in a mixture of two solvents DMSO and GBL, and the anti-solvent treatment step was done by employing toluene dripping during the spinning of the precursor. The results obtained from this research, encouraged more uses of anti-solvent treatment on different architectures of perovskite solar cells such as planar structures [74, 93], and mesoscopic TiO_2/perovskite [94].

The selection of anti-solvent is critical, since it influences the rate of nucleation and crystal growth [95]. Therefore, a reduction in the Gibbs energy during crystal formation is enforced by this treatment. The influence of three different anti-solvents including Chlorobenzene (CB), Dichloromethane (DCM), and Toluene (TL), on the morphology of the bromide-based perovskite ($CH_3NH_3PbBr_3$) thin films was examined. Under the same deposition conditions, TL resulted in a higher crystalline, denser, smoother, pinhole-free film when compared to the other anti-solvents (CB and DCM) even without being subjected to post-annealing treatment. It is worth mentioning that the organic-inorganic hybrid perovskite has hydrophilic nature. Therefore, the nonpolar solvents lead to a reduction in its solubility forming a supersaturated condition. Due to TL having a higher non-polarity than the others, rapid homogeneous nucleation was occurred and thus resulted in the formation of higher quality films with full surface coverage [95].

2.3.1.3 Solvent-Solvent Extraction (SSE)

Another solution processing strategy have been utilised in order to improve the crystallinity of perovskite film deposited by a conventional one-step spin-coating process at room temperature, which is known as solvent-solvent extraction (SSE) [96]. Such method provides a superior crystallisation of ultra-uniform films with controllable thickness without the need for a post-annealing step. The SSE process can be realised as follows: a spin-coated perovskite thin film is prepared from an equimolar solution of PbI_2 and MAI in N-Methyl-2-pyrrolidone (NMP) and then they were immediately immersed in a bath of diethyl ether ($C_2H_5OC_2H_5$: boiling point 35 ^oC) at room-temperature for 2 minutes. The perovskite planar solar cells deposited by SSE method achieved an average PCE of 10.1% [96].

Despite the improvements in the crystallinity and high efficiency of these solution methods, there are limitations to scale-up, since a preparation of full-coverage, pin-hole free and phase-pure perovskite thin film by spin-coating technique on large area substrates, still remains a challenge. The vapour-based deposition technique is a promising alternative that can provide opportunity to scaling-up of perovskite thin film solar cells.

2.3.2 Vapour-based deposition techniques

Perovskite material is also deposited by a vapour-deposition technique. This technique emerges as the preferred route since it has several predominant advantages over solution-processing, in which extremely uniform film with ordered perovskite crystallites can be formed due to the much slower gas-phase intercalation reaction rate [97]. In the meantime, the vapour deposition parameters including pressure, temperature, and the evaporation rate can be easily controlled, as these help to control the crystal structure and the film morphology along with improving the reproducibility.

2.3.2.1 Physical-Vapour-Deposition (*PVD*)

2.3.2.1.*a* Single-Step Evaporation Process

Several vapour-based methods have been reported to synthesise perovskite material. High-vacuum thermal vapour-based deposition was firstly reported by Snaith et al. [98]. Dual-source thermal evaporator was employed to co-evaporate the powder of CH_3NH_3I and $PbCl_2$ for the formation of thin film of $CH_3NH_3I_{3-x}Cl_x$. The experiment was carried out inside a glovebox under N_2 gas environment. CH_3NH_3I and $PbCl_2$ co-evaporated over c-TiO_2 coated FTO glass at 120 $^{\circ}$C for the former and 350 $^{\circ}$C for the latter at the same vacuum pressure of 10^{-5} mbar. The deposited perovskite films were then subjected to annealing process in order to enhance the film crystallinity, where a high uniform perovskite thin films with pinhole-free and nanometer-sized crystalline structure was obtained [98]. However, there is a stoichiometric problem with $MAPbI_3$ thin films due to the poor control of MAI deposition rate. To overcome this problem, a sequential layer-by-layer evaporation deposition was proposed [99].

2.3.2.1.*b* Two-Step Evaporation Process

This method is similar to the process of two-step solution deposition, where inorganic film (e.g. $PbCl_2$) and organic film (e.g. MAI) are thermally deposited onto the substrates sequentially. The substrate temperature in this method is crucial to the performance of the device. Solar cell based on perovskite film deposited at 75 ºC has been shown to have the best performance.

Since then, Yang et al. proposed a modification on the sequential evaporation process in which a layer-by-layer deposition of $PbCl_2$ and CH_3NH_3I were performed alternatively [100]. This provides films with superior uniformity, full surface coverage and high crystalline purity phase. Solar cell performance based on this method showed a PCE of 16.03%. Meanwhile, by increasing the active layer area from 0.1 cm^2 to 1 cm^2, the device achieved a PCE of 13.87%.

Perovskite solar cell of PCE 17.6% was fabricated by Hsiao et al. where all-vacuum deposition technique of the materials was employed [101]. During the sequential evaporation, the partial pressure of the organic halide of perovskite material was varied between 10^{-3}-10^{-5} torr for 2 hours at 75 ºC substrate temperature. Under the vapour pressure of 10^{-4} torr, smooth surface and high crystalline thin films with grain/crystallite sizes up to microns were obtained. However, the incomplete transformation into perovskite phase was noticed at low vapour pressure of 10^{-5} torr, indicating that longer reaction times (20 h) were required.

In summary, the films obtained by thermal evaporation show high-quality, pin-hole free film but, high-cost of equipment and energy consumption led to increased fabrication cost of perovskite solar cells [102].

2.3.2.1.c Vapour-Assisted-Solution-Process (VASP)

In contrast to the aforementioned PVD methods that require high vacuum systems, perovskite thin film can also be deposited under atmospheric condition or low vacuum (~10^{-2} torr). Vapour-Assisted-Solution-Process (VASP) technique is considered as a combination method in which the perovskite material can be prepared by the interaction between gas-solid (G-S) phases. Thus, this technique combines the advantages of vapour-deposition and solution-process, which prevents the existence of solvation intermediate phases ($MAPbI_3$-DMF) at the G-S interface as observed in the solution-based processes. The VASP is *in-situ* G-S interaction process, where the PbI_2 film is deposited by spin-coating and then subsequently treated with the MAI vapour *in-situ*. [83]. To encourage the G-S crystallisation, the PbI_2 films were annealed/kept at 150 ºC in N_2 atmosphere during the interaction with MA vapour. The reaction time is 2 hours for the conversion of 200 nm PbI_2 thin film into perovskite ($CH_3NH_3PbI_3$), with a resultant perovskite film thickness of ~350 nm. This planar solar cell yielded an efficiency of 12.1%. This method was further explored by studying the effect of different substrate temperatures and deposition time on the growth mechanism [103, 104]. Nevertheless, this approach (VASP) requires controlled atmosphere e.g. N_2 gas filled glove box, which make it inappropriate for mass production.

In short, PVD techniques either require high vacuum conditions as in co-evaporation and sequential thermal evaporation or inert ambience as is required in the vapour assisted deposition system, which will lead to their increased cost. Therefore, researchers developed another vapour-based deposition strategy that can yield good film quality under robust conditions as well as improving the device performance in order to be competitive with the solar cells fabricated by both solution and PVD methods [105].

2.3.2.2 Chemical-Vapour-Deposition (CVD)

CVD techniques are being widely used for the commercial deposition of various kinds of semiconductor materials [106- 108]. This technology supports large-scale module fabrication method. Moreover, well-controlled parameters of tubular CVD such as vapour-pressure, reaction temperature and flow rate of the carrier gas in a small quartz furnace, will provide more precise conditions for the growth of a various range of thin films with high reproducibility. There are several types of tubular CVD techniques, which can generally be categorised based on the growth process of perovskite performed via either gas-solid (G-S) reaction known as two-step CVD, or a so-called one step CVD where only gas-phase reaction take place.

2.3.2.2.*a* Gas-Solid (G-S) CVD Reaction

- **Hybrid Chemical Vapour Deposition (HCVD)**

Tubular Hybrid Chemical Vapour Deposition (HCVD) technology was developed by independent groups for the production of perovskite thin films [109- 111]. HCVD is similar to VASP in which perovskite layer can be formed in combination of two methods, but also different from VASP in regard to the MAI feed process into the reaction site. In 2014, the first PSC was demonstrated with the use of HCVD with a PCE of 11.8% and stability up to 1100 h [112]. In this study, $CH_3NH_3PbCl_3$ thin film was prepared by a two-step process, where $PbCl_2$ was thermally evaporated, onto FTO glass substrates pre-coated with TiO_2, at a high vacuum (~$2.0x10^{-6}$ torr). This coated films and MAI powder were placed inside two separate hot zones in the furnace (MAI at 185 ºC and $PbCl_2$ at 130 ºC). Once MAI vaporised, it was passed into reaction zone with carrier N_2 gas. After 1 hour reaction duration, samples were subjected to a post-annealing process at 120 °C in air. Controlling the temperature for each zone is crucial for the perovskite film especially for its stability, since high temperatures of >170 ºC does not form perovskite and low growth temperatures of >145 °C results in unstable film. The variation in temperature has a considerable effect on the MAI gas/solid diffusion rate into $PbCl_2$ film, and is also affected by MAI gas pressure according to the relation [113]: $D_g \propto T^{3/2}/P$, where D_g is the gas diffusion constant, T is growth temperature and P is gas pressure. Once the MAI gas reaches the $PbCI_2$ thin film, it has to diffuse through the film (solid diffusion) to convert the metal halide into perovskite. This solid diffusion constant is determined according to the Arrhenius equation: $D_S \propto e^{-C/kT}$, where D_S is the gas diffusion constant, C is a constant and k is Boltzmann's constant [114]. It can be stated that gas and solid diffusion rates are increased with temperature owing to fast conversion into perovskite. In addition, the flow of hot gas towards the substrate increased the growth temperature up to 160-170 °C.

In 2016, a huge progress for PSCs based on HCVD method was introduced by Zheng at el. [115] achieving the highest PCE (18.9%) compared to other PSCs fabricated by vapour-based processes. High-quality perovskite films were produced under atmospheric pressure and high humidity of 60% by using homemade vapour-assisted deposition chamber. In this setup, a commercial heat gun was employed to generate a hot air flow that led to the formation MAI gas and then transferred onto PbI_2 substrates where the G-S reaction occurred. This proposed method offers cost advantage and low energy consumption.

- **Low–Pressure Chemical Vapour Deposition (LPCVD)**

LPCVD is broadly used in the commercial production of a-Si, Si_3N_4, SiO_2, and ZnO thin films [107, 108] and it was first proposed by Lu *et al.* to deposit perovskite material ($MAPbI_3$) [97]. MAI powder and spin-coated PbI_2 films were separately placed in zone A and B of the tubular furnace, respectively. After the reactor pumped down for 10 minutes, zone A and B were heated to 180 ^oC and 140 ^oC, respectively. After 100 min reaction duration, PbI_2 thin films were fully converted into perovskite with surface homogeneity and good crystallinity. Thus, excellent optical properties were achieved such as strong absorption (9 - 10 x 10^4 cm^{-1}) and long carrier diffusion length [97].

One-zone LPCVD developed by another research group deposited perovskites in which both PbI_2 films and MAI powder were placed inside one zone [116]. Copper-graphite boat was used to hold the precursors inside the reactor, which was kept at 120 ^oC and under 1 torr pressure to induce the reaction. The power conversion efficiencies were recorded for mesoscopic and planar architecture as 14.99% and 15.37% respectively.

However, both HCVD and LPCVD require transport of vaporised MAI over a considerable distance in the CVD reactor that may affect their reproducibility. Therefore, there is a need to propose another method that can overcome this obstacle.

- **In-situ Tubular CVD (ITCVD)**

ITCVD is a simple technique proposed to reduce the flow distance of MAI vapour during the deposition, where the PbI_2 films are placed on top of MAI powder [109]. The tubular furnace is heated to 145 ^oC to produce MAI vapour that reacts with hot PbI_2 films for 120 minutes. A slow intercalating rate between MAI vapour and PbI_2 results in the formation of uniform and fully converted perovskite films; hence efficiency of 12.2% is achieved based on planar-type PSC. Interestingly, this method is scalable for the production of high-quality perovskite films over large areas of 4cm x 4cm.

Similar work was performed by Cui *et al*. to synthesise hybrid physical-chemical vapour deposition (*HPCVD*) based perovskites [117]. In a quartz tube, two placement configurations of PbI_2 coated FTO

glass substrate and MAI powder were designed to adjust the vapour pressure of MAI: 'face-to-face' and 'back-to-face'. In 'face-to-face' configuration, the PbI_2 film faces MAI powder, while in 'back-to-face' configuration; the FTO substrate faces MAI powder. In 'back-to-face', the PbI_2 receives less pressure of MAI vapour leading to a lower reaction rate. Hence, more uniform perovskite film has been produced. Thus, an efficient PSC based on this method was fabricated with a PCE of 14.7% at a temperature of 82 ºC.

High PCE of 16.2% for PSC was achieved by similar technology, called a Close Space Vapour Transport (CSVT) [118]. In an industrial technology, CSVT is well-established for low-cost, commercial-scale manufacturing of CdTe solar cells [119]. Perovskite modules on an active layer of 3 cm x 3 cm with 13.8% efficiency were obtained by this method.

2.3.2.2.*b* Gas-Phase CVD Reaction

Controlling the stoichiometry of the organic and inorganic components of perovskite and the thermal stability of the organic compound are considered as the main concerns in the two-step CVD process. Therefore, using a single-step CVD under atmospheric pressure has a great potential for low-cost and scalable fabrication of PSC from a practical point of view. This technology can be categorised based on the phase of the precursors used as follows: one-step CVD process using solid precursors and one-step CVD process using solution precursors.

- **Using solid precursors**

In this technique, only gas-phase reaction between the precursors is performed by using solid precursors in powder form, in which the formation of perovskite can be obtained by co-vaporising inorganic and organic powders. The mixture of vapours is then transferred by carrier gas (e.g. Argon (Ar) or Nitrogen (N_2)) to the hot substrates, where the precursors are reacted. In one such method, $CH_3NH_3PbI_3$ and $CH_3NH_3PbI_{(3-x)}Cl_x$ are formed by placing the powder precursors (PbI_2/$PbCl_2$ and MAI) in the hot zone (360 $^{\circ}$C) inside the furnace, while the substrates are loaded in low temperature zone [120]. Ar gas with a flow rate of 70 sccm was used for carrying the vapour to the reaction zone. Planar PSCs fabricated by this method achieved a PCE of 9.2% for an iodide-based device and 11.1% for a mixed halide (I-Cl) device.

- **Using liquid precursor**

Aerosol-Assisted One-step CVD (AACVD) is an alternative method that converts the solution precursor to aerosols by using a nebuliser and transports them to the reaction chamber by carrier gas (e.g. Ar or N_2) at ambient pressure. Deposition of various semiconductors such as PbS [121], SnS

[122], Cs_2SnI_6 [123], and CU_2ZnSnS_4 [124] is performed by AACVD. O'Brien and his group fabricated perovskite material ($MAPbBr_3$) using AACVD [125]. The diluted solution of mixed $PbBr_2$ and CH_3NH_3Br in DMF was initially heated at 60 ºC for 2 h and then nebulised using humidifier to generate the aerosol mist. This mist was transported to the preheated furnace by Ar gas (200 sccm) where the precursor thermally decomposed at 250 ºC. The structure of the film was studied by powder XRD which confirmed the perovskite phase formation with a distinct peak at 14.77º and 29.98º corresponding to (100) and (200) planes, respectively. The films produced by this method have a uniform surface with good-quality crystallisation that is comparable to those prepared by high-vacuum CVD [102].

Later, the first thin film deposition of ($CH_3NH_3PbI_3$) using AACVD was reported by Palgrave [126]. Films deposited on the hot substrates (200 ºC) were successfully formed with large covering area of glass as well as TiO_2 coated glass of 40 cm^2 in area. Cubic structure of fresh $CH_3NH_3PbI_3$ film was produced with lattice parameter of a = 6.2993 Å, however after few days of storage in a dry box, the structure transformed from cubic to tetragonal phase. Compositional uniformity of the formed films was detected by X-ray photoemission spectra which revealed that the ratio of Pb and I is 0.325 with 3.5% difference from the theoretical Pb:I ratio.

The effect of the AACVD deposition parameters such as reaction temperature, substrate placement position and the precursor delivery on the film characteristics was also investigated [127]. In order to form the mist, Vicks paediatric mini ultrasonic humidifier was employed. Hot CVD furnace was operated at 200 ºC, which resulted in a deposition of tetragonal perovskite films with poor surface coverage. The lack in film uniformity was attributed to the temperature of the substrate (140 ºC) that was lower than the reactor wall, hence most of the material condensed on the sidewalls of the tube. To improve the quality of the surface coverage uniformity in complete cross-section, the deposition was performed at higher substrate temperature (275 ºC). The difference in the substrate temperature required in this study and the aforementioned work presented by Palgrave *et al.* [126] might be attributed to the different heating methods used. In the former study, the deposition was conducted in cold wall reactor by using a flat heated susceptor, in order to keep a constant heating at the substrate surface. Whereas in the latter study, hot wall furnace was used, hence the deposition took place on the substrates and wall as both are heated. The chemical reaction of PbI_2 and MAI was not only temperature sensitive, but it was significantly affected by the distance from the gas inlet and the deposition area.

Although the gas-phase perovskite growth process via AACVD technologies is scalable, simple and does not require an expensive vacuum equipment since it occurs under atmospheric pressure, so far,

however, no one has presented an efficient solar cell using this technique. Thus, further understanding and exploration of this growth method is required.

In short, it can be stated that from the aforementioned tubular CVD technology, high-quality perovskite thin films can be produced with good controllability and versatility. Among the possible G-phase and G-S reaction presented earlier, the poor quality of the resultant perovskite films in G-S phase reactions with incomplete conversion have been proved. This is due to the solution process of the underneath solid-phase PbI_2, which can form colloidal aggregates and needle-shaped solvation intermediates influencing the S-G interaction during perovskite formation.

2.4 Stability of the Perovskite Layer

In the commercial solar cell community, three strict requirements need to be adhered to. These include PV efficiency, operational stability and the cost of manufacturing (material cost, fabrication method, and energy consumed). Perovskite solar cells (PSCs) have achieved the efficiency values similar to the one that are commercially established. In addition, such solar cells are considered a potential candidate for low-cost production since they can be fabricated with a low-temperature coating process by using inexpensive and abundant materials. Nevertheless, the limitation in such solar cells is poor stability, which makes it harder to be commercially established. More emphasis on long-time operation is required to promote commercial availability, especially for up-scaling production and solar panels, to meet the installation and replacement costs. In this section, the stability of perovskite materials will be divided under two groups as follows:

- Intrinsic perovskite layer stability
- Extrinsic factors affecting perovskite layer stability.

Herein, focus will be placed on the instability of the absorber layer of perovskite solar cells (*PSCs*) caused by intrinsic and extrinsic factors, however, the stability issues caused by other layers in *PSCs* that include the ETL, HTL and their electrodes will be explained in detail further on (in chapter 3).

2.4.1 Intrinsic Perovskite Layer Stability

There are four main aspects that influence the perovskite layer stability: crystallography structure, moisture/water, elevated temperatures and illumination. Since perovskite materials are formed from ionic compounds, the dominant parameter which determines the stability of the perovskite structure is the ionic radius. In other words, the energy of the lattice that arises from the arrangement of ionic particles in the lattice controls the crystal structure stability, which can be given by:

$$\boldsymbol{E_{lattice} = E_{static} + E_{vibrational}} \qquad \textbf{(2. 1)}$$

In ambient conditions, the lattice vibration in the semiconductor material is of a lower magnitude as compared to the static ($E_{static} >> E_{vibrational}$) and hence, it is considered to be negligible. Equation (2.1) can be rewritten as follows [128]:

$$\boldsymbol{E_{lattic} = E_{static} = E_{electrostatic} + E_{repulsion} + E_{other}} \qquad \textbf{(2. 2)}$$

In eq. (2.2), the prevalent energy that influences the lattice energy is the electrostatic energy by 70-90% [128], which can be derived as:

$$\boldsymbol{E_{electrostatic} = \frac{NMZ^{+}Z^{-}e^{2}}{r_{AB}}} \qquad \textbf{(2. 3)}$$

Where N is Avogadro's number, M is the Madelung number, Z^+ and Z^- are the cationic and anionic charges, e is the electron charge and r_{AB} the distance between cations and anions in the crystal structure according to their ionic radius.

In fact, having more stability in the crystal structure requires lower lattice energy. It is understood from the dissociation of the lattice energy that it can be determined by the ionic radius of the ionic compound present in the perovskite material. The geometrical structure between the ionic components is indicated by the Goldschmidt tolerance factor, where the size of the three ions is rigidly limited according to the tolerance factor [129] as follows:

$$\boldsymbol{t = \frac{r_A + r_X}{\sqrt{2}\,(r_B + r_X)}} \qquad \textbf{(2. 4)}$$

In Formula (2.4), r_A, r_B and r_X represent the ionic radii of A, B and X elements, respectively present in the perovskite structure. This formula applies to the empirical ionic radii at room temperature. In the majority of instances, various distortions in the perovskite structure are apparent when $0.75<t<1$. While ideal and more stable cubic perovskite structures occasionally arise where the t-value is very close to unity (in the range between 0.95 and 1); other crystal structures such as, tetragonal, orthorhombic and rhombohedral have lower tolerance values and are slightly distorted [128]. Perovskites' stability and physical properties are critically dependent on the parameters of these distortions, especially the parameters concerning their electronic, magnetic and dielectric properties. These properties are critically relevant in a large number of perovskite materials' applications.

As mentioned earlier, single and mixed-halide perovskite solar cells (PSCs) can be formed such as methylammonium lead iodide ($CH_3NH_3PbI_3$) and methylammonium lead bromide ($CH_3NH_3PbBr_3$) and mixed halide perovskites ($CH_3NH_3PbA_{3-x}B_x$, A and B = I, Br, Cl). In a mixed-halide, the substitution of big iodine atom with a small bromide atom in $CH_3NH_3Pb(I_{1-x}Br_x)_3$ ($x \geq 0.2$), results in a higher stability after exposure to higher-levels of humidity (55%) for 20 days at room temperature

[32]. A more stable perovskite structure presented in $CH_3NH_3Pb(I_{1-x}Br_x)_3$, may be due to the structure phase transition from tetragonal phase to cubic phase that results in a reduction of the lattice constant (see section 2.2.1) [32].

In this work, $CH_3NH_3PbI_3$ = $MAPbI_3$ perovskite material was used with a theoretical tolerance factor of 0.912, where $r_{Pb} = 1.03, r_I = 2.20$ *and* $r_{CH3NH3} = 1.80$ Å. Although this value is within the range of the stable phase, the material still poses problems related to its stability. Therefore, study of the tolerance factor alone is not sufficient to depict the perovskite stability issues.

Another important factor that can affect the stability of the perovskite material is the electronegativity difference between perovskite compounds, in particular, the metal cation and the halide anion, which may be given by:

$$\Delta EN = \frac{(\chi_{A-X} + \chi_{B-X})}{2} \qquad (2.5)$$

This relationship depicts the compound ionic bonding strength. If the degree of ionic bonding is high, the perovskite structure gains more stability. This should be considered while synthesising perovskite compounds [130, 131]

2.4.2 Extrinsic Factors Affecting the Perovskite Stability

Laboratory conditions influence reactivity of the perovskite. Niu *et al.* demonstrated four environmental conditions that lead to the perovskite degradation; moisture, oxygen, ultraviolet (UV) light and elevated temperature [132]. This work focusses on PSCs that use $CH_3NH_3PbI_3$ as an absorber layer. This perovskite composition in equilibrium:

$$PbI_2\,(s) + CH_3NH_3I\,(s) \rightleftharpoons CH_3NH_3PbI_3\,(s) \qquad (2.6)$$

This equilibrium can be reversible or irreversible, that means, $CH_3NH_3PbI_3$ can be decomposed to PbI_2 and CH_3NH_3I at certain conditions, or in some other situations, the perovskite decomposes to form new compounds [133]. The equilibrium components (in equation **(2. 6)**) are affected by the moisture, oxygen and UV light owing to further decomposition (hydrolysis) as follows [133]:

$$CH_3NH_3PbI_3\,(s) \rightleftharpoons PbI_2\,(s) + CH_3NH_3I\,(aq) \qquad (2.7)$$

$$CH_3NH_3I\,(aq) \rightleftharpoons CH_3NH_2\,(aq) + HI\,(aq) \qquad (2.8)$$

$$4\,HI\,(aq) + O_2\,(g) \rightleftharpoons 2\,I_2\,(aq) + 2\,H_2O\,(l) \qquad (2.9)$$

$$2\,HI\,(aq) \overset{h\gamma}{\rightleftharpoons} H_2\,(g) + I_2\,(s) \qquad (2.10)$$

It can be noticed from the above chemical reactions between perovskite material and the environmental conditions that the instability arises from the fact that the perovskites themselves are sensitive to moisture, oxygen and UV light [134- 138]. Equation **(2. 7)** demonstrated that $CH_3NH_3PbI_3$ dissociates to PbI_2 when exposed to moisture. The main concern at this stage is that PbI_2 is soluble in water [139], which leads to PbI_2 leakage risk and ecological hazards. Yang *et al.* reviewed the degradation rate of perovskite under exposure to different levels of humidity. The films that are introduced to 100% relative humidity environment, degrade faster in several hours, however at low level of humidity the degradation is slower. These experiments were carried out in dark atmosphere without illumination [139].

All solar cells would work only when exposed to visible light, which is essential requirement for their operation, hence material is expected to be stable under light. Despite perovskite film showing a good stability in the dark condition [28], it degrades under illumination in the presence of oxygen [140]. Ultraviolet (UV) light also causes decomposition of perovskite (eq. **(2. 10))** forming H_2 and I_2 [140]. In this scenario, the degradation mechanism under exposure to UV light and oxygen is as follows: electrons excited from valence band to conduction band caused by the absorption of the appropriate UV and visible photons, facilitates the reaction with oxygen, forming superoxide anion, which then reacts with MA cation and iodine, leading to $CH_3NH_3PbI_3$ decomposition [140]. The lifetime and reproducibility of perovskite solar cells is reduced due to this decomposition [133]. Perovskite must be synthesised in inert gas atmosphere (glove box in N_2 atmosphere) to avoid water and oxygen during the fabrication process [133, 139, 140].

If perovskite material reacts with water, it gets decomposed within minutes [141]. A possible dissociation pathway has been suggested by Walsh *et al.* with regard to the iodide-based perovskites ($MAPbI_3$) whenever it is present, as depicted in **Figure 2-8** [142]. Within any closed system, and in accordance with the deposition procedure, some tiny residue of H_2O shall result in the decomposition of the perovskite: (i) the H_2O is saturated by hydrogen iodide (HI), alternatively (ii) the pressure of the vapour of CH_3NH_2 has attained a state of equilibrium. In the case of sufficient availability of water within the system, the whole perovskite may potentially decompose into PbI_2.

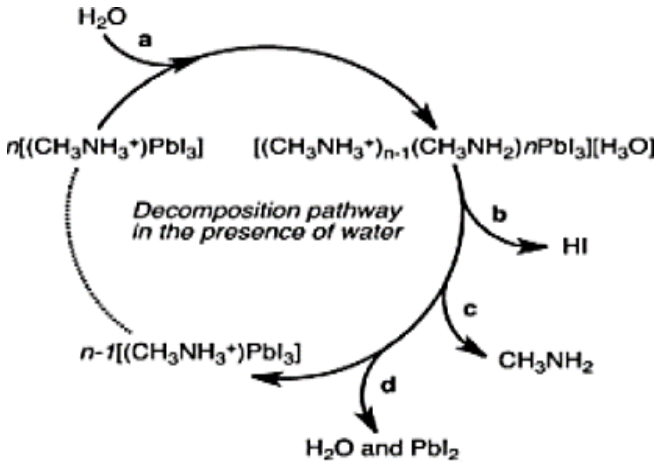

Figure 2-8: A proposed pathway of the decomposition of hybrid halide perovskites ($MAPbI_3$) when water is present (reprinted with permission [142]).

In summary, in moist condition or under UV light, perovskites can decompose [65, 143] in absence of perfect encapsulation as well as with the existence of defects within the material. The number of defects within the device layers can be reduced efficiently by proposing appropriate materials, and deposition methods that may produce perovskite material and other layers used in solar cell such as ETL and HTL with a minimum defect density.

Another essential factor affecting the stability of perovskite materials is elevated temperature. To get crystalline perovskite during the synthesis, perovskite film should be annealed, but it would degrade to its basic components at temperature >120 ºC [133]. At 300 ºC the perovskite decomposes to lead iodide, hydrogen iodide (HI), and CH_3NH_2 [141] as shown in equation **(2. 11)**:

$$CH_3NH_3PbI_3 \rightarrow PbI_2 + CH_3NH_2\uparrow + HI\uparrow \qquad (2.\ 7)$$

Thermal energy affects the individual components of perovskite material, in particular $CH_3NH_3PbI_3$ and $CH_3NH_3CI_3$ as reviewed by Dualeh et al. [144]. They explored the thermal properties of organic and inorganic components individually with the use of TGA instrument. The sublimation of the organic materials at temperatures between 200 and 350 ºC, whilst inorganic components ($PbCl_2$ and PbI_2) are still stable. This study has shown that the material is stable at temperatures up to 200 ºC [145]. Therefore, the thermal annealing of perovskite layer during the fabrication process should be at temperatures beyond 100 ºC [146].

2.5 Summary

In this chapter, the historical information relating to perovskites discovery and relative crystal structure have been provided. Further details have been given on the particular organic-inorganic halide-based perovskite materials providing their various structural phases that can be formed as a function of temperatures, as well as the outstanding optical and electrical properties that make these materials suitable for PV applications. This chapter also discussed the advantages and disadvantages of deposition routes that have been used for the synthesis of perovskite materials using two broad techniques: solution-based process and vapour-based process. An array of CVD methods were discussed that showed a simple, low-cost and scalable production, which opened the avenue towards industrial application of organic-inorganic perovskite solar cells. Finally, the stability issues related to perovskite layers caused by both intrinsic (structural) and extrinsic (environmental) factors were elaborated. In this chapter, a literature survey has been overviewed and illustrates different research outcomes, which suggests possible organic-inorganic halide perovskites material candidates as promising material for photovoltaic solar cell applications. However, in the following chapter, more details about perovskite solar cell (operation theory, characterisation and so on) will be discussed extensively.

References

[1] M. Pena and J. Fierro, "Chemical structures and performance of perovskite oxides," *Chemical reviews,* vol 101, no 7, pp. 1981-2018, 2001.

[2] C. Li, X. Lu, W. Ding, L. Feng, Y. Gao and Z. Guo, "Formability of ABX3 (X= F, cl, br, I) halide perovskites," *Acta crystallographica section B: Structural science,* vol 64, no 6, pp. 702-707, 2008.

[3] L.G. Tejuca and J.L. Fierro, *Properties and applications of perovskite-type oxides,* CRC Press, 1992.

[4] H. L. Wells, "Über die cäsium-und Kalium-Bleihalogenide," *Zeitschrift für anorganische chemie,* vol 3, no 1, pp. 195-210, 1893.

[5] C. K. MØLLER, "A phase transition in cæsium plumbochloride," 1957.

[6] C. K. MØLLER, "Crystal structure and photoconductivity of caesium plumbohalides," 1958.

[7] C. K. MØLLER, "Crystal structure and photoconductivity of caesium plumbohalides," *Nature,* vol 182, no 4647, pp. 1436, 1958.

[8] F. R. POULSEN and S. E. RASMUSSEN, "Crystal structure and phase transition of cesium trichlorostannate (II)," *Acta chem.scared,* vol 24, no 1, 1970.

[9] D. E. Scaife, P. F. Weller and W. G. Fisher, "Crystal preparation and properties of cesium tin (II) trihalides," *Journal of solid state chemistry,* vol 9, no 3, pp. 308-314, 1974.

[10] R.W.G. Wyckoff, *Crystal structures,* Krieger, 1964.

[11] D. Mitzi and K. Liang, "Synthesis, resistivity, and thermal properties of the cubic perovskite NH 2 CH= NH 2 SnI 3 and related systems," *Journal of solid state chemistry,* vol 134, no 2, pp. 376-381, 1997.

[12] R. Jakubas, "Ferroelectric phase transition in tris (dimethylammonium) nonachlorodiantimonate (III),[NH 2 (CH 3) 2] 3 sb 2 cl 9," *Solid state communications,* vol 60, no 4, pp. 389-391, 1986.

[13] D. Weber, "CH3NH3SnBrxI3-x (x= 0-3), ein sn (II)-system mit kubischer perowskitstruktur/CH3NH3SnBrxI3-x (x= 0-3), a sn (II)-system with cubic perovskite structure," *Zeitschrift für naturforschung B,* vol 33, no 8, pp. 862-865, 1978.

[14] D. Weber, "CH3NH3PbX3, ein pb (II)-system mit kubischer perowskitstruktur/CH3NH3PbX3, a pb (II)-system with cubic perovskite structure," *Zeitschrift für naturforschung B,* vol 33, no 12, pp. 1443-1445, 1978.

[15] D. B. Mitzi, K. Chondroudis and C. R. Kagan, "Organic-inorganic electronics," *IBM journal of research and development,* vol 45, no 1, pp. 29-45, 2001.

[16] A. Kojima, K. Teshima, Y. Shirai and T. Miyasaka, "Organometal halide perovskites as visible-light sensitizers for photovoltaic cells," *Journal of the american chemical society,* vol 131, no 17, pp. 6050-6051, 2009.

[17] A. Poglitsch and D. Weber, "Dynamic disorder in methylammoniumtrihalogenoplumbates (II) observed by millimeter-wave spectroscopy," *The journal of chemical physics,* vol 87, no 11, pp. 6373-6378, 1987.

[18] S. A. Bretschneider, J. Weickert, J. A. Dorman and L. Schmidt-Mende, "Research update: Physical and electrical characteristics of lead halide perovskites for solar cell applications," *APL materials,* vol 2, no 4, pp. 155204, 2014.

[19] T. Baikie, Y. Fang, J. M. Kadro, M. Schreyer, F. Wei, S. G. Mhaisalkar, M. Graetzel and T. J. White, "Synthesis and crystal chemistry of the hybrid perovskite (CH 3 NH 3) PbI 3 for solid-state sensitised solar cell applications," *Journal of materials chemistry A,* vol 1, no 18, pp. 5628-5641, 2013.

[20] C. C. Stoumpos, C. D. Malliakas and M. G. Kanatzidis, "Semiconducting tin and lead iodide perovskites with organic cations: Phase transitions, high mobilities, and near-infrared photoluminescent properties," *Inorganic chemistry,* vol 52, no 15, pp. 9019-9038, 2013.

[21] H. Kim, I. Mora-Sero, V. Gonzalez-Pedro, F. Fabregat-Santiago, E. J. Juarez-Perez, N. Park and J. Bisquert, "Mechanism of carrier accumulation in perovskite thin-absorber solar cells," *Nature communications,* vol 4, pp. 2242, 2013.

[22] I. Chung, J. Song, J. Im, J. Androulakis, C. D. Malliakas, H. Li, A. J. Freeman, J. T. Kenney and M. G. Kanatzidis, "CsSnI3: Semiconductor or metal? high electrical conductivity and strong near-infrared photoluminescence from a single material. high hole mobility and phase-transitions," *Journal of the american chemical society,* vol 134, no 20, pp. 8579-8587, 2012.

[23] J. M. Frost, K. T. Butler, F. Brivio, C. H. Hendon, M. Van Schilfgaarde and A. Walsh, "Atomistic origins of high-performance in hybrid halide perovskite solar cells," *Nano letters,* vol 14, no 5, pp. 2584-2590, 2014.

[24] F. Brivio, A. B. Walker and A. Walsh, "Structural and electronic properties of hybrid perovskites for high-efficiency thin-film photovoltaics from first-principles," *Apl materials,* vol 1, no 4, pp. 042111, 2013.

[25] C. Motta, F. El-Mellouhi, S. Kais, N. Tabet, F. Alharbi and S. Sanvito, "Revealing the role of organic cations in hybrid halide perovskite CH 3 NH 3 PbI 3," *Nature communications,* vol 6, pp. 7026, 2015.

[26] P. Kanhere, S. Chakraborty, C. J. Rupp, R. Ahuja and Z. Chen, "Substitution induced band structure shape tuning in hybrid perovskites (CH 3 NH 3 pb 1− x sn x I 3) for efficient solar cell applications," *RSC advances,* vol 5, no 130, pp. 107497-107502, 2015.

[27] H. S. Jung and N. Park, "Perovskite solar cells: From materials to devices," *Small,* vol 11, no 1, pp. 10-25, 2015.

[28] J. H. Noh, S. H. Im, J. H. Heo, T. N. Mandal and S. I. Seok, "Chemical management for colorful, efficient, and stable inorganic–organic hybrid nanostructured solar cells," *Nano letters,* vol 13, no 4, pp. 1764-1769, 2013.

[29] P. Gao, M. Grätzel and M. K. Nazeeruddin, "Organohalide lead perovskites for photovoltaic applications," *Energy & environmental science,* vol 7, no 8, pp. 2448-2463, 2014.

[30] I. Borriello, G. Cantele and D. Ninno, "Ab initio investigation of hybrid organic-inorganic perovskites based on tin halides," *Physical review B,* vol 77, no 23, pp. 235214, 2008.

[31] F. Brivio, K. T. Butler, A. Walsh and M. Van Schilfgaarde, "Relativistic quasiparticle self-consistent electronic structure of hybrid halide perovskite photovoltaic absorbers," *Physical review B,* vol 89, no 15, pp. 155204, 2014.

[32] J. H. Noh, S. H. Im, J. H. Heo, T. N. Mandal and S. I. Seok, "Chemical management for colorful, efficient, and stable inorganic–organic hybrid nanostructured solar cells," *Nano letters,* vol 13, no 4, pp. 1764-1769, 2013.

[33] S. Kazim, M. K. Nazeeruddin, M. Grätzel and S. Ahmad, "Perovskite as light harvester: A game changer in photovoltaics," *Angewandte chemie international edition,* vol 53, no 11, pp. 2812-2824, 2014.

[34] G. E. Eperon, S. D. Stranks, C. Menelaou, M. B. Johnston, L. M. Herz and H. J. Snaith, "Formamidinium lead trihalide: A broadly tunable perovskite for efficient planar heterojunction solar cells," *Energy & environmental science,* vol 7, no 3, pp. 982-988, 2014.

[35] R. E. Wasylishen, O. Knop and J. B. Macdonald, "Cation rotation in methylammonium lead halides," *Solid state communications,* vol 56, no 7, pp. 581-582, 1985.

[36] W. Zhang, M. Anaya, G. Lozano, M. E. Calvo, M. B. Johnston, H. Míguez and H. J. Snaith, "Highly efficient perovskite solar cells with tunable structural color," *Nano letters,* vol 15, no 3, pp. 1698-1702, 2015.

[37] P. Schouwink, M. B. Ley, A. Tissot, H. Hagemann, T. R. Jensen, Ľ Smrčok and R. Černý, "Structure and properties of complex hydride perovskite materials," *Nature communications,* vol 5, 2014.

[38] W. Geng, L. Zhang, Y. Zhang, W. Lau and L. Liu, "First-principles study of lead iodide perovskite tetragonal and orthorhombic phases for photovoltaics," *The journal of physical chemistry C,* vol 118, no 34, pp. 19565-19571, 2014.

[39] C. C. Stoumpos, C. D. Malliakas and M. G. Kanatzidis, "Semiconducting tin and lead iodide perovskites with organic cations: Phase transitions, high mobilities, and near-infrared photoluminescent properties," *Inorganic chemistry,* vol 52, no 15, pp. 9019-9038, 2013.

[40] H. S. Jung and N. Park, "Perovskite solar cells: From materials to devices," *Small,* vol 11, no 1, pp. 10-25, 2015.

[41] H. S. Jung and N. Park, "Perovskite solar cells: From materials to devices," *Small,* vol 11, no 1, pp. 10-25, 2015.

[42] G. Eperon, "GE eperon, SD stranks, C. menelaou, MB johnston, LM herz, and HJ snaith, energy environ. sci. 7, 982 (2014)." *Energy environ.sci.,* vol 7, pp. 982, 2014.

[43] P. W. Blom, V. D. Mihailetchi, L. J. A. Koster and D. E. Markov, "Device physics of polymer: Fullerene bulk heterojunction solar cells," *Advanced materials,* vol 19, no 12, pp. 1551-1566, 2007.

[44] X. Ziang, L. Shifeng, Q. Laixiang, P. Shuping, W. Wei, Y. Yu, Y. Li, C. Zhijian, W. Shufeng and D. Honglin, "Refractive index and extinction coefficient of CH 3 NH 3 PbI 3 studied by spectroscopic ellipsometry," *Optical materials express,* vol 5, no 1, pp. 29-43, 2015.

[45] W. Yin, T. Shi and Y. Yan, "Unique properties of halide perovskites as possible origins of the superior solar cell performance," *Advanced materials,* vol 26, no 27, pp. 4653-4658, 2014.

[46] S. D. Stranks, G. E. Eperon, G. Grancini, C. Menelaou, M. J. Alcocer, T. Leijtens, L. M. Herz, A. Petrozza and H. J. Snaith, "Electron-hole diffusion lengths exceeding 1 micrometer in an organometal trihalide perovskite absorber," *Science (new york, N.Y.),* vol 342, no 6156, pp. 341-344, Oct 18 2013.

[47] A. Miyata, A. Mitioglu, P. Plochocka, O. Portugall, J. T. Wang, S. D. Stranks, H. J. Snaith and R. J. Nicholas, "Direct measurement of the exciton binding energy and effective masses for charge carriers in organic-inorganic tri-halide perovskites," *Nature physics,* vol 11, no 7, pp. 582-587, 2015.

[48] J. Even, L. Pedesseau and C. Katan, "Analysis of multivalley and multibandgap absorption and enhancement of free carriers related to exciton screening in hybrid perovskites," *The journal of physical chemistry C,* vol 118, no 22, pp. 11566-11572, 2014.

[49] V. D'Innocenzo, G. Grancini, M. J. Alcocer, A. R. S. Kandada, S. D. Stranks, M. M. Lee, G. Lanzani, H. J. Snaith and A. Petrozza, "Excitons versus free charges in organo-lead tri-halide perovskites," *Nature communications,* vol 5, pp. 3586, 2014.

[50] C. S. Ponseca Jr, T. J. Savenije, M. Abdellah, K. Zheng, A. Yartsev, T. Pascher, T. Harlang, P. Chabera, T. Pullerits and A. Stepanov, "Organometal halide perovskite solar cell materials rationalized: Ultrafast charge generation, high and microsecond-long balanced mobilities, and slow recombination," *Journal of the american chemical society,* vol 136, no 14, pp. 5189-5192, 2014.

[51] K. Tvingstedt, O. Malinkiewicz, A. Baumann, C. Deibel, H. J. Snaith, V. Dyakonov and H. J. Bolink, "Radiative efficiency of lead iodide based perovskite solar cells," *Scientific reports,* vol 4, pp. 6071, 2014.

[52] H. J. Snaith, "Perovskites: The emergence of a new era for low-cost, high-efficiency solar cells," *The journal of physical chemistry letters,* vol 4, no 21, pp. 3623-3630, 2013.

[53] T. Leijtens, S. D. Stranks, G. E. Eperon, R. Lindblad, E. M. Johansson, I. J. McPherson, H. Rensmo, J. M. Ball, M. M. Lee and H. J. Snaith, "Electronic properties of meso-superstructured and planar organometal halide perovskite films: Charge trapping, photodoping, and carrier mobility," *ACS nano,* vol 8, no 7, pp. 7147-7155, 2014.

[54] B. C. Thompson and J. M. Fréchet, "Polymer–fullerene composite solar cells," *Angewandte chemie international edition,* vol 47, no 1, pp. 58-77, 2008.

[55] D. C. Watters, H. Yi, A. J. Pearson, J. Kingsley, A. Iraqi and D. Lidzey, "Fluorene-Based co-polymer with high hole mobility and device performance in bulk heterojunction organic solar cells," *Macromolecular rapid communications,* vol 34, no 14, pp. 1157-1162, 2013.

[56] Y. Zhao, A. M. Nardes and K. Zhu, "Solid-state mesostructured perovskite CH3NH3PbI3 solar cells: Charge transport, recombination, and diffusion length," *The journal of physical chemistry letters,* vol 5, no 3, pp. 490-494, 2014.

[57] T. Salim, J. Kadro, M. Khuc, R. Haselsberger, L. Cheng, H. Xia, G. G. Gurzadyan, H. Su, Y. M. Lam and R. A. Marcus, "Elucidating the role of disorder and free-carrier recombination kinetics in CH 3 NH 3 PbI 3 perovskite films," *Nature communications,* vol 6, pp. 7903, 2015.

[58] V. Gonzalez-Pedro, E. J. Juarez-Perez, W. Arsyad, E. M. Barea, F. Fabregat-Santiago, I. Mora-Sero and J. Bisquert, "General working principles of CH3NH3PbX3 perovskite solar cells," *Nano letters,* vol 14, no 2, pp. 888-893, 2014.

[59] Y. Hsiao, T. Wu, M. Li, Q. Liu, W. Qin and B. Hu, "Fundamental physics behind high-efficiency organo-metal halide perovskite solar cells," *Journal of materials chemistry A,* 2015.

[60] Q. Dong, Y. Fang, Y. Shao, P. Mulligan, J. Qiu, L. Cao and J. Huang, "Solar cells. electron-hole diffusion lengths > 175 mum in solution-grown CH3NH3PbI3 single crystals," *Science (new york, N.Y.),* vol 347, no 6225, pp. 967-970, Feb 27 2015.

[61] F. Li, C. Ma, H. Wang, W. Hu, W. Yu, A. D. Sheikh and T. Wu, "Ambipolar solution-processed hybrid perovskite phototransistors," *Nature communications,* vol 6, pp. 8238, 2015.

[62] G. Xing, N. Mathews, S. Sun, S. S. Lim, Y. M. Lam, M. Gratzel, S. Mhaisalkar and T. C. Sum, "Long-range balanced electron- and hole-transport lengths in organic-inorganic CH3NH3PbI3," *Science (new york, N.Y.),* vol 342, no 6156, pp. 344-347, Oct 18 2013.

[63] Y. Chen, J. Peng, D. Su, X. Chen and Z. Liang, "Efficient and balanced charge transport revealed in planar perovskite solar cells," *ACS applied materials & interfaces,* vol 7, no 8, pp. 4471-4475, 2015.

[64] Z. Yang and W. Zhang, "Organolead halide perovskite: A rising player in high-efficiency solar cells," *Chinese journal of catalysis,* vol 35, no 7, pp. 983-988, 2014.

[65] B. V. Lotsch, "New light on an old story: Perovskites go solar," *Angewandte chemie international edition,* vol 53, no 3, pp. 635-637, 2014.

[66] G. E. Eperon, V. M. Burlakov, P. Docampo, A. Goriely and H. J. Snaith, "Morphological control for high performance, solution-processed planar heterojunction perovskite solar cells," *Advanced functional materials,* vol 24, no 1, pp. 151-157, 2014.

[67] A. Dualeh, N. Tétreault, T. Moehl, P. Gao, M. K. Nazeeruddin and M. Grätzel, "Effect of annealing temperature on film morphology of organic–inorganic hybrid pervoskite solid-state solar cells," *Advanced functional materials,* vol 24, no 21, pp. 3250-3258, 2014.

[68] A. Fakharuddin, F. De Rossi, T. M. Watson, L. Schmidt-Mende and R. Jose, "Research update: Behind the high efficiency of hybrid perovskite solar cells," *APL materials,* vol 4, no 9, pp. 091505, 2016.

[69] Y. Deng, E. Peng, Y. Shao, Z. Xiao, Q. Dong and J. Huang, "Scalable fabrication of efficient organolead trihalide perovskite solar cells with doctor-bladed active layers," *Energy & environmental science,* vol 8, no 5, pp. 1544-1550, 2015.

[70] K. Hwang, Y. Jung, Y. Heo, F. H. Scholes, S. E. Watkins, J. Subbiah, D. J. Jones, D. Kim and D. Vak, "Toward large scale roll-to-roll production of fully printed perovskite solar cells," *Advanced materials,* vol 27, no 7, pp. 1241-1247, 2015.

[71] A. T. Barrows, A. J. Pearson, C. K. Kwak, A. D. Dunbar, A. R. Buckley and D. G. Lidzey, "Efficient planar heterojunction mixed-halide perovskite solar cells deposited via spray-deposition," *Energy & environmental science,* vol 7, no 9, pp. 2944-2950, 2014.

[72] Z. Wei, H. Chen, K. Yan and S. Yang, "Inkjet printing and instant chemical transformation of a CH3NH3PbI3/nanocarbon electrode and interface for planar perovskite solar cells," *Angewandte chemie international edition,* vol 53, no 48, pp. 13239-13243, 2014.

[73] D. Shen, X. Yu, X. Cai, M. Peng, Y. Ma, X. Su, L. Xiao and D. Zou, "Understanding the solvent-assisted crystallization mechanism inherent in efficient organic–inorganic halide perovskite solar cells," *Journal of materials chemistry A,* vol 2, no 48, pp. 20454-20461, 2014.

[74] K. Kara, D. A. Kara, C. Kırbıyık, M. Ersoz, O. Usluer, A. L. Briseno and M. Kus, "Solvent washing with toluene enhances efficiency and increases reproducibility in perovskite solar cells," *RSC advances,* vol 6, no 32, pp. 26606-26611, 2016.

[75] H. S. Jung and N. Park, "Perovskite solar cells: From materials to devices," *Small,* vol 11, no 1, pp. 10-25, 2015.

[76] J. Troughton, C. Charbonneau, M. J. Carnie, M. L. Davies, D. A. Worsley and T. M. Watson, "Rapid processing of perovskite solar cells in under 2.5 seconds," *Journal of materials chemistry A,* vol 3, no 17, pp. 9123-9127, 2015.

[77] J. Troughton, M. J. Carnie, M. L. Davies, C. Charbonneau, E. H. Jewell, D. A. Worsley and T. M. Watson, "Photonic flash-annealing of lead halide perovskite solar cells in 1 ms," *Journal of materials chemistry A,* vol 4, no 9, pp. 3471-3476, 2016.

[78] J. Burschka, N. Pellet, S. Moon, R. Humphry-Baker, P. Gao, M. K. Nazeeruddin and M. Grätzel, "Sequential deposition as a route to high-performance perovskite-sensitized solar cells," *Nature,* vol 499, no 7458, pp. 316, 2013.

[79] Z. Xiao, C. Bi, Y. Shao, Q. Dong, Q. Wang, Y. Yuan, C. Wang, Y. Gao and J. Huang, "Efficient, high yield perovskite photovoltaic devices grown by interdiffusion of solution-processed precursor stacking layers," *Energy & environmental science,* vol 7, no 8, pp. 2619-2623, 2014.

[80] Q. Chen, H. Zhou, Z. Hong, S. Luo, H. Duan, H. Wang, Y. Liu, G. Li and Y. Yang, "Planar heterojunction perovskite solar cells via vapor-assisted solution process," *Journal of the american chemical society,* vol 136, no 2, pp. 622-625, 2013.

[81] E. Zheng, X. Wang, J. Song, L. Yan, W. Tian and T. Miyasaka, "PbI2-based dipping-controlled material conversion for compact layer free perovskite solar cells," *ACS applied materials & interfaces,* vol 7, no 32, pp. 18156-18162, 2015.

[82] Z. Xiao, C. Bi, Y. Shao, Q. Dong, Q. Wang, Y. Yuan, C. Wang, Y. Gao and J. Huang, "Efficient, high yield perovskite photovoltaic devices grown by interdiffusion of solution-processed precursor stacking layers," *Energy & environmental science,* vol 7, no 8, pp. 2619-2623, 2014.

[83] Q. Chen, H. Zhou, Z. Hong, S. Luo, H. Duan, H. Wang, Y. Liu, G. Li and Y. Yang, "Planar heterojunction perovskite solar cells via vapor-assisted solution process," *Journal of the american chemical society,* vol 136, no 2, pp. 622-625, 2013.

[84] T. Salim, S. Sun, Y. Abe, A. Krishna, A. C. Grimsdale and Y. M. Lam, "Perovskite-based solar cells: Impact of morphology and device architecture on device performance," *Journal of materials chemistry A,* vol 3, no 17, pp. 8943-8969, 2015.

[85] L. Yang, J. Wang and W. W. Leung, "Lead iodide thin film crystallization control for high-performance and stable solution-processed perovskite solar cells," *ACS applied materials & interfaces,* vol 7, no 27, pp. 14614-14619, 2015.

[86] P. Liang, C. Liao, C. Chueh, F. Zuo, S. T. Williams, X. Xin, J. Lin and A. K. Jen, "Additive enhanced crystallization of solution-processed perovskite for highly efficient planar-heterojunction solar cells," *Advanced materials,* vol 26, no 22, pp. 3748-3754, 2014.

[87] A. Mei, X. Li, L. Liu, Z. Ku, T. Liu, Y. Rong, M. Xu, M. Hu, J. Chen, Y. Yang, M. Gratzel and H. Han, "A hole-conductor-free, fully printable mesoscopic perovskite solar cell with high stability," *Science (new york, N.Y.),* vol 345, no 6194, pp. 295-298, Jul 18 2014.

[88] Y. Jeon, S. Lee, R. Kang, J. Kim, J. Yeo, S. Lee, S. Kim, J. Yun and D. Kim, "Planar heterojunction perovskite solar cells with superior reproducibility," *Scientific reports,* vol 4, pp. 6953, 2014.

[89] C. Wu, C. Chiang, Z. Tseng, M. K. Nazeeruddin, A. Hagfeldt and M. Grätzel, "High efficiency stable inverted perovskite solar cells without current hysteresis," *Energy & environmental science,* vol 8, no 9, pp. 2725-2733, 2015.

[90] A. Nawaz, A. K. Erdinc, B. Gultekin, M. Tayyib, C. Zafer, K. Wang and M. N. Akram, "Morphology study of inverted planar heterojunction perovskite solar cells in sequential deposition," *World academy of science, engineering and technology, international science index 115, international journal of electrical, computer, energetic, electronic and communication engineering,* vol 10, no 7, pp. 922-926, 2016.

[91] N. Adhikari, A. Dubey, E. A. Gaml, B. Vaagensmith, K. M. Reza, S. A. A. Mabrouk, S. Gu, J. Zai, X. Qian and Q. Qiao, "Crystallization of a perovskite film for higher performance solar cells by controlling water concentration in methyl ammonium iodide precursor solution," *Nanoscale,* vol 8, no 5, pp. 2693-2703, 2016.

[92] N. J. Jeon, J. H. Noh, Y. C. Kim, W. S. Yang, S. Ryu and S. I. Seok, "Solvent engineering for high-performance inorganic–organic hybrid perovskite solar cells," *Nature materials,* vol 13, no 9, pp. 897, 2014.

[93] Y. Rong, Z. Tang, Y. Zhao, X. Zhong, S. Venkatesan, H. Graham, M. Patton, Y. Jing, A. M. Guloy and Y. Yao, "Solvent engineering towards controlled grain growth in perovskite planar heterojunction solar cells," *Nanoscale,* vol 7, no 24, pp. 10595-10599, 2015.

[94] Y. Wu, W. Chen, Y. Yue, J. Liu, E. Bi, X. Yang, A. Islam and L. Han, "Consecutive morphology controlling operations for highly reproducible mesostructured perovskite solar cells," *ACS applied materials & interfaces,* vol 7, no 37, pp. 20707-20713, 2015.

[95] X. Zheng, B. Chen, C. Wu and S. Priya, "Room temperature fabrication of CH3NH3PbBr3 by anti-solvent assisted crystallization approach for perovskite solar cells with fast response and small J–V hysteresis," *Nano energy,* vol 17, pp. 269-278, 2015.

[96] Y. Zhou, M. Yang, W. Wu, A. L. Vasiliev, K. Zhu and N. P. Padture, "Room-temperature crystallization of hybrid-perovskite thin films via solvent–solvent extraction for high-performance solar cells," *Journal of materials chemistry A,* vol 3, no 15, pp. 8178-8184, 2015.

[97] P. Luo, Z. Liu, W. Xia, C. Yuan, J. Cheng and Y. Lu, "Uniform, stable, and efficient planar-heterojunction perovskite solar cells by facile low-pressure chemical vapor deposition under fully open-air conditions," *ACS applied materials & interfaces,* vol 7, no 4, pp. 2708-2714, 2015.

[98] M. Liu, M. B. Johnston and H. J. Snaith, "Efficient planar heterojunction perovskite solar cells by vapour deposition," *Nature,* vol 501, no 7467, pp. 395, 2013.

[99] C. Chen, H. Kang, S. Hsiao, P. Yang, K. Chiang and H. Lin, "Efficient and uniform planar-type perovskite solar cells by simple sequential vacuum deposition," *Advanced materials,* vol 26, no 38, pp. 6647-6652, 2014.

[100] D. Yang, Z. Yang, W. Qin, Y. Zhang, S. F. Liu and C. Li, "Alternating precursor layer deposition for highly stable perovskite films towards efficient solar cells using vacuum deposition," *Journal of materials chemistry A,* vol 3, no 18, pp. 9401-9405, 2015.

[101] S. Hsiao, H. Lin, W. Lee, W. Tsai, K. Chiang, W. Liao, C. Ren-Wu, C. Chen and H. Lin, "Efficient All-Vacuum deposited perovskite solar cells by controlling reagent partial pressure in high vacuum," *Advanced materials,* vol 28, no 32, pp. 7013-7019, 2016.

[102] M. Liu, M. B. Johnston and H. J. Snaith, "Efficient planar heterojunction perovskite solar cells by vapour deposition," *Nature,* vol 501, no 7467, pp. 395, 2013.

[103] Q. Chen, H. Zhou, T. Song, S. Luo, Z. Hong, H. Duan, L. Dou, Y. Liu and Y. Yang, "Controllable self-induced passivation of hybrid lead iodide perovskites toward high performance solar cells," *Nano letters,* vol 14, no 7, pp. 4158-4163, 2014.

[104] Y. Li, J. K. Cooper, R. Buonsanti, C. Giannini, Y. Liu, F. M. Toma and I. D. Sharp, "Fabrication of planar heterojunction perovskite solar cells by controlled low-pressure vapor annealing," *The journal of physical chemistry letters,* vol 6, no 3, pp. 493-499, 2015.

[105] J. Seo, J. H. Noh and S. I. Seok, "Rational strategies for efficient perovskite solar cells," *Accounts of chemical research,* vol 49, no 3, pp. 562-572, 2016.

[106] J. Ting and N. Huang, "Thickening of chemical vapor deposited carbon fiber," *Carbon,* vol 39, no 6, pp. 835-839, 2001.

[107] S. Faÿ, J. Steinhauser, S. Nicolay and C. Ballif, "Polycrystalline ZnO: B grown by LPCVD as TCO for thin film silicon solar cells," *Thin solid films,* vol 518, no 11, pp. 2961-2966, 2010.

[108] K. F. Jensen and D. Graves, "Modeling and analysis of low pressure CVD reactors," *Journal of the electrochemical society,* vol 130, no 9, pp. 1950-1957, 1983.

[109] P. Luo, Z. Liu, W. Xia, C. Yuan, J. Cheng and Y. Lu, "A simple in situ tubular chemical vapor deposition processing of large-scale efficient perovskite solar cells and the research on their novel roll-over phenomenon in J–V curves," *Journal of materials chemistry A,* vol 3, no 23, pp. 12443-12451, 2015.

[110] M. R. Leyden, L. K. Ono, S. R. Raga, Y. Kato, S. Wang and Y. Qi, "High performance perovskite solar cells by hybrid chemical vapor deposition," *Journal of materials chemistry A,* vol 2, no 44, pp. 18742-18745, 2014.

[111] S. T. Ha, X. Liu, Q. Zhang, D. Giovanni, T. C. Sum and Q. Xiong, "Synthesis of Organic–Inorganic lead halide perovskite nanoplatelets: Towards High-Performance perovskite solar cells and optoelectronic devices," *Advanced optical materials,* vol 2, no 9, pp. 838-844, 2014.

[112] M. R. Leyden, L. K. Ono, S. R. Raga, Y. Kato, S. Wang and Y. Qi, "High performance perovskite solar cells by hybrid chemical vapor deposition," *Journal of materials chemistry A,* vol 2, no 44, pp. 18742-18745, 2014.

[113] X. Yan and Y. Xu, *Chemical vapour deposition: An integrated engineering design for advanced materials,* Springer Science & Business Media, 2010.

[114] H. Mehrer, *Diffusion in solids: Fundamentals, methods, materials, diffusion-controlled processes,* Springer Science & Business Media, 2007.

[115] J. Yin, H. Qu, J. Cao, H. Tai, J. Li and N. Zheng, "Vapor-assisted crystallization control toward high performance perovskite photovoltaics with over 18% efficiency in the ambient atmosphere," *Journal of materials chemistry A,* vol 4, no 34, pp. 13203-13210, 2016.

[116] P. Shen, J. Chen, Y. Chiang, M. Li, T. Guo and P. Chen, "Low-Pressure hybrid chemical vapor growth for efficient perovskite solar cells and Large-Area module," *Advanced materials interfaces,* vol 3, no 8, pp. 1500849, 2016.

[117] Y. Peng, G. Jing and T. Cui, "A hybrid physical–chemical deposition process at ultra-low temperatures for high-performance perovskite solar cells," *Journal of materials chemistry A,* vol 3, no 23, pp. 12436-12442, 2015.

[118] G. Li, J. Y. Ho, M. Wong and H. Kwok, "Low cost, high throughput and centimeter-scale fabrication of efficient hybrid perovskite solar cells by closed space vapor transport," *Physica status solidi (RRL)–Rapid research letters,* vol 10, no 2, pp. 153-157, 2016.

[119] M. A. Green, K. Emery, Y. Hishikawa, W. Warta and E. D. Dunlop, "Solar cell efficiency tables (version 42)," *Progress in photovoltaics: Research and applications,* vol 5, no 21, pp. 827-837, 2013.

[120] M. M. Tavakoli, L. Gu, Y. Gao, C. Reckmeier, J. He, A. L. Rogach, Y. Yao and Z. Fan, "Fabrication of efficient planar perovskite solar cells using a one-step chemical vapor deposition method," *Scientific reports,* vol 5, pp. 14083, 2015.

[121] P. Marchand, I. A. Hassan, I. P. Parkin and C. J. Carmalt, "Aerosol-assisted delivery of precursors for chemical vapour deposition: Expanding the scope of CVD for materials fabrication," *Dalton transactions,* vol 42, no 26, pp. 9406-9422, 2013.

[122] K. Ramasamy, V. L. Kuznetsov, K. Gopal, M. A. Malik, J. Raftery, P. P. Edwards and P. O'Brien, "Organotin dithiocarbamates: Single-source precursors for tin sulfide thin films by aerosol-assisted chemical vapor deposition (AACVD)," *Chemistry of materials,* vol 25, no 3, pp. 266-276, 2013.

[123] J. C. Ke, D. J. Lewis, A. S. Walton, B. F. Spencer, P. O'Brien, A. G. Thomas and W. R. Flavell, "Ambient-air-stable inorganic cs 2 SnI 6 double perovskite thin films via aerosol-assisted chemical vapour deposition," *Journal of materials chemistry A,* 2018.

[124] K. Ramasamy, M. A. Malik and P. O'Brien, "The chemical vapor deposition of cu 2 ZnSnS 4 thin films," *Chemical science,* vol 2, no 6, pp. 1170-1172, 2011.

[125] D. J. Lewis and P. O'Brien, "Ambient pressure aerosol-assisted chemical vapour deposition of (CH 3 NH 3) PbBr 3, an inorganic–organic perovskite important in photovoltaics," *Chemical communications,* vol 50, no 48, pp. 6319-6321, 2014.

[126] D. Bhachu, D. Scanlon, E. Saban, H. Bronstein, I. Parkin, C. Carmalt and R. Palgrave, "Scalable route to CH 3 NH 3 PbI 3 perovskite thin films by aerosol assisted chemical vapour deposition," *Journal of materials chemistry A,* vol 3, no 17, pp. 9071-9073, 2015.

[127] M. Afzaal and H. M. Yates, "Growth patterns and properties of aerosol-assisted chemical vapor deposition of CH3NH3PbI3 films in a single step," *Surface and coatings technology,* vol 321, pp. 336-340, 2017.

[128] B. Jaffe, W. Cook and H. Jaffe, "Piezoelectric ceramics, vol. 3," *Academic, new york,* 1971.

[129] V. Goldschmidt, "Skrifter norske videnskaps-akad," *Oslo I, mat-naturvidensk kl,* vol 8, no 2, 1926.

[130] V. K. Pecharsky and P. Y. Zavalij, "Fundamentals of diffraction," *Fundamentals of powder diffraction and structural characterization of materials,* pp. 99-260, 2003.

[131] J. Valasek, "Piezo-electric and allied phenomena in rochelle salt," *Physical review,* vol 17, no 4, pp. 475, 1921.

[132] G. Niu, X. Guo and L. Wang, "Review of recent progress in chemical stability of perovskite solar cells," *Journal of materials chemistry A,* vol 3, no 17, pp. 8970-8980, 2015.

[133] G. Niu, X. Guo and L. Wang, "Review of recent progress in chemical stability of perovskite solar cells," *Journal of materials chemistry A,* vol 3, no 17, pp. 8970-8980, 2015.

[134] G. Niu, W. Li, F. Meng, L. Wang, H. Dong and Y. Qiu, "Study on the stability of CH 3 NH 3 PbI 3 films and the effect of post-modification by aluminum oxide in all-solid-state hybrid solar cells," *Journal of materials chemistry A,* vol 2, no 3, pp. 705-710, 2014.

[135] I. Hwang, I. Jeong, J. Lee, M. J. Ko and K. Yong, "Enhancing stability of perovskite solar cells to moisture by the facile hydrophobic passivation," *ACS applied materials & interfaces,* vol 7, no 31, pp. 17330-17336, 2015.

[136] I. C. Smith, E. T. Hoke, D. Solis-Ibarra, M. D. McGehee and H. I. Karunadasa, "A layered hybrid perovskite solar-cell absorber with enhanced moisture stability," *Angewandte chemie,* vol 126, no 42, pp. 11414-11417, 2014.

[137] X. Dong, X. Fang, M. Lv, B. Lin, S. Zhang, J. Ding and N. Yuan, "Improvement of the humidity stability of organic–inorganic perovskite solar cells using ultrathin al 2 O 3 layers prepared by atomic layer deposition," *Journal of materials chemistry A,* vol 3, no 10, pp. 5360-5367, 2015.

[138] F. Bella, G. Griffini, J. P. Correa-Baena, G. Saracco, M. Gratzel, A. Hagfeldt, S. Turri and C. Gerbaldi, "Improving efficiency and stability of perovskite solar cells with photocurable fluoropolymers," *Science (new york, N.Y.),* vol 354, no 6309, pp. 203-206, Oct 14 2016.

[139] J. Yang, B. D. Siempelkamp, D. Liu and T. L. Kelly, "Investigation of CH3NH3PbI3 degradation rates and mechanisms in controlled humidity environments using in situ techniques," *ACS nano,* vol 9, no 2, pp. 1955-1963, 2015.

[140] D. Bryant, N. Aristidou, S. Pont, I. Sanchez-Molina, T. Chotchunangatchaval, S. Wheeler, J. R. Durrant and S. A. Haque, "Light and oxygen induced degradation limits the operational stability of methylammonium lead triiodide perovskite solar cells," *Energy & environmental science,* vol 9, no 5, pp. 1655-1660, 2016.

[141] B. Wang, X. Xiao and T. Chen, "Perovskite photovoltaics: A high-efficiency newcomer to the solar cell family," *Nanoscale,* vol 6, no 21, pp. 12287-12297, 2014.

[142] J. M. Frost, K. T. Butler, F. Brivio, C. H. Hendon, M. Van Schilfgaarde and A. Walsh, "Atomistic origins of high-performance in hybrid halide perovskite solar cells," *Nano letters,* vol 14, no 5, pp. 2584-2590, 2014.

[143] M. A. Green, A. Ho-Baillie and H. J. Snaith, "The emergence of perovskite solar cells," *Nature photonics,* vol 8, no 7, pp. 506-514, 2014.

[144] A. Dualeh, P. Gao, S. I. Seok, M. K. Nazeeruddin and M. Grätzel, "Thermal behavior of methylammonium lead-trihalide perovskite photovoltaic light harvesters," *Chemistry of materials,* vol 26, no 21, pp. 6160-6164, 2014.

[145] D. P. Nenon, J. A. Christians, L. M. Wheeler, J. L. Blackburn, E. M. Sanehira, B. Dou, M. L. Olsen, K. Zhu, J. J. Berry and J. M. Luther, "Structural and chemical evolution of methylammonium lead halide perovskites during thermal processing from solution," *Energy & environmental science,* vol 9, no 6, pp. 2072-2082, 2016.

[146] M. Saliba, T. Matsui, J. Seo, K. Domanski, J. Correa-Baena, M. K. Nazeeruddin, S. M. Zakeeruddin, W. Tress, A. Abate and A. Hagfeldt, "Cesium-containing triple cation perovskite solar cells: Improved stability, reproducibility and high efficiency," *Energy & environmental science,* vol 9, no 6, pp. 1989-1997, 2016.

Chapter 3 Photovoltaic cells of Perovskite

Physics of Photovoltaics, and The Perovskite Solar Cell's Structure, Characterisation and stability

3.1 Introduction

In the 1990s, the first study of organic-inorganic halide perovskite material was used as an active layer in electronic devices as demonstrated by Mitzi *et al*. [1]. The first attempt of using this material in photovoltaic (PV) devices was demonstrated in 2009 with a power conversion efficiency (PCE) of 3.8% and 3.1% for $CH_3NH_3PbI_3$ and $CH_3NH_3PbBr_3$ respectively [2]. A big breakthrough was achieved in 2012, when $CH_3NH_3PbI_3$ was utilised in all solid-state mesoscopic solar cells, which was fabricated with a PCE exceeding 9% [3]. Meanwhile, meso-superstructured perovskite solar cells established a PCE of over 10% by utilising a layer of mesoporous Al_2O_3 scaffold [4].

In this chapter, while a particular emphasis is given to Perovskite Solar Cells (PSCs) presented in section (**3.3**), the earlier section (in particular **3.2**) introduces the fundamental properties of a desirable semiconductor absorber that could potentially be used for photovoltaic applications. In addition, the physical theory behind the operation of solar cells and their characterisation is given. Information in greater detail specific to the perovskite solar cells in different architectures is presented here. Instability in various kinds of PSC structures rising from their relative layers is also discussed.

3.2 An Introduction to Photovoltaics

3.2.1 Photovoltaic Cell Generation Process

The term 'Photo-Voltaic' (PV) is derived from the Greek word 'photo', meaning 'light' and 'voltaic'-'electricity', which was named after the scientist Alessandro Volta (1745-1827). This term is described as the process whereby light produces electricity through photovoltaic (PV) effect.

A PV cell (**Figure 3-1**) is a device that uses to generate electricity from light by means of PV effect. This device contains an absorber layer sandwiched between two electrical terminals, which exhibits diode characteristics in the absence of light (in the dark condition), while in the presence of light, it generates electricity. Photons either pass through the cell, reflected or absorbed, depending on the energy of incident photons. Absorbed photons containing enough energy (equal to or greater than the energy bandgap) to excite electrons from a low energy level (valence band, VB) to a higher level (conduction band, CB) will produce free electrons. These free electrons contribute towards electricity,

which subsequently reaches the device terminals (electrodes). The current available when connected to a load is in proportion with the number of photons arriving at the absorber material 'photon in-electrons out'– in other words, the more intense the light input, the more the electricity generated.

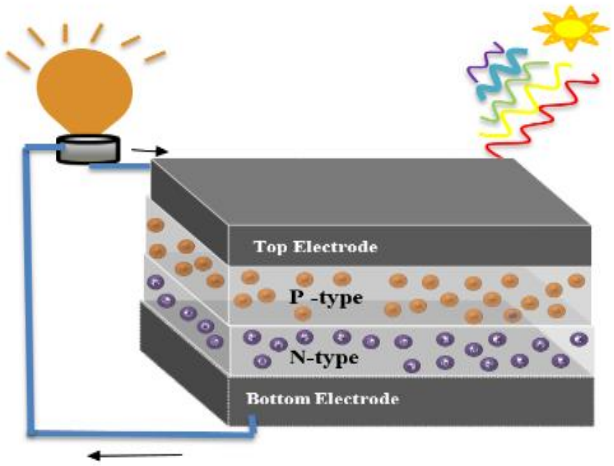

Figure 3-1: The structure of the photovoltaic cell, and conversion of light into electricity.

3.2.2 Desired Photoactive Material Properties for Photovoltaic (PV) Application

The main constituent part of the PV array is the PV cell, which in its basic form consists of two main components:

- An absorber layer that consists of a semiconductor material with properties which include the absorption of light and consequent generation of electron-hole (e-h) pairs by means of the PV effect.
- An electron and a hole collector that are known as metal electrodes in order to accumulate electrons or holes and thereby deliver the electrical current to the load.

To convert the solar energy into an electrical output, the device components must exhibit certain properties. The key properties required include the ability to efficiently absorb light and collect the charge carriers; and within them, include e-h pair generation, efficient charge separation and transportation of the free carriers. In view of this, the absorber material properties will be described in detail below.

3.2.2.1 Absorption

Photons are quantitatively discrete light energy packets, which is characterised by an energy that is dependent upon its wavelength and expressed by the De Broglie relation [5]:

$$\boldsymbol{E = \hbar\omega} \qquad \textbf{(3. 1)}$$

where ω represents the light frequency, which is equal to $c|k|$, where c represents the speed of light and $|k|$ represents the wavevector, $\hbar$ represents the reduced Plank's constant. As ($\hbar = h/2\pi$) and ($k = 2\pi/\lambda$) where, for the purposes of this consideration, λ represents the wavelength of photons, the following may be posited [6]:

$$\boldsymbol{E(eV) = \frac{hc}{\lambda} = \frac{1240}{\lambda\,(nm)}} \qquad \textbf{(3. 2)}$$

In instances where an incoming photon's energy equals or exceeds that of the energy bandgap (Eg) of a semiconductor, the photon will be absorbed in the semiconductor and an electron will transit from the VB to the CB, with the result that a hole will be left in the VB.

When light is absorbed by the semiconductor material, it is attenuated according to the Beer-Lambert Law and may be expressed for a material with a uniform absorption coefficient (α) as follows [6].

$$\boldsymbol{I(x) = I_0 e^{-\alpha x}} \qquad \textbf{(3. 3)}$$

Where *I(x)* represents the incoming light intensity at a depth denoted by (*x*), and the light intensity passes through the first surface of the material (that is, ignoring any surface-reflected light) is represented by I_0. In the case of an inhomogeneous absorbing semiconductor material, the equation (**3.3**) is expressed as follows:

$$\boldsymbol{I(x) = I_0 e^{-\int_0^x \alpha(E,x')dx'}} \qquad \textbf{(3. 8)}$$

In order to fulfil the requirements of an efficient absorber material, it should exhibit a typical optical absorption coefficient of approximately 10^5 cm^{-1}. The optical depth is increased with increasing film thickness. However, the optical absorption coefficient is inversely proportional to the material thickness, since the light intensity decreases exponentially with its propagation through the material. In order to achieve good absorption, the optical depth needs to be high for photons with energy equal to and greater than the Eg, and reflectivity needs to be low [6, 7]. In fact, efficient photon conversion into electricity is not only dependent on the material's ability to absorb the appropriate photons (material with high absorption), but also on its ability to separate charges. This means that, following the absorption of a photon with enough energy, e-h pairs will be crated and these charges then need to be separated and collected at the junction/ interface between the absorber layer and the electrodes, while charge re-combination needs to be prevented [6, 7].

3.2.2.2 Charge generation

Based on the assumption that each absorbed photon with energy equal to Eg leads to the excitation of an electron from the valence band maximum (VBM) to the conduction band minimum (CBM) leaving behind a hole in the VB. This process results in the formation of an e-h pair bounded by Columbic attraction as shown in **Figure 3-2 (a**) [6].

When the energy of an incoming photon exceeds that of the Eg **(Figure 3-2 (c)),** the charge carrier will have an excess kinetic energy causing an electronic excitation to the sub-levels located above the CBM. This electron, however, relaxes to the CBM releasing that excess energy by emission of phonons (heat), due to a phenomenon termed thermalisation. Consequently, the significant concern in charge generation is not the incoming photons' total energy, but the number of photons which has the required energy able to produce charge carriers. Since photons with the lower energy (high wavelength) cannot excite an electron to CBM, their energy is re-emitted in the form of photon (**Figure 3-2(b)**).

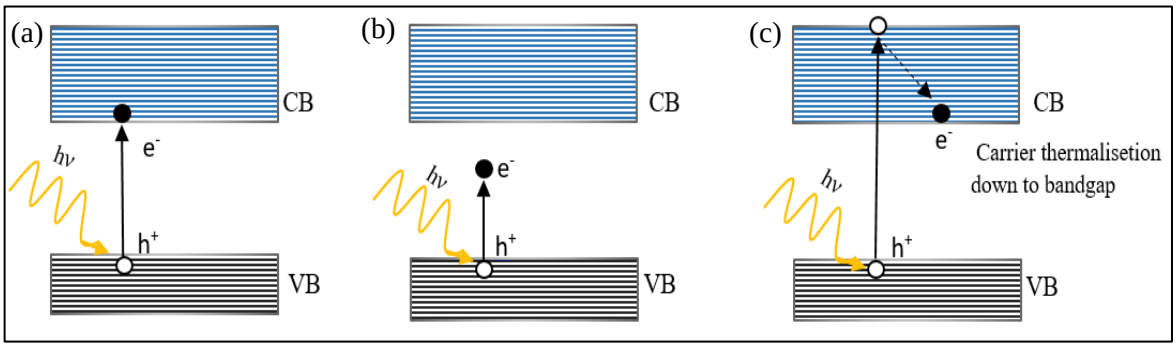

Figure 3-2: An excitation of an electron from the VB to the CB illustrating the electron transition when (a) the photon energy equals the bandgap energy (E_g), (b) the photon energy less than E_g, and (c) the photon energy higher than E_g.

3.2.2.3 Charge separation and collection

Following the excitation of an electron and its consequent promotion to a higher energy level (CB), a hole is left in the VB. Depending on the binding energy of the e-h pair, the exciton may be dissociated by thermal energy or may need another driving force. The potential difference between the two electrodes with different work functions can be a driving force. As a result, a built-in electric field is created, which acts favourably in the capture of electrons in one electrode and holes in the other. Therefore, the charge carriers are transferred to the external load with minimal losses. However, if there is no driving force, electrons may re-emit their excited energy and relax into their original state (VB). Three recombination processes are possible: radiative recombination, Auger recombination, and recombination via defect states [6]. The first two of these, radiative recombination and Auger

recombination, are usually present in intrinsic semiconductors and may additionally exist in defect-free semiconductors. The third recombination happens due to the defect states, which is observed in extrinsic semiconductors and the occurrence of defects within the lattice. These recombination processes are shown in **Figure 3-3**.

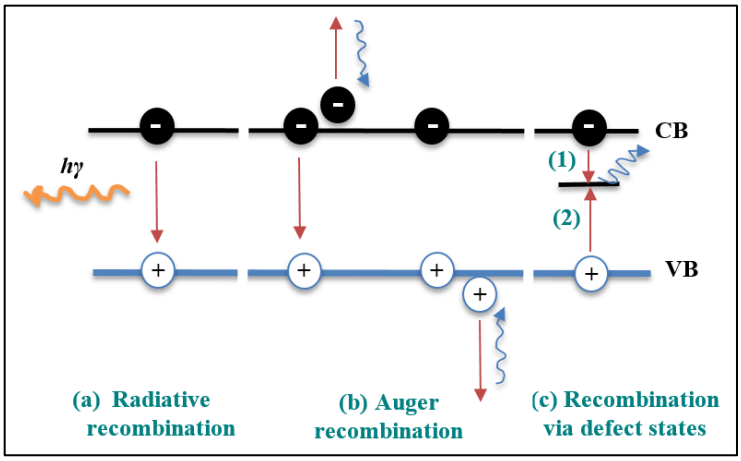

Figure 3-3: Recombination processes occurring in bulk semiconductors.

Radiative recombination is a single-recombination process, which occurs when the excited electrons recombine with holes. The energy of the recombination is then re-emitted in the form of a photon. However, band-to-band Auger recombination involves the action of three particles, whereby a combination of energy and momentum, which is produced as a result of the electron-hole recombination, is transferred to a third free charge carrier (e.g. an electron or a hole). If the free electron gaining this energy gets excited to higher sub-levels in the CB, it will then thermalise into CBM by emitting a phonon. The non-radiative recombination via a defect state, on the other hand, requires two stages to complete the recombination process of the free charge (e and h) in the defect state. In the first stage, an electron (or hole) is captured by the defect/trap through defect transition energy levels. Then, a hole (or electron) is captured by the defect, thereby completing the recombination process [8]. Hence, the recombination energy is emitted in form of phonons. This kind of recombination is also known as the Shockley-Read-Hall (SRH) recombination process [9, 10]. The rate of the SRH recombination depends on the density of traps, the occupation probability of the trap state, and the trap energy [11].

Recombination reduces the photo-generated current density; therefore, it is important to keep it as low as possible. To meet this requirement, a reduction in the density/concentration of both impurities and defects in all parts of the solar cell is important, by using high quality materials and avoiding contamination during the fabrication process. Electrodes that connect the absorber layer to the external circuit/load should exhibit superior conductivity and the contact resistivity (series resistance) should

be low. In addition, it is necessary to form good junctions between the absorber layer and the electrodes, as well as with appropriate materials that are used to establish a spatial asymmetry. As a result, an internal electrical field or a gradient in electron density is built at the interface between two materials or differently doped layers of the same material (p- and n-type). This will help to drive the electrons and holes to either electrode. Such built-in bias will ideally be considerable, and the charge recombination is minimised [6, 7].

3.2.3 Photovoltaic Device Characterisation

3.2.3.1 Standard test conditions (STC)

Typically, the characterisation of photovoltaic devices is performed under illumination of a known light spectrum, such that a voltage is applied across the device and flow of a current is measured. Therefore, it is necessary to ensure that the solar cell characteristics are measured in accordance with the standard test conditions (STC). These test conditions should be based on the quantity of the solar irradiance available at the earth's surface after light experiences absorption and scattering due to atmosphere, i.e. presence of water vapour, oxygen, carbon dioxide and ozone, have been taken into consideration. The presence of dust can cause irregularities in the absorption spectrum towards specific wavelengths.

The STC level is determined on 'air mass' (AM), usually expressed numerically by an integer specifying the characteristics of the light spectrum exhibited by light passing through the air mass at a specific angle of the incidence with respect to the zenith angle (**Figure 3-4**). The AM factor may be expressed as follows [6].

$$\boldsymbol{AM}\ [\boldsymbol{number} = \frac{\mathbf{1}}{\boldsymbol{cos\theta}}] \qquad \textbf{(3. 5)}$$

In the above expression, θ represents the angle between the sun and zenith, as shown in **Figure 3-4**.

Three AM curves may arise, according to the circumstance, as follows:

- AM0 - is applicable to the space such as the blackbody spectral region at 5760K at an irradiance value equal to 1353 W/m^2 [6, 12];
- AM1 - is applicable to the spectrum when the sun is at its zenith with an incident power equal to 925 W/m^2 [12];
- AM1.5 - is applicable to the conditions representing the characteristic adjusted mean for terrestrial environments, where the sun is 45^o above the horizon at an irradiance equal to 844 W/m^2 [12].

The AM1.5 spectrum is applicable in the STC, but this is adjusted such that the integrated incident power intensity equates to 1000 W/m^2 at a temperature of 25 $^{\circ}$C and with the sun at 42° above the horizon [6]. In the case of a solar cell with a test area of 1 cm^2, the incident power will be equal to 0.1W.

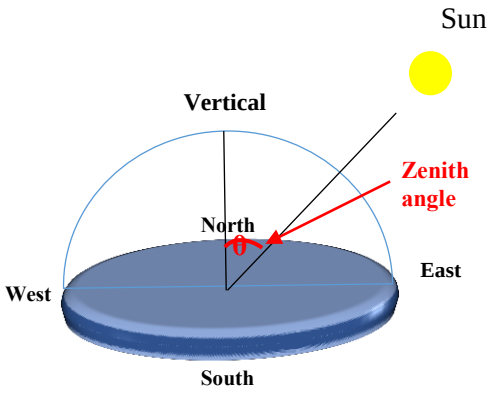

Figure 3-4: Illustration of zenith angle.

3.2.3.2 Equivalent Circuit Model

The operation of a solar cell can be explained by means of a simple equivalent electrical circuit, as illustrated in **Figure 3-5** below.

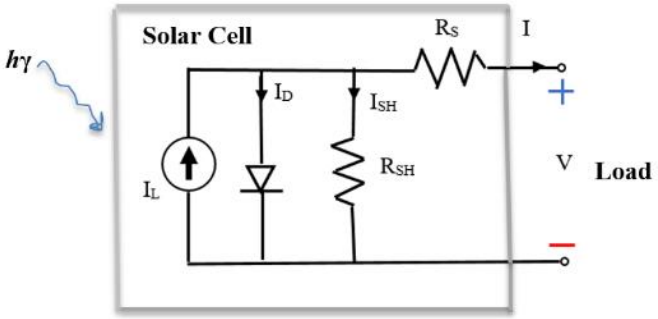

Figure 3-5: Solar cell Equivalent electrical circuit.

This circuit consists of a current source connected with a diode in parallel where the photocurrent is produced, which is proportional to the intensity of light under illumination [6]. In practice, two resistances are presented (i.e. series resistance (R_S) and shunt/parallel resistance (R_{SH})), as being

connected in series and in parallel with the current source and the diode, respectively. R_S represents the resistance of the absorber layer, contact resistance (between the absorber layer and the metal contact) and the resistance of the metal contacts (electrodes) that reduces the current flow [6, 13, 14]. Whereas, R_{SH} represents parallel paths (pinholes) that exist within a solar cell (e.g. impurities, crystal damage), providing an alternative path for the flow of current. In addition, these pinholes might allow undesirable material to pass through between the hole and electron transport layers. Ideally, when the R_S of a solar cell is equal to zero, and R_{SH} is equal to infinity, the resistive losses will reduce to zero.

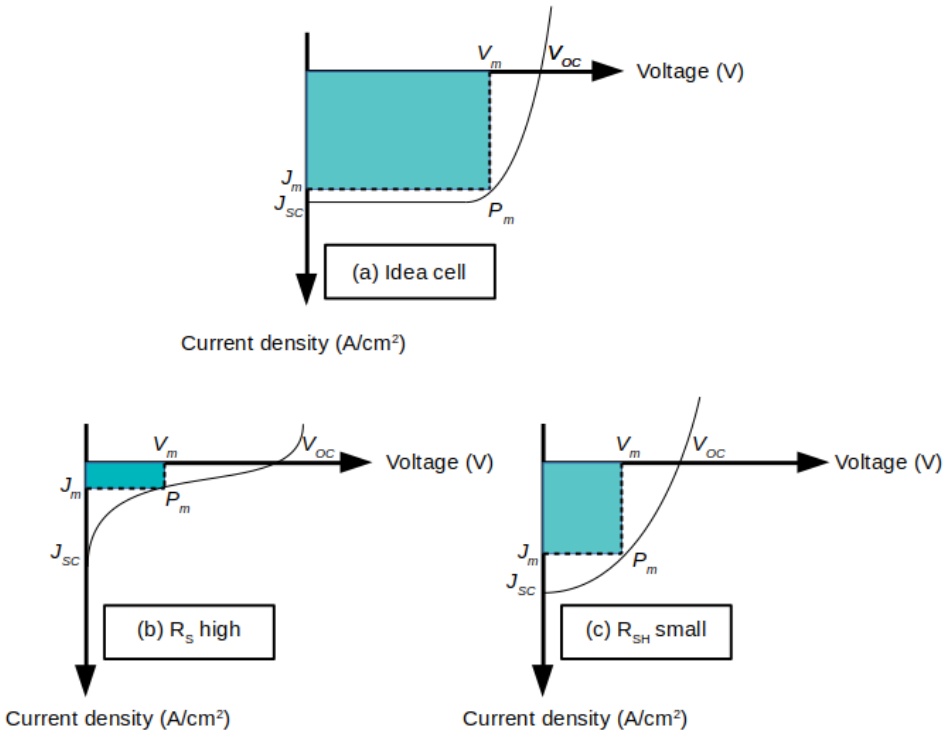

Figure 3-6: *J-V* characteristics of solar cells illustrating (a) the ideal curve, (b) the effect of increasing series resistance, and (c) the effect of decreasing shunt resistances.

As shown in **Figure 3-6 (b)**, a high value of series resistance results in the *J-V* curve becoming flattened on the y-axis (*J*) as compared to an ideal *J-V* curve **Figure 3-6 (a)**, with the result that the cell's maximum current and short circuit current density (J_{SC}) are reduced. It is also shown in **Figure 3-6 (c)** that, once the shunt resistance reduces, the leakage current increases within the diode, resulting in the flattening of the curve on the x-axis (*V*), with a consequent of reduction in the diode's open circuit voltage (V_{oc}). The leakage currents can occur as a result of the recombination of traps and pinholes that may be present in the active layer of the device [13, 15].

3.2.3.3 Solar Cell Characterisation

To characterise a solar cell, three parameters are important; the short circuit current (J_{SC}), open circuit voltage (V_{oc}) and the fill factor (FF), presented in **Figure 3-7**.

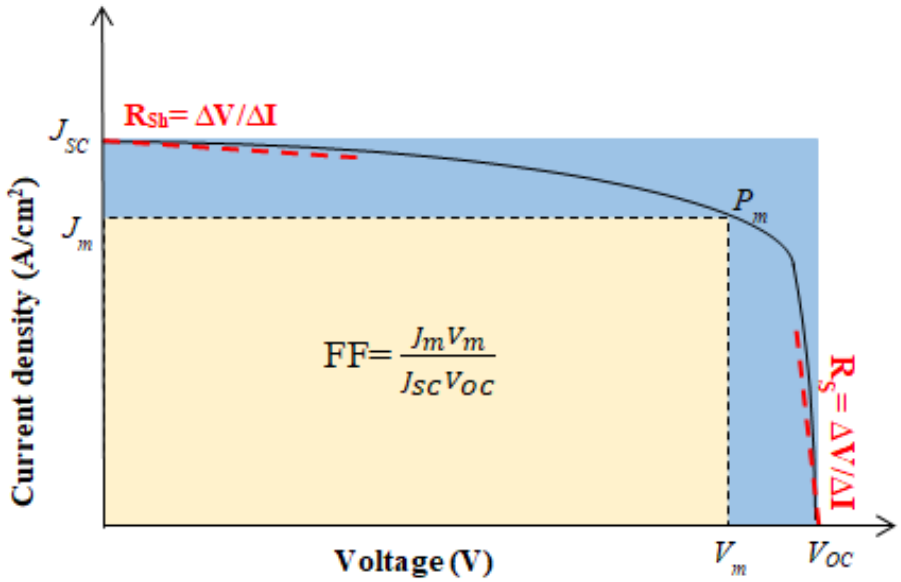

Figure 3-7: The current density-voltage (*J-V*) curve of photovoltaic device represents the solar cell parameters (J_{SC}, V_{oc}, *FF*, R_{sh} *and* R_s).

When no voltage is applied (V=0), current (photocurrent) flowing from the solar cell to the external load as a result of the incident light is termed as short-circuit current (I_{SC}). However, in the absence of incident light (dark condition), most of the solar cells behave like a diode, thereby permitting large current to flow in the forward-bias condition after a threshold (V> 0), while the current produced in the reverse–bias (V< 0) is negligible. This current is known as dark current ($I_{dark}(V)$). Dark current acts in the opposite direction to the photocurrent, thereby forming a reduced net current from the short-circuit value [16],

$$J(V) = J_{SC} - J_{dark}(V) \qquad (3.6)$$

As the *J(V)* represents the net current density, J_{sc} is the short-circuit current density and J_{dark} is the dark current density.

Open-circuit voltage (V_{OC}) is the electrical potential difference between the cell's contacts (terminals)

when disconnected to the load, resulting in no current flow under illuminated condition. This is analogous to the dark current and the short-circuit photocurrent cancel each other [6].

The fill factor (*FF*) is a term used to describe the rectangular shape of the *J-V* curve, which is given by this expression:

$$\boldsymbol{FF = \frac{J_m V_m}{J_{SC} V_{OC}}} \qquad \textbf{(3.7)}$$

This relationship presented in **Figure 3-7**, where the ratio of small rectangle to the big rectangle giving the *FF* magnitude. *FF* will determine the efficiency of charge transport, recombination losses and indication about the parasitic resistance (series and shunt resistance) losses.

A solar cell's Power Conversion Efficiency (PCE) is the percentage of collected solar power, which is converted into electricity. It is denoted by η and may be expressed as follows [6]:

$$\boldsymbol{\eta = \frac{P_m}{E \times A_C} = \frac{V_{OC} I_{SC} FF}{E \times A_C}} \qquad \textbf{(3.8)}$$

Where P_m represents the maximum power point, i.e. the point at which the device's power output is at maximum, expressed as ($V_m \times I_m$). A_C represents the solar cell's surface area and *E* represents the energy (irradiance) of sunlight received in the STC (see section 3.2.3.1) expressed in W/m^2. The energy that is not converted into electricity may be lost in a number of ways, such as, reflectance losses, thermodynamic efficiency losses, recombination losses and parasitic resistance losses.

3.3 Perovskite Photovoltaics

3.3.1 Introduction

Photovoltaic (PV) technologies are classified into three generations. The first generation of PV was based on crystalline silicon (c-Si), which still dominates 90% of the current PV market. Consumption of the required energy to prepare the high purity c-Si wafers led to high manufacturing costs and hindered its flexibility. The residential 10% solar cells market is covered by the second generation termed as thin-film PV technology, by which single or several thin layers of absorber materials are deposited on the substrate. This thin-film PV technology significantly reduced the production cost, and facilitated its flexibility and widespread adaptability. Cadmium telluride (CdTe), copper indium gallium selenide (CIGS) and amorphous silicon are the most common thin films used successfully in the second-generation PV technology. However, the presence of indium and telluride in these solar cells hindered their scalability. Potential solar cells have been fabricated and improved under the third generation such as dye-sensitized solar cells (DSSC), multijunction solar cells, quantum dot solar cells, organic solar cells, nanowire solar cells and perovskite solar cells (PSC).

3.3.2 The development/discovery of hybrid Perovskite PV: a brief history

O'Regan and Grazel (1991) were the first to publish dye-sensitized solar cell (DSSC), which had 7.1-7.9% efficiency, and tested under AM1.5 solar spectrum through the employment of a mesoporous TiO_2 architecture. The cell was able to significantly increase the light harvesting by means of a light-sensitive dye. Several issues remain with regard to these dyes' stability; the dyes are hydrophilic and could be separated from the TiO_2 surface when it absorbs moisture from the surrounding atmosphere or environment [17]. Additionally, liquid electrolytes employed are comprised of volatile organic solvents into which I^-/I_3^- redox couple is dissolved. These may potentially percolate into the sealant or evaporate into the atmosphere. Further developments of the electrolyte were then undertaken with the aim of boosting the cell stability at higher temperatures. The development of an organic solvent-free ionic liquid-based electrolyte by Bai et al. (2008) was comprised of three salts, and, under a sun illumination, showed a cell efficiency of 8.2% over a period of 1000 hours at 60 °C [18]. Hereafter, much attention is paid towards the fabrication of stable DSSCs, however no reports are presented, and research is undertaken due to improve stability within the layers.

Since they are cheap to fabricate, several researchers hoped for dye-sensitised solar cells to replace the conventional inorganic silicon-based solar cells. However, leakage of electrolyte is a major issue with the dye-sensitised solar cells. Instead of a liquid electrolyte, a solid hole transporting material (HTM) is used, and this is called as solid-state dye-sensitised solar cells (ssDSSC) [19]. However, the highest efficiency that was measured after many experiments was 11.9%, which is less than the theoretical predicted value (>20%) [20, 21].

Organometal halide-based perovskites were first used as photo-sensitisers in the PV cells in early 2009 [22]. About this, Miyasaka et al. experimented using the elementary structure of electrolyte based DSSCs. Perovskite nanocrystalline particles (MAPbX3 (X=I, Br)) was used in the place of the absorber dye on a mesoporous TiO_2 (m-TiO_2) film (photoanode). The PCEs achieved were rather unsatisfactory ($\eta = 3.81\%$ for the triiodide and 3.13% for the tri-bromide). In addition, the cell stability in a liquid electrolyte was also not efficient. In 2011, Park et al. synthesised perovskite quantum-dots solar cells by means of a liquid DSSCs, using 2-3 nm MAPbI3 nanocrystals. They succeeded in raising the efficiency to 6.54% at 1 sun illumination [23]. However, the cells degraded within a few minutes due to the perovskite decomposed in the electrolyte.

In 2012, all solid-state perovskite solar cells (similar to ssDSSCs architecture) were published by Grätzel's research team and Park et al. $MAPbI_3$ was used as a light harvester in conjunction with the solid hole conductor 2,20,7,7,0-tetrakis-9N, N-dimethoxyphenyl-amine0-9,90-spirobi-fluorene (spiro-

MeOTAD) on a m-TiO_2, resulting in a PCE of 9.7% [24]. Significant improvements were subsequently made regarding cell efficiency. By the middle of 2014, PSC with a certified 17.9% PCE was achieved [25] and by the end of 2015 it reached 21.02% [26]. The most recent confirmed efficiency (as of early 2019) of such cell is nearly 25% [27]. This breakthrough retains its competitiveness with existing thin film PV technologies. As a result of this, the research interest is beginning to work on stability improvements as well as the streamlining of the manufacturing procedure.

3.3.3 Structure of Perovskite Solar Cells (PSCs)

Typical PSCs are composed of a number of layers - a bottom electrode, a top electrode, an electron transport layer (ETL), a hole transport layer (HTL), and a perovskite layer which is sandwiched in-between.

The bottom electrode (working electrode) consists of a transparent conducting oxide (TCO) such as fluorine-doped tin oxide SnO_2:F (FTO) or tin-doped indium oxide (ITO) that are often coated on glass or plastic substrates. The role of this electrode is to receive the electrons generated in a perovskite absorber layer and transport them to the external circuit. However, the top electrode (counter electrode) allows the flow of electrons from the external circuit, as well as the flow of holes that are carried by the HTL. Therefore, the counter electrode requires the following properties: high-conductivity, and chemical stability [28, 29]. Noble metals like Pt, Ag, Au are often used to form this kind of electrode [30]. An electron transport layer (ETL) is directly deposited on the top of the TCO, which extracts the photo-generated electrons from perovskite, as the conduction band of the ETL is lower than the perovskite excited state (CB) and these electrons are transported by ETL to the working electrode (TCO). An organic or inorganic hole transport layer (HTL) is coated on top of the perovskite layer [31]. The HTL, on the other hand, facilitates the flow of holes to the counter electrode and prevents a direct contact between the perovskite layer and the electrode. The best HTLs are required to have the following properties: high hole mobility, thermally stable, UV stable, and energy levels that match with the valance band of perovskite [32]. Mostly spiro-OMeTAD is used as HTM in perovskite solar cells [19].

Perovskite solar cells do not always require HTLs, but with the capping layer of HTLs, high-performance and efficiency could be achieved. PSCs can rely on a p-n junction between perovskite and n-type metal oxide, because the perovskite acts as a light harvester as well as hole conductor. Without HTL, the cell could be more stable, cheaper and easier to make [19]. However, for high efficiency, a thicker and smoother layer of perovskite is needed to prevent shunt contacts [33]. The PSC anode is made of TCO and ETL, while the cathode is made of a counter electrode and the HTM [34].

There are three types of PSC device architectures, which are mesoscopic, meso-super structured, and planar heterojunction perovskite solar cells. The planar heterojunction could be of two different structures (n-i-p and inverted p-i-n structure) [19, 35]. **Figure 3-8** shows mesoscopic and planar solar cell structure.

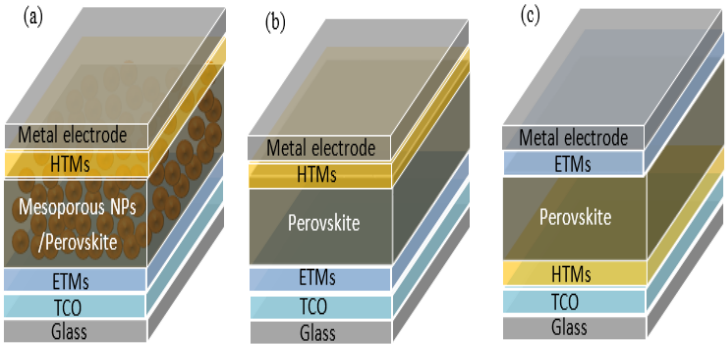

Figure 3-8: Structures of perovskite solar cell architectures. (a) mesoscopic. (b) n-i-p planar. (c) p-i-n inverted planar.

3.3.3.1 Mesoscopic and Meso-Superstructured Structure

Perovskite-sensitised mesoporous solar cells (mesoscopic PSCs) (**Figure 3-8 (a)**) was the first explored cell architecture, which is not different from the solid-state dye-sensitized solar cells (ssDSSCs). In this architecture, a perovskite material is deposited on m-TiO_2 layer, and then it is capped by the HTL with the counter electrode [19, 35, 36]. The mesoporous surface of the m-TiO_2 layer increases the surface-area for the perovskite material. Increasing perovskite/TiO_2 interfacial area improves the density of photon-generated carriers due to increase in light scattering, which is crucial for the PSC performance [37].

The working mechanism of the mesoscopic PSCs is also like the ssDSSCs. The mechanism is based on photoexcitation (that occurs in the perovskite layer) and efficiently injecting the electrons into the m-TiO_2. This structure also reduces the diffusion length for carrier transport and enhances electron–hole separation [37]. Thickness of the m-TiO_2 layer and its porosity have a significant influence on the quality of the perovskite capping layer [38] and on the electron flux density [39]. Undesired processes like charge recombination can happen, but occurs at a much lower rate compared to the desired processes, such that it results in a well-performing device [19, 35].

Adopting such architecture, a highly reproducible PCE of 15% and certified value of 14.1% have been achieved by Grätzel's research team [36]. Hereafter, Park et al. and Grätzel's research team developed

a perovskite solar cell based on m-TiO_2 by controlling the size of $CH_3NH_3PbI_3$ cuboids which yielded an PCE of 17% [40]. Following these significant discoveries, particularly over the last few years, there have been substantial advances made by several researchers in this field [41].

Despite the higher efficiencies in mesoscopic PSCs that have been demonstrated, the fabrication process that involves sintering at 500 $^{\circ}$C is not suitable for low-cost production and infeasible for applications that use plastic substrates [42]. Moreover, instability of photocatalyst TiO_2 (see section 3.3.4.1) is another barrier, which affects the overall device stability [43]. Therefore, alternative inorganic oxides have been proposed to address this problem employing a meso-super structured SCs (MSSCs) architecture, with the same design architecture as that of mesoporous PSCs. In MSSCs, instead of a mesoporous n-type conducting metal oxide, a porous insulating metal oxide layer is incorporated [32]. The perovskite layer, here, behaves as the intrinsic absorber and electron transport material [19].

In 2012, Snaith and Miyasaka demonstrated solar cells based on the MSSCs structure. Here, an n-type mesoporous oxide is replaced with scaffold alumina layer (Al2O3), covered with CH3NH3PbI3-XCix and spiro-MeOTAD [44]. An increase in the Voc (1.13 V) with an efficiency rating of 10.9% was achieved. A low temperature processed MSSCs with an efficiency of 15.9% was contributed [45]. It was found, however, that without the m-TiO2 layer, a qualified compact TiO2 (c-TiO2) layer is required for achieving a device with improved performance. This layer separates the HTM from TCO layers – such that direct contact between these two layers would cause a short circuit in a solar cell. This layer do also not allow the holes that are generated in the perovskite layer to be injected to the TCO anode as if they are attracted by the anode, the net current of the PSC minimises.

3.3.3.2 Planar Structure

Due to the established properties of the perovskite material, particularly, its long carrier diffusion length and ambipolar charge transport (see chapter 2), a planar type structure has been explored [37], [42]. In such structures, two device architectures were proposed; n-i-p and inverted p-i-n, as presented in **Figure 3-8 (b) & (c)**. Originally, the hole transport and electron transport layers were separated by an ambipolar layer of perovskite [19, 37, 46].

Planar heterojunction perovskite solar cell fabricated by vapour deposition yielded a *PCE* of 15.4% [47]. Kelly and Liu have also developed planar structure perovskite solar cells based on a room temperature processed ZnO layer, which exhibited a *PCE* of 15.7% [48]. In 2014, Yang et al. had achieved an efficiency of 19.3% with an average efficiency of 16.6% [49].

Despite the simplicity and low consumption of energy, this architecture has several limitations. The interface contact area between the perovskite and ETL can affect the extraction of electrons [37]. As a

result, the unbalanced electron and hole flux can lead to charge accumulation into the trap sites, resulting in the creation of hysteresis in the planar structure. A reduction in the hysteresis loop has been noticed when utilizing a fullerene which acts as an ETL due to its passivation effect, resulting in a balance between hole and electron collections [37, 42, 50, 51].

.

3.3.4 Instability of Perovskite SCs- Intrinsic Device Architecture Stability

The *PSCs* that are the imminent successor of *ssDSSCs* have increased their PV conversion efficiency to 24.2± 0.8%, in 2019, from 3.81% in 2009 [52]. This means that they are comparable with C-Si *PV*. Despite this, they have relatively poor environmental stability as it prone to damage from O_2, high temperature, *UV*-light and moisture. As laboratory studies are the first stage in the path towards commercialisation, the devices need lifetime testing due to their 25-year outdoor operation, different characterisation tests are needed to justify the solar cell reliability in a realistic environment.

In fact, the operational temperature of a typical solar cell increases from 10 – 45 ℃ above the environmental temperature [53], which implies, if the temperature of the environment is approximately 40 ℃, the operational temperature of the solar cell can potentially reach as high as 85 ℃ [54]. In addition to environmental temperature, the device is also exposed to moisture during their operation. Therefore, it must undergo a laboratory stability test of several thousands of hours at 85 °*C* and 50% humidity conditions, as well as thermal cycling stability of over few hundreds of cycles from 40 to 85 °*C* [55]. Passing all these tests successfully, gives the device under question great opportunity to transit from the laboratory to the commercial stage.

3.3.4.1 Instability Caused in Electron Transport Layer

The most commonly used material for ETL (photoanode) in mesoscopic PSCs is Titania (TiO_2). The drawback of TiO_2 is the defects arising from non-stoichiometry such as titanium interstitials and oxygen vacancies [56]. As a result, deep-trap levels within bandgap energy are formed that significantly reduce PV cell performance. Many attempts are made to overcome these obstacles. Pathak *et al.* investigated that low doping levels of TiO_2 with aluminium to help reduce the density of trap states by passivating the defects, and an improvement in the device stability was noticed with Al-doped TiO_2 [56].

In addition, TiO_2 is generally known to act as a photo catalyst for breaking down water into hydroxyl radicals that could lead to oxidation of the organic cation in the perovskite material. Under UV light, TiO2 oxidises iodide ions (I^-) in perovskite by extracting electrons, and it was found that the perovskite material was transformed into PbI_2 after 12 hours of exposure to UV light [32, 57]. A

planar structure was proposed by Song et al. to replace TiO_2 mesoporous layer with SnO_2 [58]. This kind of structure (SnO_2 based device) achieved efficiency of 13% and it showed more stability in ambient conditions for 700 hrs than the TiO_2 based devices. The improved stability may be caused by the passivation of the residual PbI_2 present at the interface between SnO_2 and $CH_3NH_3PbI_3$**.**

3.3.4.2 Instability Caused in Hole Transport Layer

$CH_3NH_3PbI_3$ could potentially be corroded by 4-tert-butylpyridine (TBP) as shown by Li et al., as TBP is a significant additive in the hole-transport material, Spiro-OMeTAD, to improve the conductivity [59]. However, the TBP reduces the device stability since it dissolves PbI_2, and thus creating the [PbI_2–xTBP] complex material. To overcome this problem, the author used a montmorillonite (MMT) buffer layer between the perovskite layer and the Spiro-OMeTAD layer so that the perovskite corrosion could be prevented [59]. By adding MMT, the device efficiency was improved by 32.2%, achieving 11.9% efficiency under AM1.5 sunlight.

Three most common HTL materials used are: Spiro-OMeTAD, poly[bis(4-phenyl) (2,4,6-trimethylphenyl) (PTAA), and poly(3-hexylthiophene) (P3HT). These materials produced higher efficiencies and their influence on the degradation rates of PSCs under controlled humidity environment were investigated [60, 61]. The mixed halide perovskite ($CH_3NH_3PbI_2Br$) device structure built by replacing the conventional thick layer of Spiro-OMeTAD with thin P3HT layer [61] found that the P3HT-based device showed a superior stability over a test period of 250 hrs in ambient condition, with a lower rate of degradation by 6-folds as compared with the other two materials [61]. The faster decomposition rate in Spiro-OMeTAD-based device was attributed to the presence of pinholes within the layer, which provide pathways for moisture to affect the perovskite material. Thus, this induces the fast degradation rate at ambient condition. In addition to the higher stability of P3HT-based device, the low-cost of P3HT is also one of the advantages (10 times cheaper than Spiro-OMeTAD). Moreover, a quite thin layer of P3HT is required (50 nm) compared to the required thickness of Spiro-OMeTAD (100-300nm), which reduces the fabrication cost [61].

Kim *et al.* replaced organic HTL with an inorganic material, NiO_x [62]. A higher environmental stability was achieved by using such inorganic oxide film; however, the device efficiency was not as high as what achieved by using organic material for HTL [62]. In order to improve the efficiency, NiO_x films are doped with copper by incorporating a copper-containing precursor, hence an increase in the device efficiency is approved. By comparing the efficiency and stability of three devices; PEDOT: PSS device, NiO_x device and Cu-NiO_X device, it has been found that a maximum efficiency of 15.4% is achieved by Cu-NiO_x device which was higher than undoped NiO_x device (8.94%) and even higher than PEDOT:PSS device (11.16%). In addition, the Cu-NiO_x device shows a good stability over a test

period of 240h with efficiency equal to 90% of initial value, however the efficiency of PEDOT: PSS device decreases after 144h to less than 50% of initial efficiency. This reduction is due to the degradation of ITO electrode and perovskite layer. The degradation is caused by absorbing the moisture by the PEDOT: PSS layer, since PEDOT: PSS is a hygroscopic material.

More importantly, a published research study presented a fabricated device that was unsealed, and showed a PCE of 11.5% with 1008 hrs of stability in ambient condition under AM 1.5 of artificial sunlight [63]. $(5\text{-AVA})_x(MA)_{(1-x)}PbI_3$ perovskite material was utilised as an active layer in HTL-free device. The authors asserted that the total time, 1008 hrs of stability, without a decrease in PV conversion efficiency resulted from the protection of the perovskite by a carbon layer that acted as a back contact [63].

3.3.4.3 Instability Caused in Buffer Layer

Different approaches have been taken to improve the device stability by incorporating a buffer layer. Cuarnera et al. proposed the use of Al_2O_3 nanoparticles as a buffer layer between the perovskite layer and the HTL in the standard meso-super structured solar cell (MSSC) [64]. The benefits of adding this layer included improving the FF and reducing series resistance. Rapid degradation within 200 hrs was observed in the control device, which is due to the metal migration from top contact into the perovskite layer leading to shunting in a solar cell. However, good stability was noticed in the device with a buffer layer which maintained 95% of its initial efficiency over a test period of 350 hrs of light exposure. This stability was attributed to the incorporation of the buffer layer that eliminated the migration of the metal from the metal electrode, to the perovskite layer [64].

3.3.4.4 Instability Caused in Electrode

One of the highly efficient and stable materials used as a counter electrode in perovskite solar cells is gold (Au); however, this electrode suffers from a major disadvantage in terms of its high costs [65-68]. As a low-cost alternative, silver (Ag) is used [68]. The environmental instability, however, is the main obstacle for Ag usage due to the corrosion of Ag by perovskite material, which results in the oxidation of Ag. After few days of the fabrication of Ag-based solar cell, the Ag electrode colour changes from the shiny reflective silver-colour to yellowish-colour, and, eventually, substantially reduces the device efficiency [69]. The colour change is corresponding to the formation of silver iodide (AgI), which is formed by the migration of methyl ammonium iodide into the Ag electrode via the pinholes existing in Spiro-OMeTAD (the HTL) [69]. This reaction could be effectively suppressed by modeling the interfaces between each layer (e.g. Spiro-oMeTad/Ag interface), which prevents the

ion migration towards the electrode and accumulation of the volatile iodide at the interfaces. Hence, long-term stability of PSCs is achieved [70]. .

3.4 Summary

Within this chapter, the important physical background information for understanding the mechanisms of PV devices and the key concepts for the desired properties of the photoactive semiconductors has been covered and explained. Moreover, the critical parameters necessary for evaluating and characterising solar cells have been introduced. Then, the promises photovoltaic cells which based on the organic-inorganic tri-halide perovskite material have been presented in deeper detail with focus on their discovery, the various architectures have been established to date, and the materials which constitute the perovskite photovoltaics layers. Finally, the stability issues particularly relevant to each constituent layer in the perovskite solar cell architectures have been discussed.

References

[1] C. R. Kagan, D. B. Mitzi and C. D. Dimitrakopoulos, "Organic-inorganic hybrid materials as semiconducting channels in thin-film field-effect transistors," *Science (new york, N.Y.),* vol 286, no 5441, pp. 945-947, Oct 29 1999.

[2] A. Kojima, K. Teshima, Y. Shirai and T. Miyasaka, "Organometal halide perovskites as visible-light sensitizers for photovoltaic cells," *Journal of the american chemical society,* vol 131, no 17, pp. 6050-6051, 2009.

[3] H. Kim, C. Lee, J. Im, K. Lee, T. Moehl, A. Marchioro, S. Moon, R. Humphry-Baker, J. Yum and J. E. Moser, "Lead iodide perovskite sensitized all-solid-state submicron thin film mesoscopic solar cell with efficiency exceeding 9%," *Scientific reports,* vol 2, pp. 591, 2012.

[4] M. M. Lee, J. Teuscher, T. Miyasaka, T. N. Murakami and H. J. Snaith, "Efficient hybrid solar cells based on meso-superstructured organometal halide perovskites," *Science (new york, N.Y.),* vol 338, no 6107, pp. 643-647, Nov 2 2012.

[5] A. Rae, "Quantum mechanics, chapter 6.5," 2002.

[6] J. Nelson, *The physics of solar cells,* World Scientific, 2003.

[7] K. Chopra, P. Paulson and V. Dutta, "Thin-film solar cells: An overview," *Progress in photovoltaics,* vol 12, no 2-3, pp. 69-92, 2004.

[8] J. Yang, L. Shi, L. Wang and S. Wei, "Non-radiative carrier recombination enhanced by two-level process: A first-principles study," *Scientific reports,* vol 6, pp. 21712, 2016.

[9] R. N. Hall, "Electron-hole recombination in germanium," *Physical review,* vol 87, no 2, pp. 387, 1952.

[10] W. Shockley and W. Read Jr, "Statistics of the recombinations of holes and electrons," *Physical review,* vol 87, no 5, pp. 835, 1952.

[11] A.G. Aberle, *Crystalline silicon solar cells: Advanced surface passivation and analysis,* Centre for Photovoltaic Engineering. University of New South Wales, 1999.

[12] S.M. Sze, ***Physics of semiconductor devices, 2nd edition****,* Wiley- India, 1991.

[13] J. Bernede, "Organic photovoltaic cells: History, principle and techniques," *Journal of the chilean chemical society,* vol 53, no 3, pp. 1549-1564, 2008.

[14] J. Xue, S. Uchida, B. P. Rand and S. R. Forrest, "4.2% efficient organic photovoltaic cells with low series resistances," *Applied physics letters,* vol 84, pp. 3013, 2004.

[15] B. Kippelen, S. Yoo, J. A. Haddock, B. Domercq, S. Barlow, B. Minch, W. Xia, S. R. Marder and N. Armstrong, "Liquid-crystal approaches to organic photovoltaics," *Optical engineering-new york-marcel dekker incorporated-,* vol 99, pp. 271, 2005.

[16] A. M. Roy, *Tunneling contacts for novel semiconductor devices,* 2012.

[17] M. I. Asghar, K. Miettunen, J. Halme, P. Vahermaa, M. Toivola, K. Aitola and P. Lund, "Review of stability for advanced dye solar cells," *Energy & environmental science,* vol 3, no 4, pp. 418-426, 2010.

[18] Y. Bai, Y. Cao, J. Zhang, M. Wang, R. Li, P. Wang, S. M. Zakeeruddin and M. Grätzel, "High-performance dye-sensitized solar cells based on solvent-free electrolytes produced from eutectic melts," *Nature materials,* vol 7, no 8, pp. 626-630, 2008.

[19] S. Shi, Y. Li, X. Li and H. Wang, "Advancements in all-solid-state hybrid solar cells based on organometal halide perovskites," *Materials horizons,* 2015.

[20] P. Docampo, S. Guldin, T. Leijtens, N. K. Noel, U. Steiner and H. J. Snaith, "Lessons learned: From dye-sensitized solar cells to all-solid-state hybrid devices," *Advanced materials,* vol 26, no 24, pp. 4013-4030, 2014.

[21] M. A. Green, K. Emery, Y. Hishikawa, W. Warta and E. D. Dunlop, "Solar cell efficiency tables (version 46)," *Progress in photovoltaics: Research and applications,* vol 23, no 7, pp. 805-812, 2015.

[22] A. Kojima, K. Teshima, Y. Shirai and T. Miyasaka, "Organometal halide perovskites as visible-light sensitizers for photovoltaic cells," *Journal of the american chemical society,* vol 131, no 17, pp. 6050-6051, 2009.

[23] J. Im, C. Lee, J. Lee, S. Park and N. Park, "6.5% efficient perovskite quantum-dot-sensitized solar cell," *Nanoscale,* vol 3, no 10, pp. 4088-4093, 2011.

[24] H. Kim, C. Lee, J. Im, K. Lee, T. Moehl, A. Marchioro, S. Moon, R. Humphry-Baker, J. Yum and J. E. Moser, "Lead iodide perovskite sensitized all-solid-state submicron thin film mesoscopic solar cell with efficiency exceeding 9%," *Scientific reports,* vol 2, 2012.

[25] Anonymous *"Best research-cell efficiencies",* [Online] .

[26] DYESOL, *EPFL achieves 21% efficiency for perovskites,* www.dyesol.com.: a media Release, 2015.

[27] E. H. Jung, N. J. Jeon, E. Y. Park, C. S. Moon, T. J. Shin, T. Yang, J. H. Noh and J. Seo, "Efficient, stable and scalable perovskite solar cells using poly (3-hexylthiophene)," *Nature,* vol 567, no 7749, pp. 511, 2019.

[28] J. Halme, P. Vahermaa, K. Miettunen and P. Lund, "Device physics of dye solar cells," *Advanced materials,* vol 22, no 35, pp. E210-E234, 2010.

[29] T. C. Sum and N. Mathews, "Advancements in perovskite solar cells: Photophysics behind the photovoltaics," *Energy & environmental science,* vol 7, no 8, pp. 2518-2534, 2014.

[30] M. Ye, X. Wen, M. Wang, J. Iocozzia, N. Zhang, C. Lin and Z. Lin, "Recent advances in dye-sensitized solar cells: From photoanodes, sensitizers and electrolytes to counter electrodes," *Materials today,* vol 18, no 3, pp. 155-162, 2015.

[31] Y. Zhang, W. Liu, F. Tan and Y. Gu, "The essential role of the poly (3-hexylthiophene) hole transport layer in perovskite solar cells," *Journal of power sources,* vol 274, pp. 1224-1230, 2015.

[32] Z. Yang and W. Zhang, "Organolead halide perovskite: A rising player in high-efficiency solar cells," *Chinese journal of catalysis,* vol 35, no 7, pp. 983-988, 2014.

[33] H. S. Jung and N. Park, "Perovskite solar cells: From materials to devices," *Small,* vol 11, no 1, pp. 10-25, 2015.

[34] N. Park, "Organometal perovskite light absorbers toward a 20% efficiency low-cost solid-state mesoscopic solar cell," *The journal of physical chemistry letters,* vol 4, no 15, pp. 2423-2429, 2013.

[35] B. Wang, X. Xiao and T. Chen, "Perovskite photovoltaics: A high-efficiency newcomer to the solar cell family," *Nanoscale,* vol 6, no 21, pp. 12287-12297, 2014.

[36] S. Kazim, M. K. Nazeeruddin, M. Grätzel and S. Ahmad, "Perovskite as light harvester: A game changer in photovoltaics," *Angewandte chemie international edition,* vol 53, no 11, pp. 2812-2824, 2014.

[37] Z. Song, S. C. Watthage, A. B. Phillips and M. J. Heben, "Pathways toward high-performance perovskite solar cells: Review of recent advances in organo-metal halide perovskites for photovoltaic applications," *Journal of photonics for energy,* vol 6, no 2, pp. 022001, 2016.

[38] C. Jiang, S. L. Lim, W. P. Goh, F. X. Wei and J. Zhang, "Improvement of CH3NH3PbI3 formation for efficient and better reproducible mesoscopic perovskite solar cells," *ACS applied materials & interfaces,* vol 7, no 44, pp. 24726-24732, 2015.

[39] J. H. Heo, H. J. Han, D. Kim, T. K. Ahn and S. H. Im, "Hysteresis-less inverted CH 3 NH 3 PbI 3 planar perovskite hybrid solar cells with 18.1% power conversion efficiency," *Energy & environmental science,* vol 8, no 5, pp. 1602-1608, 2015.

[40] J. Im, I. Jang, N. Pellet, M. Grätzel and N. Park, "Growth of CH3NH3PbI3 cuboids with controlled size for high-efficiency perovskite solar cells," *Nature nanotechnology,* vol 9, no 11, pp. 927-932, 2014.

[41] J. J. Choi, X. Yang, Z. M. Norman, S. J. Billinge and J. S. Owen, "Structure of methylammonium lead iodide within mesoporous titanium dioxide: Active material in high-performance perovskite solar cells," *Nano letters,* vol 14, no 1, pp. 127-133, 2013.

[42] L. Meng, J. You, T. Guo and Y. Yang, "Recent advances in the inverted planar structure of perovskite solar cells," *Accounts of chemical research,* vol 49, no 1, pp. 155-165, 2015.

[43] C. Bi, Y. Shao, Y. Yuan, Z. Xiao, C. Wang, Y. Gao and J. Huang, "Understanding the formation and evolution of interdiffusion grown organolead halide perovskite thin films by thermal annealing," *Journal of materials chemistry A,* vol 2, no 43, pp. 18508-18514, 2014.

[44] M. M. Lee, J. Teuscher, T. Miyasaka, T. N. Murakami and H. J. Snaith, "Efficient hybrid solar cells based on meso-superstructured organometal halide perovskites," *Science (new york, N.Y.),* vol 338, no 6107, pp. 643-647, Nov 2 2012.

[45] K. Wojciechowski, M. Saliba, T. Leijtens, A. Abate and H. J. Snaith, "Sub-150 C processed meso-superstructured perovskite solar cells with enhanced efficiency," *Energy & environmental science,* vol 7, no 3, pp. 1142-1147, 2014.

[46] S. Gamliel and L. Etgar, "Organo-metal perovskite based solar cells: Sensitized versus planar architecture," *RSC advances,* vol 4, no 55, pp. 29012-29021, 2014.

[47] M. Liu, M. B. Johnston and H. J. Snaith, "Efficient planar heterojunction perovskite solar cells by vapour deposition," *Nature,* vol 501, no 7467, pp. 395-398, 2013.

[48] D. Liu and T. L. Kelly, "Perovskite solar cells with a planar heterojunction structure prepared using room-temperature solution processing techniques," *Nature photonics,* vol 8, no 2, pp. 133-138, 2014.

[49] H. Zhou, Q. Chen, G. Li, S. Luo, T. B. Song, H. S. Duan, Z. Hong, J. You, Y. Liu and Y. Yang, "Photovoltaics. interface engineering of highly efficient perovskite solar cells," *Science (new york, N.Y.),* vol 345, no 6196, pp. 542-546, Aug 1 2014.

[50] Y. Shao, Z. Xiao, C. Bi, Y. Yuan and J. Huang, "Origin and elimination of photocurrent hysteresis by fullerene passivation in CH 3 NH 3 PbI 3 planar heterojunction solar cells," *Nature communications,* vol 5, pp. 5784, 2014.

[51] C. Bi, Q. Wang, Y. Shao, Y. Yuan, Z. Xiao and J. Huang, "Non-wetting surface-driven high-aspect-ratio crystalline grain growth for efficient hybrid perovskite solar cells," *Nature communications,* vol 6, pp. 7747, 2015.

[52] Best Research-Cell Efficiency Chart, *"Https://Www.nrel.gov/pv/cell-efficiency.html",* [Online] .

[53] E. Cuddihy, C. Coulbert, A. Gupta and R. Liang, "Electricity from photovoltaic solar cells: Flat-plate solar array project final report. volume VII: Module encapsulation," 1986.

[54] M. A. García and J. Balenzategui, "Estimation of photovoltaic module yearly temperature and performance based on nominal operation cell temperature calculations," *Renewable energy,* vol 29, no 12, pp. 1997-2010, 2004.

[55] M. O. Reese, S. A. Gevorgyan, M. Jørgensen, E. Bundgaard, S. R. Kurtz, D. S. Ginley, D. C. Olson, M. T. Lloyd, P. Morvillo and E. A. Katz, "Consensus stability testing protocols for organic photovoltaic materials and devices," *Solar energy materials and solar cells,* vol 95, no 5, pp. 1253-1267, 2011.

[56] S. K. Pathak, A. Abate, P. Ruckdeschel, B. Roose, K. C. Gödel, Y. Vaynzof, A. Santhala, S. Watanabe, D. J. Hollman and N. Noel, "Performance and stability enhancement of dye-sensitized and perovskite solar cells by al doping of TiO2," *Advanced functional materials,* vol 24, no 38, pp. 6046-6055, 2014.

[57] G. Niu, X. Guo and L. Wang, "Review of recent progress in chemical stability of perovskite solar cells," *Journal of materials chemistry A,* vol 3, no 17, pp. 8970-8980, 2015.

[58] J. Song, E. Zheng, J. Bian, X. Wang, W. Tian, Y. Sanehira and T. Miyasaka, "Low-temperature SnO 2-based electron selective contact for efficient and stable perovskite solar cells," *Journal of materials chemistry A,* vol 3, no 20, pp. 10837-10844, 2015.

[59] W. Li, H. Dong, L. Wang, N. Li, X. Guo, J. Li and Y. Qiu, "Montmorillonite as bifunctional buffer layer material for hybrid perovskite solar cells with protection from corrosion and retarding recombination," *Journal of materials chemistry A,* vol 2, no 33, pp. 13587-13592, 2014.

[60] J. Yang, B. D. Siempelkamp, D. Liu and T. L. Kelly, "Investigation of CH3NH3PbI3 degradation rates and mechanisms in controlled humidity environments using in situ techniques," *ACS nano,* vol 9, no 2, pp. 1955-1963, 2015.

[61] M. Zhang, M. Lyu, H. Yu, J. Yun, Q. Wang and L. Wang, "Stable and Low-Cost mesoscopic CH3NH3PbI2Br perovskite solar cells by using a thin poly (3-hexylthiophene) layer as a hole transporter," *Chemistry-A european journal,* vol 21, no 1, pp. 434-439, 2015.

[62] J. H. Kim, P. Liang, S. T. Williams, N. Cho, C. Chueh, M. S. Glaz, D. S. Ginger and A. K. Jen, "High-Performance and environmentally stable planar heterojunction perovskite solar cells based on a Solution-Processed Copper-Doped nickel oxide Hole-Transporting layer," *Advanced materials,* vol 27, no 4, pp. 695-701, 2015.

[63] A. Mei, X. Li, L. Liu, Z. Ku, T. Liu, Y. Rong, M. Xu, M. Hu, J. Chen, Y. Yang, M. Gratzel and H. Han, "A hole-conductor-free, fully printable mesoscopic perovskite solar cell with high stability," *Science (new york, N.Y.),* vol 345, no 6194, pp. 295-298, Jul 18 2014.

[64] S. Guarnera, A. Abate, W. Zhang, J. M. Foster, G. Richardson, A. Petrozza and H. J. Snaith, "Improving the long-term stability of perovskite solar cells with a porous Al2O3 buffer layer," *The journal of physical chemistry letters,* vol 6, no 3, pp. 432-437, 2015.

[65] J. Xu, A. Buin, A. H. Ip, W. Li, O. Voznyy, R. Comin, M. Yuan, S. Jeon, Z. Ning and J. J. McDowell, "Perovskite–fullerene hybrid materials suppress hysteresis in planar diodes," *Nature communications,* vol 6, pp. 7081, 2015.

[66] A. D. Sheikh, A. Bera, M. A. Haque, R. B. Rakhi, S. Del Gobbo, H. N. Alshareef and T. Wu, "Atmospheric effects on the photovoltaic performance of hybrid perovskite solar cells," *Solar energy materials and solar cells,* vol 137, pp. 6-14, 2015.

[67] G. Sfyri, C. V. Kumar, D. Raptis, V. Dracopoulos and P. Lianos, "Study of perovskite solar cells synthesized under ambient conditions and of the performance of small cell modules," *Solar energy materials and solar cells,* vol 134, pp. 60-63, 2015.

[68] F. Machui, M. Hösel, N. Li, G. D. Spyropoulos, T. Ameri, R. R. Søndergaard, M. Jørgensen, A. Scheel, D. Gaiser and K. Kreul, "Cost analysis of roll-to-roll fabricated ITO free single and tandem organic solar modules based on data from manufacture," *Energy & environmental science,* vol 7, no 9, pp. 2792-2802, 2014.

[69] Y. Kato, L. K. Ono, M. V. Lee, S. Wang, S. R. Raga and Y. Qi, "Silver iodide formation in methyl ammonium lead iodide perovskite solar cells with silver top electrodes," *Advanced materials interfaces,* vol 2, no 13, 2015.

[70] J. Wang, X. Chen, F. Jiang, Q. Luo, L. Zhang, M. Tan, M. Xie, Y. Li, Y. Zhou and W. Su, "Electrochemical corrosion of ag electrode in the silver grid Electrode-Based flexible perovskite solar cells and the suppression method," *Solar RRL,* vol 2, no 9, pp. 1800118, 2018.

Chapter 4 Synthesising Techniques of Perovskite Material

This chapter introduces various experimental methods used in this research study. Two novel CVD growth routes have been proposed and explored to develop organic-inorganic lead tri-halide perovskite thin films, in particular $MAPbI_3$ ($MA= CH_3NH_3$); atmospheric pressure chemical vapour deposition (APCVD) and plasma-enhanced chemical vapour deposition (PECVD). APCVD growth is a one-step deposition technique that uses a liquid precursor (PbI_2 • MA in DMF), while in order to form perovskite film by PECVD route, two-step deposition methods were used. This two-step deposition approach involves the deposition of PbI_2 thin films on clean substrates, initially, that were deposited by spin-coating and thermal evaporation techniques. That was followed by exposure of PbI_2 films to the methane (CH_4) and ammonia (NH_3) gaseous in plasma phase that was performed in vacuum by PECVD process.

Although this chapter emphasises on CVD growth process including PECVD and APCVD processes, it is devoted discussing both the aforementioned methods from initial preparation of the substrates' surface and the techniques that are used to deposit PbI_2 thin films.

4.1 Surface Preparation

4.1.1 Surface Cleaning

In this work, the wet cleaning process was undertaken in the class 100 clean room and encompassed the following procedures. To begin with, a 5% Decon-90 soap detergent was mixed with de-ionized water inside a beaker before being sonicated and agitated in an ultrasonic bath (35 *kHz*) for a period of 40 minutes. Thereafter, the substrates were rinsed for two minutes for five times using fresh de-ionized water. Later, samples were sonicated in acetone for 15 minutes, and then underwent an additional sonication for 15 minutes in isopropyl alcohol (IPA). Then, the substrates were rinsed for a period of two minutes using deionized water on five occasions. Samples were finally dried on an individual basis with a nitrogen gun, before they were left to dry on a plate or oven at 100℃ for an hour. All aforementioned steps were performed in a laminar flow workbench in order to avoid contamination induced by the environment.

4.1.2 Surface Modification with Plasma Treatment

In order to improve adhesive bonding with another material, there are various methods that can be used to modify the surface of the substrate. In this regard, methods involving the use of plasma are

very common treatment for modifying/altering the surface energy. One of the modifications is to make substrate surface more adhesive and wettable (hydrophilic) which is the objective of this cleaning process [2]. In addition, plasma is also used for its ability to remove contaminants from the surface of the substrate [1].

Plasma contains positive and negative ions along with atoms, molecules and free radicals of the gas used [2]. In the surface treatments involving plasma, charged particles were created by the excited gas atoms get accelerated towards the substrate surface in the presence of external electric field, resulting in the release of excitation energies when they impinged on the surface [1]. Plasma-based treatments are categorised based on the energies of gases and charged particles. Plasma (glow discharge) treatment is undertaken at reduced pressure, and it is possible for the plasma species to be either reactive (e.g. hydrogen, oxygen) or inert (e.g. argon) [2]. Bombardment of high-energy particles leads to transfer its energy on the loosely bonded particles over the surface that are being removed, such process is referred as cleaning, which, in turn, leads to collision cascade in close proximity to the surface. Energy of the bombarding particles is released in the form of heat, although some portion of the energy is transferred to surface atoms, which, in turn, will be removed with contaminants. In a plasma region, sputter cleaning can lead to a reaction between the surface and activated contaminants such as oxygen. Therefore, plasma formation can take place in a distinct area using either inert or reactive gases, wherefrom ions are bombarded and accelerated to the substrate at appropriate vacuum conditions. The bombardment of low-energy ions from the inert gas aids in desorption of surface contaminants without causing damage to the surface [1]. Ion etching involving a reactive gas is referred to as reactive plasma cleaning since reactive species are capable of reacting with contaminants and forming volatile products [1].

In this work, a Bio-Rad PT7100 barrel etcher was used for the substrate cleaning. In addition, a suitable quartz holder was utilized for holding the samples that have to undergo cleaning process. Subsequently, this holder was placed inside the chamber, and the system was pumped down to a vacuum ~10^{-2} *torr*. Then, Argon gas was filled in the chamber until the pressure reached ~10^{-1} *torr*. Thereafter, radio frequency (RF) power was introduced in order to ionize the gas and generate the plasma. After turning on the RF power of 100 Watts, the reflected power was kept at minimal (< 5 Watts). The glass surface substrates were cleaned under Ar^- plasma for ~10 minutes, while the surface of silicon (*Si*) substrates were introduced into oxygen plasma due to its effective in removing hydrocarbons and absorbing water vapour from surfaces [1].

4.2 Synthesis of Perovskite Layer

In this work, two novel routes were used to synthesise methyl ammonium lead iodide ($MAPbI_3$) as presented in **Figure 4-1**. The first route of synthesis this material involves two-step approach in which an incorporation of thermal evaporator or spin-coater with plasma-enhanced chemical vapour deposition (PECVD) was applied. The first step involves deposition of thin film of PbI_2, while the second step was used to convert the deposited film into perovskite. The second route used to synthesise the perovskite material involves a single-step process through atmospheric pressure chemical vapour deposition (APCVD). The following sections explain the working principle of the deposition methods used in both routes that include spin coating and thermal evaporation techniques followed by PECVD, in addition to APCVD.

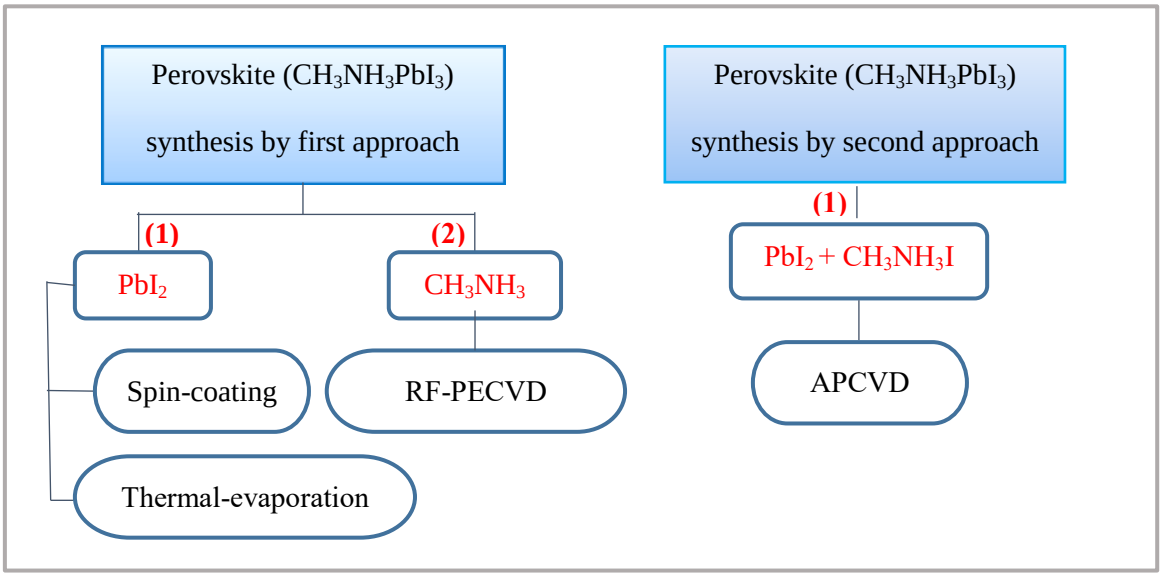

Figure 4-1: The two novel methods were used in this study for the deposition of perovskite thin films.

4.2.1 Lead Iodide (PbI_2) Thin Film Deposition Methods

4.2.1.1 Spin-Coating

The numerous deposition methods used in the deposition of perovskite material are based on solution processing, such as spin coating, drop casting, and printing (for example ink-jet printing, screen printing, pad printing, roll-to-roll printing and knife over edge coating). All these methods require a suitable solvent for the specific material.

Among aforementioned wet methods, in this work, spin coating was used to deposit PbI_2 layer and then introduced into a PECVD process. This method requires a liquid processor that was prepared by dissolving PbI_2 powder in a polar solvent (DMF). Few drops of the solution were dropped onto a substrate, which was held on a rotating chuck by assisted vacuum. Pumping a neutral gas into the chamber (usually N_2 gas) was another requirement in order to maintain the dryness of the chamber. Parameters such as rotating speed (from five hundred to several thousand revolutions per minute) and rotation total time were monitored and controlled by means of control panel that was attached to the spin-coater system. Two rotating approaches can be applied including static and dynamic conditions that effectively influence the properties of the coated film. In the static coating approach, the solution was introduced on a fixed substrate, followed by spun. However, the coating takes place whereby the solution is dropped onto a spinning substrate is known as dynamic approach. During the spin, the solution spreads across the substrate by centrifugal force resulting in a deposition of a uniform thin film after the solvent is evaporated (**Figure 4-2**). The drawback of this method, especially when employing the dynamic condition, is the amount of material being wasted.

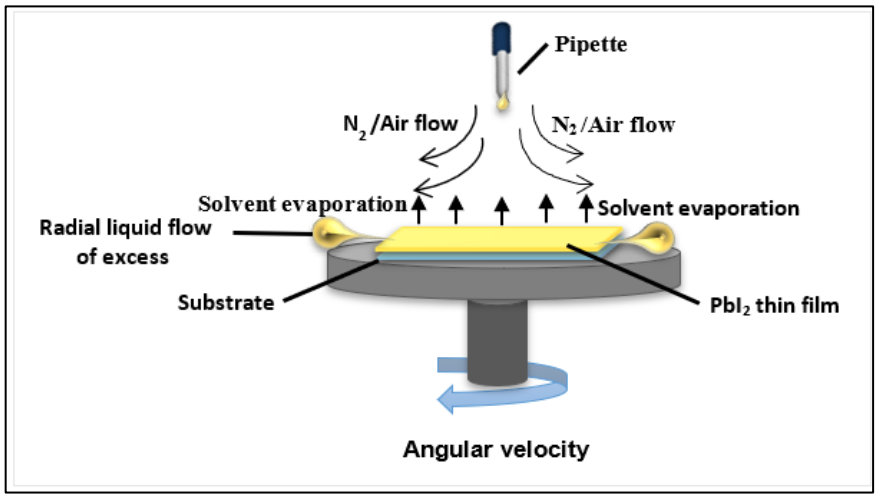

Figure 4-2: Schematic of the major spin coating process.

Many other factors should be controlled which make this technique a complex in nature. These include the solution's viscosity and the concentration of the material, N_2 gas flow rate and the evaporation rate of the solvent, which also have a great impact on the thickness and uniformity of the coated film. Therefore, the generalised relationship between the thickness of the film (d) and the angular velocity (ω) is described according to the observed experimental results, with introducing two relative empirical constants that are related to the characteristics of the solution (e.g. the viscosity of solution) denoted as k and α [3]:

$$d = k\,\omega^{\alpha} \qquad (4.9)$$

According to this relationship, an inverse proportional relationship between the angular rotating velocity (ω) and film thickness (d) and the direct proportional relationship between the solution concentration (k) and film thickness (d) can be noticed. Therefore, applying higher angular velocities and lower concentration, results in the reduction in the film thickness, as shown in **Figure 4-3:**

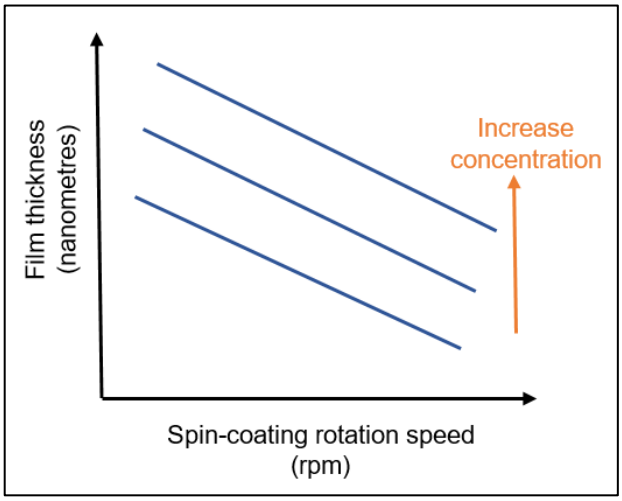

Figure 4-3: relationship between the thickness of the film and angular velocity in a spin coating method (adopted from [3]).

4.2.1.2 Thermal Evaporation

Thermal evaporation is one of the deposition technologies, used in this work, which is performed in a chamber kept under vacuum. It is a physical vapour deposition process (PVD) that can be used to deposit thin films in a high vacuum environment (10^{-5} – 10^{-6} *mbar*). The reasons for using the vacuum systems are as follows:

- The possibility of oxidation or contamination of the materials is quite low because this system removes air and any dust particles within the chamber before the deposition.
- The quality of the film deposition can be improved by increasing the mean free path (MFP), which is inversely proportional to the pressure inside the chamber. Physically, the magnitude of the MFP of the atoms/molecules before colliding with another in the air is ~10×10^{-6} cm. However, at a pressure of $10^{-6} mbar$, the MFP is increased to around 5 cm [4]. Typically,

after 10 collisions of the molecule/atom, a noticeable deviation from its original path occurred. Therefore, if the distance between the material position and the substrate is less than 10 MFP, the scattering will be reduced, resulting in a better uniformity in the deposited film.

This technique has two pumps; namely, rotary and diffusion pumps. When the system is pumped down to 10^{-2} *mbar* by the rotary pump, the diffusion pump begins to further reduce the pressure to 10^{-6} *mbar*. The principle working of the diffusion pump depends on evaporating the boiling silicone oil through centred tubes into the chamber, during which cold water is pumped outside the diffusion pump to condense the oil (**Figure 4-4**). As a result, the oil is dropped down from the chamber into the pump, taking the contamination and air with it. When the oil is fully contaminated, it will need to be replaced periodically [5].

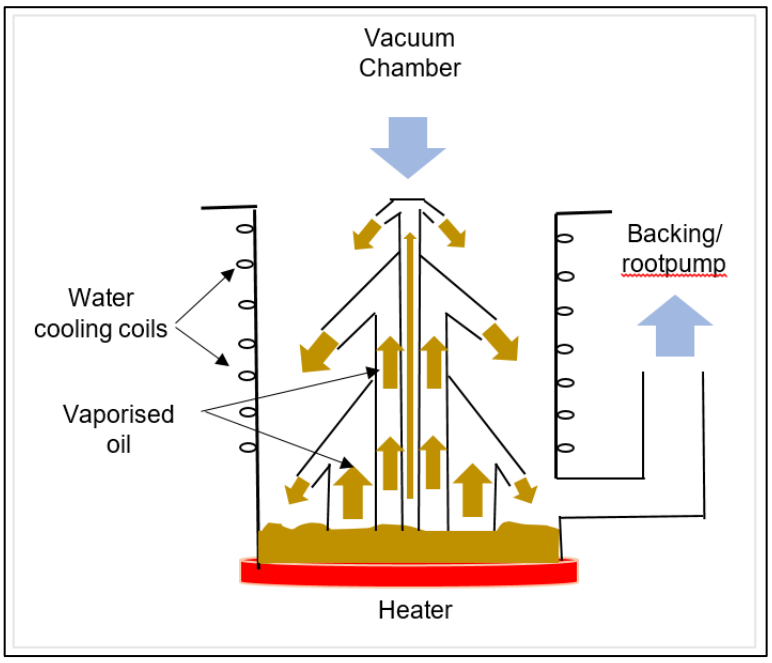

Figure 4-4: Schematic of working principle of diffusion pump.

The working principle of this technique, as its name suggests, is that it evaporates the target material, which is placed onto a crucible such as a boat, coil, and basket of a metal (e.g. tungsten). The required energy for material evaporation is supplied by a DC current passing through the conducting metal holder, which is known as Joule effect [6]. These conducting holders are made from materials with very high melting temperatures exceeding 3000 °C, such as tungsten, molybdenum or tantalum, in order to withstand high temperatures. By applying an electric current (~20-30 A) to the filament, the material will initially melt, resulting in the evaporation of the atomic/molecular species [7]. Once the

hot species reach the unheated substrates, they condense on cold surface of a substrate forming a thin film. The mean free path (MFP) of the travelling species mainly depends on the vacuum pressure of the chamber, where it is mean travel distance will increase in the existence of unwanted gases leading to a decrease in the average kinetic energy of the evaporated species (in order tenths of *eV*) [8]. This will result in the formation of porous and weak adhesive layer [8]. Therefore, to deposit high purity thin film, high vacuum (~ 4 x 10^{-6} *mbar*) is required [8]. This technique works efficiently with a huge number of materials that have melting point less than 1500 ℃, including pure metals, non-metals, metal oxides and some organic materials [9]. However, it is not employed for those materials that have melting point higher than 1500 ℃ [8]. E-beam thermal evaporation is an alternative technique that is recommend for such materials with high melting point [8].

In this work, an Edwards Auto 306 thermal evaporator was used to evaporate the inorganic material of perovskite (PbI_2) and the metal electrodes (aluminum, silver) as cathode/anode for current-voltage measurements. This equipment has glass bell jar, filament or crucible, and a substrate holder as seen in **Figure 4-5**. In addition, a quartz crystal oscillator is fixed at the similar height of the positioned substrates to monitor the thickness of the deposited layer.

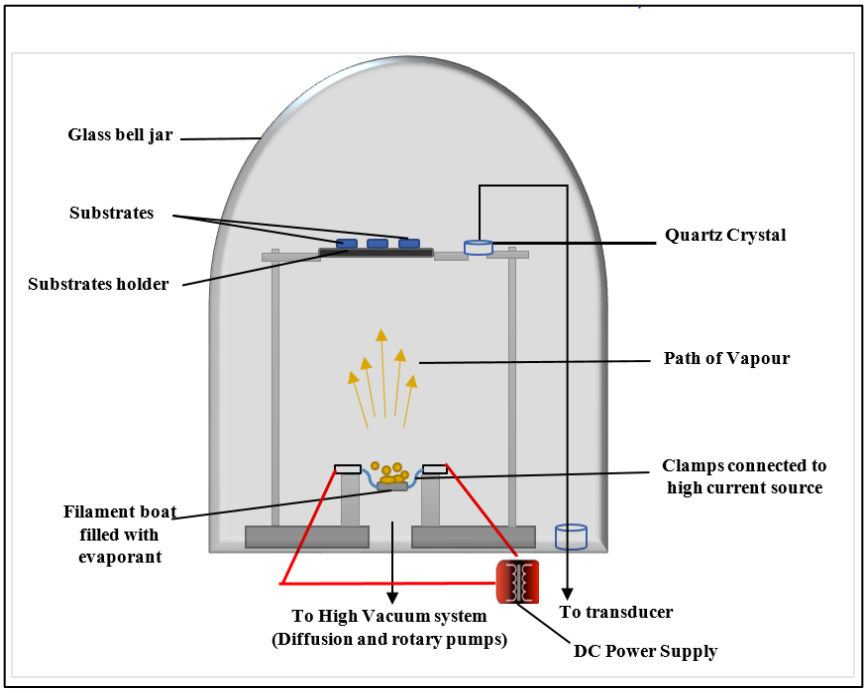

Figure 4-5: Schematic diagram of a thermal evaporator.

4.2.2 Perovskite Thin Film Deposition Methods

Both proposed routes used in this work to synthesis perovskite thin films ($MAPbI_3$) are based on chemical vapour deposition (CVD). Therefore, this section is begun with the description of CVD process.

4.2.2.1 Overview of Chemical Vapour Deposition (CVD)

CVD, as the name suggests, is a chemical reaction (CR) process to synthesise a material from vapour-phase. This vapour compound species is decomposed on the substrate surface in the presence of thermal energy producing desired non-volatile product to form thin film [7].

CVD is a sequential process that comprises several steps; (1) mass transport of the gas precursors supply either from the gas flow region or gas generator into the reactor (deposition zone); (2) the diffusion of the gas precursors across the boundary layer to a substrate surface; (3) once the precursors reach the substrate surface, they are adsorbed; (4) the adsorbed gas have to migrate on the substrate's surface (surface mobility); (5) a number of chemical reactions then take place on the substrate surface, starting with small nuclei initially formed from the first few molecules arriving onto the substrate and further chemically reacted resulting into the growth of islands; (6) the grown islands merge with each other to form a continuous thin film; (7) desorption of by-products (volatile products) from the substrate's surface occur by crossing the boundary layer out of the reactor [10]. **Figure 4-6** (a) illustrates step (1), (2), (3) and (7), while step (4), (5) and (6) are illustrated in **Figure 4-6** (b).

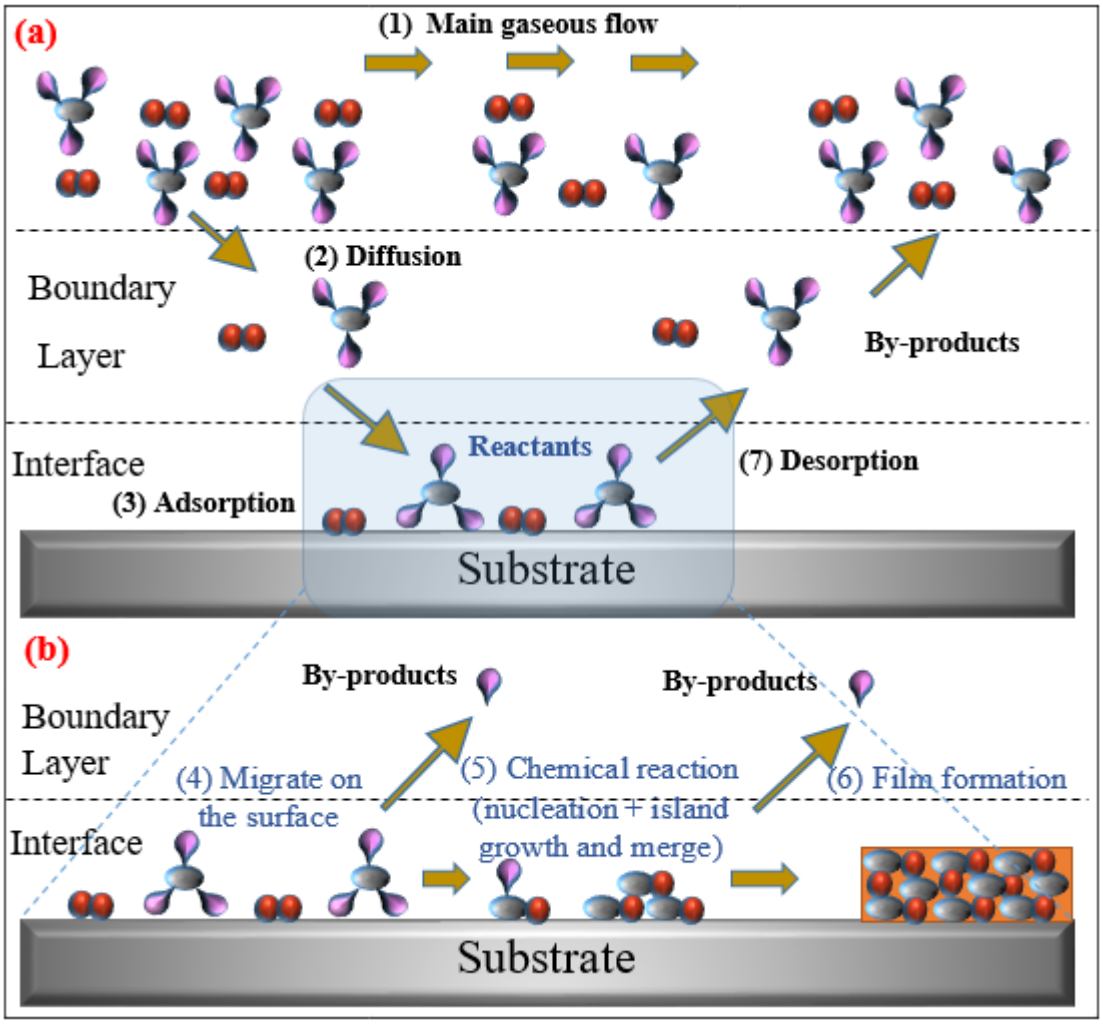

Figure 4-6: CVD process sequence showing the interaction between the adsorbed molecules and the substrate surface.

The adsorption of the diffused precursor molecules through the boundary by the substrate surface can undergo two kinds of adsorptions (see **Figure 4-7**). One is possibility known as chemisorption which exhibits strong chemical bonds (> *2 eV* of energy per molecule) forming between atoms on the substrate's surface and the adsorbed precursor. Due to the strong chemical bond of chemisorbed atoms, they have limited migration on the surface (very low surface mobility); and hence they bond with the surface's dangling bonds and contribute to the film growth [10]. Physisorption is, as the name suggests, physical adsorption. This bond is much weaker than the chemical bond, which requires energy less than 0.5 *eV* per molecule to be formed due to the nature of the forces involved (Van der Waals and dipole–dipole forces) [10]. Therefore, it has high surface mobility, which is necessary to reduce the roughness and porosity of the film surface, hence increasing the film quality [10].

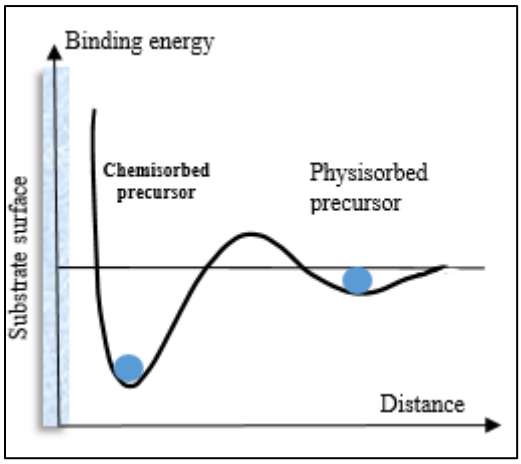

Figure 4-7: Relationship of bonding energy to chemical and physical adsorption (Adapted from [10]).

According to the Arrhenius equation, the chemical reaction (CR) is mainly affected by the substrate temperature (T) and the activation energy (E_a) as follow:

$$\boldsymbol{CR = A\, exp(-E_a/k_B T)} \qquad \textbf{(4. 2)}$$

Where A is a constant, k_B is the Boltzmann constant. In the case of low activation energy (E_a), an easier chemical reaction can be achieved since a low barrier exists (**Figure 4-8**). However, in the case of existence of high activation energy, external sources of energy are required to overcome this barrier such as thermal energy, RF power, or UV radiation.

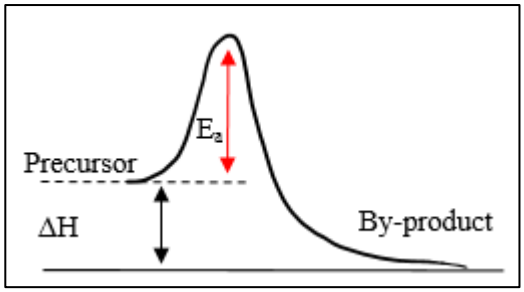

Figure 4-8: Chemical activation energy (Adapted from [10]).

The exponential relation between the CR and T can dramatically affect the deposition rate (DR). In addition, the DR can be altered by the rate of the precursor diffusion (D) across the boundary layer and the adsorption rate (AR). The dependence of DR on temperatures is illustrated in **Figure 4-9**. At low temperature, in particularly at the surface-reaction-limited regime, the DR is low since the chemical reaction rate is mainly related to temperature (according to equation (4.2)) as the elevation of temperature is needed to overcome the E_a. The low effect of temperature variation appears in the mass-transport-limited regime. Further increasing the temperature, a sharp decrease in the DR is noticed due to the gas-phase-nucleation.[10].

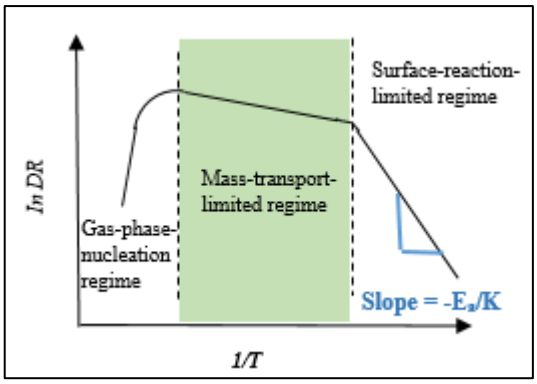

Figure 4-9: Deposition rate regimes as a function of temperatures (Adapted from [10]).

Due to high surface chemical reaction rate presents in the mass-transport-limited regime, it is preferable to synthesise the material at this regime and set it as the optimal operation in most of CVD reactors. Moreover, its low sensitivity to the temperature changes, which is however difficult to maintain constant, is another advantage. Meanwhile, CR becomes mainly affected by the other controllable parameters such as precursor diffusion and chemisorption rates that can be altered by the gas flow rate [10].

One of the alternatives to standard CVD reactors is plasma-enhanced chemical vapour deposition (PECVD). Plasmas can easily achieve mass-transport-limited regime at low temperatures by generating reactive free radicals and accelerating ions that provide enough energy to increase the chemical reaction rate, once they are diffused and bombarded the surface by their high energy (*10 to 20 eV*) [10]. The advantage of using PECVD over CVD growth process is that the activation energy required for the gaseous reaction is provided by energetic plasma beside the thermal energy which allows the reduction in the temperature during the deposition process. Therefore, it is needed to further discuss about such an advance CVD technique, already in use by both academic and manufacturing for fabricating several semiconductor devices such as solar cells, MOSFET, TFT, and flash memory.

4.2.2.2 Plasma-Enhanced Chemical Vapour Deposition (PECVD)

4.2.2.2.*a* Generation of Plasma

To generate plasma from a gas, an external source of energy is required such as direct current (DC) power or radio frequency (RF) power. DC power is commonly applied, in a PVD system, while RF power is most commonly applied in a plasma enhanced CVD for semiconductor processing. For semiconductor materials that require high growth temperatures (above 400 $^{\circ}$C) for deposition, the PECVD technique is considered to be a suitable technique, as stated earlier in section (4.2.2.1).
Most PECVD systems are subjected to RF power that is performed in low or high pressure. The plasma is generated between two parallel electrodes, which are a capacitively coupled electrodes to control the reflected power (**Figure 4-10**).

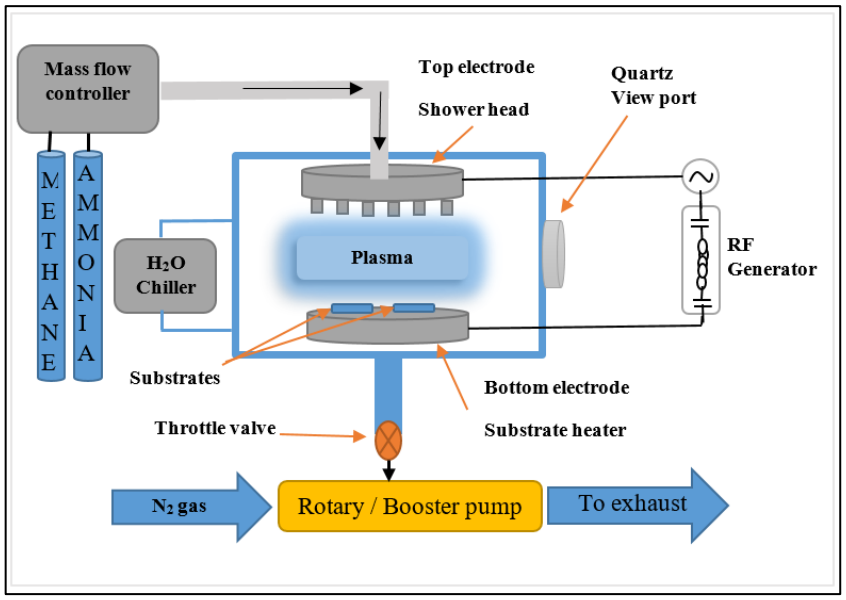

Figure 4-10: Schematic diagram of a PECVD.

When RF power is applied between the two electrodes, an alternating electric field (AC power) is established where each electrode acts alternatively as a cathode and as an anode. As a result, free electrons are accelerated with sufficient kinetic energy (in the order of *10 eV*) from the negative electrode to the positive electrode causing ionisation, excitation, and dissociation of an introduced gas. Some of the excited atoms, due to electron collisions, are relaxed back to a lower energy level, leading to the emission of photons, hence the plasma glow is observed during a PECVD process. Although, most of the transitions take place in the *UV* spectrum region that can excite the molecules to higher

electronic states, other collisions can also excite the gas molecules to higher vibrational or rotational states. The most important reactions for the deposition process are those, which can produce ionised species to sustain the plasma. The number of ions generated in the plasma is equal to those electrons achieving a quasi-neutral state overall, however not locally.

4.2.2.2.*b* Collisions in the Plasma

Energetic electrons play an important role in promoting electron-molecule collisions causing elastic and inelastic collisions. The most frequent collision in the plasma is elastic; however, it is inessential since there is no exchange in energy between the colliding particles. However, the exchange of energy between colliding particles results into inelastic collision. Inelastic collisions are occurred simultaneously in plasma and can be summarised as follow:

1. Electron-neutral collisions.
2. Neutral-neutral collisions.
3. Ion-neutral collisions.
4. Ion-ion collisions.
5. Electron-ion collisions.

Electron-molecule collisions are the reactions, which can cause ionisation, electronic excitation-relaxation, and dissociation of the neutral gas molecules through the inelastic collisions.

- **Ionisation**

The ionisation state of a molecule or an atom is reached when they are collided by an energetic electron. When sufficient energy is transferred from the electron to the molecule or atom, it can break the electron from its orbital and leave the nucleus's constraint. The generated ions can play a major part in the deposition process as well as sustain the plasma. This is known as electron impact ionisation process, which produces a positive ion (A^+) and two free electrons (e^-) as shown in **Figure 4-11** and it can be expressed as:

$$e^- + A \rightarrow A^+ + 2\,e^- \qquad (4.3)$$

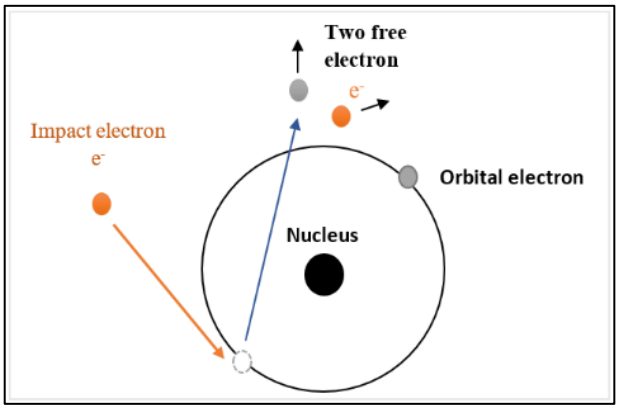

Figure 4-11: Ionisation collision before and after electron impact (Adapted from [10]).

- **Excitation-relaxation**

When the energy transferred from the impacted electron to the atom or molecule is not enough to break the orbital electron and free the electron, the electron becomes excited to a higher orbital energy level. This process is known as excitation as shown in **Figure 4-12** and it can be expressed as

$$e^- + A \rightarrow A^* + e^- \qquad (4.4)$$

Due to the short lifetime of the excited state, the excited electron falls from the excited orbital to the lower orbital and meanwhile release the extra energy in the form of a photon ($h\nu$) as light emission as shown in **Figure 4-12**. This process is called relaxation and it can be expressed as follow:

$$A^* \rightarrow A + h\nu \qquad (4.5)$$

Where, $h\nu$ is the emitted photon energy, and h and ν are the Planck's constant and the light emission frequency, respectively.

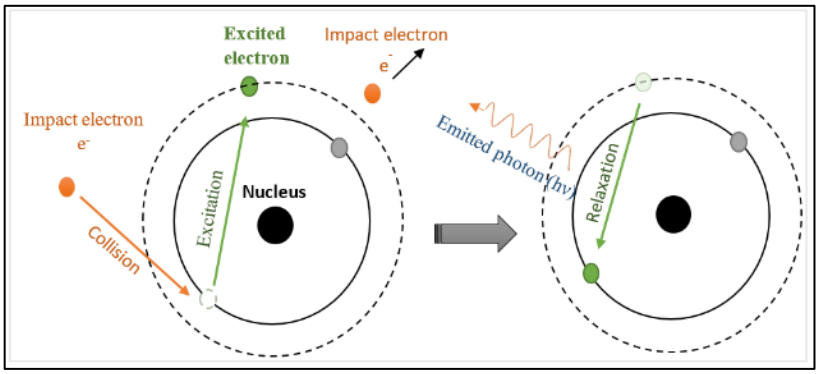

Figure 4-12: Excitation and Relaxation process (Adapted from [10]).

- **Dissociation**

When the energy transferred during the collision between an electron and a molecule is higher than the molecule's bonding energy, free radicals are generated (**Figure 4-13**). This process is called as dissociation collision and can be expressed as

$$e^- + AB \rightarrow A + B + e^- \qquad (4.6)$$

In this expression, molecule represented as *AB*, and the generated free radicals after dissociation collision is represented as *A*, and *B*. These free radicals employ a strong tendency to grab an electron from the surrounding atoms or molecules which enhance the chemical reaction.

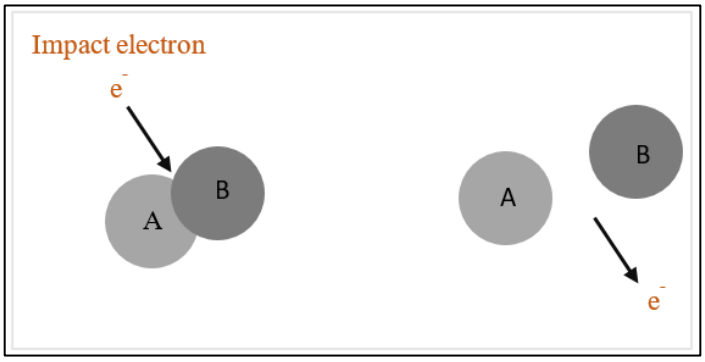

Figure 4-13: Dissociation collision (Adapted from [10]).

In this work, the gaseous phase reactions that take place within the plasma are generated from a mixture of methane and ammonia gas to form perovskite material by exposing the initial layer PbI_2 thin film to the organic cation ($CH_3NH_3^+$). It has been suggested that when the precursor gases (CH_4 and NH_3) are mixed, the primary ions that can be produced as a result of ionisation and dissociation of their molecules are CH_4^+, CH_3^+, CH_2^+, and NH_3^+, NH_2^+, NH^+as they are required low energies to be produced [11]. These primary ions react rapidly with each other and with neutral molecules of methane and ammonia, resulting in the following reactions [11- 12]:

$$CH_4^+ + NH_3 \rightarrow NH_4^+ + CH_3 \quad (4.7), \qquad NH_3^+ + CH_4 \rightarrow NH_4^+ + CH_3 \quad (4.8),$$

$$CH_3^+ + NH_3 \rightarrow NH_4^+ + CH_2 \quad (4.9), \qquad CH_2^+ + NH_3 \rightarrow NH_4^+ + CH \quad (4.10),$$

$$C_2H_5^+ + NH_3 \rightarrow NH_4^+ + C_2H_4 \quad (4.11), \qquad C_2H_4^+ + NH_3 \rightarrow NH_4^+ + C_2H_3 \quad (4.12),$$

$$C_2H_3^+ + NH_3 \rightarrow NH_4^+ + C_2H_2 \quad (4.13), \qquad CH_4^+ + NH_3 \rightarrow CNH_3^+ + 2H_2 \quad (4.14),$$

$$NH_3^+ + CH_4 \rightarrow CNH_3^+ + 2H_2 \quad (4.15), \qquad CH_4^+ + NH_3 \rightarrow CNH_4^+ + H_2 + H \quad (4.16),$$

$$CH_3^+ + NH_3 \rightarrow CNH_4^+ + H_2 \quad (4.17), \qquad CH_2^+ + NH_3 \rightarrow CNH_4^+ + H \quad (4.18),$$

$$NH_3^+ + CH_4 \rightarrow CNH_4^+ + H_2 + H \quad (4.19), \qquad NH_2^+ + CH_4 \rightarrow CNH_4^+ + H_2 \quad (4.20),$$

$$CH_4^+ + NH_3 \rightarrow CNH_6^+ + H \quad (4.21), \qquad NH_3^+ + CH_4 \rightarrow CNH_6^+ + H \quad (4.22).$$

It must be noted that at different pressures, the concentration of the species in the mixture and the *RF* power, can result into different concentration of by-products [12].

4.2.2.2.c PECVD Parameters

The main plasma parameters that control the properties of a deposited thin film material include, RF discharge, chamber pressure, reactor geometry, pumping speed, substrate temperature and precursors flow rates. This work is studied the effect of PECVD parameters on the properties of perovskite material ($MAPbI_3$) towards finding the optimum parameters to deposit the material. The flow rate of the gases was kept a constant at 10 *sccm* for methane and 20 *sccm* for ammonia as well as the reactor geometry, such as the area of the upper and lower electrodes, and the pumping speed were also constant, while RF-discharge, chamber pressure and substrate temperatures were varied.

- **RF Discharge**

The most PECVD systems use alternating polarity of the supplied power to deposit insulating or dielectric thin film in order to avoid floating potential at the surface of the substrate. The floating potential is normally formed in a DC power since the equal fluxes of electrons and negatively charged ions accumulate on the electrode (anode) and recombine with the positive/available ions. As a result, the insulator thin film starts to lose electrons as ions are neutralised on its surface, leading the potential to reach zero value. Once the insulator surface potential drops below the sustaining voltage, eventually, the *DC* discharge will quickly extinguish.

To sustain a DC discharge, an alternating electric field AC power is applied between the two electrodes, each electrode acts alternatively as a cathode and as an anode. The accumulated positively charged ions on the electrode during the first half cycle could be neutralised by electrons bombardment during the second half cycle. The discharge could be only maintained at high frequency, as a temporary DC 'self-bias' voltage is obtained when the breakdown potential is surpassed on each half cycle of the AC supply (**Figure 4-14**). In this manner, the period of half cycle of the AC supply should be more than the time taken to charge the insulator and the frequency should be high enough to avoid the extinguish of the plasma. In other words, ions created close to the anode cannot approach the cathode before the field is reversed.

The range of such frequencies, typically above 100 *kHz*, that can give the high-frequency discharges to sustain plasma, this range is closer to frequencies of transmitted radio signals, generally known as radio frequency, or shortly, RF discharges [13].

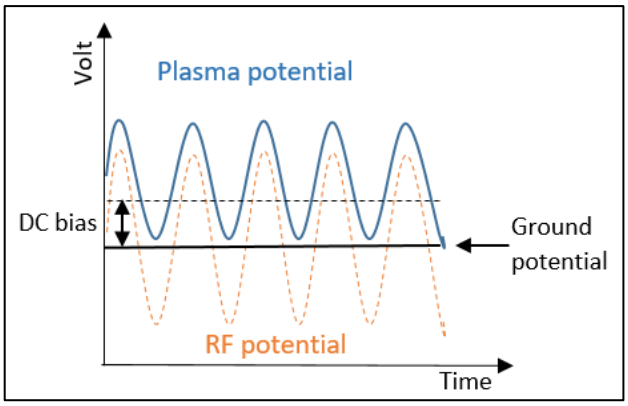

Figure 4-14: development of DC bias and its relation to RF power (Adapted from [14]).

In **Figure 4-14**, it can be seen that the plasma potential (solid curve) is higher than the RF potential (dashed curve) in the positive cycle, however, in the negative cycle; plasma potential is maintained higher than the ground potential. Therefore, a DC potential difference is sustained between the bulk plasma and electrode (plasma sheath). Thus, ions travel in the electric field along a distance that is less than the thickness of the plasma sheath. A positively spaced charge is partially retained between the two half cycles of the alternating electrical field. This leads to the re-initiation of the discharge.

A vast majority of frequencies used in RF-PECVD are higher frequencies (f >1*MHz*). Therefore, the plasma is stable and surface charging can be avoided as mentioned earlier. Generally, the accepted frequencies by the International Telecommunications Union (*ITU*) are found to be 13.56 *MHz* for radio frequency (RF) and 2.45 *GHz* for microwave (*MW*) [15]. The self-bias (V_b) generated depends mainly on the RF power input (P_{rf}) and chamber pressure (p) according to [16]: $V_b \propto \left(P_{rf}/p\right)^{1/2}$, however, it varies between 100 *V* to 1 *KV* [17].

During the positive and negative cycles of the *RF* bias, a rapid change in the direction of the varied electric field is established. This electric field accelerates electrons and ions according to this expression [14]:

$$\boldsymbol{a = \frac{F}{m} = \frac{qE}{m}} \qquad \textbf{(4.23)}$$

Where F is the electric force applied on charged particles, q is the negative and positive electrical charge for electron and ion respectively, E is the internal electric field established by the external RF power, and m is the mass of the charged particles. Due to the lighter mass of electron, which is much less than ion (of a factor of 1/10,000), it quickly responds to the varying electric filed exceeding 10,000 times faster than ions [14]. This means that the electrons accelerate rapidly and begin collisions with the surrounding particles in each cycle of RF field. During these movements, electrons absorb most of the RF energy that is transferred as inelastic collisions into the molecules.

The magnitude supply of RF power has a great impact on the deposition process. Since ions, that are the most important species of plasma, can gain a little more energy under the condition of lower RF power comparing to higher RF power. In this case, offering more times for ions to respond and gain higher energy, thus providing more energy for ion bombardment.

- **Chamber pressure**

The ion energy is also be affected by the chamber pressure. The variation of the pressure can change the mean free path (MFP,λ) of the particles, as shown in the following equation:

$$\lambda = \frac{1}{\sqrt{2}n\sigma} \qquad (4.24)$$

Where *n* represents the particle density, and σ represents the collision cross section. When the particle density increases, the pressure in the chamber increases, which leads to a decrease in λ, according to the expression above. In addition, λ can also be affected by the size of molecules in the plasma. The larger the size, the lower the *MFP*, this is because larger particles have a larger cross section.

The MFP of electrons is two times higher than other particles present in the plasma, because of their smaller masses that have higher kinetic energies. Chamber pressure is a critical parameter since it can control the MFP. In addition, it alters the ion bombardment energy and direction which affect the deposition rate and stress within the film.

4.2.2.2.d Plasma-Surface Interaction

The properties of perovskite thin films are mainly dependent on how the plasma interacts with the exposed substrate surface. Ion bombardment can promote the surface reaction by providing appropriate required energy. It was mentioned previously, that ions can gain energy from the inelastic collision (see section 4.2.2.2.b). In addition, ions can obtain more energy from the interface region (donated as x in **Figure 4-15**) between the plasma bulk and the substrate surface, this region is known as plasma sheath where an electric filed is created. This electric field forms since the plasma sheath is electrically non-neutral, in contact to plasma bulk, therefor, a potential difference is established where a floating potential (V_f) is formed at the electrode with respect to the plasma potential (V_p). Since $V_f < V_p$, the potential difference across the sheath accelerates positive ions from the plasma towards the substrate surface, causing ion bombardment with energy $E_i = e(V_P - V_f)$, meanwhile some of the electrons are repelled. The existence of fewer electrons in sheath region results in fewer excitation-relaxation collisions that emit fewer photons thereby causing reduction of intensity compared to the bulk plasma. Thus, the sheath region is dark.

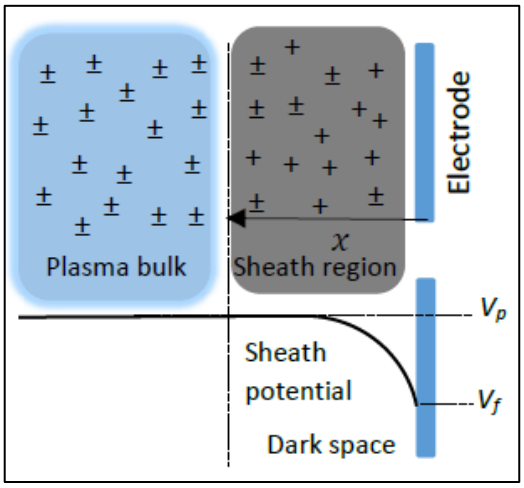

Figure 4-15: Sheath potential nears the plasma surface (Adapted from [14]).

In this research, PECVD system (Built in-house) was employed for the deposition of the organic cation part ($CH_3NH_3^+$=MA) of perovskite material on the evaporated/spin coated PbI_2 thin films (200 *nm*/50 *nm*) in order to obtain $MAPbI_3$. The effect of varying RF power from 5, 10, to 25 *W* was studied. Mass flow controller (MFC) was connected to the gas cylinders to regulate the flow of methane (CH_4) and ammonia (NH_3) gases, which were controlled at 100 *sccm* and 500 *sccm*, respectively. The precursor gases were introduced to the vacuum chamber through a gas inlet (showerhead). The chamber pressure was varied between (250 – 1000 *mtorr*). Plasma was observed, when *RF* power was applied between two electrodes in which the samples were positioned onto the grounded electrode. In this work, a range of temperatures from 50 to 120 °C was used to study the temperature dependence on perovskite films. The by-products were expunged from the system by pumping out with the help of the vacuum pumps connected to the PECVD system [18].

4.2.2.3 Atmospheric Pressure Chemical Vapour Deposition (APCVD)

It is argued that utilising single-source precursor for thin film production facilitates greater control over the stoichiometry of the film as well as synthesising a homogeneous material. The resulting films meet the exact stoichiometry as it is presented in the single precursor [19].

4.2.2.3.a APCVD Parameters

Generally, a *CVD* deposition process can be divided into three main sub-processes [18]: **(1)** the precursor delivery; **(2)** the precursor-substrate reaction; and **(3)** the exhaust management. In this work,

different deliveries' systems were used such as, bubbler and piezoelectric controlled particle size. The delivery systems have been adjusted to meet their function, which is to sufficiently convert the liquid containing solid materials (PbI_2 and *MAI*) into gas phase reactants. Therefore, the following discussion will be emphasised on the delivery mechanism to obtain a "vapour" from the liquid precursor by using physical concepts of bubbler and piezoelectric/ultrasonic transducer.

- **Bubbler**

A special container has been used not only to deliver the appropriate quantity of precursors to the *CVD* reactor but also to convert the precursors in the liquid to the vapour phase by a mechanism that is fed into the reactor. In a simplest way, a hotplate is used in which the precursors containing beaker are heated above their boiling points. In this situation, the evaporation rate can be varied by varying the temperature. Another method is by using a 'bubbler' (**Figure 4-16**), in which a liquid is converted into a vapour by heating and bubbling in a non-reactive carrier gas passing through the solution which has a significant vapour pressure, therefore, the resultant gas carrying the precursor is derived into the reactor. Unlike the previous mentioned method, the evaporation rate in the bubbler system not just depends on the temperature of the precursor to alter the vapour pressure, but alto on the gas flow rate, the volatility of precursor, and the liquid level [18].

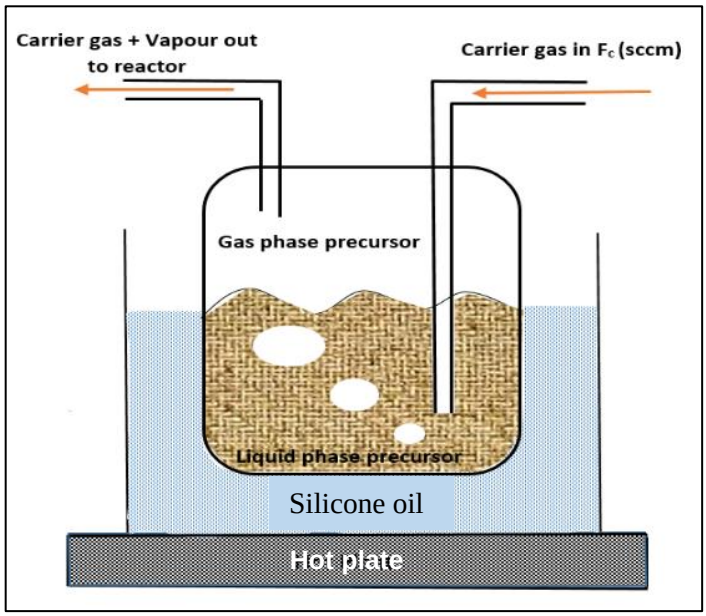

Figure 4-16: Schematic of a bubbler system connected to a CVD.

In **Figure 4-16** it can be seen that a sealed container, 'bubbler', containing a dry carrier-gas inlet tube (dipped in the solution) flowed from the liquid, and another outlet tube positioned near the top right of the container for flowing the carrier gas and vaporising liquid out of the bubbler which is driven to the reactor. A uniform temperature is provided by immersing the bubbler in a beaker containing silicone oil. The bubbler concept depends on small bubbles formed by the carrier gas. A common carrier gas can be argon or nitrogen. The vapour reaches its equilibrium vapour pressure once the bubbles float to the surface of the liquid. When the equilibrium vapour pressure in a liquid exceeds the total pressure of the system, the vapour bubbles begin to displace the gas, and the liquid starts to boil. Due to the difference in pressure between the delivery system and the reactor, gas flow occurs from the higher vapour pressure within the bubbler to the lower pressure in the reactor (in the current work, atmospheric pressure) [20, 21]. Since the functioning of the bubbler depends on the height of the liquid level, the liquid level should not be lower than the end of the carrier gas tube; otherwise, the liquid will not be bubbled. A quartz or glass bubbler would be recommended to visualise the level of the liquid. However, for a bubbler made of stainless steel, a level sensor should be used for this purpose.

Assuming a bubbler system contains an ideal binary mixture where Dalton's and Raoult's Laws apply, the vapour-liquid equilibrium (*VLE*) can be established according to:

$$\frac{N_P}{N_C} = \frac{P_P}{P_C} \qquad \textbf{(4. 25)}$$

Where N_P and N_C are the number of moles in precursor and carrier gas, respectively, and P_P and P_C are the partial pressures (a part of the total gas pressure) of the precursor gas and carrier gas respectively. According to Dalton's law, P_{total} is expressed as:

$$P_{total} = (P_C + P_P) \qquad \textbf{(4. 26)}$$

At atmospheric pressure (*760 torr*) and by substituting equation (4.26) into (4.25), the following equation would be:

$$N_P = \frac{N_C \times P_P}{(760 - P_P)} \qquad \textbf{(4. 27)}$$

At the room temperature and the atmospheric pressure, the molar flow of the precursor (F_P) from the bubbler, in moles/s, based on known vapour pressure values can be calculated from the following expression:

$$F_P = \frac{f_c \times P_P}{22.4\,(760 - P_P)} \qquad (4.28)$$

Where f_c is the flow rate of carrier gas in L/s.

There is, however, a serious problem when bubbler is used for the transport of the precursor. In general, volatile compounds are considered as precursor along with heat treatment used for the bubbler. However, most solid materials are less volatile under standard atmosphere conditions. Therefore, modified delivery system is required to provide more energy required to transport the dissolved compounds contained in the solvent, in this work PbI_2 and MAI.

.

- **Piezoelectric Transducer**

Piezoelectric materials have gained more interest in the scientific community due to their use in the various applications such as transducers, acoustic devices, motion sensors and pressure sensors. Piezoelectric transducers are made from various materials that include traditional crystals such as quartz, and plastics such as polyvinylidenefluoride (PVDF), but the most of transducers are made of piezoelectric ceramics such as Lead Zirconate Titanate (PZT) [22].

Energy has to be provided in such a manner that the liquid and the solids dissolved in the liquid have to be carried. When a solution is subjected to heat, mostly liquid will vaporise leaving behind the solid. If solid has to be transported, more thermal energy is required, however, in such conditions, liquid is initially transported and then solid is transported. Such process is undesirable for a CVD deposition process where all the contents in the precursor should be transported together at any given time. Such precursor should decompose and/or react at the surface of the substrate to form a desirable film. Therefore, to provide more and/or appropriate energy that allows transportation (atomisation) of both the solvent and the solid material dissolved in the chosen solvent, a piezoelectric transducer was proposed in this research study.

The piezoelectric transducers are electro-mechanical devices. They convert the electrical energy into periodic mechanical vibrations/waves) (**Figure 4-17**). The device was used in this work comprises of a

thin metal circular plate, which bonds a piezoelectric element with 20 mm in diameter and 0.01 mm thickness. The piezoelectric element contains a sintered body of poly-crystals of piezoelectric ceramic material which is sandwiched between two electrodes. The piezoelectric ceramic is made of PZT and the bottom metal plate is a metal alloy.

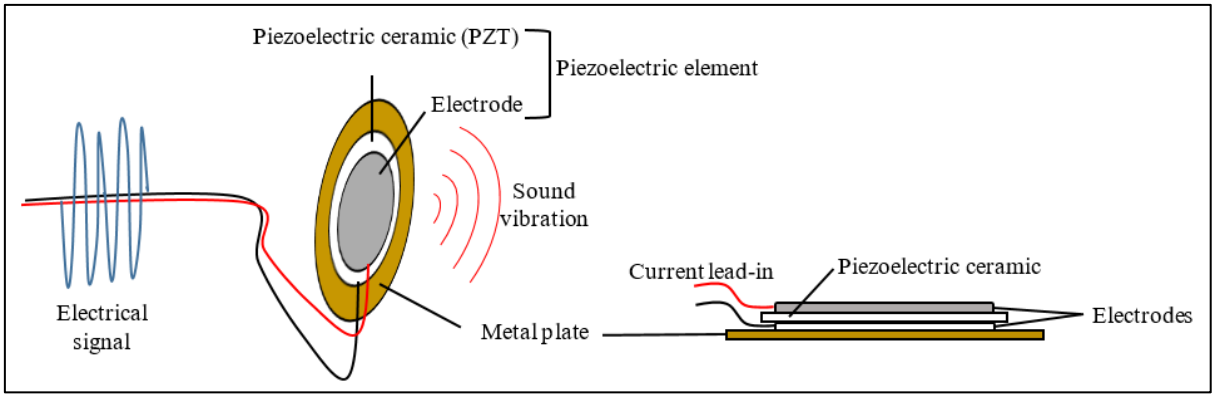

Figure 4-17: Schematic of ultrasonic piezoelectric transducer and their components shows that applying electrical signal produces vibration of sound.

When the AC voltage is applied to the piezoelectric disc, the poly-crystals present in the disc between the metal electrodes are distorted by a radial expansion in +ve cycle of the AC signal (**Figure 4-18 (a)**) and contraction at 0V and again a radial expansion in -ve cycle of the AC signal (**Figure 4-18 (c)).** As a result, the metal plate frequently bends up and down (**Figure 4-18 (d))** corresponding to the motion of PZT (piezoelectric) ceramic crystals. This alternative bending of the metal plate is observed in both directions at the frequency of the applied AC voltage; thus, vibrations are produced. Liquid present on the top of the piezoelectric disc will form the droplets with a diameter that is defined by the resonant frequency of the chosen ceramic transducer. Therefore, the vibrations of the flexible piezoelectric disc will lead to the droplet formation. Deposition parameters can be altered by controlling the parameters of the applied AC signal.

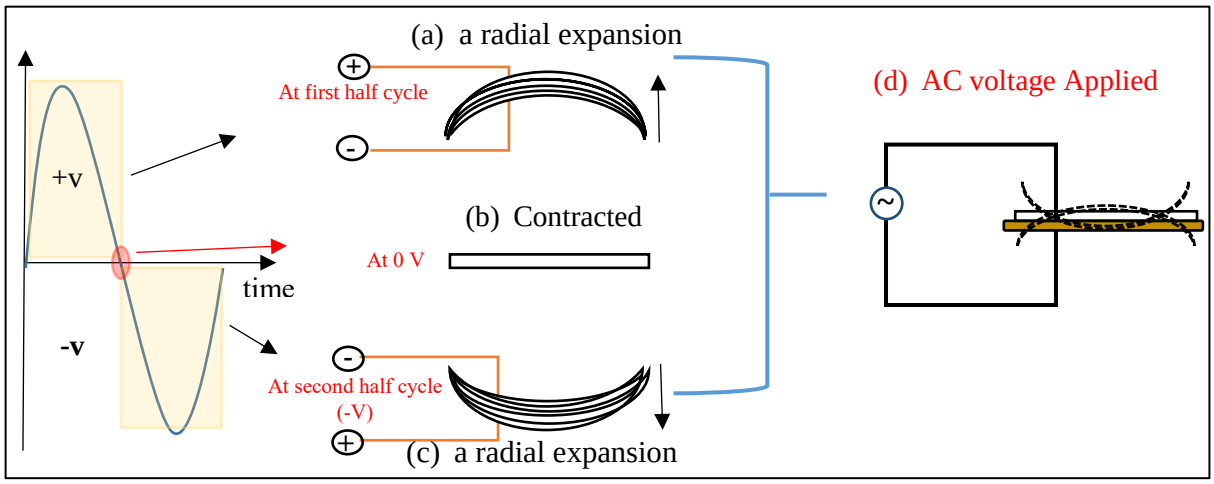

Figure 4-18: Schematic of the deflection of transducer as a result of shear stresses employed by the piezoelectric element.

To obtain a vapour of precursor contained in the solvent, small droplets of liquid (commonly called as mist) are required to be generated, which are reproducible and reliable. Generally, the droplet is ejected from the surface of the liquid precursor when is subjected to an energy (e.g. mechanical vibrations/ waves were used in this work). The external energy (e.g. electric field was used in this work) was supplied to the piezoelectric transducer to form such mechanical vibrations. As a consequence, a fountain (numerous microns sized liquid particles suspended above the surface of a liquid) was produced due to vibrations caused by the transducer [23].

The physical mechanism of the droplet formation (mist) is mostly based on the well-known capillary wave theory [24]. In fact, the capillary surface waves of the liquid experience a number of states before it is capable of producing droplets, which mainly depend on the frequency of the applied AC signal where the amplitude of the input signal, the surface tension and the viscosity of the liquid precursor are fixed. The states of capillary surface waves involving:

- Non-ejecting turbulent state; occurs at low frequency. In this state, the initial smooth/flat liquid surface will change into periodic standing waves.
- Droplet-ejecting state; occurs at sufficient high frequency. Large-amplitude waves are produced with upward direction that will tear/break up into droplets.

In fact, formation of a mist based on ultrasonic waves is not only governed by aforementioned effect of capillary surface waves but also the process is connected with the effect of the sonically induced cavitation waves. As mentioned above, the capillary wave of the droplet-ejecting state stands on an assumption that it occurs at high frequency where the droplets are released from Reyleigh instability arising at wave crests on the liquid surface [25]. The cavitation theory suggests that the implosions of tiny cavitation bubbles near the surface of the liquid lead to a disturbance in the surrounding liquid that induces the liquid particles to be scattered and spread around. The interaction of the effect of both waves (capillary and cavitation) results in the formation of droplets.

In theory and based on the surface wave effect, the piezoelectric resonator parametrically launches capillary waves on the liquid/air interface. The increase of the input power that is supplied the piezoelectric crystal raises the amplitudes of these waves exponentially. As the waves' amplitude growing up, the droplets will be distinguished and broken off from the crests of standing waves at a certain wavelength. In low-viscous liquids, the wavelength of the capillary waves can be expressed as:

$$\boldsymbol{\lambda = 2\sqrt[3]{\frac{\gamma\,\pi}{\rho\,F^2}}} \qquad \textbf{(4. 29)}$$

Where γ, ρ and F represents the coefficient of surface tension, the mass density and the driving frequency of the ultrasonic transducer, respectively.

The main advantage of such delivery of precursor is an ability to provide a steady flow of fine mist of the low-volatility precursor. Moreover, the frequency of the capillary waves that is formed at the surface determines the droplet size. Therefore, piezoelectric disc with appropriate resonant frequency is required to alter the size of droplet. However, it is worth to mention that these piezoelectric crystals do not resonate at fixed frequency value, and they have +/-5% tolerance, so a Gaussian distribution of droplet size in the produced mist is expected. According to a correlation factor between the mean diameter of droplets and the wavelength of capillary waves; the convenient relation is $D = \lambda/3$. By using equation (4. 29) it can be obtained that

$$\boldsymbol{D = \frac{2\pi^{\frac{1}{3}}}{3}\left(\frac{\gamma}{\rho}\frac{1}{F^2}\right)^{\frac{1}{3}}} \qquad \textbf{(4. 30)}$$

It should be noted that the excessive frequency energy is converted to heat. In this case, the liquid temperature within the nebuliser is increased [23, 26].

Discrete frequencies are required for vibrating the liquid layer in order to exert an additional restoring force on the surface layer and thus form capillary waves. At certain frequencies, the amplitude of the capillary waves traveling on the liquid surface is increased and droplets are ejected from the wave crests. In the other words, droplet is ejected when a critical oscillation frequency with appropriate amplitude causes the momentum of liquid in these standing waves to overcome the surface tension. Such waves are created with the use of piezoelectric crystal when it is subjected to applied AC signal.

The small size of this powerful PZT disc is well suited for the generation of vapour phase of $MAPbI_3$. The challenge now is to design a holder or disc mount that can accommodate this piezoelectric crystal. At this point and based on the physics of the operation principle, it is assumed that this new design would provide an appropriate energy required to form an equilibrium vapour that was not possible by conventional bubbler. This new technique provides better controllable deposition parameters than nebulizer that is used to obtain the material [27- 29]. This modification is advantageous with solid materials with less volatility.

References

[1] P. Martin, "Chapter 3-surface preparation for film and coating deposition processes," *Handbook of deposition technologies for films and coatings (third edition), william andrew publishing, boston,* pp. 93-134, 2010.

[2] A.H. Landrock and S. Ebnesajjad, *Adhesives technology handbook,* William Andrew, 2008.

[3] K. Norrman, A. Ghanbari-Siahkali and N. Larsen, "6 studies of spin-coated polymer films," *Annual reports section" C"(physical chemistry),* vol 101, pp. 174-201, 2005.

[4] R. Stuart, "Vacuum technology, thin films, and sputtering: An introduction.(retroactive coverage)," *Academic press, inc, 111 fifth ave, new york, new york 10003, USA, 1983.151,* 1983.

[5] N. Harris, *Modern vacuum practice,* Nigel Harris, 2007.

[6] A. Greco and G. P. Vanoli, "Evaporation of refrigerants in a smooth horizontal tube: Prediction of R22 and R507 heat transfer coefficients and pressure drop," *Applied thermal engineering,* vol 24, no 14-15, pp. 2189-2206, 2004.

[7] D.M. Mattox and V. Mattox, *Vacuum coating technology,* Springer, 2003.

[8] A. Roth, *Vacuum technology,* Elsevier, 2012.

[9] S.A. Campbell, *Fabrication engineering at the micro and nanoscale,* Oxford University Press New York, 2008.

[10] H. Xiao, *Introduction to semiconductor manufacturing technology,* 2nd ed. Bellingham: Society of Photo-Optical Instrumentation Engineers (SPIE), 2012.

[11] L. Wojcik and A. Markowski, "Mass spectrometric study of ion/molecule reaction in methane and ammonia mixtures," *Vacuum,* vol 78, no 2-4, pp. 235-240, 2005.

[12] G. Smith, M. Saunders and R. Cross Jr, "Crossed beam studies of ion-molecule reactions in methane and ammonia," *Journal of the american chemical society,* vol 98, no 6, pp. 1324-1330, 1976.

[13] G.K. Wehner, "Advances in electronics and electron physics," in *Sputtering by ion bombardment,* Anonymous Elsevier, 1955, pp. 239- 239-298.

[14] H. Xiao, *Introduction to semiconductor manufacturing technology {B},* nd ed, Anonymous Bellingham: Society of Photo-Optical Instrumentation Engineers (SPIE), 2012, .

[15] L. Martinu, O. Zabeida and J. Klemberg-Sapieha, "Handbook of Deposition Technologies for Films and Coatings," in *Plasma-enhanced chemical vapor deposition of functional coatings,* Anonymous Elsevier, 2010, pp. 392- 392-465.

[16] Y. Catherine, "Diamond and diamond-like films and coatings," *NATO ASI series B,* vol 266, pp. 661, 1991.

[17] M.A. Lieberman and R.A. Gottscho, "Physics of thin films," in *Design of high-density plasma sources for materials processing,* Anonymous Elsevier, 1994, pp. 1- 1-119.

[18] R.F. Bunshah, *Handbook of deposition technologies for films and coatings: Science, technology, and applications,* William Andrew, 1994.

[19] T. S. Lewkebandara and C. H. Winter, "CVD routes to titanium disulfide films," *Advanced materials,* vol 6, no 3, pp. 237-239, 1994.

[20] D. M. Hausmann, E. Kim, J. Becker and R. G. Gordon, "Atomic layer deposition of hafnium and zirconium oxides using metal amide precursors," *Chemistry of materials,* vol 14, no 10, pp. 4350-4358, 2002.

[21] J. Elam, M. Groner and S. George, "Viscous flow reactor with quartz crystal microbalance for thin film growth by atomic layer deposition," *Review of scientific instruments,* vol 73, no 8, pp. 2981-2987, 2002.

[22] N. Guo, *The vibration characteristics of piezoelectric discs,* 1989.

[23] R. W. Niven, A. Y. Ip, S. Mittelman, S. Prestrelski and T. Arakawa, "Some factors associated with the ultrasonic nebulization of proteins," *Pharmaceutical research,* vol 12, no 1, pp. 53-59, 1995.

[24] W. Eisenmenger, "Dynamic properties of the surface tension of water and aqueous solutions of surface active agents with standing capillary waves in the frequency range from 10 kc/s to 1.5 mc/s," *Acta acustica united with acustica,* vol 9, no 4, pp. 327-340, 1959.

[25] L. Rayleigh, "On the capillary phenomena of jets," *Proc.R.soc.london,* vol 29, no 196-199, pp. 71-97, 1879.

[26] D. Cipolla, A. Clark, H. Chan, I. Gonda and S. Shire, "Assessment cf aerosol delivery systems 2 for recombinant human deoxyribonuclease," *STP pharma sciences,* vol 4, no 1, pp. 5062, 1994.

[27] M. Afzaal and H. M. Yates, "Growth patterns and properties of aerosol-assisted chemical vapor deposition of CH3NH3PbI3 films in a single step," *Surface and coatings technology,* vol 321, pp. 336-340, 2017.

[28] D. Bhachu, D. Scanlon, E. Saban, H. Bronstein, I. Parkin, C. Carmalt and R. Palgrave, "Scalable route to CH 3 NH 3 PbI 3 perovskite thin films by aerosol assisted chemical vapour deposition," *Journal of materials chemistry A,* vol 3, no 17, pp. 9071-9073, 2015.

[29] D. J. Lewis and P. O'Brien, "Ambient pressure aerosol-assisted chemical vapour deposition of (CH 3 NH 3) PbBr 3, an inorganic–organic perovskite important in photovoltaics," *Chemical communications,* vol 50, no 48, pp. 6319-6321, 2014.

Chapter 5 Characterisation Techniques of Perovskite

This chapter discusses the working principle of the methods that are used to characterise the thin-film materials including lead iodide (PbI_2) and methylammonium lead iodide perovskite ($CH_3NH_3PbI_3$). These characterisation techniques or methods were involved four main investigations; structural, optical, electrical and thermal that were be fully studied in order to gain full understanding of the fundamental properties of the thin film. These methods were provided appropriate parameters to obtain an optimised perovskite material for photovoltaic application.

5.1 Structural Characterisation Methods

5.1.1 Scanning Electron Microscopy (SEM)

SEM technique is used to investigate morphology of a material at nanoscale with a resolution of ~1nm. The SEM uses an electron beam that is generated by a metal filament such as tungsten. The images are constructed when electrons are focused onto a sample surface by a rastering process. The sequence of the interaction of the electrons with the material can result into different scattering mechanisms; elastic and inelastic scattering, which depend on the energy of the accelerated electron and sample density. Hence, a variety of emitted signals are observed from different penetration depths. **Figure 5-1** illustrates the different interaction mechanisms between the incident electrons and the sample. The generated signals can be detected by various techniques such as X-ray diffraction (XRD), transmittance electron microscopy (TEM) and scanning electron microscopy (SEM) [1]. The SEM can be used to detect the secondary electrons (SE) and backscattered electrons (BSE) from the sample.

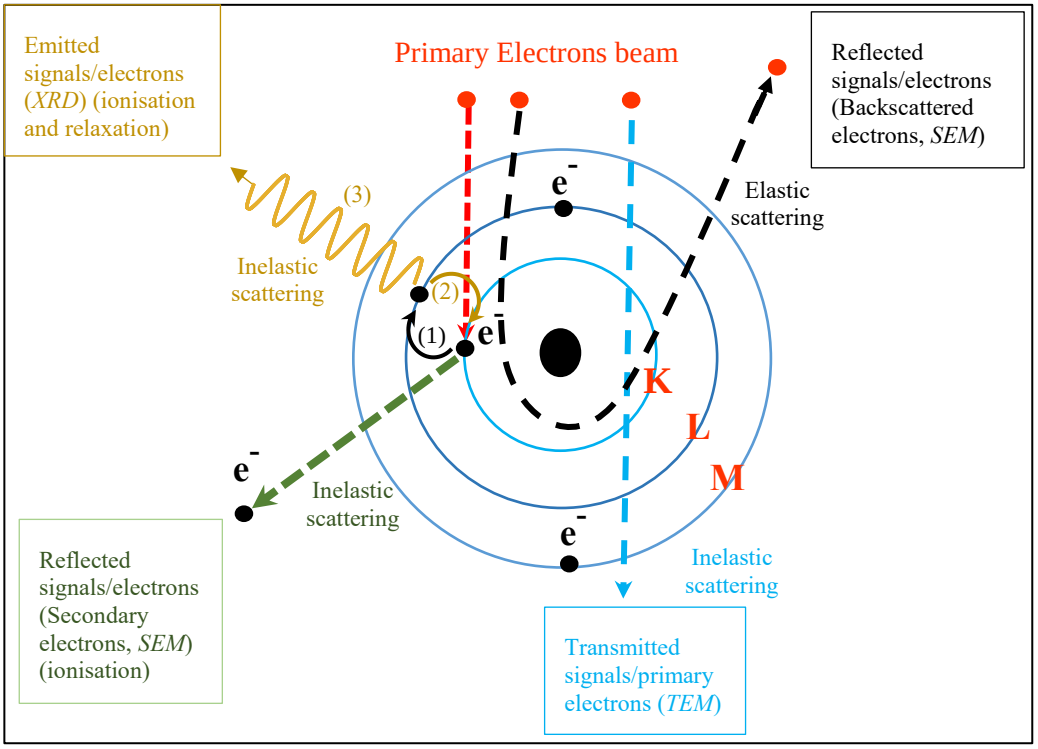

Figure 5-1: Electron beam- specimen interaction and their detected techniques.

SE and BSE signals are originated from different scattering mechanisms. The SE signal is produced by an inelastic scattering, when a loosely-bounded electron of an atom gains an energy from the primary electron beam, once it bombards the specimen nuclei with low energy, typical 50 eV or less, resulting in atomic ionisation [1]. This scattering is presented in

Figure 5-1- green dashed line. Due to the low energy of SE, it is scattered by the surface atoms of the specimen, giving detailed information of the surface structure by producing high resolution images.

In contrast to SE, the BSE is produced when the incident electron beam undergoes large-angle-elastic collisions > 90^{o} [2], as presented in

Figure 5-1-black dashed curve. This is a consequence of the mass difference between the primary electron beam and the atomic nuclei of the specimen that changes the original trajectory of the incident electrons whilst conserves their kinetic energy. BSE is propagated deeply through the specimen before it is scattered by the subsurface layers, due to its high energy.

A typical SEM consists of an electron beam gun, series of lenses, scanning coils and detector (see **Figure 5-2**). Electromagnetic and objective lenses are used to focus the electrons, while the coils are used to position the electrons over the sample surface. SE mode was used in this work to not only

acquire the topographical images but also the thickness of the thin film, which are collected from SEM (model Zeiss Evo 15, Leica S430) at De Montfort University.

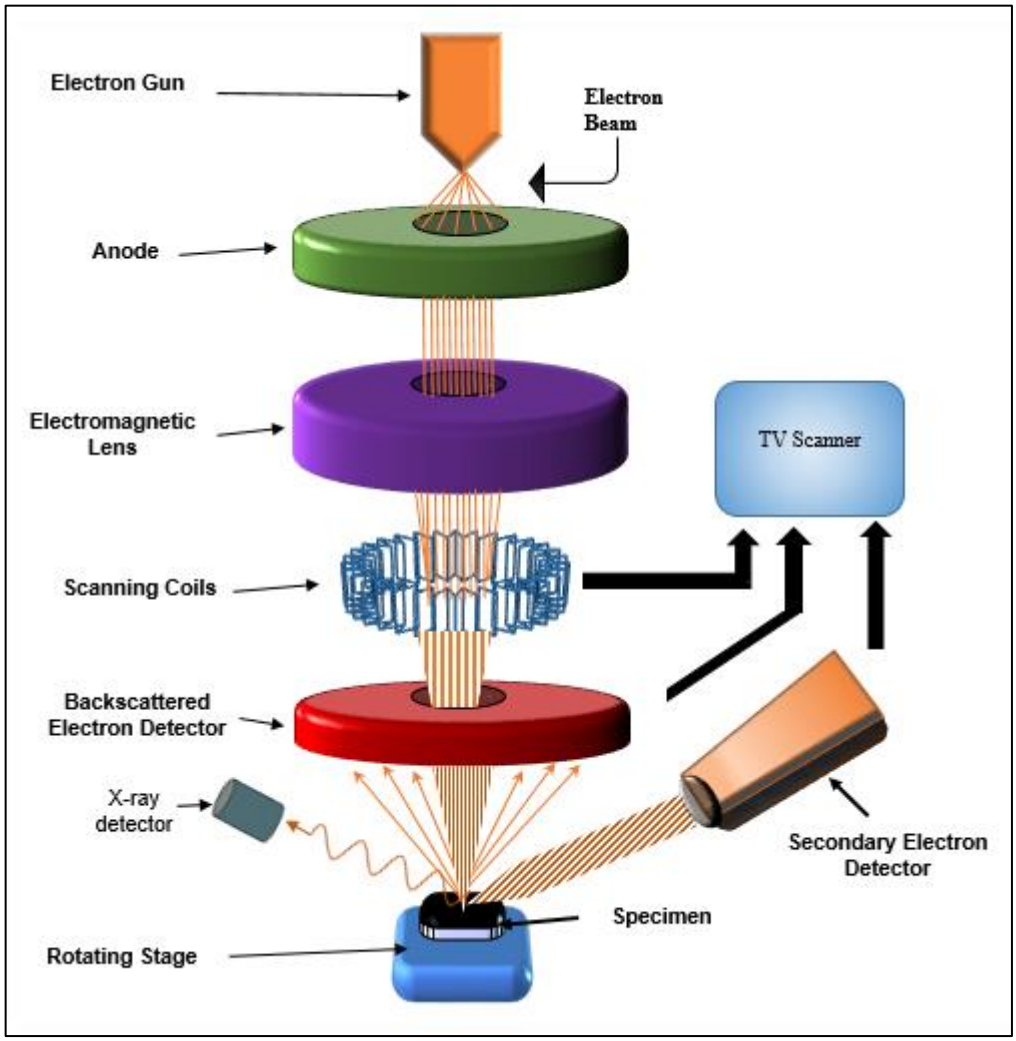

Figure 5-2: Schematic diagram of scanning electron microscope (SEM).

5.1.2 Atomic Force Microscopy (AFM)

AFM is a powerful technique employed to characterise the surface of the sample (semiconductor/ conductor/ insulator), such as, average grain size and surface roughness by using a sharp microfabricated tip with a radius of ~10 nm which is raster-scanned over sample surface acquiring 3D atomic resolution images [3]. This tip is mounted at the end of a flexible cantilever, see **Figure 5-3 (a)**. When the tip is scanned across the surface, it faces an attractive and repulsive forces; e.g. Van der Walls and coulomb forces [4]. Interatomic interaction forces fluctuate up and down the cantilever. To sense the cantilever bending, a laser beam is usually used which is reflected from the back of the

cantilever onto a photodetector, as depicted in **Figure 5-3 (a)**. Detecting the laser deflection is processed to construct topographical surface images. Two tip/surface interaction modes of AFM are commonly used; contact mode and non-contact mode (**Figure 5-3 (**b)) [3].

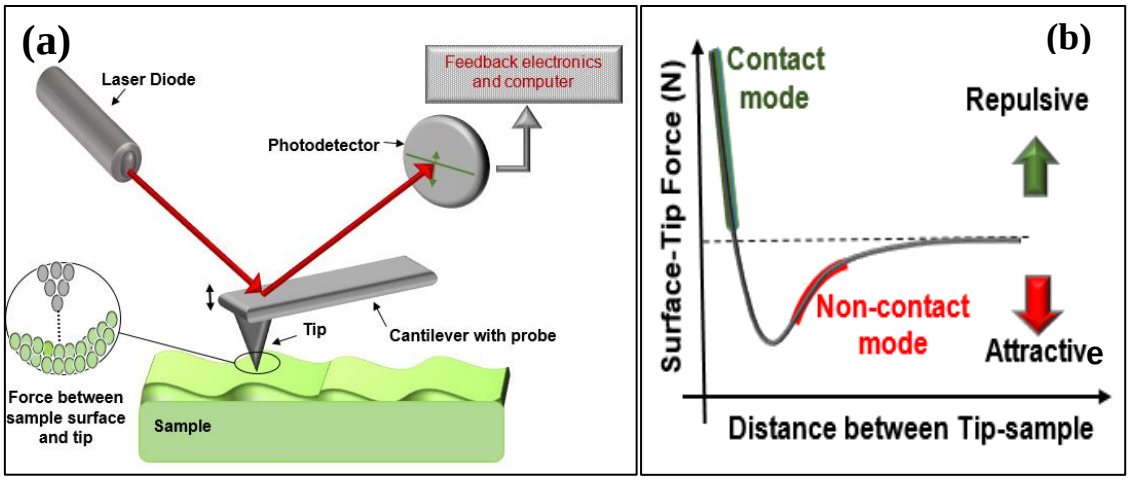

Figure 5-3: (a) Schematic of AFM operating in contact mode and (b) the interatomic force in respect to the distance between tip and sample that showing two different AFM modes.

In contact mode, the tip is brought in a close contact with the surface of a sample while it is being scanned over the surface. The tip is moved under a constant force that results in a constant deflection of the cantilever. As a consequence of the close interatomic distances, the electron cloud in the atoms repels each other electrostatically; such contact mode is considered to be repulsive in nature (**Figure 5-3 (b)**) [5]. Although, this mode is dominated by means of the repulsive Van der Waals force, an attractive force is also influenced by the sample [6]. The drawback of this mode is that the actual physical contact between the tip and sample can damage both the sample's surface and the tip resulting in artefacts in the recorded image [7].

In non-contact mode, there is a distance between the tip and the sample surface (typically 50-150 Å), so that the attractive forces are dominated in providing morphological information of the sample (**Figure 5-3 (b)**) [4]. The vertical oscillation in relation to the surface, which is formed as a result of the Van der Waals forces, changes the oscillation amplitude, the resonance frequency and the phase of the reflected laser [7].

A typical *AFM* instrument consists of a micro-mechanical cantilever probe and a sharp tip mounted to a piezoelectric actuator, laser diode and photo-detector that detects a laser beam reflected from the cantilever (**Figure 5-3 (a)**). In this work, Park System XE-100 with a non-contact mode is employed to acquire the morphology and the roughness of the sample's surface.

5.1.3 X-Ray Diffraction (XRD)

The XRD technique is a non-destructive technique commonly used to determine the structural properties of a specimen; whether it has a crystalline structure (regular arrangement of atoms) or an amorphous structure (random arrangement of atoms). Furthermore, it is also used to determine other properties of a specimen such as phase structure (e.g. cubic, tetragonal, orthorhombic), atomic spacing, plane orientation, crystallite size, stress and strain within the material.

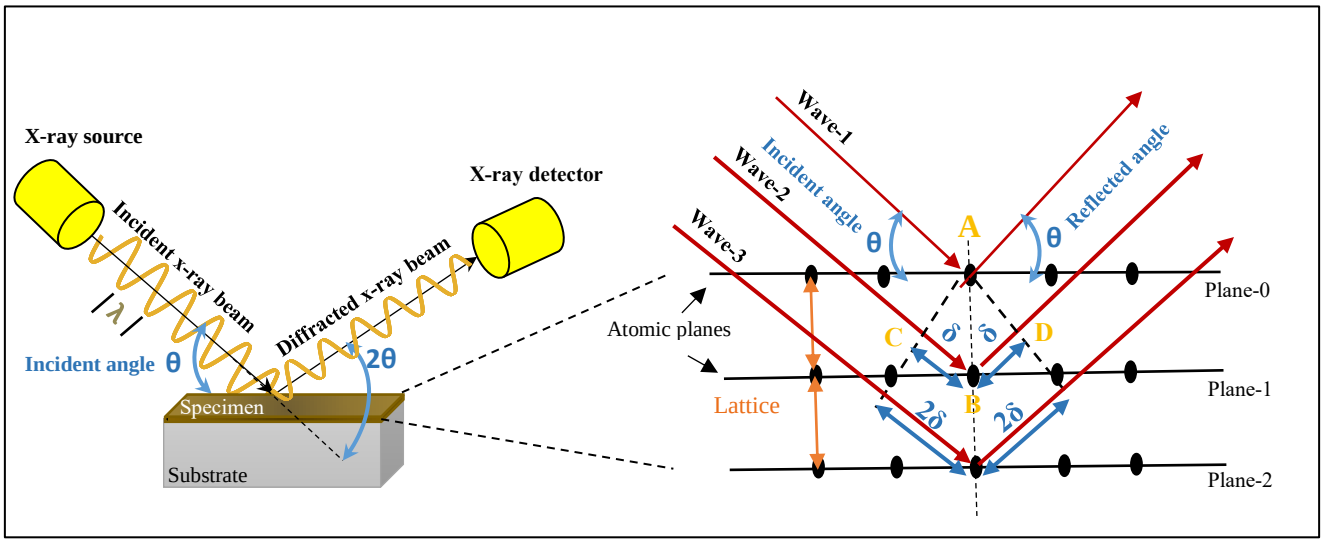

Figure 5-4: Geometry of X-ray diffraction and the constructive interference resulted from the interaction of X-rays from a set of crystal planes present in the material.

To generate the X-rays, an applied current (usually 37 mA) is required in order to heat up a tungsten filament [8]. As a result, electrons are generated and accelerated towards a copper target with an accelerating voltage of 8-40 kV [8]. Consequently, X-rays from the copper target are generated and incident towards the test sample where they are diffracted onto a detector. The X-rays diffraction on a three-dimensional lattice can be seen in **Figure 5-4**. The working principle is based on a constructive interference of monochromatic X-rays that are reflected from periodic arrangement of atoms,

positioned in crystallographic planes separated by a distance *d* [9]. From **Figure 5-4**, there is a difference in the path length (δ) between wave-1, -2, and -3 when these waves are reflected from the lattice's interplanar (e.g. zeroth, first and second planes). The relation of variable path length to the interplanar spacing (*d*) and the reflected angle (θ) can be given as $\delta = d\sin\theta$ [10]. Accordingly, the doubled path length difference is apparent between zeroth and second planes; $\delta = 2d\sin\theta$, and so on for n^{th} planes. Thus, the total path length difference is 2nδ which is only true when the waves are reflected under the same angle, resulting into a constructive interference of the reflected waves, known as Bragg's condition, which is given by [10]:

$$\boldsymbol{2d\,sin\theta = n\lambda,} \quad \boldsymbol{n = 1.2.3,\ldots} \qquad \textbf{(5.1)}$$

Where d is the interplanar spacing, n is the integral order of diffraction line, and λ is the wavelength. This condition causes a single spike at a specific angle forming diffracted pattern that provides information about the physical structure of the test sample. If the incident angle corresponds to fractional '*n*' (e.g. 0.5, 0.3, 0.56), the reflected waves will be out of phase that lead to a destructive interference [9].

In this work, the crystallographic structure of PbI_2, $CH_3NH_3PbI_3$ thin films were characterised by using XRD (Bruker 2D with *Cu-K_X-ray* radiation with λ of 1.5418 Å with 2 ^{o}/min scanning speed) at De Montfort University. The scanned angles (2θ) were selected to be in the range of 10-70^{o} where the diffraction peaks of PbI_2 and $CH_3NH_3PbI_3$ material are expected.

5.2 Optical Characterisation Method

5.2.1 Ultraviolet-Visible-Infrared (UV-Vis-IR) Spectroscopy

UV-Vis-IR Spectroscopy is a broadly utilised instrument for the investigation of the optical properties of a material such as transmittance (T%), absorption (A), reflectance (R), scattering, bandgap (Eg), refractive index (n), extinction coefficient (k), dielectric constants (real (ε_r) and imaginary (ε_i)), and optical conductivity [11]. Three properties; T%, A, R, can be determined directly by measuring the attenuation of the light that can either be transmitted through the sample, absorbed by the sample and/or reflected from its surface, while the others are derived from these basic parameters [12].

The electronic transition occurs in the molecules when the energy of the absorbed light is higher than or equal to the bandgap of a material. This means that the electrons gain enough energy to be excited from an occupied valence band to an unoccupied conduction band. However, the interaction between low energy wavelengths (e.g. IR) and the sample result in a molecular vibration. Therefore, incident

light could be transmitted or absorbed, reflected, scattered and/or undergo interference, which depends on the energy of E-M waves and the transparency of the material.

Thermo Scientific Evolution *300 UV-Vis* spectrometer was used in this study that has a dual beam. The light wavelength is in the range of 190 nm-1100 nm, so the ultraviolet, visible and near-IR were covered. The measurement of the referenced substrate was required as an initial step to obtain more accurate results for the deposited film.

Percentage transmittance (T%) of the light at each wavelength can be calculated by the ratio of final intensity (*I*) to initial intensity (I_0) of the incident light via the following equation [11]:

$$\boldsymbol{T = \frac{I}{I_0} \times 100\%} \qquad \textbf{(5. 2)}$$

In the case of measuring the absorbance, the relation between the absorbance and transmittance can be expressed as follows [13]:

$$\boldsymbol{A = -log_{10} T = -log_{10} \frac{I}{I_0}} \qquad \textbf{(5. 3)}$$

Depending on the transmission and absorption spectra obtained from spectroscopy, the band gap is calculated using the *Tauc* equation [14]:

$$\boldsymbol{(\alpha h\nu)^n = A\left(h\nu - E_g\right)} \qquad \textbf{(5. 4)}$$

Since $h\nu = E$, the above equation can be written as:

$$\boldsymbol{(\alpha E)^n = A\left(E - E_g\right)} \qquad \textbf{(5. 5)}$$

Where α is the absorption coefficient, *n* is the distribution of state density assuming values of *n=2* for direct band gap materials and *n=1/2* for indirect band gap materials [15], E_g is the optical bandgap, A a constant and *E* is the photon energy in electron volt (eV) given at a specific wavelength (λ) of the E-M waves by $h\gamma/\lambda = 1240/\lambda$; *h* is the Plank's constant and c is the speed of ME waves in vacuum. Thus, E_g can be determined by plotting $(\alpha E)^n$ on y-axis and (E) on the x-axis, the extrapolation of the linear part onto the x-axis (at y=0) gives the optical bandgap of the material.

In addition to the above mentioned *Tauc* method, *a* derivative method was also used in this work that is more precise method to find the E_g when dealing with nanomaterials [16, 17]. In this method, a plot of the derivative of the transmittance with respect to photon energies (DT/DE) in y-axis against photon energy ($\boldsymbol{E_{ph}}$) in x-axis, hence at $\boldsymbol{E_{ph}} = E_g$ a minimum energy of photons should be recorded [16]. In this condition, spike towards negative infinity corresponds to the bandgap of the material.

In equation **(5. 3)**, α can be calculated using the Beer-Lambert law for thin films as follows [12]:

$$\boldsymbol{I = I_0\, e^{-\alpha d}} \qquad \textbf{(5. 6)}$$

By applying the logarithm on both sides of the equation (5.6), it becomes:

$$\boldsymbol{\alpha = -\frac{1}{d} ln \frac{I}{I_0}} \qquad \textbf{(5. 7)}$$

Where *I* is the transmitted intensity of E-M waves and *d* is the film thickness.

Theoretically, from the basic measurements (*T*, *A* and *R* vs *λ*), many other properties of the material can be calculated, such as the refractive index, extinction coefficient, dielectric constant and optical conductivity.
The following equation is used to calculate the refractive index [11]:

$$\boldsymbol{n = \sqrt{\left(\frac{1+R}{1-R}\right)^2 - (k^2 + 1)} + \frac{1+R}{1-R}} \qquad \textbf{(5. 8)}$$

Where *R* is reflectance and *k* is the extinction coefficient, which can be calculated by [11]:

$$\boldsymbol{k = \frac{\alpha\lambda}{4\pi} = \frac{\lambda}{4\pi d} ln\left(\frac{1}{A}\right)} \qquad \textbf{(5. 9)}$$

Where α is the absorption coefficient, *d* is the film thickness and *A* is the absorbance.

By using *n* and *k* values, two parts of dielectric constants including real and imaginary can be calculated as follows:

The real part of dielectric constants is expressed as [11]:

$$\varepsilon_r = n^2 - k^2 \qquad (5.10)$$

The imaginary part is as follows [11]:

$$\varepsilon_i = 2nk \qquad (5.11)$$

In terms of optical conductivity resulting from the movement of the excited electrons into the conduction band after absorbing the light, the following calculation could be used [11]:

$$\sigma_{opt} = \alpha nc/4\pi \qquad (5.12)$$

Where α is the absorption coefficient, *n* is the refractive index and *c* is the velocity of light.

5.3 Electrical Characterisation Method

Electrical characteristics are essential to be studied for the electronic devices such as solar cells, diodes, sensors, memories and their component materials. Therefore, this section focuses on the electrical methods or techniques that were used to determine the fundamental properties of the initial layer lead iodide (PbI_2), the converted material- perovskite ($MAPbI_3$) and for the solar cell.

Current-Voltage (*I-V*) or Current density -Voltage (*J-V*) measurements provide the basic parameters that are required to understand the behaviour of material and device. These parameters involve the solar cell characteristics such as open-circuit voltage (V_{oc}), short-circuit current (J_{sc}), fill factor (*FF*), leakage currents and power conversion efficiency (*PCE*) that can be obtained in illuminated condition [18]. Moreover, some more fundamental parameters can be determined from dark condition such as series (R_s) and shunt (R_{sh}) resistances, ideality factor (*n*), dark saturation current (I_o) and rectification ratio (*RR*). These parameters could result from the perovskite itself or from the interface between the

active layer and its metal electrodes (anode and cathode) in a completed solar cell device as discussed in **Chapter 3**.

In this work, a Hewlett Packard (*HP*) *HP4140B* picoammeter (current range from ± 1pA to 10mA) and *DC* voltage source (voltage range from ± 0 to 100V) were constructed for the *J-V* measurements. The *J-V* characteristics computer-controlled programs for automation were written by Prof. Shashi Paul. For illumination, *Oriel 96005* 150W from Newport was used that has a filter to supply 100 mW/cm^2 (*AM 1.5*). However, this light source, aged more than 20 years, that was tested recently by light intensity meter and its power was found to be 8.58 mW/cm^2, which is considerably lower than the *STC* (100 mW/cm^2) (see **Chapter 3**). Similar observation has been reported which states that a light source can be significantly reduced in power value over usage with time (years) [19]. The solar cell parameters were previously discussed in more details in **Chapter 2**. However, all these parameters and the photosensitivity that are possible to be detected from IV measurements are described here.

5.3.1 Photoconductivity Measurements

Photoconductivity measurements show the material's response in light and dark conditions that is isolated inside a dark box. Therefore, the conductivity is increased when it is exposed to light as compared with dark conditions, due to electrons are gained enough energy and excited from *VB* to *CB*. Dark- and Photoconductivity measurements were performed using a sourcemeter, multimeter and a solar simulator with an AM 1.5 light source. This is measured by applying voltage between gap cell electrodes (100μm gap) – see **Figure 5-5**. Current on the y-axis and voltage on x-axis are plotted for each measurement. A comparison between the two curves (dark and light curves) is required to understand the electrical properties of the device. By applying the voltage, the current is flowed which should be higher in the illumination condition than that in the dark condition.

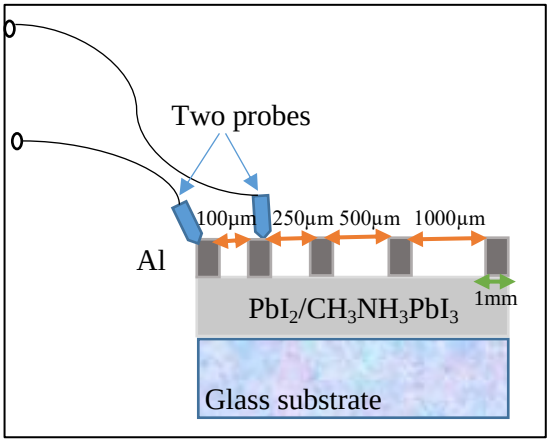

Figure 5-5: Schematic view of the setup for two probes J-V measurement for characterising thin film photoconductivity.

This measurement was carried out several times during this study to understand the photosensitivity of each deposited layer, including the PbI_2 thin film and $CH_3NH_3PbI_3$ layer. A two-probe system is used for testing the sample before applying an appropriate voltage, starting with low voltages of +/-2V and +/-5V to avoid the destruction of the device (**Figure 5-5**).

5.3.2 Solar Cells Characterisation

Solar cell characteristics such as open-circuit voltage (V_{oc}), short-circuit current (J_{sc}), maximum power output P_m and fill factor (FF) can be directly determined from a standard J-V measurement under illuminated condition. The ratio of V_{mp} and J_{mp} to V_{oc} and J_{sc} gives a fill factor (FF) of the solar cell.

Using the above parameters, solar cell efficiency that is denoted by η can be expressed as follow [21], [22]:

$$\eta = \frac{V_{oc} I_{sc} FF}{E\, A_c} \qquad (5.13)$$

Where the E is the incident sunlight energy (in Watt/cm^2) and A_c is the solar cell surface area (in cm^2) where the light falls (collector area).

5.4 Thermal Characterisation Technique

5.4.1 Thermo-Gravimetric Analyser (TGA)

There are a number of thermal analysis techniques such as differential scanning calorimetry (DSC), differential thermal analysis (DTA), thermogravimetric analysis (TGA), thermomechanical analysis (TMA) and dynamic mechanical analysis (DMA) [23, 24]. Among these techniques, TGA, *Perkin Elmer Pyris-1* is used in this work to examine thermal stability of PbI_2 and perovskite materials by measuring and recording the weight loss in the material with gradual increase in the temperature up to the desired value. The decomposition temperature, purity of material, composition of multi-component, the kinetic energy of decomposition reaction and estimated material lifetime can be also examined.

Typically, TGA instrument consists of thermobalance system to monitor the weight changes as a function of change in temperature, which involves furnace, temperature controller and electronic microbalance [23]. A range of temperatures can be applied with a specific heat rate in controllable atmosphere (e.g. Argon, Nitrogen, air and/or Oxygen) to record the weight changes with a resolution of 0.1 microgram. Several conditions can affect the resultant data such as the sample properties, its weight and the atmosphere used [25]. Argon or nitrogen gas is commonly used to prevent oxidation of a chosen material. To investigate the degradation of the organic part (CH_3NH_3I) and the inorganic part (PbI_2) of perovskite material, the applied temperature was in the range of room temperature and 700^{o}C under nitrogen atmosphere. The TGA collected data of PbI_2 powder, which is presented in **Figure 5-6** (a), showed one-step decomposition process at temperature of 400^{o}C. The construction of this instrument is presented in **Figure 5-6** (b).

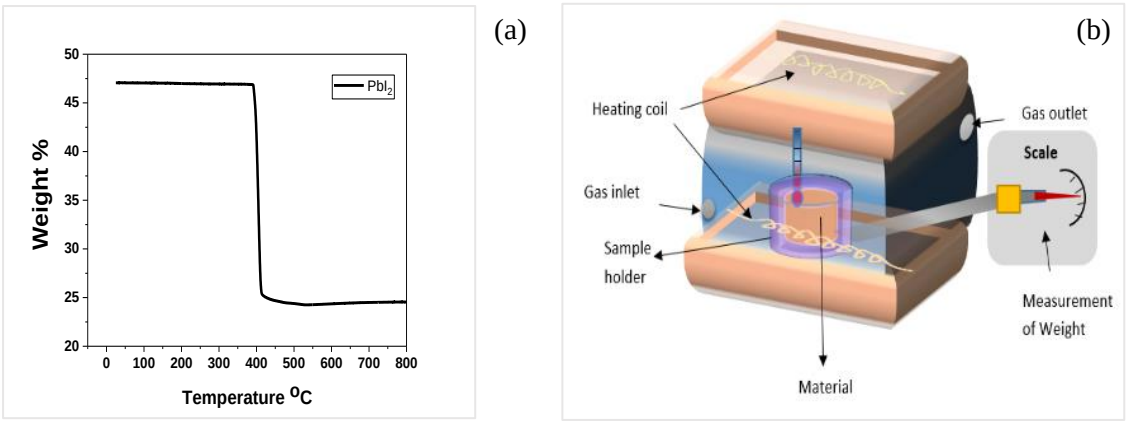

Figure 5-6: (a) Determine the decomposition of PbI_2 powder by TGA (b) illustration of a typical TGA system.

References

[1] D.K. Schroder, *Semiconductor material and device characterization,* John Wiley & Sons, 2006.

[2] Z.L. Wang and J.L. Lee, "Developments in Surface Contamination and Cleaning," in *Electron microscopy techniques for imaging and analysis of nanoparticles,* Anonymous Elsevier, 2008, pp. 531- 531-584.

[3] D. P. Allison, N. P. Mortensen, C. J. Sullivan and M. J. Doktycz, "Atomic force microscopy of biological samples," *Wiley interdisciplinary reviews: Nanomedicine and nanobiotechnology,* vol 2, no 6, pp. 618-634, 2010.

[4] N. Jalili and K. Laxminarayana, "A review of atomic force microscopy imaging systems: Application to molecular metrology and biological sciences," *Mechatronics,* vol 14, no 8, pp. 907-945, 2004.

[5] Y. Seo and W. Jhe, "Atomic force microscopy and spectroscopy," *Reports on progress in physics,* vol 71, no 1, pp. 016101, 2007.

[6] P. Eaton and P. West, *Atomic force microscopy,* 1st ed. ed. Oxford university press, pp. 1-10, 2010.

[7] N. Kumar and S. Kumbhat, "Essentials in nanoscience and nanotechnology," 2016.

[8] J. Drenth, *Principles of protein X-ray crystallography,* Springer Science & Business Media, 2007.

[9] R. Guinebretière, *X-ray diffraction by polycrystalline materials,* John Wiley & Sons, 2013.

[10] D. Vollath and W. V. G. KGaA, "An introduction to synthesis, properties and application," *And management,* vol 7, no 6, pp. 865-870, 2008.

[11] K. N. Manjunatha and S. Paul, "Investigation of optical properties of nickel oxide thin films deposited on different substrates," *Applied surface science,* vol 352, pp. 10-15, 2015.

[12] N. Elton, "Kaufmann, characterization of materials, vol. 1," 2003.

[13] H. Qiao, Z. Wei, H. Yang, L. Zhu and X. Yan, "Preparation and characterization of NiO nanoparticles by anodic arc plasma method," *Journal of nanomaterials,* vol 2009, pp. 2, 2009.

[14] V. Huxter, "Optical and material properties of colloidal semiconductor nanocrystals," 2009.

[15] B. D. Viezbicke, S. Patel, B. E. Davis and D. P. Birnie III, "Evaluation of the tauc method for optical absorption edge determination: ZnO thin films as a model system," *Physica status solidi (b),* vol 252, no 8, pp. 1700-1710, 2015.

[16] H. Che, J. Huso, J. L. Morrison, D. Thapa, M. Huso, W. J. Yeh, M. Tarun, M. McCluskey and L. Bergman, "Optical properties of ZnO-alloyed nanocrystalline films," *Journal of nanomaterials,* vol 2012, pp. 7, 2012.

[17] M. Wang, E. J. Kim, S. Kim, J. S. Chung, I. Yoo, E. W. Shin, S. H. Hahn and C. Park, "Optical and structural properties of sol–gel prepared MgZnO alloy thin films," *Thin solid films,* vol 516, no 6, pp. 1124-1129, 2008.

[18] A. McEvoy, L. Castaner and T. Markvart, *Solar cells: Materials, manufacture and operation,* Academic Press, 2012.

[19] M. J. Morgan, G. Jakovidis and I. McLeod, "An experiment to measure the IV characteristics of a silicon solar cell," *Physics education,* vol 29, no 4, pp. 252, 1994.

[20] G. Woan, *The cambridge handbook of physics formulas,* Cambridge University Press, 2000.

[21] J. Nelson, *The physics of solar cells,* World Scientific, 2003.

[22] C.S. Solanki, *Solar photovoltaics: Fundamentals, technologies and applications,* PHI Learning Pvt. Ltd., 2015.

[23] J.D. Menczel and R.B. Prime, *Thermal analysis of polymers,* Wiley Online Library, 2009.

[24] D.A. Skoog, F.J. Holler and S.R. Crouch, *Principles of instrumental analysis,* Cengage learning, 2017.

[25] P. Gabbott, *Principles and applications of thermal analysis,* John Wiley & Sons, 2008.

Chapter 6 Structural, Morphological and Optical Behaviour of Lead iodide (PbI_2) Thin Films

6.1 Introduction

As discussed in **Chapter 2**, despite perovskite thin films being deposited by several methodologies including single- or sequential- step process, their stability is still needed further improvement. Two-step sequential deposition of the perovskite is a promising route offering more controllable morphology. However, the morphology and properties of the final material ($CH_3NH_3PbI_3$) are mainly depended on the physical properties of the initial layer (lead iodide (PbI_2)) as well as on the method that is used to convert the initial layer into perovskite. Therefore, it is vital to investigate the physical properties of the PbI_2 layer prior to applying the second step.

Herein, two-step deposition was employed to achieve one of the main goals and novelty of this research which was synthesising perovskite material by the help of a plasma-enhanced chemical vapour deposition (PECVD). To achieve that, PbI_2 layer was initially deposited, followed by the conversion of the PbI_2 layer to perovskite ($CH_3NH_3PbI_3$). The work presented in this chapter was to provide in detail the first step of the deposition and the second step thereafter (in **Chapter 7**). Two methods, that were: spin-coating and thermal evaporation were employed for the deposition of the inorganic part of perovskite (lead iodide, PbI_2). The instruments and working principles of both techniques were discussed previously in **Chapter 4**. This chapter will further address the characteristics of PbI_2 films which were performed in order to investigate their crystallinity, morphology and optical properties using XRD, SEM, AFM, and UV-VIS-IR spectroscopy that were discussed in **Chapter 5**.

6.2 PbI_2 Thin Films Deposition

Lead iodide (PbI_2) has shown paramount interest in the scientific community owing to its unique characteristics in the field of radiation detector for *X*- and γ-rays and optoelectronic devices [1-4]. However, the PbI_2 has been a key inorganic material for use in perovskites which may have a significant effect to enhance the stability of the final material, since it can accommodate the organic molecules within its crystal structure. PbI_2 is an anisotropic semiconductor with a bandgap of 2.3-2.4 eV, it is formed by two elements that have a high atomic number (Z_{Pb} = 82, Z_I = 53) [5]. These two

elements are arranged in hexagonal crystals of I-Pb-I covalent bonded layers stacked by weakly van-der-Waals bonds forming polytypes [6, 7].

In this work, PbI_2 was considered a partial part of the active perovskite layer ($CH_3NH_3PbI_3$) of the solar cell and required to be initially deposited. Then, the PECVD technique was used to deposit methyl ammonium (CH_3NH_3) (the organic component of the active perovskite layer) into PbI_2 thin film using gaseous precursors. Therefore, the bandgap of the active layer will be appropriate for the photovoltaic applications (~1.6eV) (see **Chapter 2**). There are several fabrication procedures that have been used by scientific researchers to obtain PbI_2 thin films that include spin coating [8], dip coating [9], thermal evaporation [10], electron beam evaporation [11], sol-gel [12] and doctor blade technique [13].

An attempt to investigate an uniform film of PbI_2 with an approximate thickness of 200 nm that was determined from an extensive review of the literature will be explained in this section [14-16]. Initially, due to the cost-effectiveness and simplicity, spin-coating method was used for the preparation of PbI_2 thin film where commercially available yellow powder PbI_2 (99.999% purity with Particle size <10 nm) (purchased from Sigma-Aldrich), with molecular weight 461.01 g/mole and density 6.16 g/mL was used without further purification.

6.2.1 Spin-Coated PbI_2 Thin Films and its Characterisation

6.2.1.1 Solubility Test of PbI_2

Due to the requirement of a pure liquid precursor for the above-mentioned deposition technique, the solubility test of PbI_2 was carried out. The selection of an appropriate solvent and the concentration of solution were essential to completely dissolve PbI_2. In addition, it was important to avoid/prevent the formation of any new reactions between the solute and the solvent that may produce a different compound. In view of this, 2.5 mg of PbI_2 with 1ml of the variety of organic and inorganic solvents were used (details are reported in **Table 6.1**).

With different conditions, as mentioned in **Table 6.1,** four solvents were dissolved the PbI_2 at different time periods in the ultrasonic bath. These solvents were propan-2-ol (IPA), Chloroform, Dimethyl sulfoxide (DMSO) and N,N-Dimethylformamide (DMF). In the first two solvents, PbI_2 powder was found to be settled at the bottom when left unattended for 10 min. DMSO and DMF were the two optimum solvents that dissolved PbI_2 completely.

From this test, it was also observed that DMSO dissolved PbI_2 quicker than DMF. Approximately 15 minutes sonication in an ultrasonic bath dissolved PbI_2 in DMSO, whereas, in DMF an additional 15 minutes was required to dissolve the equal amount of PbI_2. This could be attributed to the strong

coordination between Pb-O with a bond length of 2.38 Å in DMSO as compared to 2.431 Å in DMF, resulting from the high value of the dielectric constant of DMSO, which is 36.7 and 46.6 for DMF and DMSO respectively [17-19]. Therefore, a higher internal electric field in DMSO would help to dissolve PbI_2 faster as it was observed in this research study.

Table 6.1: Solubilises of PbI_2 in the variety of solvents

	SOLVENTS	Sonication for 30 min	Sonication for 1 hour	Heating at 70 °C for 30min	Magnetic Stirring + Heating (70 °C)	Kept on table (10min)
1	DI Water	Insoluble	Insoluble	Insoluble	Insoluble	
2	IPA 2	Partially soluble	Suspension			Settled down
3	Acetone	Insoluble	Insoluble	Insoluble	Insoluble	
4	Methanol	Insoluble	Insoluble	Insoluble	Insoluble	
5	Ethanol	Insoluble	Insoluble	Insoluble	Insoluble	
6	Dichlorobenzene	Insoluble	Insoluble	Insoluble	Insoluble	
7	Chloroform	Partial dissolve	Suspension			Settled down
8	Benzene	Insoluble	Insoluble	Insoluble	Insoluble	
9	DMSO	Soluble	Soluble			Soluble
10	DMF	Soluble	Soluble			Soluble

The rich-yellow colour solution was obtained when 1ml of DMF was used as a solvent to dissolve 18.4 mg of PbI_2, but, the colour of the solution when PbI_2 was dissolved in DMSO was not similar (i.e. not yellow colour). The colourless transparent solution was obtained when 9 mg/ml solution was prepared in DMSO. Whereas, the colour was changed to light brown with a higher concentration (18.4

mg/ml) of PbI_2 in DMSO. This was an interesting phenomenon, which might be due to the reaction of PbI_2 and DMSO molecules (C_2H_6OS) that could lead to a new/other by-product in the solution [21, 22].

One of the important properties of a solvent that was influential in this work was its boiling point which is 187 °C and 154 °C for DMSO and DMF, respectively. Choice of solvent used for preparing a solution should show three key features which include **(1)** a solute should dissolve in a solvent, **(2)** solute and solvent should not take part in a new reaction producing a different compound and **(3)** solvent should evaporate quickly leaving behind the material. Considering these requirements, the appropriate solvent to dissolve PbI_2 in this work was DMF.

6.2.1.2 Experimental Procedure

PbI_2 was dissolved in DMF in a concentration of 55.2 mg/3ml gradually and sonicated for 30 minutes to yield a homogenous solution. The Corning 2875 glass and 4"diameter B-doped p-type silicon of thickness 500-550 µm with a resistivity of 1-20 Ωcm and orientation <100> substrates were used after cutting/cleaving to obtain ~2 cm^2 piece and then subjected to cleaning process as described in **Chapter 4**. Si wafer substrates were used as sample substrates for SEM and AFM analysis to have better resolution images, while glass substrates were used for another analysis such as XRD, optical and electrical measurements.

PbI_2 thin films were deposited by, static dispenses mode of the spin-coating technique, to ensure the full coverage onto the substrate. Then, it was spun at 3000 rpm for 30 seconds, where it was produced the best uniform films with full substrate coverage. In order to evaporate the DMF solvent that was adsorbed on the surface or among the crystal planes, a post-thermal treatment was required. To select the optimal temperature, thermogravimetric (TGA) analysis of PbI_2 dissolved in DMF was made in a form of paste and then used. The TGA thermogram curve, shown in **Figure 6-1**, was obtained under continuously flowing nitrogen at a flow rate of 20 mL/min and steady constant heating rate of 20°/min for temperatures between a minimum of 30 °C to a maximum of 700 °C. It can be seen that from **Figure 6-1** there are two main weight loss processes. The TG test revealed that PbI_2 • DMF began thermal decomposition at temperature of 70 °C and was completed at around 112 °C with the release of DMF from the material [23]. The material was continued to decompose at a temperature above 400 °C corresponding to the Iodine vaporisation [24]. Considering this notion, the spin-coated PbI_2 films were thermally annealed in the air atmosphere at 70 °C [16] for different time durations, 60, 120, 180, 240 and 300 minutes. The control sample was not annealed and was used as a reference to compare and understand the effect of annealing on the structural and optical properties.

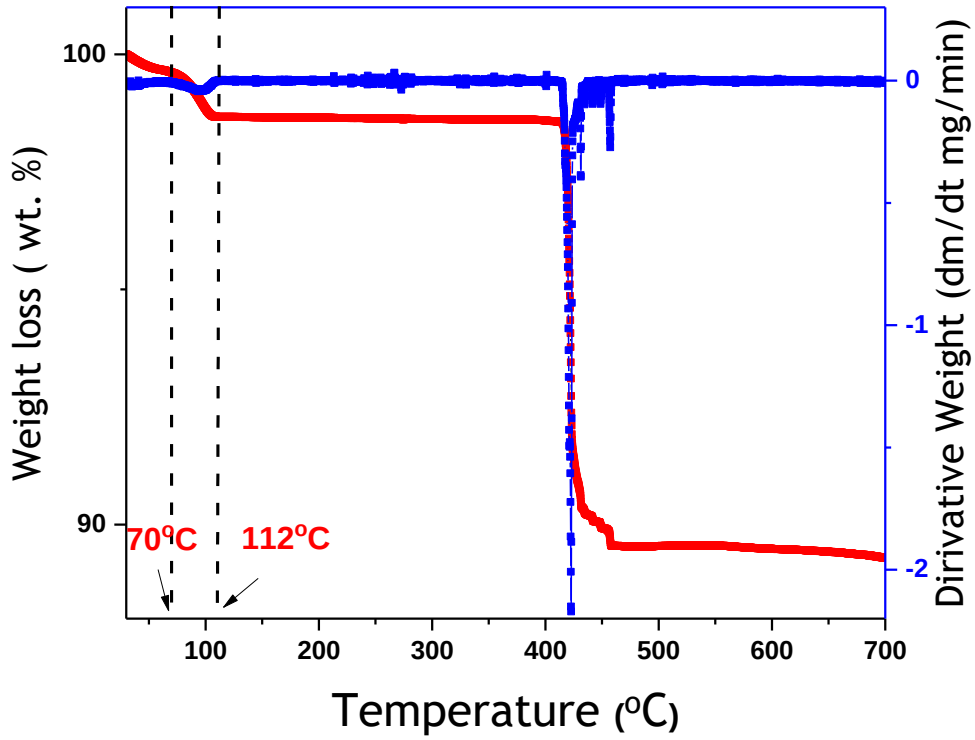

Figure 6-1: TGA analysis of PbI_2 • DMF.

6.2.1.3 Structural Characterisation

Figure 6-2(a) depicts the x-ray diffraction pattern of the PbI_2 thin films by spin-coating technique before and after annealing at 70 °C for different time durations. It was important to mention that the prepared films were exhibited four diffraction peaks at 2θ = 12.8°, 25.4°, 38.1° and 52.6° which were corresponding to the reflection from the (001), (002), (003) and (004) planes of the hexagonal PbI_2 crystal structure [10, 12, 25]. In comparison with the XRD patterns of the as-purchased PbI_2 powder shown in **Figure 6-2 (b),** one might note that the prepared films were showed diffraction peaks along (00*l*) planes only, implying that the prepared PbI_2 films were showed a prefential orientation along the c-axis direction perpendicular to the glass substrate [5].

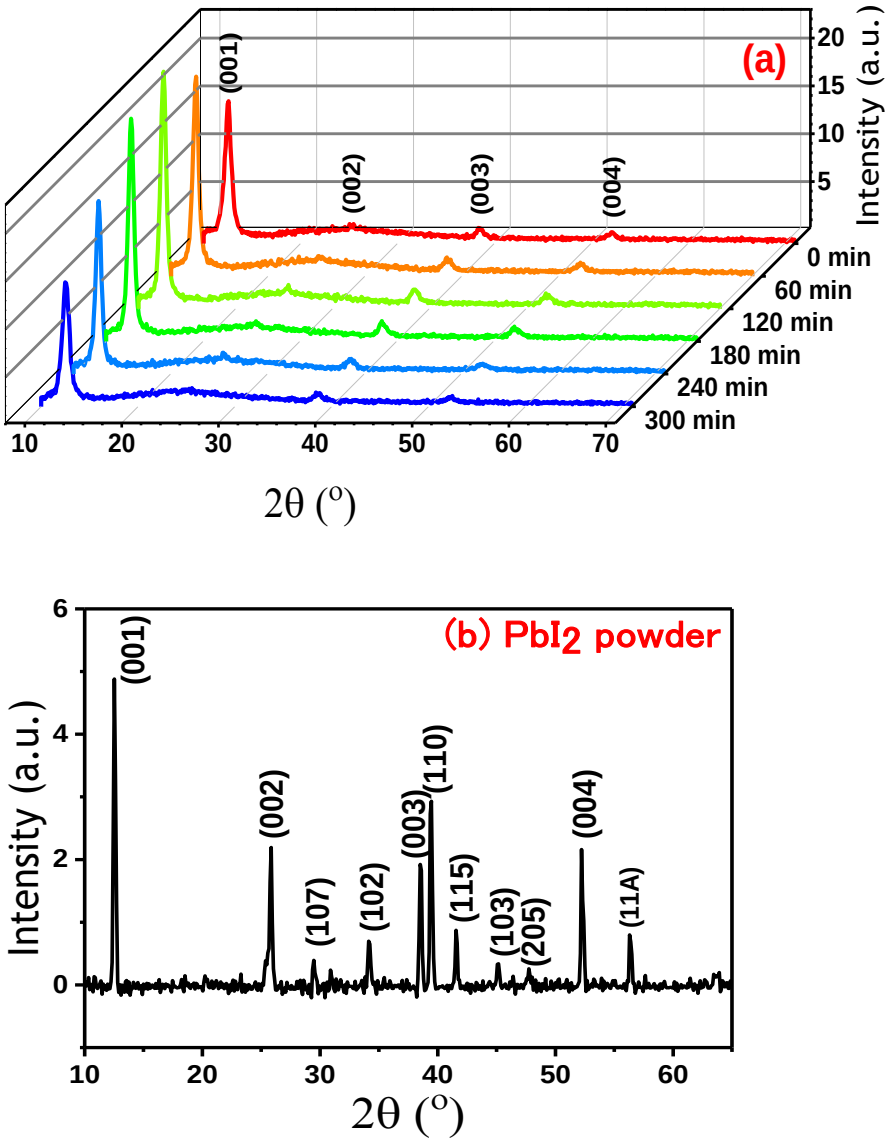

Figure 6-2: The XRD diffraction patterns of the (a) annealed PbI_2 thin films and (b) purchased PbI_2 powder from Sigma-Aldrich (A=15).

The effect of annealing time on the lattice constants of the lead iodide films was investigated through the calculation of lattice constants according to Bragg's law [26, 27]

$$\lambda = 2d_{hkl} \sin\theta \qquad (6.1)$$

Where λ is the wavelength of the XRD source, d is the interplanar spacing and θ is the diffraction angle. This equation can be written in the form:

$$\frac{1}{d_{hkl}^2} = \frac{4sin^2\theta}{\lambda^2} \qquad \textbf{(6.2)}$$

For the hexagonal crystal structure, the lattice constants a and c may be given by [17, 26]

$$\frac{1}{d_{hkl}^2} = \frac{4[h^2+hk+k^2]}{3a^2} + \frac{l^2}{c^2} \qquad \textbf{(6.3)}$$

Combining eq. **(6.2)** & **(6.3)** one may get

$$sin^2\theta = \left[\frac{\lambda^2}{3a^2}\left(h^2 + hk + k^2\right)\right] + \frac{\lambda^2 l^2}{4c^2} \qquad \textbf{(6.4)}$$

Since all the lead iodide films were grown along the (00l) planes, equation **(6.4),** may be summarized as

$$sin^2\theta = \frac{\lambda^2 l^2}{4c^2} \qquad (6.5)$$

The calculated lattice constant, c, for the annealed films at various durations is presented in **Figure 6-3**. However, the relative intensity (I_{002}/I_{001}) against the annealing time is also presented in **Figure 6-3**. It was clearly seen that both the lattice constant and relative intensity were followed the same behaviour, where both were decreased up to annealing time of 120 min and then started to increase. This behaviour might be attributed to the fact that the annealing at 70 $^{\circ}$C below the optimum time (120 min) resulted in the evaporation of the solvent along the PbI_2 planes with the annealing time when the solvent was completely evaporated at 120 min, the crystal size was tended to slightly increase due to the Ostwald ripening effect [28-30]. This observation was confirmed by calculating the crystallite size of the lead iodide particles at different annealing durations according to the Williamson-Hall method [31]:

$$\beta\, cos\Theta = \eta \sin\Theta + \frac{K\lambda}{D} \qquad \textbf{(6.6)}$$

Where D is the crystallite size and η is the microstrain. The values of the crystallite size and lattice microstarin were estimated from the plot of β cos θ versus sin θ (not presented here) and obtained the crystallite size (Kλ/D) from the y-axis intercept and the microstrain (ε) from the slop. The values of the crystallite size and lattice microstarin are presented in **Figure 6-4**.

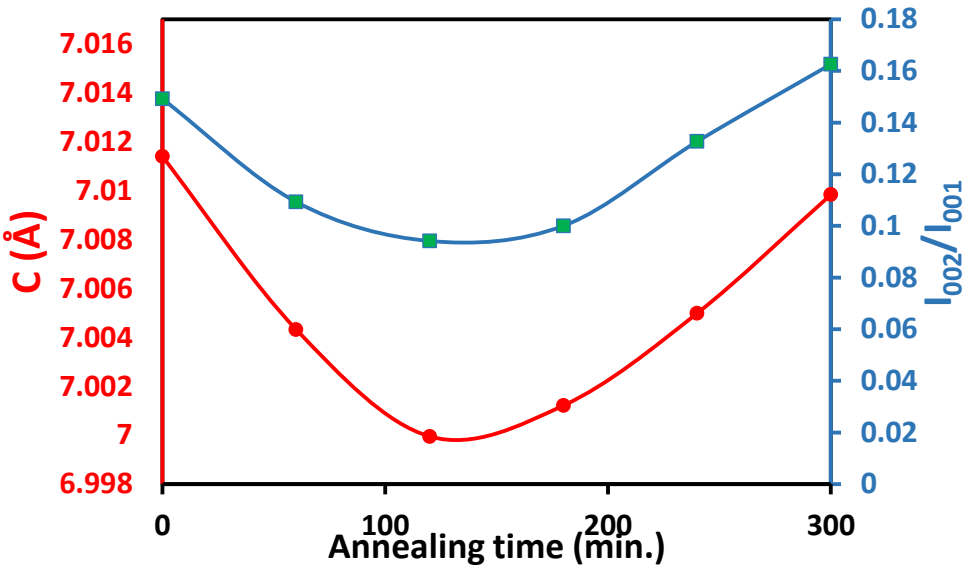

Figure 6-3: The relation between the lattice constant and relative intensity (I_{002}/I_{001}) against the annealing time of the PbI_2 thin films deposited by the spin coating technique.

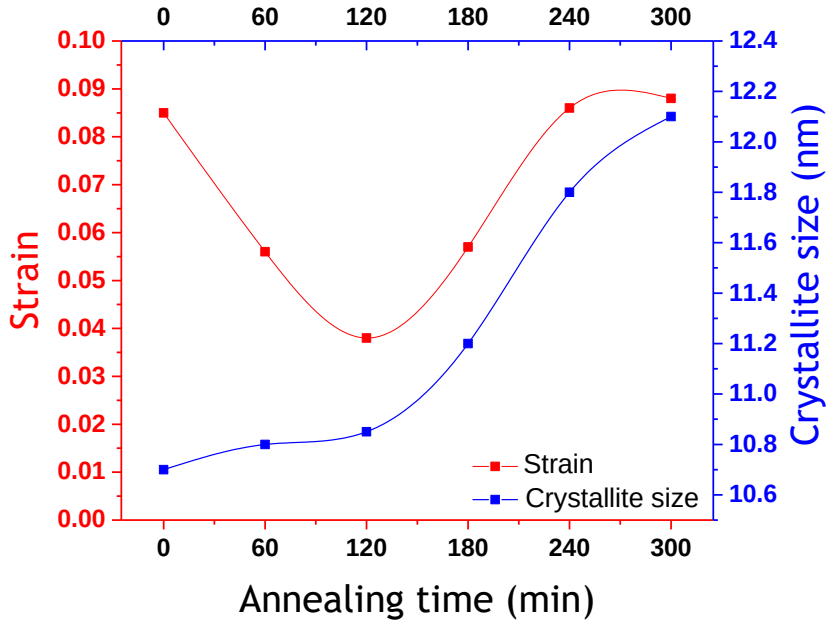

Figure 6-4: The crystallite size and strain within the lattice of the PbI_2 thin films were annealed at 70 °C for different duration time from 0 to 300 min.

The crystallite size was found to be 10.8 ± 0.1 nm along with the annealing time range from 0 to 120 min, followed by an increase of the crystallite size to 12.1 nm up to the annealing time of 240 min (Figure 6-4 blue line). However, the red line in Figure 6-4 illustrated the lattice microstrain that was decreased from 0.085 to 0.04 when the annealing time was increased from 0 to 120 min followed by an increase to 0.095 at the annealing time of 240 min. The decrease of the microstrain and the unchanged crystallite size below 120 min, confirmed time of 120 min was required to evaporate the DMF solvent that was present along the crystal planes and reduced the strain on the lead iodide crystal planes. Above the optimum time, the lead iodide crystals were started to grow and their crystallite sizes were increased [32].

6.2.1.4 Morphological Characteristic

To further understand the above observations, the surface morphology and topography of the deposited films at various annealing times were investigated by means of SEM and AFM measurements. **Figure 6-5** shows a cross-sectional SEM image view for the deposited films at various annealing times. Notably, the as-deposited film was showed a smooth surface. The increase of the annealing time was resulted in an increase of the grain size and then the surface became rougher. The mean thickness of all films was found to be around 50±3 nm. **Figure 6-6** depicts the AFM topography of the films at all annealing times. One might note that below the annealing time of 120 min, the root mean square roughness of the deposited films was around 1.7±0.2 nm. For the annealing time above this optimum time, the root mean square roughness started to increase to 2.4 nm, 3.5 nm and 4.6 nm at annealing times of 180, 240 and 300 min, respectively.

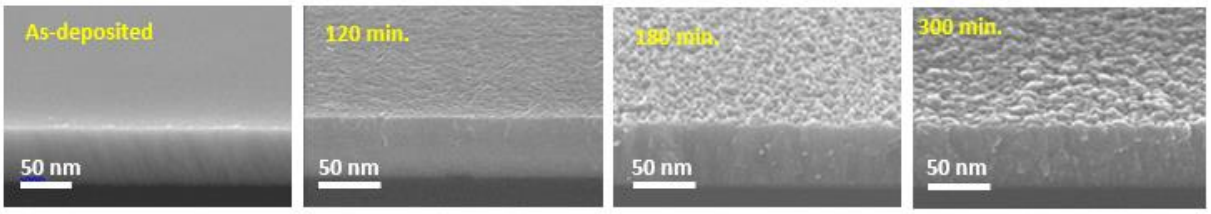

Figure 6-5: Cross-sectional SEM images of the PbI_2 thin films annealed at 70^{o}C for various time.

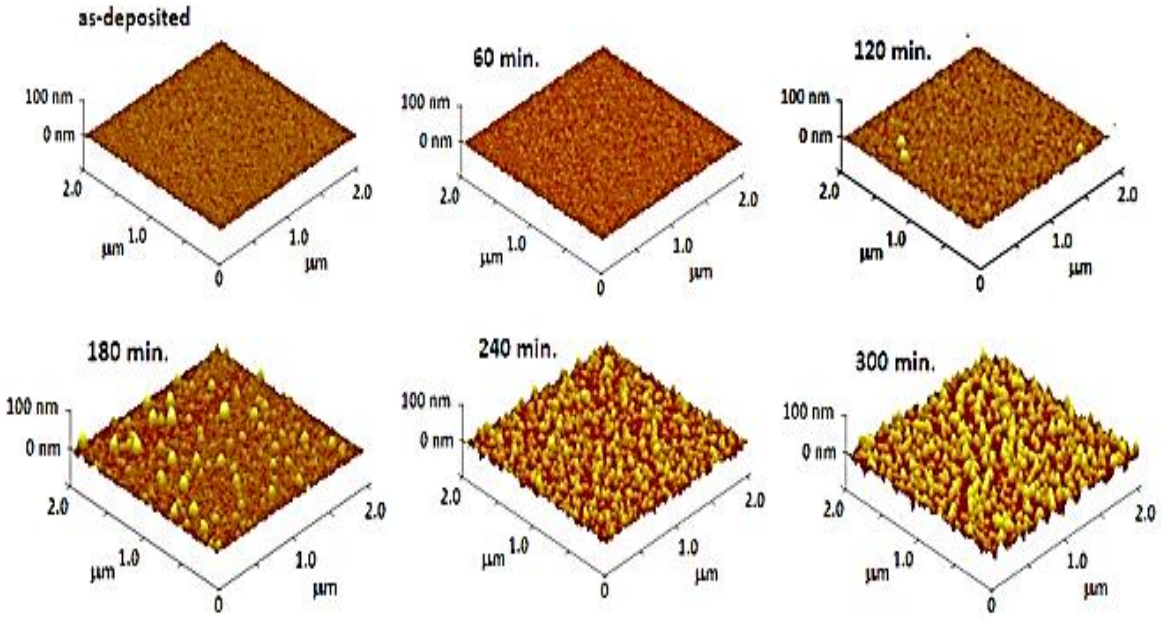

Figure 6-6: AFM images of the PbI_2 thin films annealed at 70 °C for various time.

6.2.1.5 Optical Characteristic

To investigate the influence of the annealing time on the optical properties of the c-oriented lead iodide thin films which were prepared by the spin-coating, the transmittance and absorbance spectra were measured along the spectrum region 300-1100 nm as shown in **Figure 6-7 (a)**. It was noted that all films were showed high transparency above 550 nm with an average value of 85%. Moreover, the annealing time did not show a significant change in the transparency along the visible and near IR spectrum region. The absorption spectra of the prepared films was showed a shoulder peak around 498 nm which was ascribed to the band-to-band transition (from VB to CB) that was corresponding to the transition/excitation energy of 2.45 eV. The absorption coefficient of the annealed films was in the range of 10^5 cm^{-1}. The higher absorption coefficient value of 1.33×10^5 cm^{-1} was achieved at the optimum annealing time of 120 min as shown in **Figure 6-7 (c).**

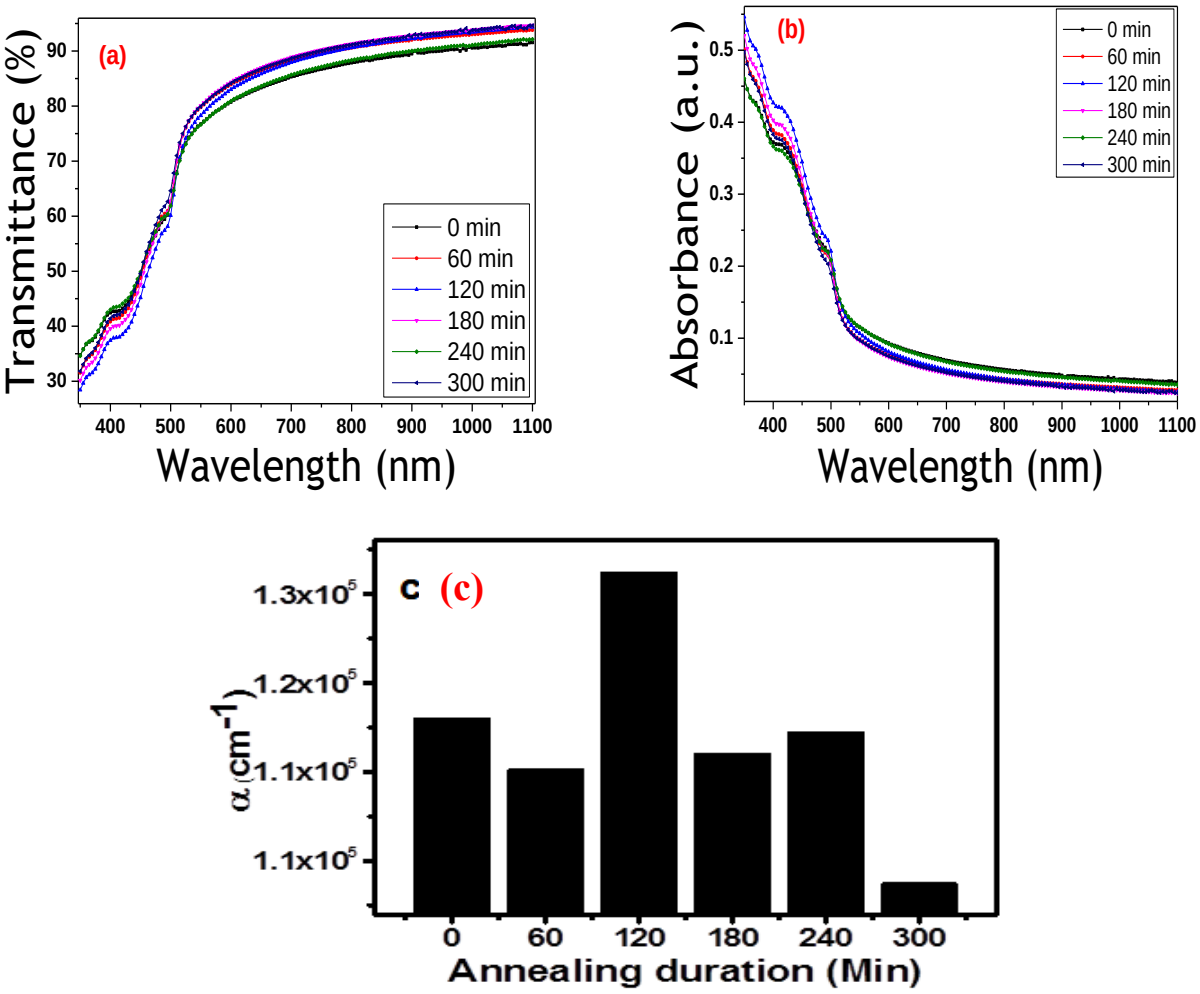

Figure 6-7: (a) Transmittance of PbI_2 thin films deposited by the help spin coating technique at different annealing duration, (b) the absorbance of the PbI_2 spin-coated films and (c) the values of absorption coefficient for the annealed PbI_2 thin films at 2.5 eV.

The value of the optical band gap for the annealed films was estimated by using Tauc's relation [33]

$$(\alpha hv)^n = A\left(hv - E_g\right) \qquad \textbf{(6.7)}$$

Where a is the absorption coefficient, h is a Plank's constant, A is a constant and E_g is the energy bandgap. Since the PbI_2 is a direct band gap semiconductor [5, 12, 34], the exponent value (n) in the Tauc relation substituted by n=2 [35, 36]. Therefore, one may get

$$(\alpha h\nu)^2 = A\,(h\nu - E_g) \qquad \textbf{(6.8)}$$

Figure 6-8 (a) depicts the Tauc plot for the annealed films at various durations. The estimated values of band energy gap versus the duration of annealing are presented in **Figure 6-8** (b). The average value of optical band gap was showed a slight increase up to the optimum annealing time of 120 min from 2.4 eV to 2.45 eV, followed by a decrease from 2.45 eV to 2.41 eV. This behaviour confirmed the fact that the evaporation of the solvent among the planes of PbI_2 crystal structure caused a change in the lattice constant and in turn a decrease of the crystallite size. This decrease of the crystallite size resulted in increasing of the optical band gap up to 120 min. Once the solvent was completely evaporated an increase of the lattice constant and in turn, the crystallite size was led to a decrease of the band gap [37].

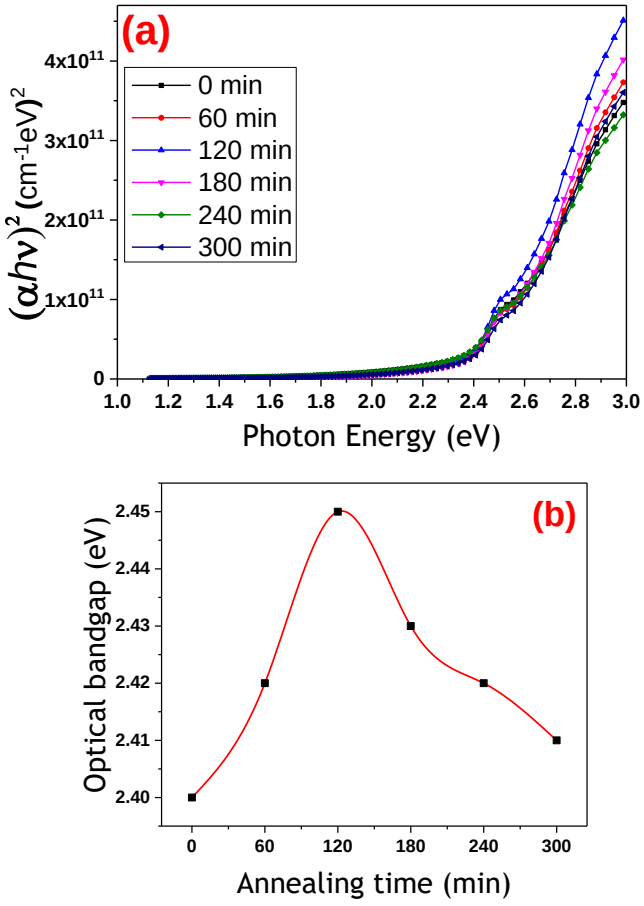

Figure 6-8: (a) Plot of Tauc relation and (b) The variation of optical band gap of PbI_2 thin films at different annealed durations at 70 °C.

The optical conductivity is a concept for a material response to the incident photons and hence optically excited transitions can happen, the optical conductivity of the annealed PbI_2 films was determined from the relation [33]

$$\sigma_{opt} = \alpha nc/4\pi \qquad (6.9)$$

Where α is the absorption coefficient, n is the refractive index and c is the velocity of light. **Figure 6-9** shows the relation between optical conductivity and photon energies for annealed films. It was obvious that the conductivity of the material was increased with the energy of photons in certain photon energies starting from the band gap of the PbI_2. The maximum optical conductivity was $2.6 \times 10^{16}\ S^{-1}$ at the optimum annealing time of 120 min at a photon energy of ~2.75 eV. Then, the conductivity decreased for photon energy higher than 2.75 eV. This was argued to the fact that as the wavelength of photons decreases, their associated energy increases. That means high energy photons will be absorbed near the surface of the film, whose absorption is less compared to low energy photons. In addition, at energy $2.5eV \leq E \leq$2.75eV the electrons that were excited to the sub-levels located above the CB tended to change the direction of momentum to reach the minimum of CB) [38].

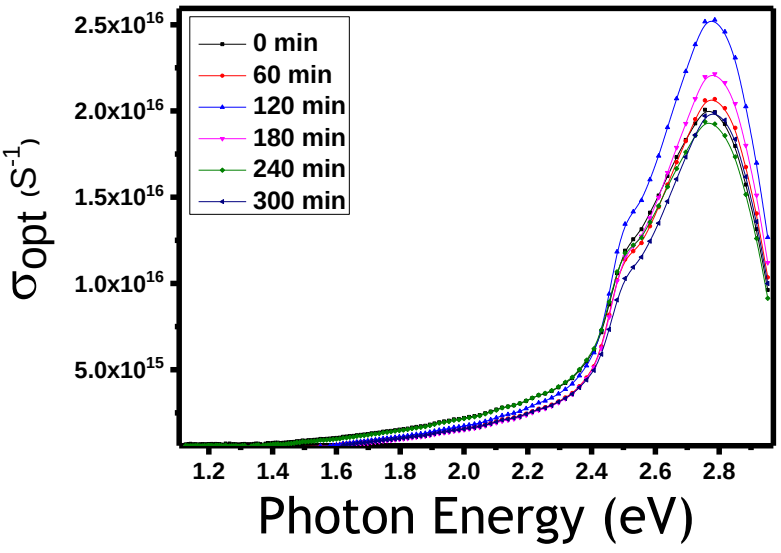

Figure 6-9: Optical conductivity of PbI_2 thin films versus photon energy.

Optical constants of the PbI_2 thin films were calculated, as it was an important parameter to understand their atomic interactions with a range of wavelengths of light. According to these interactions, dispersion of the light was observed. Hence, a scattering of light would reduce the amount of light

being absorbed by the material. Which was determined by mathematically calculating the extinction coefficient formula shown below [33, 39]:

$$\mathbf{k} = \frac{\boldsymbol{\alpha\lambda}}{\mathbf{4\pi}} = \frac{\boldsymbol{\lambda}}{\mathbf{4\pi d}} \mathbf{ln}\left(\frac{\mathbf{1}}{\mathbf{a}}\right) \qquad \textbf{(6.10)}$$

Where α is the absorption coefficient, d is the film thickness and a is the absorbance. The refractive index value is related to the local polarizability of the material and the velocity of light when it propagates within the material compared to the space. The following equation can be used to calculate the refractive index [33, 40]:

$$\mathbf{n} = \sqrt{\left[\frac{\boldsymbol{4R}}{\boldsymbol{(R-1)}} - \boldsymbol{k^2}\right]} - \frac{\mathbf{R+1}}{\mathbf{R-1}} \qquad \textbf{(6.11)}$$

Where R is the reflectance and k is the extinction coefficient.

Figure 6-10 showed that at lower wavelengths the maximum value of the extinction coefficient and refractive index were obtained due to an anomalous dispersion [41, 42]. A certain amount of energy will be consumed during the oscillation of electrons. However, the transition of an electron may not happen unless the frequency of the electron is the same as the electromagnetic radiation [43]. Hence, the coupling of electrons is achieved then the electronic transition is occurred [44]. From **Figure 6-10**, the k value of annealed thin film for 120 min was determined to be 0.8 and the n value was determined to be 6. These results were close to those of evaporated films of PbI_2 [5, 45, 46].

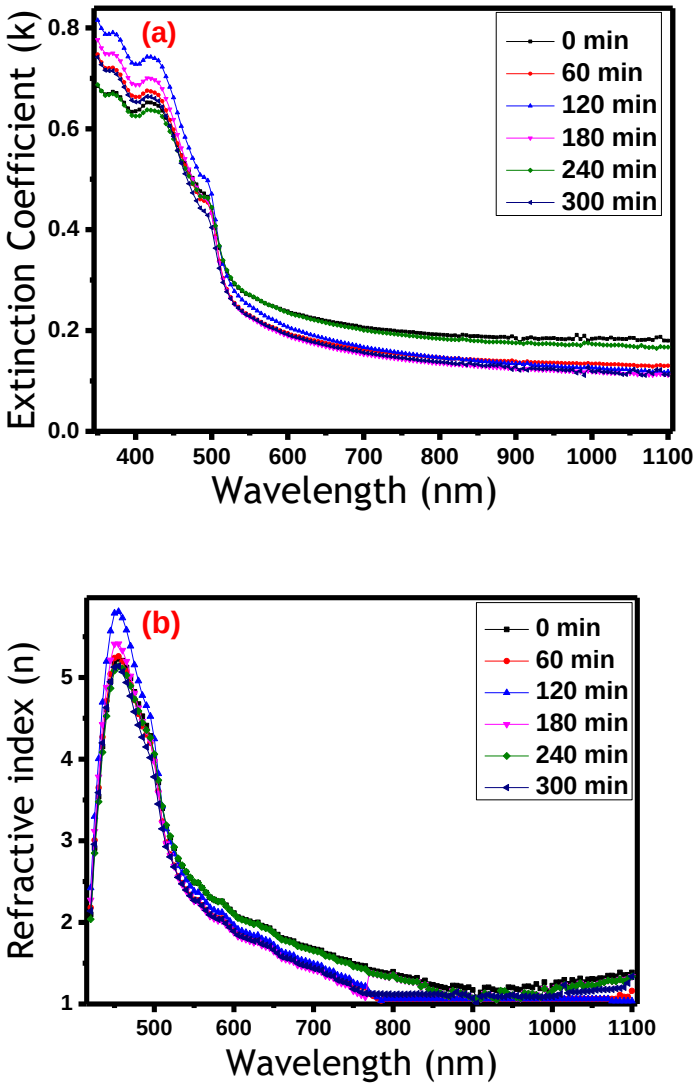

Figure 6-10: Optical constants of PbI_2 thin films: extinction coefficient and Refractive index versus wavelength.

The dielectric constants of PbI_2 thin films provide more information at the microscopic scale. These constants determine the permittivity and polarizability of a material that is affected by the density of states located within the forbidden gap. The real and imaginary parts of the dielectric constant were calculated for each film as follows [39] and presented in **Figure 6-11**

$$\varepsilon_r = n^2 - k^2 \qquad (6.12)$$

$$\varepsilon_i = 2nk \qquad (6.13)$$

It was clear that the real and imaginary dielectric constants were presented the similar behaviour. However, the real dielectric constant value was higher than the imaginary. The highest values were

observed around the bandgap region as a result of the highest rate of the absorption of the incident photons, followed by a decrease at low photon energies because of the decrease of the photons absorption. The average values of the real and imaginary dielectric constants of PbI_2 thin films which were treated thermally for 120 min were ~27.3 and ~6.35, respectively. The obtained values of the dielectric constants were in a good agreement with others [47, 48].

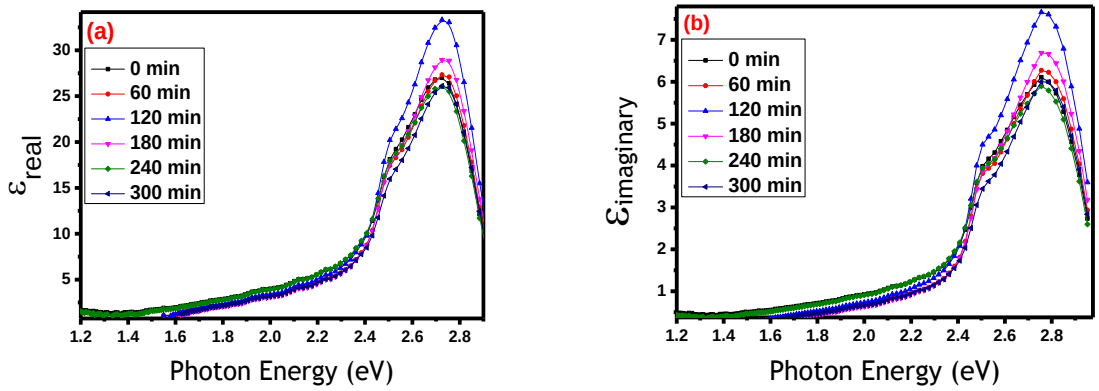

Figure 6-11: Dielectric constants of PbI_2 thin films: a real part and Imaginary part versus photon energy.

Having considered the analysis on the films at different annealing time, it was discovered that film annealed at 120 min was possessed a suitable structure for the continuous growth of perovskite material. In a further study, this film will be considered for the use for the subsequent experiment that will be presented in the next chapter (**Chapter 7**).

6.2.2 Thermal-Evaporated PbI_2 Thin Film

After consulting available literature, it was understood that the thickness of PbI_2 thin film should be thick enough to achieve the growth of perovskite film. In this study, a 200 nm thickness of PbI_2 film cannot be deposited by spin-coating, therefore, the thermal evaporation technique was explored to deposit such PbI_2 thickness due to its relatively low melting and boiling points, which are 402 $^{\circ}$C and 954 ^{o}C, respectively [14-16]. The advantages of using this technique over spin coating were that a uniform defined film thickness can be achieved which was hard to obtain in the formerly mentioned technique. This was the motivation for choosing the thermal evaporation compared to the spin-coating as well as improving the film purity since this deposition technique was performed in a vacuum. Therefore, the possibility of cross-contamination of the resultant film was less compared to the wet deposition methods, in this case, the spin coating [49].

6.2.2.1 Experimental Procedure

The same source of the PbI_2 powder that used for the spin coating was used for the thermal evaporation. The powder was placed on a tungsten boat. Cleaned Glass and silicon (Si) substrates were loaded into the evaporation chamber that was exposed to PbI_2 vapour. The system was under a vacuum of 2 x 10^{-6} mbar. At such pressure, the current was applied to the tungsten boat which was heated to a temperature higher than the boiling point of PbI_2 powder (954 ºC). The deposition conditions are given in **Table 6-2.**

Table 6-2: A summary of the deposition conditions.

Vacuum (mbar)	Substrate to film gap distance (cm)	Deposition rate (nm sec^{-1})	Applied electric current (A)
2 x 10^{-6}	10	~ 0.5 to 1.0	20

6.2.2.2 Structural Characterisation

Figure 6-12 depicts the x-ray diffraction pattern of PbI_2 thin films that were deposited on a glass substrate by both techniques; thermal evaporation (the red colour) and spin-coating (the blue colour). The main diffraction peaks of the hexagonal crystal structure of PbI_2 were dominated by (00*l*) where *l* = 1,2,3,4 lattice planes [25, 50]. This data showed the same signature/diffraction peaks of a spin-coated film. The thin-films obtained from the two techniques (spin coating and evaporation processes) had strong prefential orientation along the c-axis (00*l*) direction [50], with no difference observed in the formed structure. However, the discrepancy in the peak broadening and intensity of the dominant peak at ~ 12.63^o could be clearly observed between the two methods that implied increase in the peak intensity and the width of the PbI_2 thin film obtained by the evaporation process in comparison to the spin-coated film. The increase in the peak intensity might be attributed to the thicker film which was obtained from the thermal evaporation process or to the fact that the thermal evaporation technique was provided thin film with bigger crystallite size, in contrast to a spin-coated film [25]. This observation was confirmed by increasing the mean crystallite size of PbI_2 particles and reducing the lattice strain. The crystallite size and lattice strain were extracted from the XRD data and the obtained average values were approximately 34.97 nm and 0.005, respectively. However, the width of the peak in the evaporated film became broadened compared to the spin-coated film indicating that the

coexistence of amorphous and crystalline regions which were appeared within the evaporated PbI_2 matrix as shown in **Figure 6-12**.

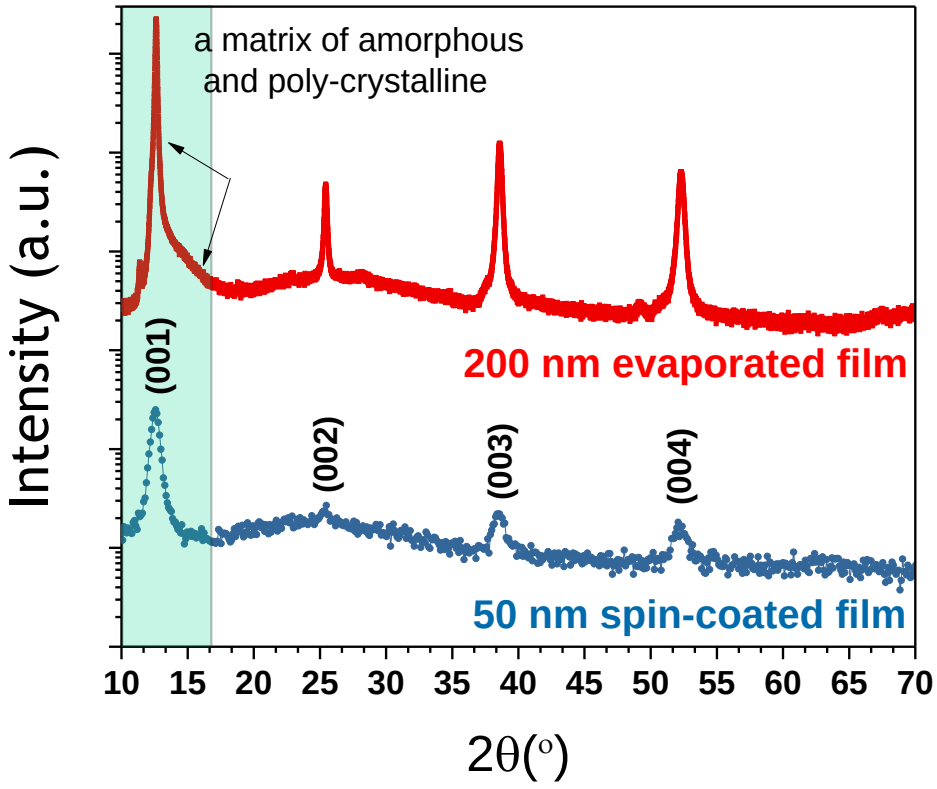

Figure 6-12: The XRD diffraction patterns of the thermal-evaporated and spin-coated PbI_2 thin films.

6.2.2.3 Morphological Characteristic

The scanning electron microscopy (SEM) images of a 200 nm-thick PbI_2 polycrystalline thin films deposited using the thermal evaporation were carried out. **Figure 6-13** reveals that the surface morphology of the evaporated film was plate-like grain structures [25, 51]. The PbI_2 crystal arrangement produced voids in-between the grains as can be seen that clearly in **Figure 6-13 (b)** [14].

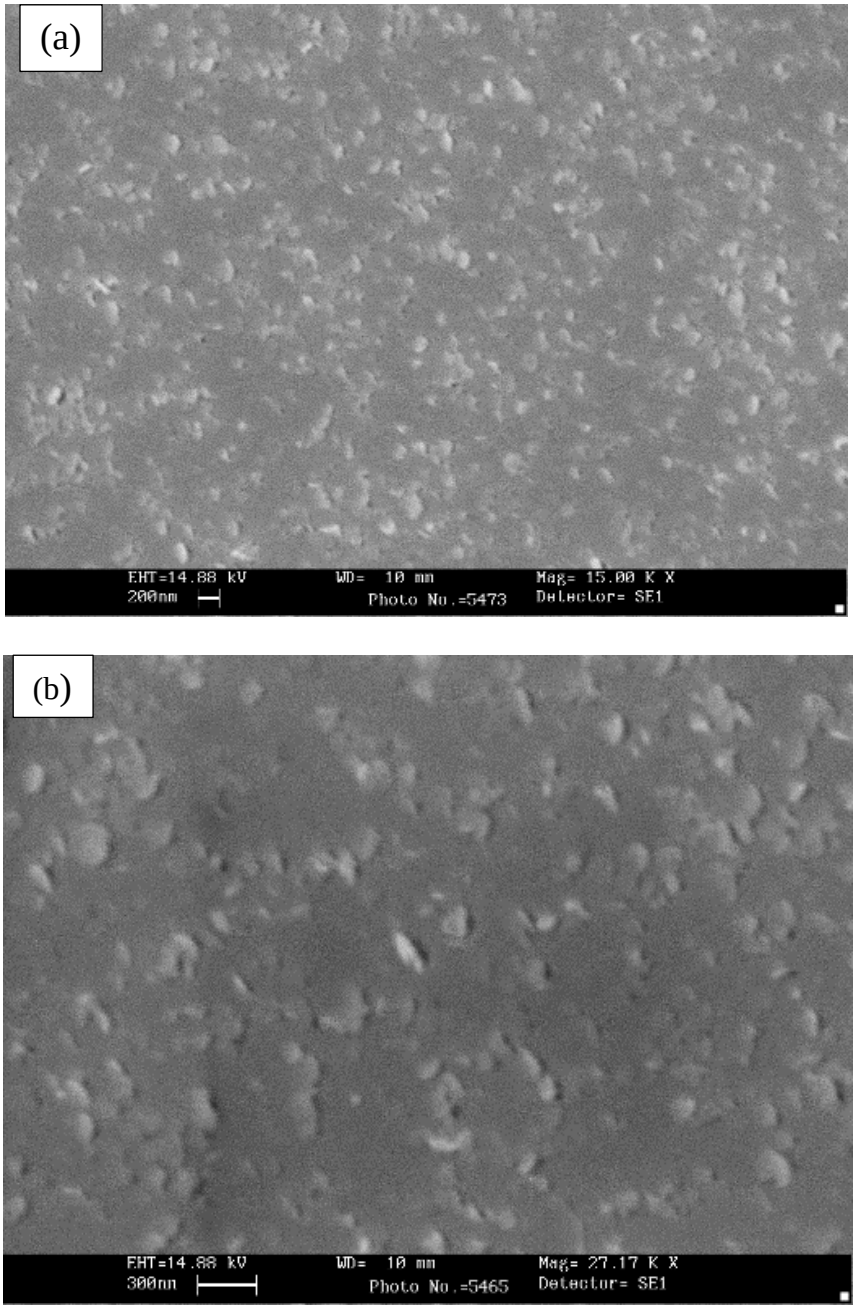

Figure 6-13: Top view SEM images of evaporated PbI_2 thin film at different magnification (a) 15,000 x and (b) 27,000 x.

This variation in the film' morphology resulted from the different growth orientations of the hexagonal shaped plate-like grains. In the spin-coated films, the c-axis crystals growth was oriented parallel to a substrate plane, while the orientation became varied in the films creating such inter-grain voids (**Figure 6-13**). Mainly, the I-Pb-I covalent monolayer begins to grow parallel to a substrate plane (in-

plane) and build of a new monolayer in the perpendicular direction to c-axis via the construction of van der Waals bonding (**Figure 6-14 (a))** [7]. Such crystallographic orientation has been observed in the solution growth of PbI_2 crystals [38]. Thus, it could be explained by the homogeneity surface of as-deposited spin-coated PbI_2 film as was observed from SEM and AFM images (**Figure 6-5** and **Figure 6-6**). In the evaporated film, the formed monolayer could act as a substrate for growing new nuclei which can further grow new crystals in the perpendicular direction to the substrate plane (out-of-plane) as can be seen in **Figure 6-14** (b). The reason for such varied growth orientations might come from the exothermal heating of the reverse sublimation (deposition) which elevates the substrate temperature [7]. Similar growth characteristics were observed when the substrate temperature was in the range of 180- 210 $^{\circ}C$ [7]. This morphology could facilitate the diffusion of the organic cation ($CH_3NH_3^+$) through the intergrain voids, and thereby promote the conversion into perovskite. These observations were similar to the literature [14, 25, 52].

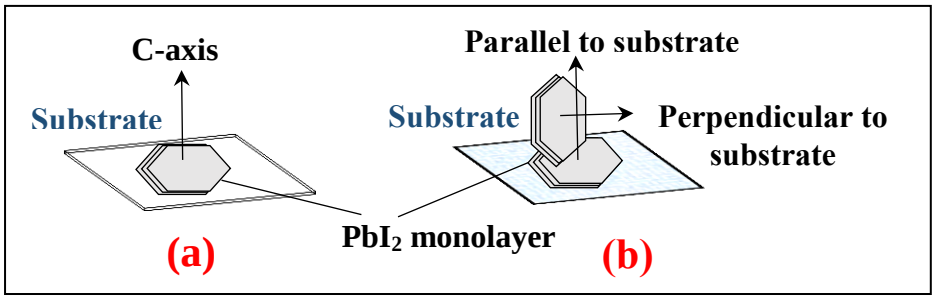

Figure 6-14: A schematic diagram of the variation of growth mechanism obtained in PbI_2 polycrystalline thin films which were resulted in different grain orientations with respect to the deposition methods; (a) spin-coated PbI_2 film and (b) thermal-evaporated PbI_2 film.

6.2.2.4 Optical Characteristic

In order to investigate the optical properties of the films, transmittance spectrum for the range of light wavelengths (300-1100 nm) was measured as presented in **Figure 6-15**. A sharp absorption onset/edge was observed around 520 nm corresponding to a sharp electronic transition at the bandgap of PbI_2 and then the transmittance was increased with higher wavelengths [53].

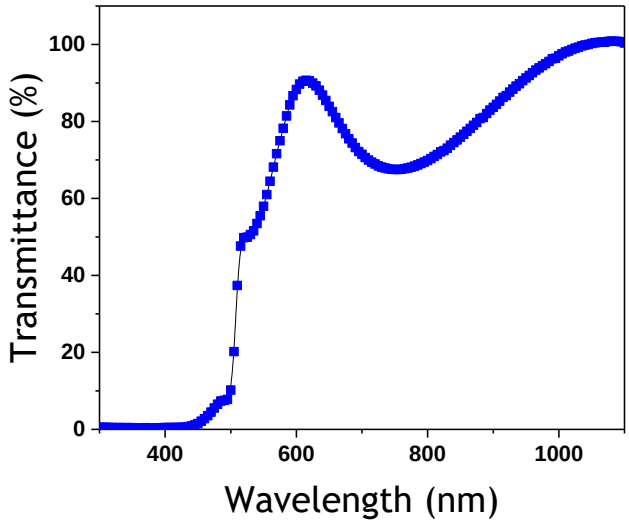

Figure 6-15: Transmittance spectrum of the thermal-evaporated PbI_2 thin film.

The optical properties including absorption coefficient, band gap, optical conductivity, optical constants and dielectric constants of the thin films were estimated and extracted from the transmittance spectra. **Figure 6-16** shows the absorption coefficient of PbI_2 and the respective band gap that was estimated by Tauc plot. Exponential decay of the absorption coefficient was observed with increasing wavelength. A higher absorption coefficient value was showed at the visible region, as high as 10^5 cm^{-1} corresponding to an onset of the direct interband transitions from the valence to conduction band [53], while the strength of absorption was decreased with increasing the wavelength (decreasing the photon energy) as most of electrons did not have sufficient energy to excite to the conducted level through its bandgap. The estimated direct band gap value was found to be 2.65 eV. The increase in the bandgap of the evaporated film in respect to the bandgap of the spin-coated films (~2.45 eV) may be attributed to the increase in the structural disorder of the atomic arrangement within the evaporated PbI_2 film, as it was observed from **XRD** data that the film was contained an amorphous and polycrystalline matrix. Such disorder structure in the evaporated film comparing to as-deposited film by spin coating technique was further investigated

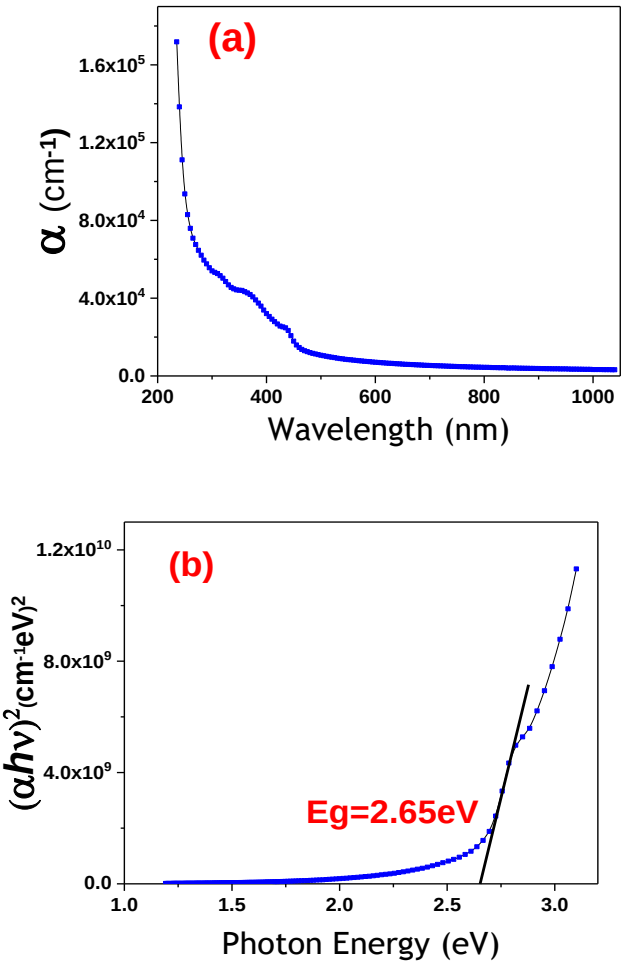

Figure 6-16: (a) the thermal-evaporated PbI_2 absorption coefficient and (b) its band gap extracted from Tauc plot.

The disordered grains/structures can produce deep defect levels near the conduction band minima which is governed by Urbach tail [54]. Therefore, tail localised states which are generated within the optical bandgap can be empirically analysed with the tail width by the following expression [54]

$$ln\,\alpha(v) = \frac{hv}{E_u} + C \qquad (6.14)$$

Eq. (**6.14**) is an exponential relation between the absorption coefficient (α) of the Urbach energy (E_u) and the photon energy (*hv*). It can be determined the E_u from the reciprocal slope of the linear part in the plotting curve between the logarithm of (α) versus (*hv*) as shown in **Figure** 6-17. It can be seen that from **Figure 6-17** the increase in the tail width (Urbach energy) for the evaporated film (**Figure 6-17 (b))** in contrast to the spin-coated film (**Figure 6-17 (a))** may be attributed to the

evaporated film has more an amorphous structure in nature. This result in a good agreement with the result that was obtained from XRD analysis.

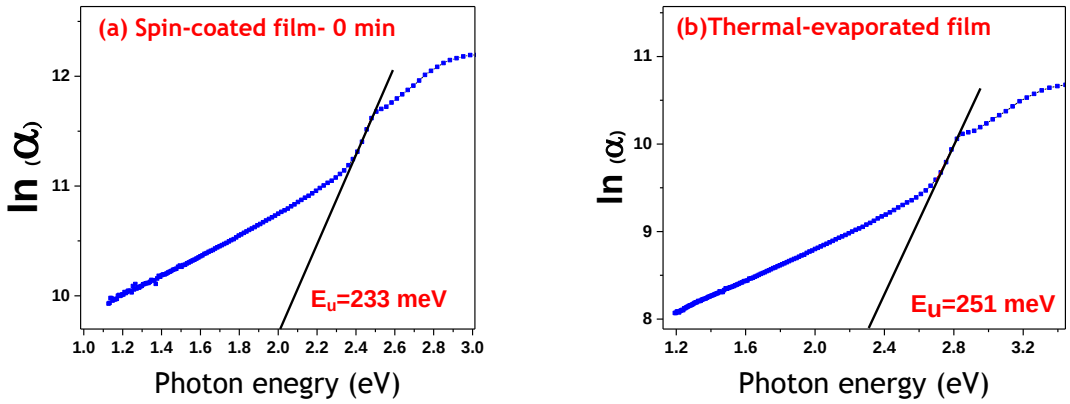

Figure 6-17: determination of the energy tail or Urbach energy (E_u) from the plot of ln (α) versus photon energy of as-deposited films by (a) spin-coating and (b) thermal-evaporation techniques.

The relationship between the optical conductivity and the photon energies is shown in **Figure 6-18**. It was obvious that the PbI_2 conductivity increased with the photon energy starting from the energy bandgap. A broad shoulder/band was observed at energy $2.75eV \leq E \leq 4.5eV$ which showed an exponential increase of the conductivity where the maximum optical conductivity was achieved at $1.2x10^{16}\ S^{-1}$. Then, the conductivity decreased for the photon energy higher than ~4.3 eV. This was argued to the fact that at energy higher than 4 eV the electrons tend to change the direction of momentum to enable their transitions to the excited level (CB).

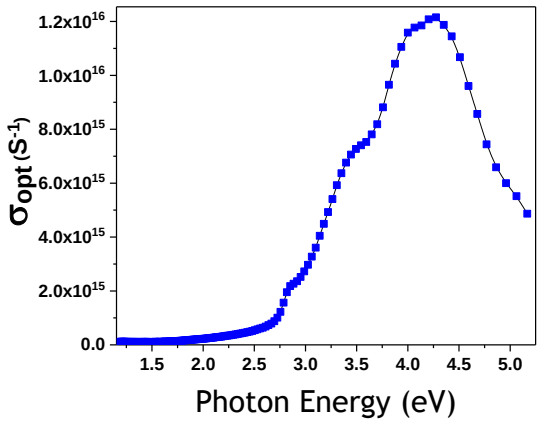

Figure 6-18: Optical conductivity of thermal-evaporated PbI_2 thin films versus photon energy.

The refractive index (n) and the extinction coefficient (k) for the evaporated film were extracted from its transmittance to understand the microscopic atomic interactions. **Figure 6-19** showed that the n and k dispersion curves that exhibit two kinds of dispersion (anomalous and normal) with respect of the wavelengths. At low wavelengths (λ < 520 nm), the anomalous dispersion region of n and k were shown where the energy of photons was equal or higher than the energy bandgap which produced electronic transitions [41, 42]. **Figure 6-19** showed that the conductivity was increased with the energy of photons starting from the bandgap of the film. A further increase of n and k at higher energies indicated more electronic transitions occurrence. The reason for the absence of the normal dispersion at lower wavelengths after the band edge could be a consequence of the absorption which was shown by the substrate at λ<300 nm. The maximum k value was found to be 0.13 which was much lower than the spin-coated film. The n value was increased from 1.2 to a maximum value of 10 that was higher than the film prepared by the spin-coating. On the other hand, the absorption decreased in the material at higher wavelengths/ lower energies (the infrared region), in which the values of n and k were decreased exponentially referring to the normal dispersion and absorption of some amount of photons at the grain boundaries.

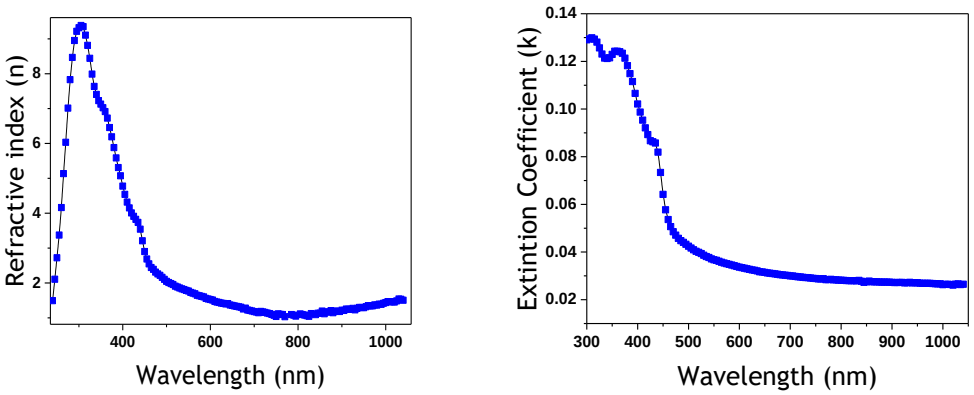

Figure 6-19: The refractive index (n) and extinction coefficient (k) in the function of wavelength for an evaporated PbI_2 thin film.

The interactions between electrons and photons at each wavelength can be described by the dielectric constants. The real and imaginary parts of the dielectric constant of the evaporated PbI_2 thin film were calculated (**Figure 6-20**). These results followed the same trend with the values of the real and

imaginary dielectric constants of 90 and 2.5, respectively. However, the real part had higher value than the reported value in the literature [47, 48].

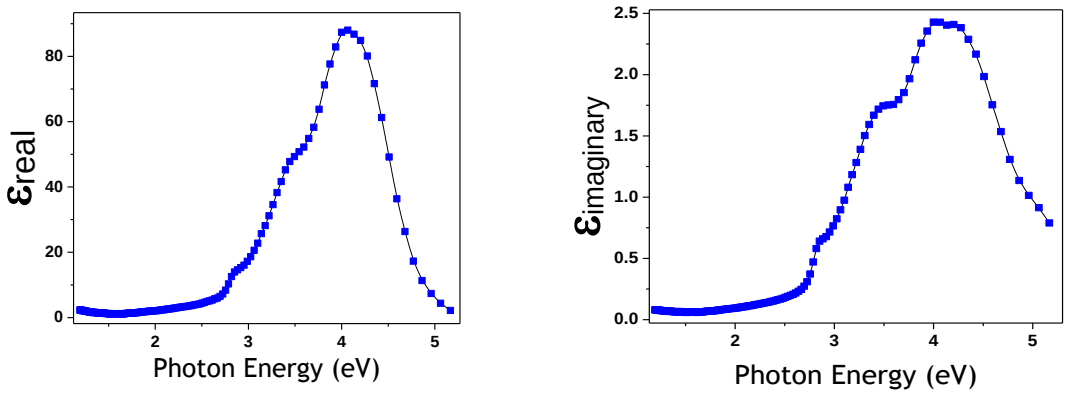

Figure 6-20: The dielectric constant (a) real and (b) imaginary in the function of photon energy for an evaporated PbI_2 thin film.

6.3 Summary

PbI_2 thin films were prepared by the spin-coating and the thermal evaporation techniques on glass and silicon substrates. In spin coating, a post-annealing step was required to extract the solvent (DMF) from the film. The 50nm films that were deposited by the spin-coating were annealed at 70 $^{\circ}$C under different time intervals. On the other hand, the 200 nm films were deposited by the thermal evaporation. The structural, morphological and optical properties of the spin-coated and evaporated films were investigated. The XRD measurement was showon that the deposited films were tended to grow along the c-axis. Bigger crystallite size and lower microstrain with the formation of amorphous and polycrystalline matrix were observed in the evaporated films. The density packed crystals growth in the spin-coated film was observed, while the plate-like grain structure with the present intergrain voids was observed in the evaporated films which might induce the intercalation of an organic compound into the lattice to form perovskite. The optical transmittance property of the two materials was measured using UV-VIS spectroscopy. The measurement allowed for the determination of other optical properties such as refractive index, optical conductivity, dielectric constants and dielectric loss. An increase in the bandgap of the evaporated film implied that, there was a direct correlation between the disordered structures of the atomic arrangement within the film having more amorphous behaviour in contrast to the spin-coated film. Understanding of the discrepancy in the properties of films which

were prepared by different methods (spin-coating and thermal evaporation) enabled to further comprehending of the effect of the film's nature on the subsequent deposition. The investigation carried out in this chapter was on the initial step of the perovskite materials deposition. The next chapter was dedicated to a study of the detailed properties of the resultant films "perovskite materials" that were deposited by the PECVD process.

References

[1] X. Zhu, Z. Wei, Y. Jin and A. Xiang, "Growth and characterization of a PbI2 single crystal used for gamma ray detectors," *Crystal research and technology,* vol 42, no 5, pp. 456-459, 2007.

[2] D. Bhavsar and K. Saraf, "Optical and structural properties of zn-doped lead iodide thin films," *Materials chemistry and physics,* vol 78, no 3, pp. 630-636, 2003.

[3] E. Lifshitz and L. Bykov, "Microwave modulated and thermal modulated photoluminescence studies of 2H-lead iodide," *The journal of physical chemistry,* vol 97, no 37, pp. 9288-9292, 1993.

[4] D. Edwards, J. Gier, K. Nelson and R. Roddick, "Spectral and directional thermal radiation characteristics of selective sufaces for solar collectors," *Solar energy,* vol 6, no 1, pp. 1-8, 1962.

[5] S. I. Mohammed, Y. Al-Douri, U. Hashim, N. Ahmed and R. Al-Gaashani, "Structural and optical properties of PbI2 nanostructures obtained using the thermal evaporation method," *Canadian journal of physics,* vol 91, no 10, pp. 826-832, 2013.

[6] M. Tubbs, "The optical properties and chemical decomposition of halides with layer structures. I. crystal structures, optical properties, and electronic structure," *Physica status solidi (b),* vol 49, no 1, pp. 11-50, 1972.

[7] M. Schieber, N. Zamoshchik, O. Khakhan and A. Zuck, "Structural changes during vapor-phase deposition of polycrystalline-PbI2 films," *Journal of crystal growth,* vol 310, no 13, pp. 3168-3173, 2008.

[8] D. Bi, S. Moon, L. Häggman, G. Boschloo, L. Yang, E. M. Johansson, M. K. Nazeeruddin, M. Grätzel and A. Hagfeldt, "Using a two-step deposition technique to prepare perovskite (CH 3 NH 3 PbI 3) for thin film solar cells based on ZrO 2 and TiO 2 mesostructures," *Rsc advances,* vol 3, no 41, pp. 18762-18766, 2013.

[9] K. Liang, D. B. Mitzi and M. T. Prikas, "Synthesis and characterization of organic-inorganic perovskite thin films prepared using a versatile two-step dipping technique," *Chemistry of materials,* vol 10, no 1, pp. 403-411, 1998.

[10] M. Shkir, H. Abbas and Z. R. Khan, "Effect of thickness on the structural, optical and electrical properties of thermally evaporated PbI 2 thin films," *Journal of physics and chemistry of solids,* vol 73, no 11, pp. 1309-1313, 2012.

[11] Z. Xinghua, Y. Dingyu, W. Zhaorong, S. Hui, W. Zhiguo and Z. Xiaotao, "Photoconductive properties of lead iodide films prepared by electron beam evaporation," *Journal of semiconductors,* vol 31, no 8, pp. 083002, 2010.

[12] D. Bhavsar and K. Saraf, "Optical and structural properties of zn-doped lead iodide thin films," *Materials chemistry and physics,* vol 78, no 3, pp. 630-636, 2003.

[13] S. Ito, S. Tanaka and H. Nishino, "Lead-halide perovskite solar cells by CH3NH3I dripping on PbI2–CH3NH3I–DMSO precursor layer for planar and porous structures using CuSCN hole-transporting material," *The journal of physical chemistry letters,* vol 6, no 5, pp. 881-886, 2015.

[14] F. Fu, L. Kranz, S. Yoon, J. Löckinger, T. Jäger, J. Perrenoud, T. Feurer, C. Gretener, S. Buecheler and A. N. Tiwari, "Controlled growth of PbI2 nanoplates for rapid preparation of CH3NH3PbI3 in planar perovskite solar cells," *Physica status solidi (a),* vol 212, no 12, pp. 2708-2717, 2015.

[15] Y. Wu, A. Islam, X. Yang, C. Qin, J. Liu, K. Zhang, W. Peng and L. Han, "Retarding the crystallization of PbI 2 for highly reproducible planar-structured perovskite solar cells via sequential deposition," *Energy & environmental science,* vol 7, no 9, pp. 2934-2938, 2014.

[16] T. Liu, Q. Hu, J. Wu, K. Chen, L. Zhao, F. Liu, C. Wang, H. Lu, S. Jia and T. Russell, "Mesoporous PbI2 scaffold for high-performance planar heterojunction perovskite solar cells," *Advanced energy materials,* vol 6, no 3, pp. 1501890, 2016.

[17] U. S. Waware and S. S. Umare, "Chemical synthesis, spectral characterization and electrical properties of poly (aniline-co-m-chloroaniline)," *Reactive and functional polymers,* vol 65, no 3, pp. 343-350, 2005.

[18] A. Wakamiya, M. Endo, T. Sasamori, N. Tokitoh, Y. Ogomi, S. Hayase and Y. Murata, "Reproducible fabrication of efficient perovskite-based solar cells: X-ray crystallographic studies on the formation of CH3NH3PbI3 layers," *Chemistry letters,* vol 43, no 5, pp. 711-713, 2014.

[19] H. Miyamae, Y. Numahata and M. Nagata, "The crystal structure of lead (II) iodide-dimethylsulphoxide (1/2), PbI2 (dmso) 2," *Chemistry letters,* vol 9, no 6, pp. 663-664, 1980.

[20] M. Monajjemi, M. Razavian, F. Mollaamin, F. Naderi and B. Honarparvar, "A theoretical thermochemical study of solute-solvent dielectric effects in the displacement of codon-anticodon base pairs," *Russian journal of physical chemistry A, focus on chemistry,* vol 82, no 13, pp. 2277-2285, 2008.

[21] H. Miyamae, Y. Numahata and M. Nagata, "The crystal structure of lead (II) iodide-dimethylsulphoxide (1/2), PbI2 (dmso) 2." *Chemistry letters,* no 6, pp. 663-664, 1980.

[22] Y. Wu, A. Islam, X. Yang, C. Qin, J. Liu, K. Zhang, W. Peng and L. Han, "Retarding the crystallization of PbI 2 for highly reproducible planar-structured perovskite solar cells via sequential deposition," *Energy & environmental science,* vol 7, no 9, pp. 2934-2938, 2014.

[23] A. Wakamiya, M. Endo, T. Sasamori, N. Tokitoh, Y. Ogomi, S. Hayase and Y. Murata, "Reproducible fabrication of efficient perovskite-based solar cells: X-ray crystallographic studies on the formation of CH3NH3PbI3 layers," *Chemistry letters,* vol 43, no 5, pp. 711-713, 2014.

[24] E. W. Jones, P. J. Holliman, A. Connell, M. L. Davies, J. Baker, R. J. Hobbs, S. Ghosh, L. Furnell, R. Anthony and C. Pleydell-Pearce, "A novel dimethylformamide (DMF) free bar-cast method to deposit organolead perovskite thin films with improved stability," *Chemical communications,* vol 52, no 23, pp. 4301-4304, 2016.

[25] Y. Peng, Y. Wu, L. Tang, J. Li, J. Xu, Y. Du, L. Huang, H. Cai, J. Ni and J. Zhang, "The influence of PbI 2 on characteristic of organic–inorganic hybrid perovskite thin films," *Model.numer.simul.mater.sci,* vol 7, pp. 04-47, 2017.

[26] P. Bindu and S. Thomas, "Estimation of lattice strain in ZnO nanoparticles: X-ray peak profile analysis," *Journal of theoretical and applied physics,* vol 8, no 4, pp. 123-134, 2014.

[27] B. Cullity and S. Stock, "Elements of X-ray diffraction, 3rd edn prentice hall," *New york*, pp. 174-177, 2001.

[28] W. Ostwald, "Studien über die bildung und umwandlung fester körper," *Zeitschrift für physikalische chemie*, vol 22, no 1, pp. 289-330, 1897.

[29] Y. Ren, X. Ding, Y. Wu, J. Zhu, T. Hayat, A. Alsaedi, Y. Xu, Z. Li, S. Yang and S. Dai, "Temperature-assisted rapid nucleation: A facile method to optimize the film morphology for perovskite solar cells," *Journal of materials chemistry A*, vol 5, no 38, pp. 20327-20333, 2017.

[30] X. Cao, L. Zhi, Y. Li, F. Fang, X. Cui, L. Ci, K. Ding and J. Wei, "Fabrication of perovskite films with large columnar grains via solvent-mediated ostwald ripening for efficient inverted perovskite solar cells," *ACS applied energy materials*, vol 1, no 2, pp. 868-875, 2018.

[31] G. Williamson and W. Hall, "X-ray line broadening from filed aluminium and wolfram," *Acta metallurgica*, vol 1, no 1, pp. 22-31, 1953.

[32] W.D. Callister and D.G. Rethwisch, *Materials science and engineering: An introduction*, Wiley New York, 2007.

[33] K. N. Manjunatha and S. Paul, "Investigation of optical properties of nickel oxide thin films deposited on different substrates," *Applied surface science*, vol 352, pp. 10-15, 2015.

[34] J. Robertson, "Electronic structure of SnS2, SnSe2, CdI2 and PbI2," *Journal of physics C: Solid state physics*, vol 12, no 22, pp. 4753, 1979.

[35] S. I. Mohammed, Y. Al-Douri, U. Hashim, N. Ahmed and R. Al-Gaashani, "Structural and optical properties of PbI2 nanostructures obtained using the thermal evaporation method," *Canadian journal of physics*, vol 91, no 10, pp. 826-832, 2013.

[36] D. Bhavsar and K. Saraf, "Optical and structural properties of zn-doped lead iodide thin films," *Materials chemistry and physics*, vol 78, no 3, pp. 630-636, 2003.

[37] T. Chaudhuri and H. Acharya, "Preparation of lead iodide films by iodination of chemically deposited lead sulphide films," *Materials research bulletin*, vol 17, no 3, pp. 279-286, 1982.

[38] Z. Zheng, A. Liu, S. Wang, Y. Wang, Z. Li, W. M. Lau and L. Zhang, "In situ growth of epitaxial lead iodide films composed of hexagonal single crystals," *Journal of materials chemistry*, vol 15, no 42, pp. 4555-4559, 2005.

[39] S. Tripathi, S. Gupta, F. Mustafa, N. Goyal and G. Saini, "Laser induced changes on a-Ga50Se50 thin films," *Journal of physics D: Applied physics*, vol 42, no 18, pp. 185404, 2009.

[40] T. K. Hamad, "Refractive index dispersion and analysis of the optical parameters of (PMMA/PVA) thin film," *Journal of al-nahrain university*, vol 16, no 3, pp. 164-170, 2013.

[41] R. N. Hall, "Electron-hole recombination in germanium," *Physical review*, vol 87, no 2, pp. 387, 1952.

[42] W. Shockley and W. Read Jr, "Statistics of the recombinations of holes and electrons," *Physical review*, vol 87, no 5, pp. 835, 1952.

[43] P. Yu, "M. cardona. fundamentals of semiconductors," *Physics and materials properties.springer*, 2005.

[44] P.Y. Yu and M. Cardona, *Fundamentals of semiconductors*, Springer, 2005.

[45] M. Tubbs, , "The optical properties and chemical decomposition of lead iodide," In *Proceedings of the royal society of london A: Mathematical, physical and engineering sciences*, 1964, pp. 566-585.

[46] A. Buckman, N. Hong and D. Wilson, "Large refractive-index change in PbI 2 films by photolysis at 150–180° C," *Josa*, vol 65, no 8, pp. 914-918, 1975.

[47] R. Clasen, P. Grosse, A. Krost, F. Levy, S. Marenkin, W. Richter, N. Ringelstein, R. Schmechel, G. Weiser and H. Werheit, "Non-tetrahedrally bonded elements and binary compounds I," *Landolt-bornstein, new series, group III*, vol 17, no Pt B, 1998.

[48] O. Madelung, *Semiconductors: Data handbook*, Springer Science & Business Media, 2012.

[49] E. Lee, "Simulation of the thin-film thickness distribution for an OLED thermal evaporation process," *Vacuum*, vol 83, no 5, pp. 848-852, 2009.

[50] F. Fu, L. Kranz, S. Yoon, J. Löckinger, T. Jäger, J. Perrenoud, T. Feurer, C. Gretener, S. Buecheler and A. N. Tiwari, "Controlled growth of PbI2 nanoplates for rapid preparation of CH3NH3PbI3 in planar perovskite solar cells," *Physica status solidi (a)*, vol 212, no 12, pp. 2708-2717, 2015.

[51] H. Agrawal, A. Vedeshwar and V.K. Saraswat, , "Growth and characterization of PbI2 thin films by vacuum thermal evaporation," In *Journal of nano research*, 2013, pp. 1-6.

[52] D. Bhavsar and K. Saraf, "Optical properties of lead iodide between 0.4946 and 6.185 eV," *Journal of materials science: Materials in electronics*, vol 14, no 4, pp. 195-198, 2003.

[53] A. Ahmad, S. Saq'an, B. Lahlouh, M. Hassan, A. Alsaad and H. El-Nasser, "Ellipsometric characterization of PbI2 thin film on glass," *Physica B: Condensed matter*, vol 404, no 1, pp. 1-6, 2009.

[54] F. Urbach, "The long-wavelength edge of photographic sensitivity and of the electronic absorption of solids," *Physical review*, vol 92, no 5, pp. 1324, 1953.

Chapter 7 PECVD Growth and Optimisation of Perovskite

7.1 Introduction

The previous chapter (chapter-6) was devoted to discuss the properties of PbI_2 thin films deposited by two different methods; spin-coating and thermal evaporated techniques; which It was termed as *the initial* deposition step of perovskite material. This chapter describes the second deposition step that was used to introduce the organic part ($CH_3NH_3^+$) onto PbI_2 thin film in order to synthesise perovskite material ($CH_3NH_3PbI_3$) using RF-PECVD reactor. To the best of our knowledge, this novel methodology to grow $CH_3NH_3PbI_3$ thin film has not been reported in any literature. Thus, it is vital to understand the growth dynamics and how the variation of PECVD growth parameters affects the structural, optical and electrical properties of the resultant films. Different characterisation techniques including XRD, UV-VIS, I-V were used in order to study the effect of this novel growth on the film properties. As it is known that the PECVD process is chemical process and all the thermodynamic parameters (such as temperature, pressure, molar concentration, average ion energy, etc) will have a strong influence on the properties of the deposited films. The effect of some of PECVD parameters that is discussed here includes:

- Variation in the substrate temperature.
- Variation in the RF- power.
- Variation in the chamber pressure.

7.2 PECVD Growth

The second step deposition, to realise perovskite material, was performed in a RF-PECVD reactor with methane (CH_4) and ammonia (NH_3) gases as the precursor source of CH_3^+ and NH_3^+ ions to induce the conversion of PbI_2 film into $CH_3NH_3PbI_3$ film. The gas flow rate of both gases was controlled by MFC to set the flow rate at 10 sccm and 20 sccm for CH_3 and NH_3 respectively, for all experiments. NH_3 gas concentration was chosen to be higher than the CH_4 gas to prevent the formation of carbon film [1]. It is reported that the use of ammonia gas has resulted in an increase in the deposition temperature boundary > 500 ℃ of carbon phase formation [2]. This means that at a low deposition temperature < 500 ℃, the amorphous carbon (a-C) and the weakly bonded carbon atoms as

well as the small graphitic fragments that present in the plasma, would be etched and possibly avoid the formation of graphene layers.

Using PECVD tool, the effect of different mixture of these gases (CH_4/ NH_3) was studied on the properties of amorphous hydrogenated carbon-nitrogen (a-C(N):H) films [3, 4] and nitrogen-doped amorphous hydrogenated carbon (a-C:H(N)) films [1, 5]. However, this is the first study using this mixture as a source of the organic part ($CH_3NH_3^+$) for synthesising such perovskite since PECVD has the ability to generate highly reactive ions (e.g. CH_m^+ and NH_m^+) and free radicals (e.g. CH_m^0 and NH_m^0) of the sources that are required to convert PbI_2 thin films into perovskite material ($CH_3NH_3PbI_3$). The likely scheme of producing perovskite materials, using PECVD technique, is shown in Figure 7-1. The energy supplied by the RF power will lead to highly reactive ions generated from the collisions between high energetic, electrons and the molecules of CH_4 and NH_3 that may result in a production of the primary ions, which include CH_4^+, CH_3^+, CH_2^+, and NH_3^+, NH_2^+, NH^+ [6]. As a consequence of a succession of reactions between the primary ions and neutral species, secondary ions would be formed, which in turn react with each other to form other ions (see **chapter 4**, section 4.2.2.2.b) [6].

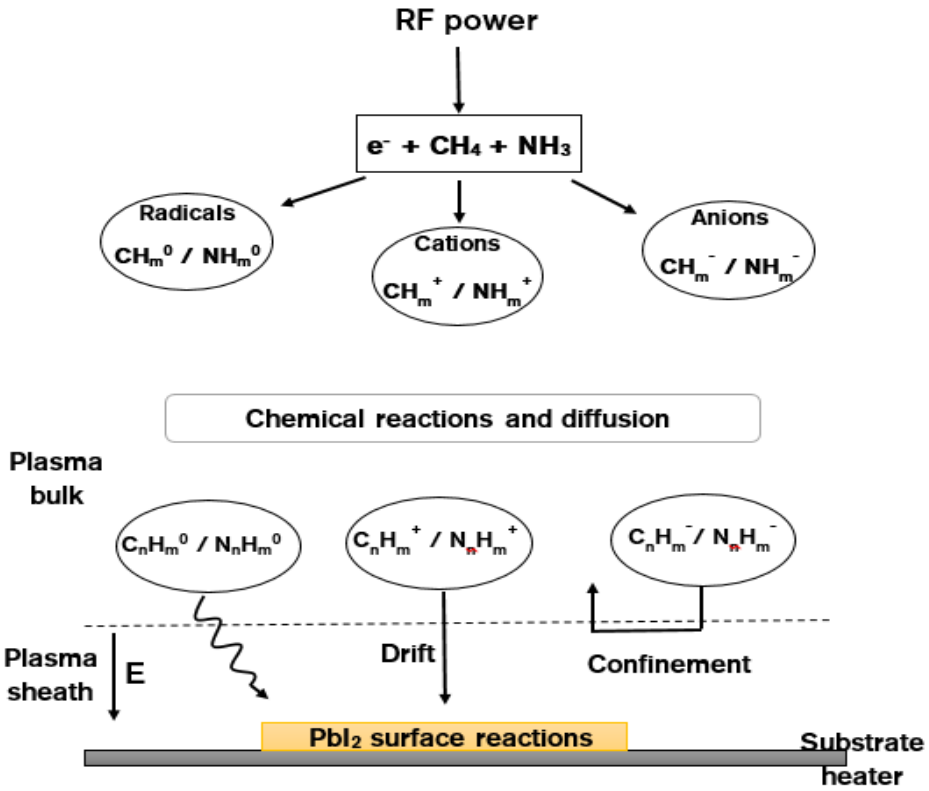

Figure 7-1: schematic of the predicted processes occurring during convert pbi_2 thin film into perovskite via reacting with a CH_4 / NH_3 discharge.

To simplify the plasma chemistry process that may occur when PbI_2 thin film is exposed to a CH_4 / NH_3 discharge, the reactions that are taken place can be divided into two processes:

- The chemical chamber reactions (electron-molecule reactions such as excitation, dissociation, and ionisation (see **chapter 4**)).
- The chemical surface reactions (absorption, desorption, etching/sputtering).

In the PECVD chamber, the reaction commences once the gases are introduced into the PECVD reactor and exposed to the RF power (**Figure 7-1**). Neutral radicals and both positive and negative ions are produced by a plenty of electron-molecule collisions. On the first half-cycle of the field, the positively charged electrode attracts more electrons, while there is an attraction of the positive ions at the negatively charged electrode. On the second half-cycle, the reversal of the polarity of the electrodes is established which results in attracting electrons to the positively charged electrode and repelling the positive ions. The continuous bombardment of the negative charges on the electrodes and the wall of the chamber in each subsequent half-cycle leads to a continuous repulsion of further negative flux. Thus, there is an attraction of positive ions [7]. As a result, the radical species are diffused into the PbI_2 surface, whilst the negative ions are confined in the bulk plasma leading to the recombination of these negatively charged ions with the positively charged radicals and thus forming small clusters. In addition, due to the negative potential of the substrate surface relative to the plasma, the positive ions are accelerated towards the PbI_2 surface by the sheath plasma potential created at the plasma-PbI_2 surface interface [7].

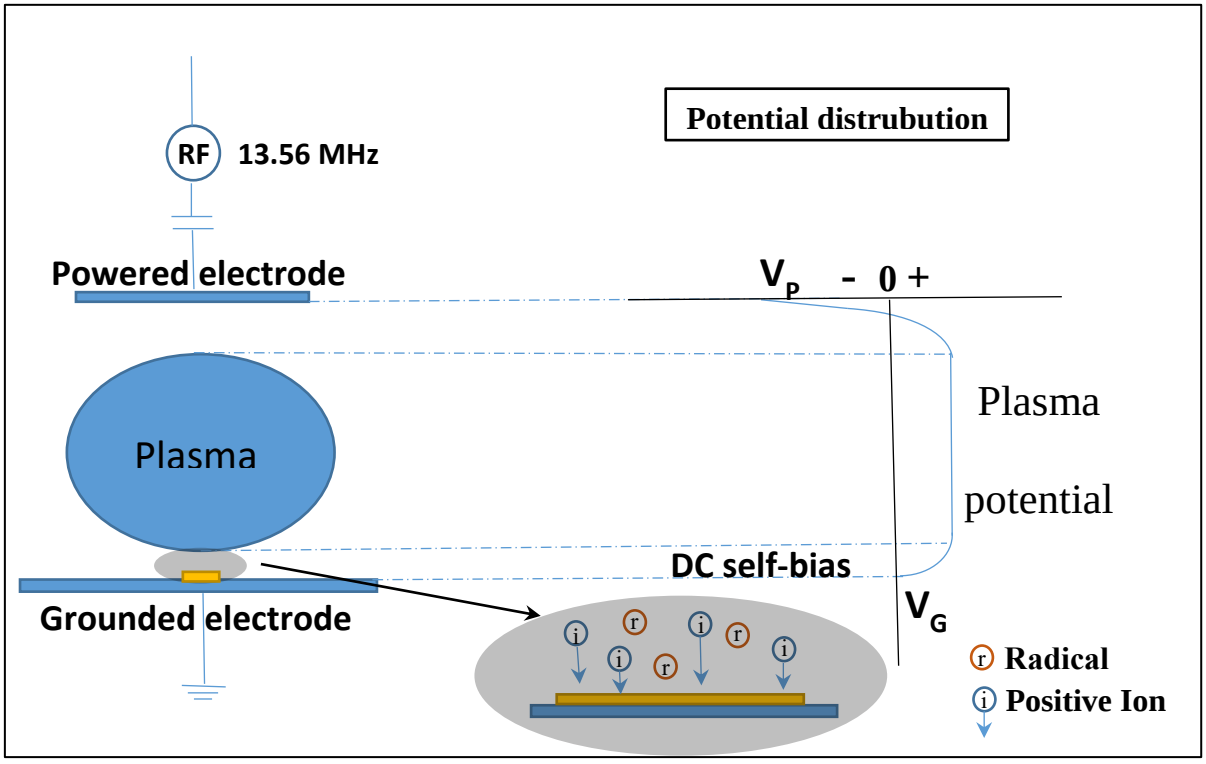

Figure 7-2: Schematic diagram of the capacitively-coupled RF-PECVD geometry where a blocking capacitor is used with two electrodes of different areas, together with presenting the developed potential distribution.

The creation of the sheaths near the two electrodes with a negative self-bias relative to the plasma is due to the variety of the charge distributions and their relative electric field between the plasma bulk and the surrounding surfaces as was explained in **Chapter 4**. It is worthy to mention that the potential distribution across the sheaths is nonsymmetric because of the grounded electrode has a bigger area causing the powered electrode to have much more negativity (**Figure 7-2**). However, the plasma is leaving at a higher potential than both electrodes due to the fast diffusion of electrons out of the plasma than ions as shown in **Figure 7-2**. The asymmetry of the PECVD system leads to minimising the bombardment effect of ions at the substrate surface.

Surface reactions have a significant influence on the plasma chemistry and the thin film growth. The variety of the surface chemistry in this study is strongly depending on the morphology, temperature of the PbI_2 surface and the energy of the incoming particles. The heating of the substrate surface is not only the source of its temperature but also the inner parameters such as an energy flux resulting from a particle bombardment as well as the chemical surface reactions and the heat radiation which play a role in the surface thermal energy [8]. The resultant substrate temperature has a great influence on an elementary process such as adsorption, desorption, and diffusion as well as other chemical reactions that might have caused sputtering of PbI_2 film and/or the growing/converting film [9]. In view of this

and for the sake of ease of representation, it is assumed that the positively charged ion of CH_3^+ or NH_3^+ is accelerated towards the PbI_2 thin film. The basic reactions of such ions with surfaces may occur as it is illustrated in **Figure 7-3**.

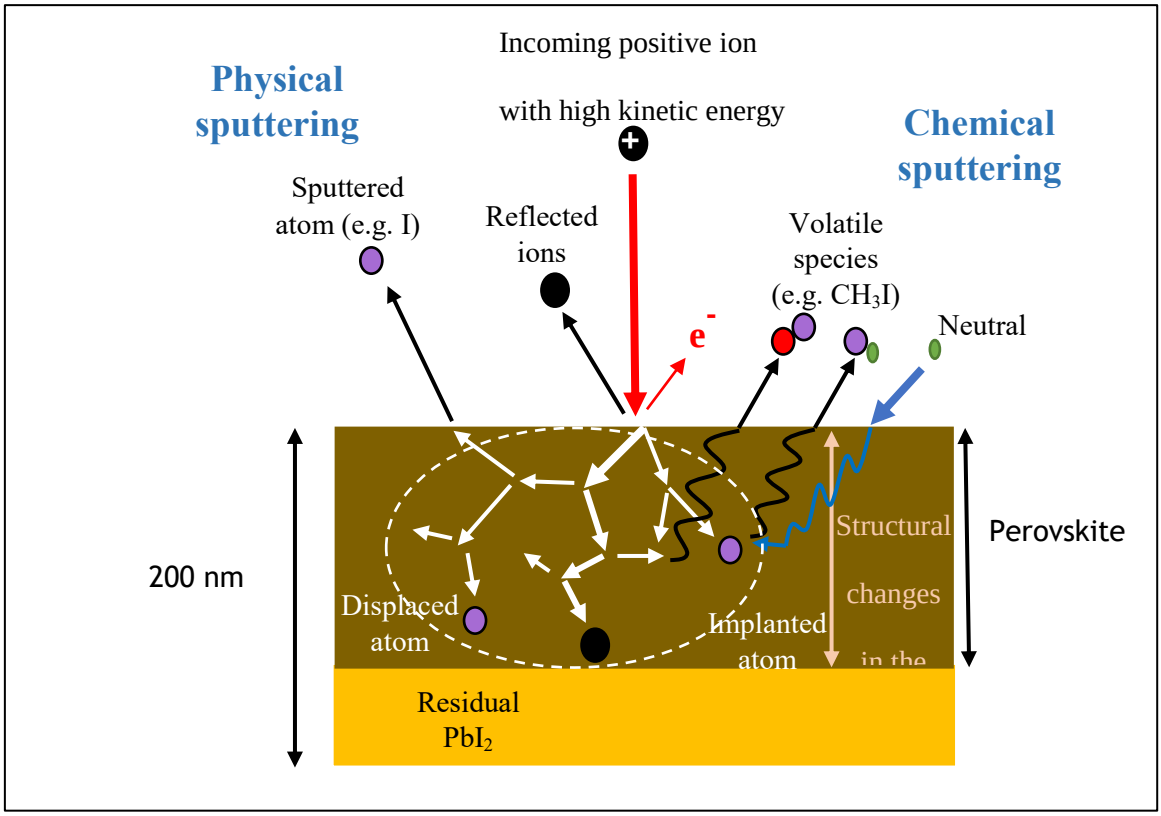

Figure 7-3: Schematic of surface reaction of energetic positive ions and neutral species with PbI_2 thin film.

The ion is accelerated across the potential that is built up between plasma and electrode (sheath region) toward the surface of PbI_2 thin film gaining a substantial amount of kinetic energy from the sheath potential. A consequence is that when the ion collides with the surface, it is neutralised by emitting secondary electron which serves as a source for sustaining the plasma. In addition, the ion energy is transferred to the lattice of PbI_2 crystals in two ways; **(1)** electron loss- occurs in which electronic collisions are taken place through ion interactions with the PbI_2 electrons, causing an excitation and an ionisation. **(2)** nuclear loss- occurs when the incoming ion interacts with the lattice atoms. However, the most important surface reaction that results from the impinging ions is the nuclear loss since the electron loss is much smaller [10]. In the nuclear loss, the transfer of ion's energy into the lattice can be occurred through collision cascades of moving lattice atoms. Such cascades can promote chemical reactions by undergoing a number of reactions such as radiation-

enhanced diffusion of implanted ions, backscattering of the incident ion, a bond breakage and an atom displacement causing a lattice damage as well as sputtering.

Two kinds of sputtering can occur; **(1)** physical- occurs in which the momentum transformation takes place between the incoming ion and surface atom during the collision cascade. According to the energy and momentum conservation law, this leads to the transformation of ion energy to a surface atom. If the gained energy is exceeding the atom surface binding energy, the atom will be sputtered from the surface and created dangling bonds which serve as preferred chemisorption/adsorption sites (defect site) for other incoming species that is, in turn, contributed to the film growth. **(2)** chemical- results in the formation of a volatile species from the deposited material. This type of sputtering will be formed when the incoming ion or incident reactive neutral particle interacts with the atom below the surface (within the film). In such case, the reacted species needs initially to diffuse to the film surface and then leave the film. These volatile species can be either generated by ion-neutral reaction when the ion is reacted with neighbouring displaced atoms (for instance CH_3^+ ion recombines with iodine atom producing CH_3I that releases from the film [11]) or via the reaction of an incident neutral particles with the dangling bonds (defect sites), which were generated by collision cascade on the PbI_2 surface and within the film [12]. These ion-neutral reactions are exploited either in an anisotropic etching which was observed in this study when high RF power densities (44, 55 mW/cm) and low pressures (250-500 mTorr) were applied or in an ion-assisted film growth when these sputtered atoms redeposit the thin film.

The transfer of ion's momentum to the film is another important process taking place during ion/surface interaction. This process can cause heating and generation of defects in the film surface. A consequence is that it would enhance self-diffusion or mobility of an adatom on a surface (surface migration) which is an important concept in the perovskite phase formation.

The reaction mechanism of the neutral particles/ PbI_2 surface can occur in different ways than what can occur in high energetic ions/ PbI_2 surface reaction, as shown in **Figure 7-4**, due to the low kinetic energy of neutral particles.

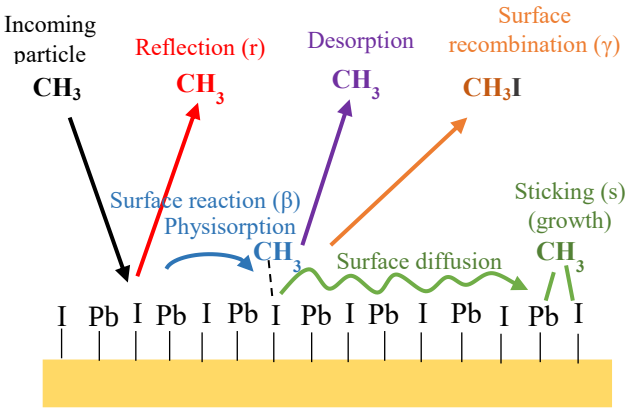

Figure 7-4: Schematic of the interactions between the one neutral species (CH_3) and the PbI_2 thin film during PECVD process.

These neutral particles involve those particles which were created by the chemical reactions in the background gaseous and the etched products (sputtered atoms and volatile species; resulted from the ion-neutral reactions) [8]. This neutral particle may be physiosorbed, chemosorbed or reflected from the surface with a surface reaction probability (β); $\beta = \gamma + s = 1 - r$. The following reaction probabilities (γ, s, r) may occur [8]:

- The probability of recombination (γ) (physisorption) at the surface and hence the production of volatile species such as CH_3I, HI.
- The probability of sticking (s) by the formation of a chemical bond with the surface (chemisorption) that is incorporated into the film growth.
- The probability of reflection (r) after impinging onto the substrate surface and reflecting back to the bulk plasma

In this study, three main parameters were varied, including the substrate temperature, the chamber pressure, and the RF-power towards finding the optimum parameters for an effective conversion of PbI_2 to $CH_3NH_3PbI_3$. The effect of each parameter, in turn, with the others held constant on the physical structure, optical and electrical properties of the growth has been investigated through methods described in **Chapter 5**. The following subsections discuss separately the effect of the PECVD parameters on the resultant films.

7.3 Effect of Deposition Parameters on PbI_2 Thin Films

In chapter 6, the properties of two sets of PbI_2 thin films; spin-coated films and thermal-evaporated films were investigated. The difficulty encountered with the spin-coating technique was that control of the film thickness and uniformity due to most of the liquid precursor was ejected off the substrate resulted in the formation of the inhomogeneous film with ultrathin thickness. This problem made this technique an inappropriate to use where the layer thickness required more than 50 nm. And, needless to say, a uniform film is crucial to grow the $MAPbI_3$ perovskite material. A thicker layer of PbI_2 of 200 nm was required to achieve the growth of perovskite thin film as proposed in the literature [13, 14]. Therefore, thermal-evaporated PbI_2 thin films might be a potential candidate for the growth of perovskite films.

One of the fundamental steps in the PECVD process towards producing $MAPbI_3$ perovskite material with controllable morphology, structural properties and compositions is a growth temperature. Although the annealing temperature of the PbI_2 films promotes/induces the reactions between the organic ions and the molecules of PbI_2, it also has a profound effect on the microstructure of the resultant film as well as on the PbI_2 stability [15-17]. Therefore, prior to investigating the possibility of growing perovskite material by RF-PECVD technique at different substrate temperatures, it is vital to understand PbI_2 decomposition behaviour as a function of temperature.

The study of the thermal stability of PbI_2 material is inherently important to avoid its decomposition. The information about the decomposition temperature for PbI_2 material can be obtained via thermogravimetric analyses (TGA). The TGA thermogram curve, as shown in **Figure 7-5**, was obtained under continuous flowing of nitrogen at a flow rate of 20 mL/min with a steady constant heating rate of 20^{o}/min for a range of temperatures between a minimum of 30 ℃ to a maximum of 700 ℃. It can be seen from **Figure 7-5** that PbI_2 decomposes in a single step. A noticeable weight loss at above 400 ℃ corresponds to the volatilisation of the iodine gas phase with the complete decomposition to Pb metal [18] as depicted in the following equation:

$$\boldsymbol{PbI_2 \xrightarrow{\Delta} Pb(s) + I_2(g) \uparrow} \qquad \textbf{(7. 1)}$$

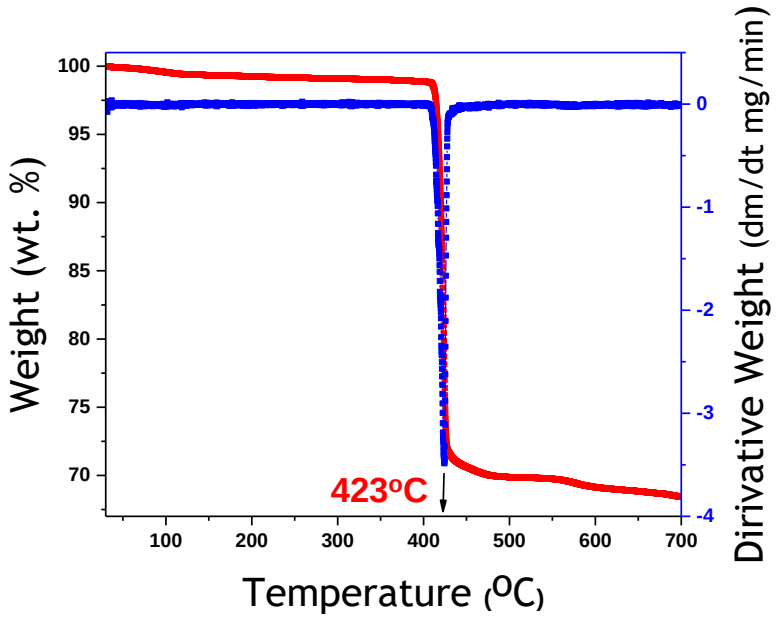

Figure 7-5: TGA curve for PbI_2.

During a RF-PECVD process, the required temperature for the growth process is not only provided by the external heating source, but the energy transferred from the ions bombardment also promotes further heat which elevates the substrate temperature. Therefore, this study was carried out at substrate temperatures of ≤ 150 ℃ suppling from a Honeywell temperature controller which was attached to the PECVD reactor.

Since this growth method was being firstly utilised for the perovskite growth, the extensive investigations have been conducted. These investigations including studying the effect of the variation in the substrate temperatures on the growth as well as the chamber pressure and RF- power. The following sections evaluate the effects of individual process variables on the growth properties, physically, optically and electrically.

7.3.1 Effect of the Variation in the Substrate Temperature

One of the most important parameters affecting the conversion of PbI_2 thin films to perovskite material is the temperature of the initial layer during the deposition. Diffusion of organic cation into PbI_2 is mainly governed by the substrate temperature [16, 19].

In order to evaluate the influence of the temperature on the growth, PbI_2 thin films were annealed at five different temperatures between 50°C to 150°C. Other PECVD parameters that were kept a constant were presented in **Table 7.1** and the films were resulted from these experiments can be seen in **Figure 7-6**.

Table 7.1: PECVD parameters were used to study the effect of the variation in the substrate temperatures.

RF- power density (mW/ cm^2)	Chamber pressure (mTorr)	CH_4 flow rate (sccm)	NH_3 flow rate (sccm)	Deposition duration (min)
22	1000	10	20	60

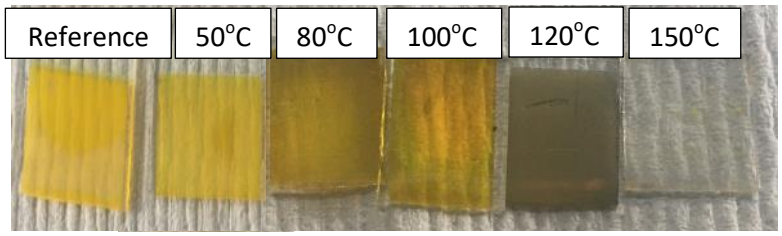

Figure 7-6: An optical image of grown films deposited at a range of temperatures.

It is evident from the image that the temperature has an important influence on the growth obtained at temperatures of 50℃ -120℃ or etching film (observed at 150℃). It is noticeable from the above image that the colour was changed indicating that a reaction between the PbI_2 thin films and the energetic organic ions created by plasma was taken place during the deposition.

7.3.1.1 Structural Characterisation

To investigate the crystallinity of the grown films and the effect of a variation of the temperatures on their microstructures, X-ray diffraction analysis of these samples was performed. The samples were prepared on 200-nm-thickness of PbI_2 coated glass substrates. The XRD pattern of samples can be seen in **Figure 7-7** which confirms the chemical and structural changes over a range of temperatures (50℃, 80℃, 100℃, 120℃, 150℃) were occurred.

It can be seen from the XRD data, the sample was deposited at 50℃ (**Figure 7-7** (a)) did not show a significant difference, however with raising the temperature, some new peaks were appeared. At 80℃ (**Figure 7-7** (b)), the intensity of the PbI_2 peaks increased, which was attributed to an increase in the

crystallisation and grain size of the partly amorphous PbI_2 film, caused by the thermal treatment [20]. Moreover, there are clear peaks of (004) and (220) splitting from (200) peak of the perovskite cubic phase, as it can be seen in the inset magnified plot in **Figure 7-7** (b), which confirms that this sample possess a tetragonal structure which is most critical to a solar cell operation [21, 22]. The XRD pattern of a deposited sample at 100℃ (**Figure 7-7** (c)) shows the main characteristic peaks of perovskite at ~ 14.2^o, ~ 28.1^o and ~ 28.7^o which are corresponding to the (110). (004) and (220) diffraction planes of tetragonal $CH_3NH_3PbI_3$ crystals [23, 24]. Apart from the perovskite, the PbI_2 crystalline phase was still presented. Moreover, an increase in the intensity of the characteristic peak of PbI_2 was noticed for the temperature range from 50 to 120℃, confirming an increase in the amounts of excess PbI_2 that does not involve in the reaction [25]. It can be indicated that PbI_2 formed a separate crystalline phase instead of being incorporated in the perovskite structure [25]. The reason for that could be (i) due to the duration of PECVD process and/or the substrate temperature were not enough, which undermined the incomplete nature of the reaction [26, 27] or (ii) due to the reaction temperature and/or the exposure time to plasma slightly longer than the required time to complete the conversion into perovskite material, which results in the formation phase of perovskite may decompose into PbI_2 [28, 29]. To find out the real issue, a further increase in the substrate temperature was suggested, while keeping the deposition time a constant at 60 min. Remarkably, the perovskite formation was destroyed by a further increases in the substrate temperature to 120℃ (**Figure 7-7** (d)) and it has been pointed out that diffraction peaks of metallic Pb have appeared in the film [30]. The suggestion is that at such high temperature (120℃) some of the iodine atoms were etched from the surface after the breakage of the Pb - I bonds. This could be due to the fact that an ion bombardment on the substrate surface provides an extra energy, making the Pb - I bond more loosely and easy to break. Therefore, breaking the chemical bond of Pb – I with the aid of energy transferred from those ions together with the elevation of the substrate temperature result in etching of the iodine atoms and leaving behind the Pb atoms. PbI_2 is being fully etched from the substrate surface at higher temperature (150℃), resulting in no material left on the glass substrate, hence preventing the perovskite growth (**Figure 7-7** (e)) and this is observed in the **Figure 7-6**.

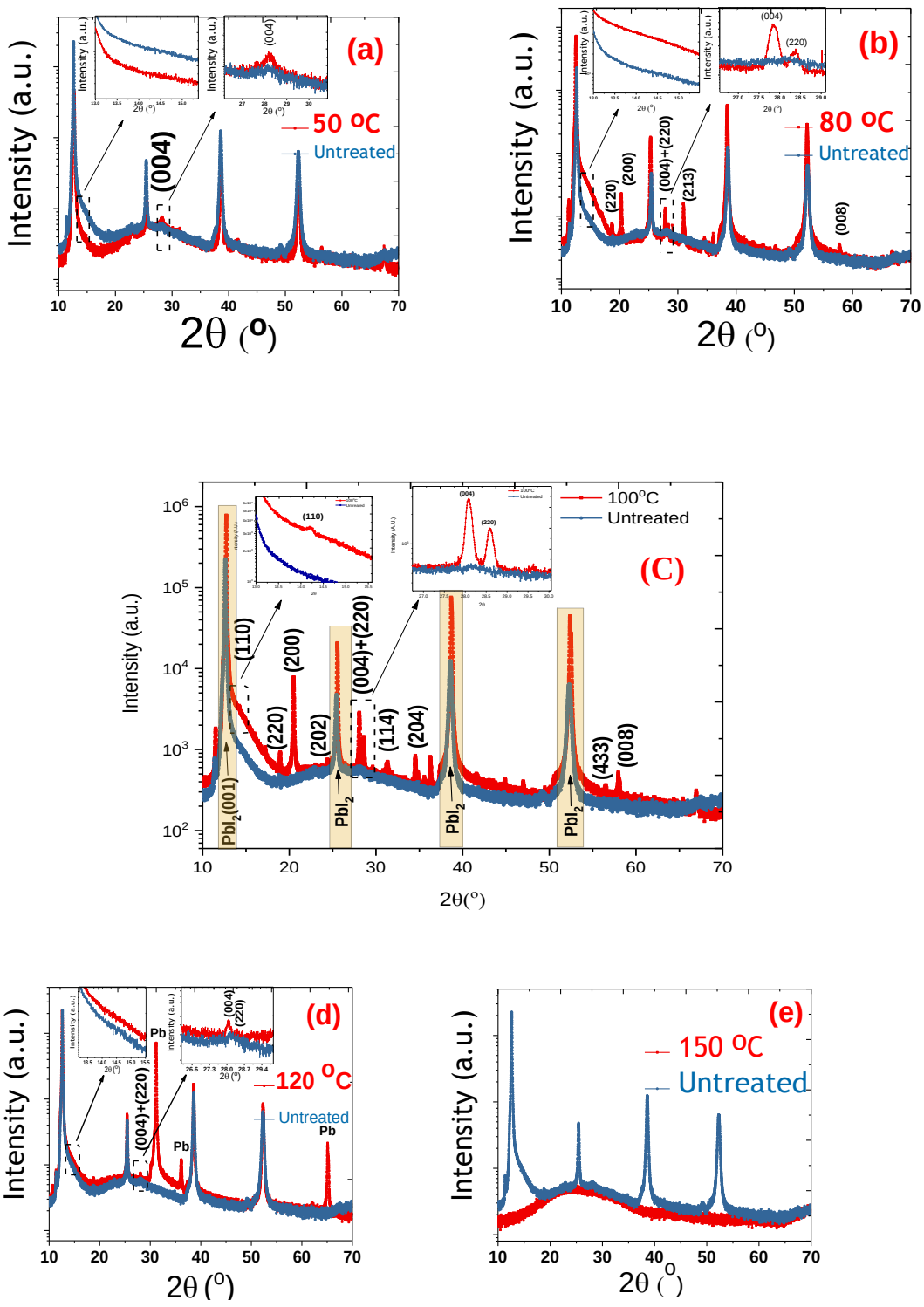

Figure 7-7: The XRD peaks of RF-PECVD growth samples deposited at different substrate tempreatures; (a) at 50°C (b) at 80°C (c) at 100°C (d) at 120°C and (e) at 150°C. The inset graphs is magnifica of the main peaks of perovskite.

Another observation noticed from XRD data (**Figure 7-7**) is that the (001) reflection peak of PbI_2 became narrow for the deposited sample at 50℃, which indicates that the reaction commences with an increase in PbI_2 crystallinity. Whereas, at a higher temperatures >50 ℃, the width of (001) reflected peak became broadened due to the consumption of the crystalline PbI_2 in the formation of perovskite [31]. A similar observation is consistent with the sequential deposition whereas this phenomenon was also noticed from photoluminescence (PL) imaging concluding that in such two-step deposition protocols the initial step occurrence is PbI_2 crystallisation before the diffusion of the organic ions into PbI_2 structure to commence their intercalation [31- 34].

7.3.1.2 Optical Characterisation

An additional analysis was necessary to reveal the influence of the substrate temperatures and the excess PbI_2 alongside the perovskite. Optical properties of the deposited films were assessed by UV-VIS spectroscopy and the absorption spectra presented in **Figure 7-8**. It can be observed from the absorption spectrum of grown samples at different substrate temperatures, in particular for those treated at a temperature range below 120 ℃, the presence of intensity absorption bands at low wavelengths (< 500 nm) that was matching with the identical absorption spectral features exhibited by PbI_2 film. This behaviour can be linked to the existence of complexes of [Pb_x^{n-}] that did not react with precursor ions or the existence of PbI_2 phase which segregated within the growth films [35], and this is in a good agreement with XRD data. The variation in the absorption intensity in particular wavelength region (< 500 nm) was reflected from a different amount of excess PbI_2 content in the film. For instance, the XRD of the grown film subjected to 80℃ showed an increase in the crystallinity of PbI_2 which was reflected by the optical properties by presenting a higher level of an absorption in the region below 500 nm. However, for the sample deposited at 120℃, it was shown a decrease in the absorption due to the formation of metallic Pb after the reduction of PbI_2. The presence of Pb correlates with the significant density of states above the valence band maximum and close to a fermi level that has a detrimental impact upon the optoelectronic properties of the thin film [36]. Moreover, the observation of a distinct hump around 500 nm was attributed to a high Pb precursor concentration [37]. In addition, a deviation in the absorption slopes was observed above the band edge that could appear from strong light scattering originating from the metallic nature. For the sample treated at 150 ℃, no absorption was present, as expected. Therefore, this behaviour was assigned to glass material, which was also in agreement with XRD data. It was worthy to mention that optical analysis revealed the predominant absence of the optical absorption onset of the perovskite material which was expected to be at ~750 nm although the presence of the perovskite diffraction peaks in the XRD data. It was suggested that the presence of PbI_2 impurities can affect the optoelectronic response of the perovskite

material, whereas the electronic structure of $(PbI_3)^-$ cage is likely to have the contribution to the excitonic properties of $CH_3NH_3PbI_3$ [22].

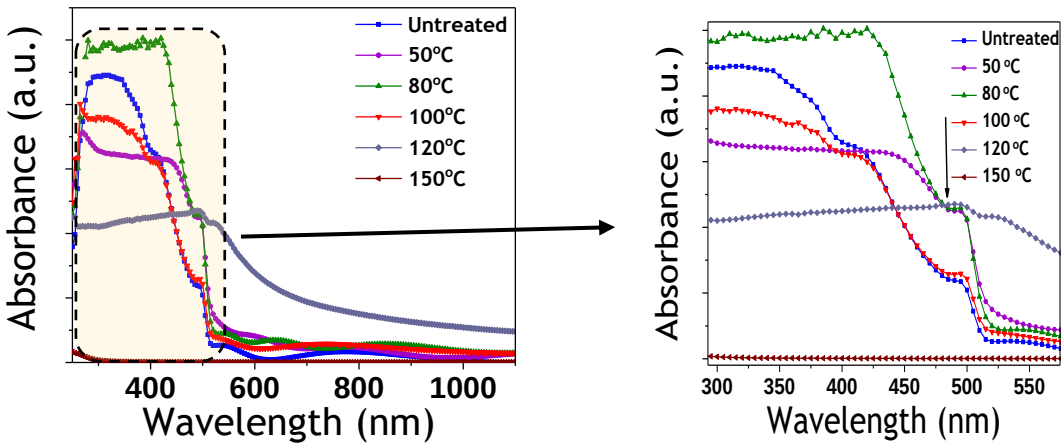

Figure 7-8: The absorption spectra of thermal evaporated PbI_2 thin film (untreated) and the PECVD growth samples deposited at different temperatures.

To determine an optical energy bandgap, the differential method was used instead of using the Tauc method. To avoid the errors that can be added in Tauc plot which could be produced from the fitting line in the line region of the $(\alpha h\nu)^2$ vs photon energy. Moreover, it was suggested that the derivative method is a more precise method when dealing with nanomaterials [38, 39]. In this method, at $E_{ph} = E_g$ a minimum photons energy should be recorded [38]. Once this condition is occurred, a spike towards negative infinity should be seen determining the energy bandgap of a substance. Employing this method (**Figure 7-9**), the energy bandgap of PbI_2 film (untreated) was found to be ~2.44 eV. Films deposited at 50, 80, and 100 ℃ were showed a slight reduction (2.43 eV) compared to that one of PbI_2. However, the optical energy bandgaps of the samples deposited at elevated temperatures above 100 ℃ were not corresponding to either PbI_2 or perovskite. These features were due to the presence of metallic Pb [40], which can be predicted from the absorption spectra and XRD results.

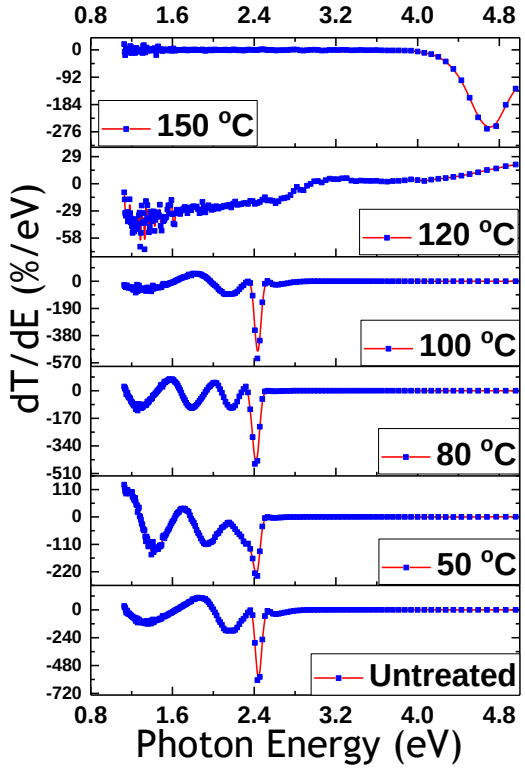

Figure 7-9: the energy bandgap plots determined from the derivative of transmittance with respect to photon energy for the samples grown at different substrate temperatures. (the peak observed for the top curve at 150°C corresponding to the glass substrate due to the film being etced away).

7.3.1.3 Electrical Characterisation

As a final point, it was aimed to understand whether the variation of the substrate temperatures and the unreacted PbI_2 still affect the electrical properties of the growth thin films. To allow the conductivity measurement of the films to be compared, a top electrode contact (Aluminium) was deposited to approximately the same thickness (~ 100 nm) and at the same deposition rate and pressure (~ 3 nm/s) at the ~ $5x10^{-6}$ mbar, respectively. Since the gap cell length can result in the variations in the electrical properties, all results presented were taken from the 100 µm gap cell.

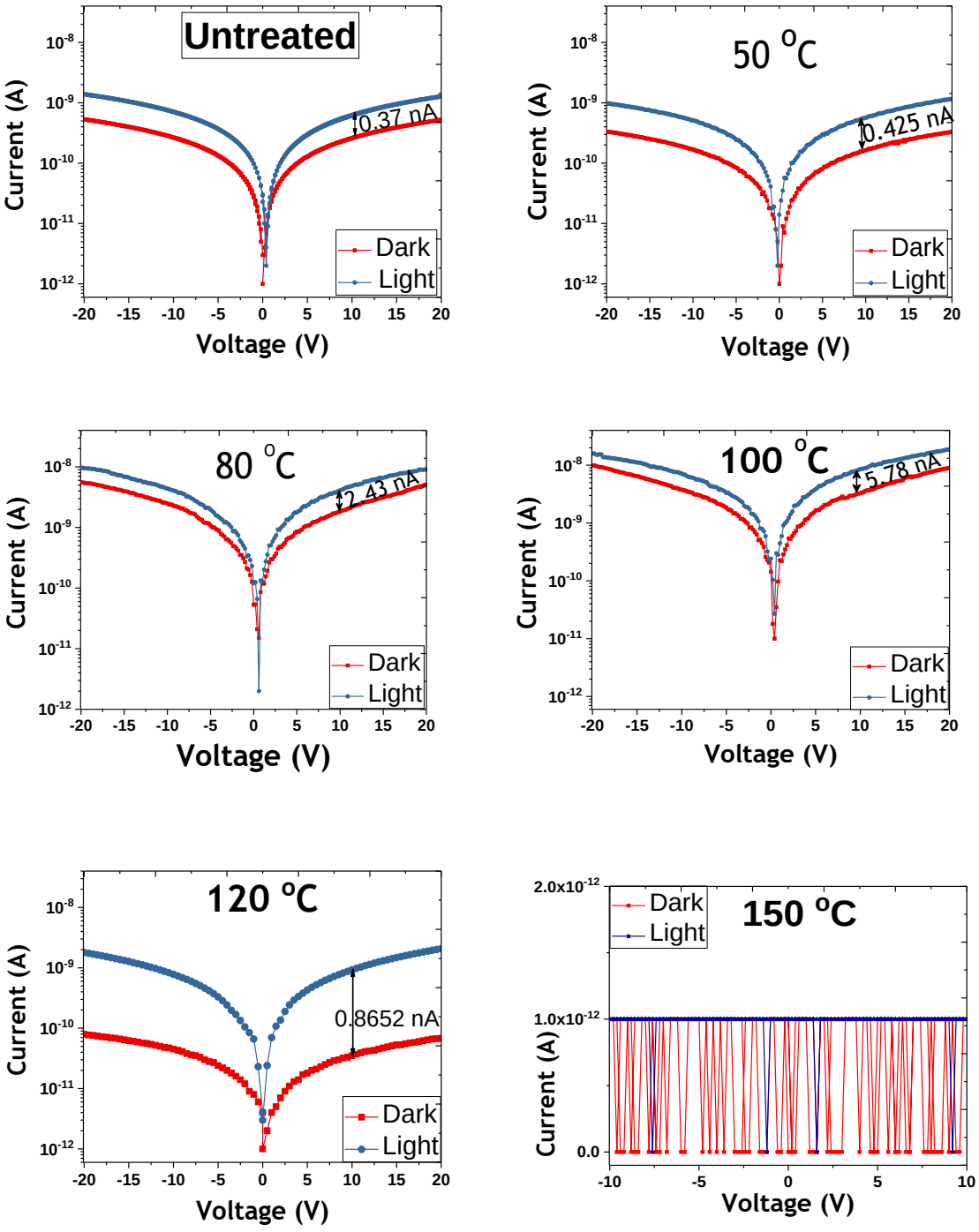

Figure 7-10: Photo- and dark conductivity measurements of the growth films at different substrate temperatures.

The effect of the variation of the substrate temperatures on the photo- and dark current of the PECVD growth samples was illustrated in **Figure 7-10**. For an easy data presentation, only one current value

of the I-V plots was selected (10V) as presented in **Figure 7-11.** An increase in the current of the films was observed when the films were illuminated under a xenon light source as compared to the dark conductivity, confirming that these films possess a semiconductor nature, except the film which was prepared at 150 ℃. However, the variation in the photo-current and dark-current were consistent with the XRD results that the growth was started with the crystallisation of PbI_2 followed by intercalation of the organic ions at which the perovskite was formed [31- 33]. Essentially, it means that the increased PbI_2 crystallinity observing at 80 ℃, in XRD data, results in an increase in the photo-current compared to the untreated sample. Whereas at 100 ℃ a further increasing was noticed, which could be attributed to an embedded perovskite phase in the grown film. However, the considerable amount of PbI_2 within the film still influenced the photoresponsivity [41]. That was followed by a reduction in the current at the film deposited at 120 ℃ due to the presence of a high concentration of Pb since it could act as traps for the extraction of the electrons [37]. At 150 ℃, I-V behaviour of the sample resembled an insulator (glass) behaviour, suggesting that the film was etched almost completely from the glass substrate and this data was supported the conclusions of the XRD data and the optical properties. Having considered these analyses, 100 ℃ was considered as the optimum substrate temperature and was used for a further optimisation.

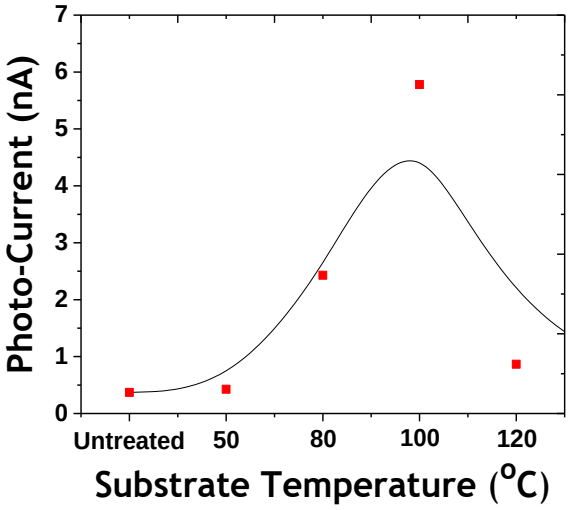

Figure 7-11: The change in photo- and dark- currents for films grown as a function of different substrate temperatures (this data was taken at fixed voltage = 10V).

7.3.2 Effect of the Variation in RF-Power

RF power is another parameter that can be used to control the growth formation. The film growth rate and its quality are significantly affected by the RF power applied to the precursors in order to create

the plasma. As it might be expected, low RF powers produce a film with a denser texture in comparison with a film deposited at high RF powers. Therefore, low RF powers were used in these experiments including 10, 20, and 25 W, equivalent to power densities of 22, 44, and 55 mW/cm^2, respectively. The rest of the deposition conditions were kept a constant as presented in **Table 7.**2 **Figure 7-12** shows the RF-PECVD growth films, which were deposited at different values of RF power densities. It is clear from **Figure 7-12** that as the RF power increases the film colour becomes darker.

Table 7.2: PECVD parameters were used to study the effect of the variation in RF-power.

Temperature (^{O}C)	Chamber pressure (mTorr)	CH_4 flow rate (sccm)	NH_3 flow rate (sccm)	Deposition duration (min)
100	1000	10	20	30

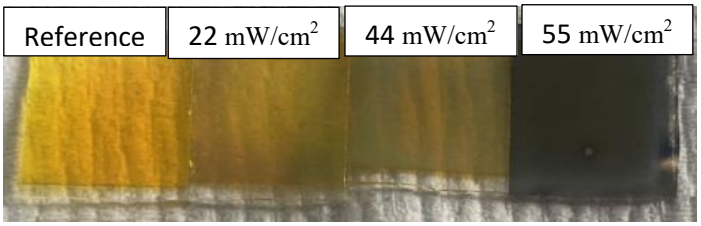

Figure 7-12: An optical image of grown films deposited at different RF power values.

7.3.2.1 Structural Characterisation

In an effort to better understanding of the effect of RF power densities in the resultant growth, XRD measurement of these samples was conducted as shown in **Figure 7-13**. It can be observed from the figure that there was a significant difference in the microstructure of films upon varying the RF power densities. The crystal structure grown at a lower power density would most probably develop into a perovskite structure. The characteristic peaks of the perovskite phase were detected at ~ 14.2^o, 28.1^o and 28.7^o, corresponding to the (110), (004) and (220) reflections of the tetragonal phase of the

$CH_3NH_3PbI_3$, respectively [23, 24, 42]. Moreover, XRD measurements were shown that a significant quantity of PbI_2 was unconverted, reflecting the bilayer structure of the created film.

However, these perovskite characteristics peaks did not appear for the films formation at a higher RF power density values that were somewhat resulted in a different crystal structure in this a particular magnitude (44 and 55 mW/cm^2) of RF power densities as shown in **Figure 7-13**. A higher power density (55 mW/cm^2) can lead to an increase in an ions flux towards the substrate surface. Such highly energetic ion bombardment in turn causes an increase in the PbI_2 atomic energy and hence removal of the iodine atoms from the most material and leaving behind metallic lead (Pb) atoms [30]. These results of an appearance of a quite small peak of (001) reflection of PbI_2 and five diffraction peaks at $2\theta \approx 31.2^{o}$ (111), 36.2^{o} (200), 52.3^{o} (220), 62.2^{o} (311), and 65.2^{o} (222) were in a good agreement with the American Mineralogist Crystal Structure Database of the lead element (AMCSD 0011154).

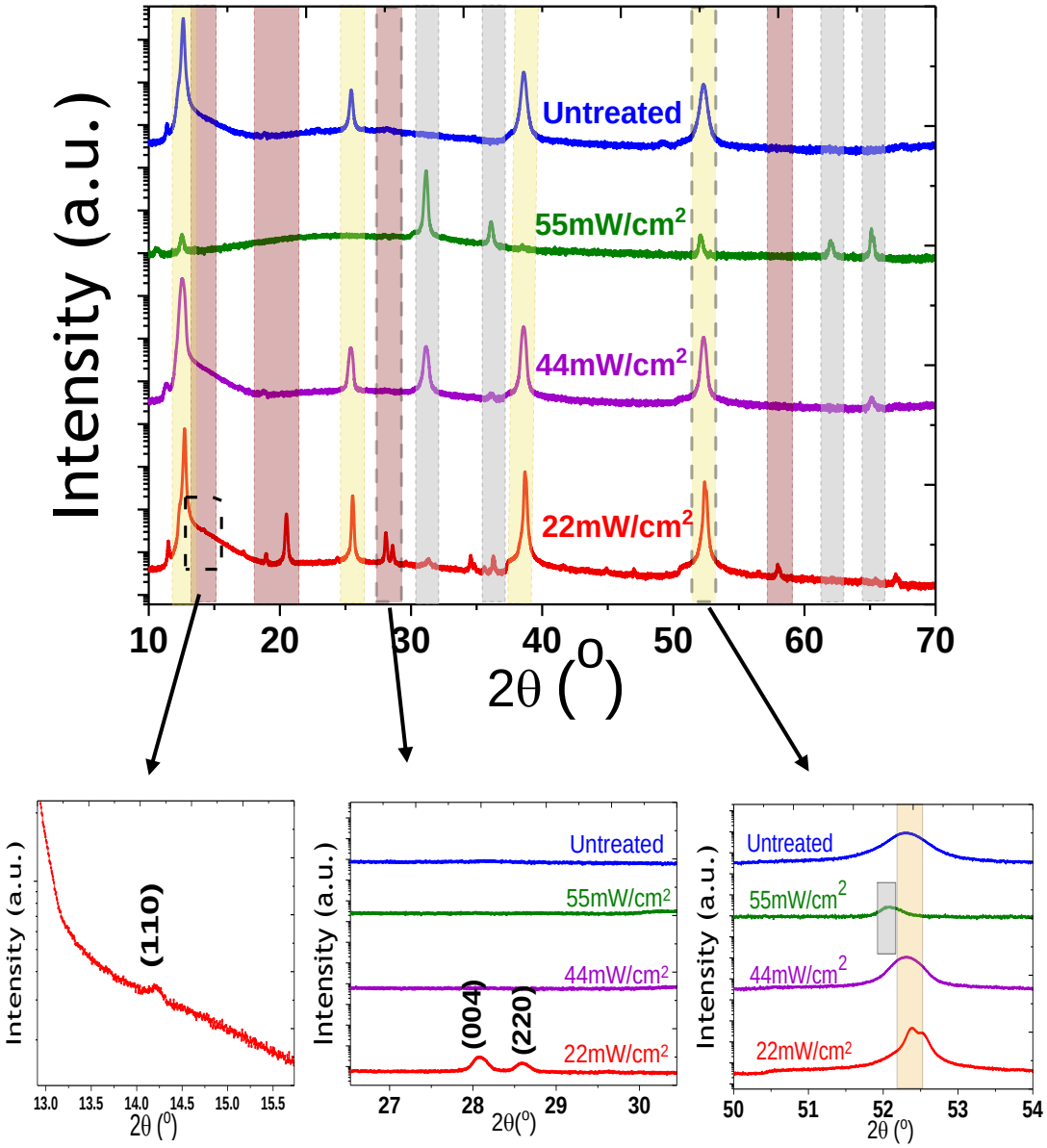

Figure 7-13: The XRD peaks of PECVD growth samples deposited at different RF power values (top graph) with magnification of the three important differences in the spetra (bottm graphes).

7.3.2.2 Optical Charactrisation

The RF power comparison experiments were also conducted by UV-VIS-IR spectroscopy for the optical analysis. An optical transmittance of the untreated PbI_2 film and PECVD growth films was recorded as a function of wavelength in the range of 300-1100 nm and presented in **Figure 7**- 14 **(a)**. It

was found that the transmittance was decreased at the energy bandgap of PbI_2 as the RF power densities increased. A slight red shift in the absorption edge was noticed with an increase in the power densities (**Figure 7-14 (b)**). It was suggested that less light was passed through the films resulting in the decrease of the energy bandgap. However, the complex structure that involving Pb and PbI_2, must be put into a consideration and the key consequence of this combination could be caused in the absence of a signature of the perovskite on the optical transition of the corresponding excitons at the wavelength of ~750 nm.

By employing the derivative method (**Figure 7-14 (c)**), no an obvious change in the energy bandgap for the films treated with PECVD was observed at 22 and 44 mW/cm^2. However, at a higher power density, no a clear energy bandgap was found. It indicated that the relative concentration of metallic Pb was higher in the film compared to PbI_2 as the XRD data of this sample was shown the metallic Pb has a higher intensity than that of PbI_2.

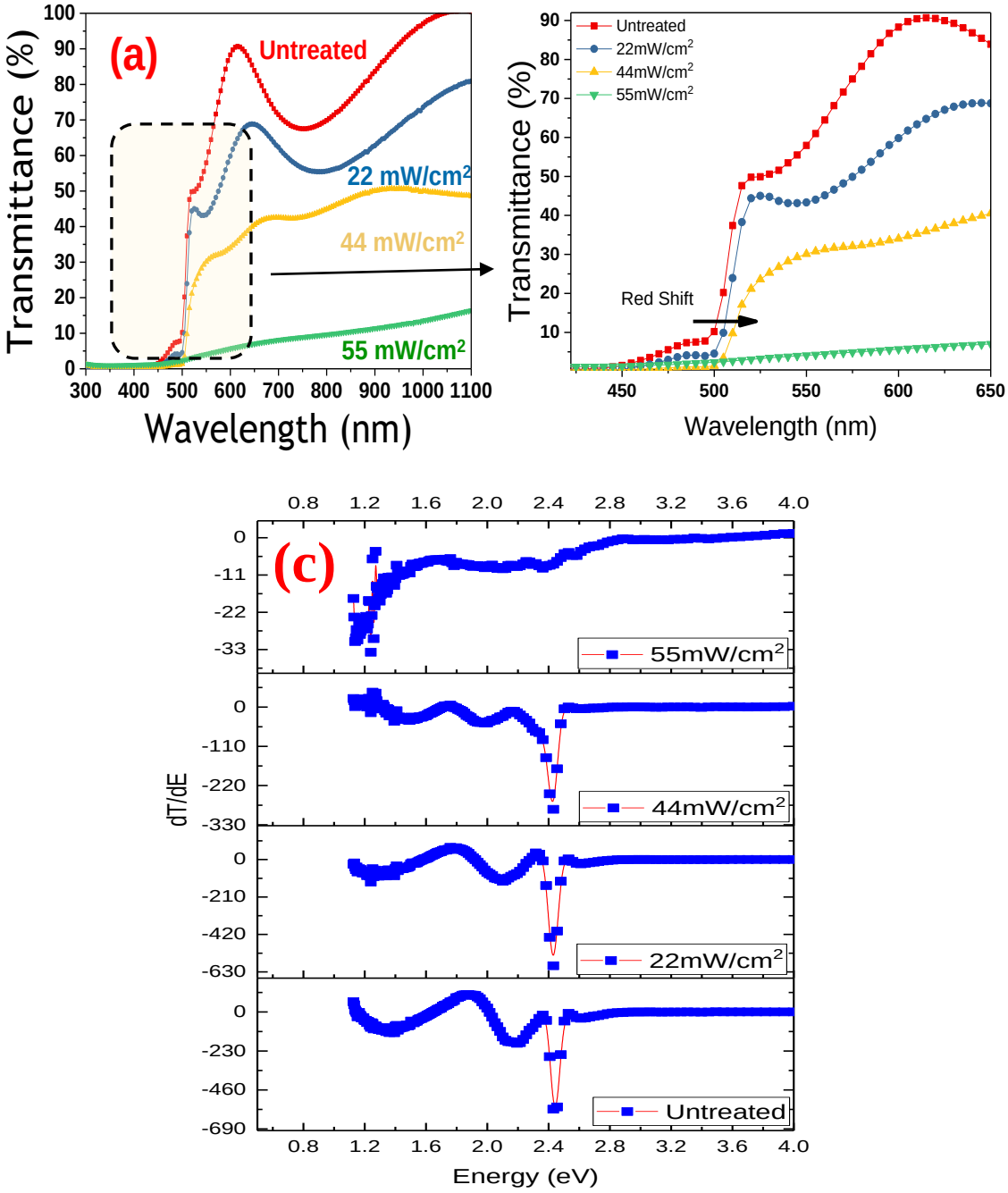

Figure 7-14: Optical transmittance spectra of PbI_2 thin film (untreated) and the PECVD growth films at different RF power values (a) with magnification the graph that focuses on the EM spectra at the absorption inset (~ 500nm) showing red shift with increasing the RF power densities (b) and the bandgap energy plots of these films determine from the derivative of transmittance with respect to photon energy (c).

7.3.2.3 Electrical Characterisation

Photo- and dark-conductivity measurments of the same subset of the samples grown at different RF power densities for 100 µm gap are shown in **Figure 7-15**. Generally, when films were exposed to a light, they would show an increase in a current in contrast to a dark current. Upon close inspection, a selective value of the current (located at 10V) was plotted for each film in one graph for simplicity as it can be seen in **Figure 7-16**.

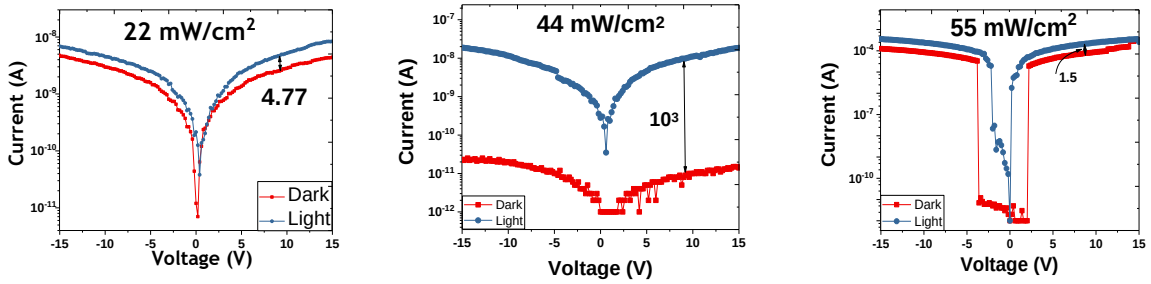

Figure 7-15: Photoconductivity of films grown at various RF power densities.

Figure 7-16 represents two different base currents; at the higher base current value, the difference between dark- and light- current was become higher. This dramatic increasing in the dark- and photo-current at a higher RF-power density was in a good agreement with XRD data which was confirmed that when the RF-power intensity was increased, a combination of semiconductor (PbI_2) and conductor (Pb) phases was appeared in the material. However, it was become more conductor (less semiconductor) at 55 mW/cm^2 due to the relative concentration of the Pb phase which was shown a higher conductor nature compared with the sample treated at lower RF-power density. Hence, many of conducting paths were built up through the material, which increased the drift current. At a lower power (22 mW/cm^2), there was a slight increase in the dark and photo currents difference compared to the untreated sample, however, the right characteristic of the perovskite material did not observe. This could be because of the existence of a combination of PbI_2 and perovskite semiconductor phases in the sample as it was observed from XRD. Such an observation could indicate that a high amount of PbI_2 was presented which formed a separate crystalline phase instead of being incorporated in the perovskite structure [25]. Such a type of the phase separation of PbI_2 and perovskite was likely the cause behind the unusual electrical characterisation of perovskite. From the results above, the lower RF power density (22 mW/ cm^2) might be a potential optimum condition in this work for the growth of perovskite film.

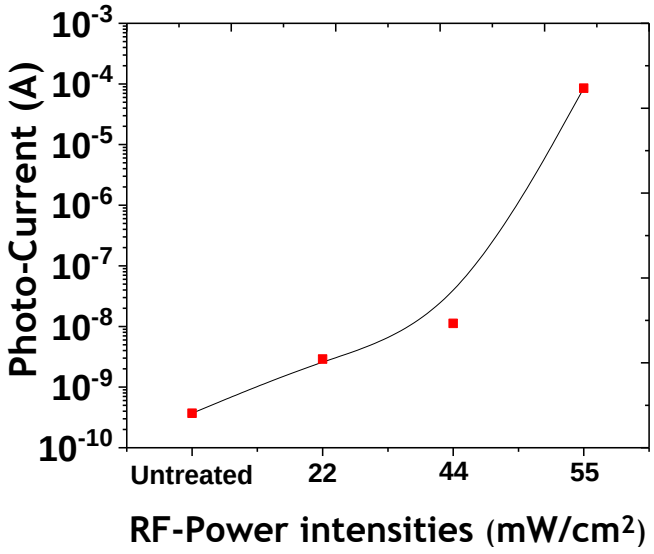

Figure 7-16: The change in current during dark and illumination conditions for films grown as a function of different RF power densities (this data was taken at fixed voltage = 10V).

7.3.3 Effect of the Variation in Chamber Pressure

The mean free path for the collision of the gas molecules can be altered by the chamber pressure. This, in turn, determines whether the reaction is occurred in the gas phase or at the sample surface [43]. To understand the effect of the chamber pressure within the deposition process on the film properties, a series of samples were deposited at different values of the total pressure of the mixture gaseous (CH4/NH3) inside the collision chamber, which were ranged from 250 to 1000 mtorr. During these experiments, the controlled total pressure was performed employing a gate valve with all other conditions held a constant as shown in **Table 7.3**.

Table 7.3: PECVD parameters were used to study the effect of the variation in chamber pressures.

Temperature (^{O}C)	RF-power density (mW/ cm^2)	CH_4 flow rate (sccm)	NH_3 flow rate (sccm)	Deposition duration (min)
100	22	10	20	30

7.3.3.1 Structural Characteristic

Figure 7-17 illuminates the variation in the crystal structure with the chamber pressure. The lower pressure (250 and 500 mtorr) was resulted in no perovskite growth, whereas the growth was observed for the sample grown at 1000 mtorr. The diffraction reflections of the grown films at 1000 mtorr can be well indexed to the tetragonal phase of CH3NH3PbI3 with a detectable PbI2 phase. It was noteworthy to mention that double-peaks were existed at around 14o which were also confirmed that CH3NH3PbI3 was manifested a tetragonal crystal structure [44, 45]. The variation in the crystal structures was determined as a function of the total gas pressure inside the chamber which may be promoted by the interaction of energetic particles with the growing surfaces. This was governed by the self-bias voltage originating at the plasma sheath that can strongly affect the ionic flux towards the substrate [46]. Therefore, as the pressure was increased, the thickness of the plasma sheath could be reduced and hence its potential (self-bias voltage) decreased. Subsequently, the energy of the ions which were come to rest on the substrate surface also was diminished and this did not cause damage to the surface. The damage was caused to the PbI2 thin films which were exposed to a relatively low pressure (250 and 500 mtorr) was confirmed from the XRD results obtained in this work. A high ion energy bombardment to the surface broke Pb-I bond and resulted in reducing PbI2 into the metallic Pb as it can be seen in **Figure 7-17**.

.

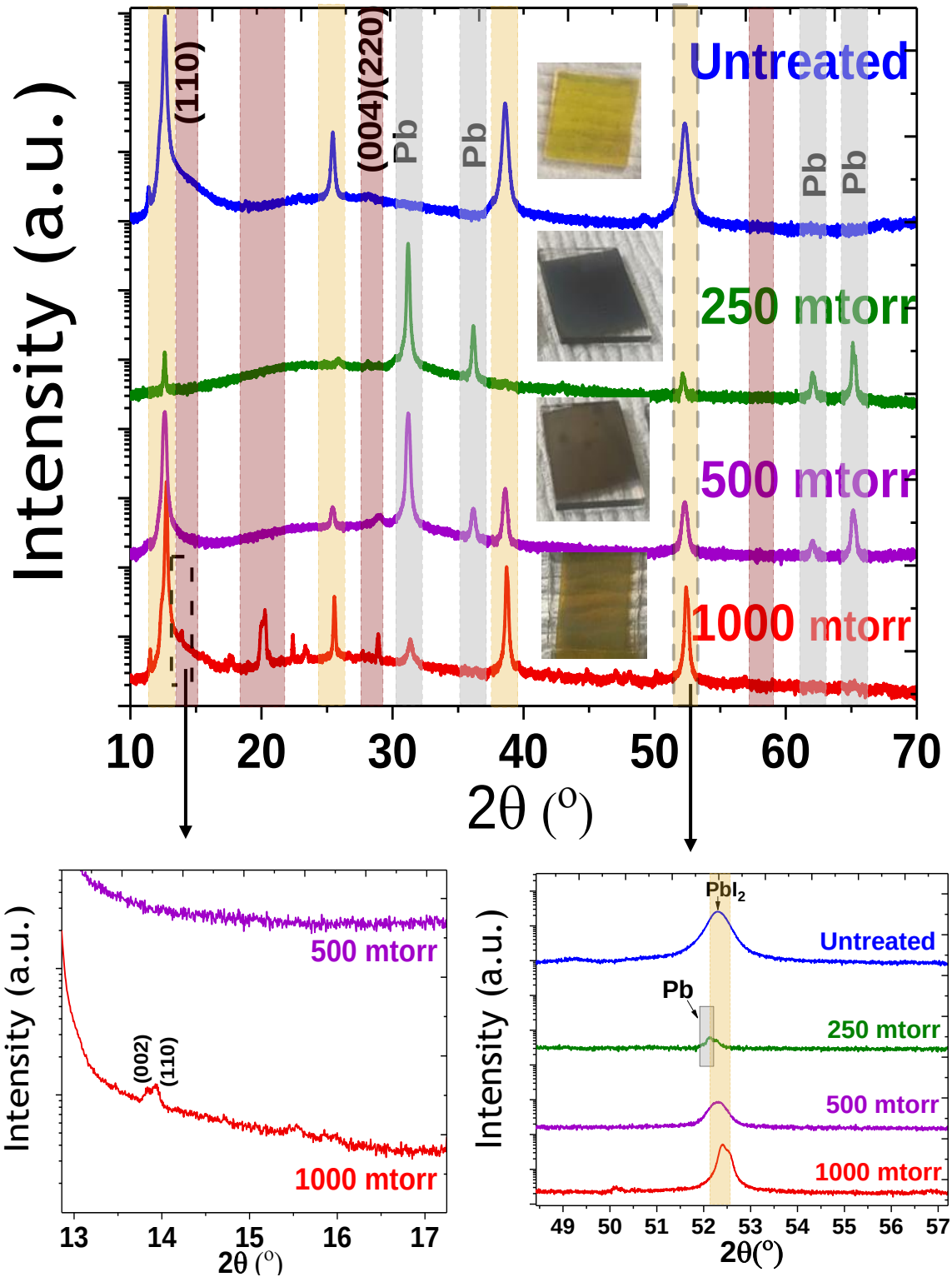

Figure 7-17: The XRD peaks of PECVD growth samples deposited at different chamber pressure values (top graph) with magnification of the important differences in the spetra (bottom graphes). The inset images in top graph present the films grown at various pressures.

7.3.3.2 Optical Characteristic

For this study, the optical transmission spectra of these films growing with a various gas pressure inside the ion source collision chamber were recorded as a function of a wavelength as it was seen in **Figure 7-18 (a)**. The transmittance of light was reduced with a decrease in chamber pressure. As it might be expected, the presence of the metallic Pb and wide-energy bandgap-semiconductor PbI_2 alongside the perovskite within the film was caused a transient change in the excitonic population and properties. Whilst at a high pressure (1000 mtorr) the spectrum was exhibited the same trend of PbI_2, there was a slight reduction in the transmittance with a red shift in the absorption edge. It was becauese of a reduction in the energy bandgap allowing less light to pass across the film **(Figure 7-18 (b)).** The formation of the perovskite phase was consistent with this an observation although there was no sign showing a corresponding to perovskite in the optical analysis. Again, the electronic structure of $(PbI_3)^-$ cage was likely to have the contribution to the excitonic properties of $CH_3NH_3PbI_3$ [22]. At low pressures, there was a further reduction in the transmittance spectra which was ascribed to a considerable amount of Pb existence in the films.

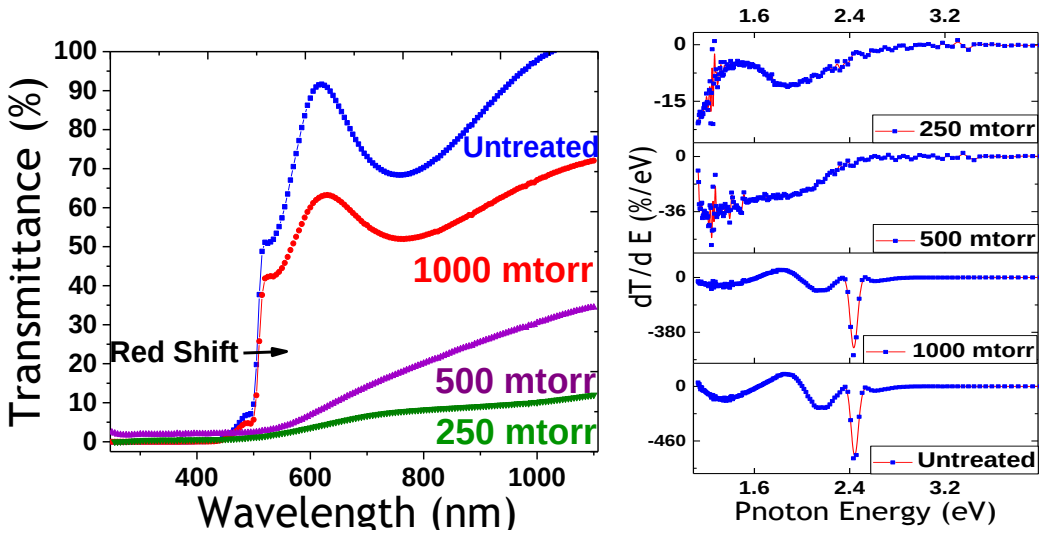

Figure 7-18: Optical transmittance spectra of PbI_2 thin film (untreated) and the PECVD growth films at different chamber pressure (left) and the plots of the derivaiative of transmittance with respect to photon energy (right) for determination of bandgap energy of these films.

7.3.3.3 Electrical Characterisation

To study the effect of the chamber pressure on the electrical properties of the grown films, photoconductivity measurements were performed and presented in **Figure 7-19**. To gain a simplified

representation of these data, a single value of a current that was located at 10V was taken from the IV plots of all samples and included in one graph (**Figure 7-20**).

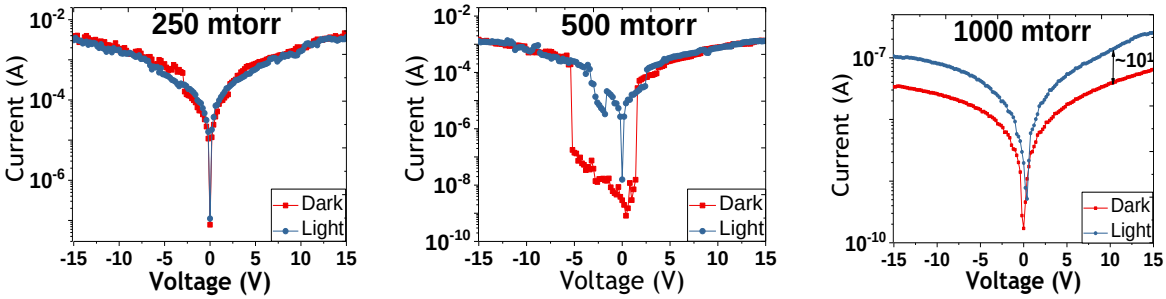

Figure 7-19: Photoconductivity of films grown at various chamber pressure.

A metallic nature of films grown at lower pressures (250, 500 mtorr) was noticed from XRD data, which was reflected in the electrical characteristic of the films. A noticeable increase in the current of those films indicating that the relative concentration of lead (Pb) was highly showing a conductor nature in both dark- and light-conditions. These results were in a good agreement with the optical results. Meanwhile, the film which was grown at a high pressure (1000 mtorr) possesses properties of a semiconductor since there was an increase in its conductivity when it was exposed to the light. This feature was due to the formation of the perovskite phase

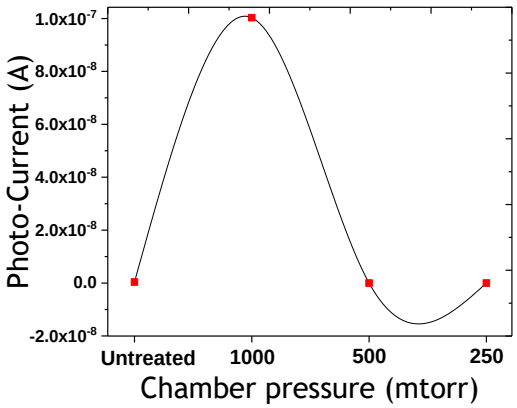

Figure 7-20: The change in photo- and dark currents for films grown as a function of different chamber pressure (this data was taken at fixied voltage = 10V).

7.4 Additional Observation

For more clear representation and in attempt to understand the effect of relatively low chamber pressure with applying a high RF power, an experiment for 30 minutes was performed at a pressure of 250 mtorr and RF power of 25 W. It was expected that as RF power was increased, more highly reaction species were involved in the deposition that resulted in an increase in the ions flux towards the substrate surface. A strong ion bombardment of the growing surface can lead to an increase in the levels of etching and hence remove the volatile species from the material [47].

To evaluate this process, the XRD data was conducted at low (10W) and high (25W) RF power as shown in **Figure 7-21**. It can be clearly seen from the inset graphs, as would be expected, the film was deposited at a lower RF power had a denser texture than that at a high RF power. This effect was further demonstrated by etching of the material from the substrate at a higher RF power. The XRD data was shown the damage caused to the PbI_2 thin films exposing to relatively low power (10W) by the reduction of PbI_2 to Pb. This can be attributed to the action of low pressure as described earlier. When the surface was exposed to a high power (25W) at relatively a low pressure, further damaging was caused. It was demonstrated from XRD data (red-pattern) by a further reduction in the intensity of both PbI_2 and Pb diffraction peaks due to the etching effect.

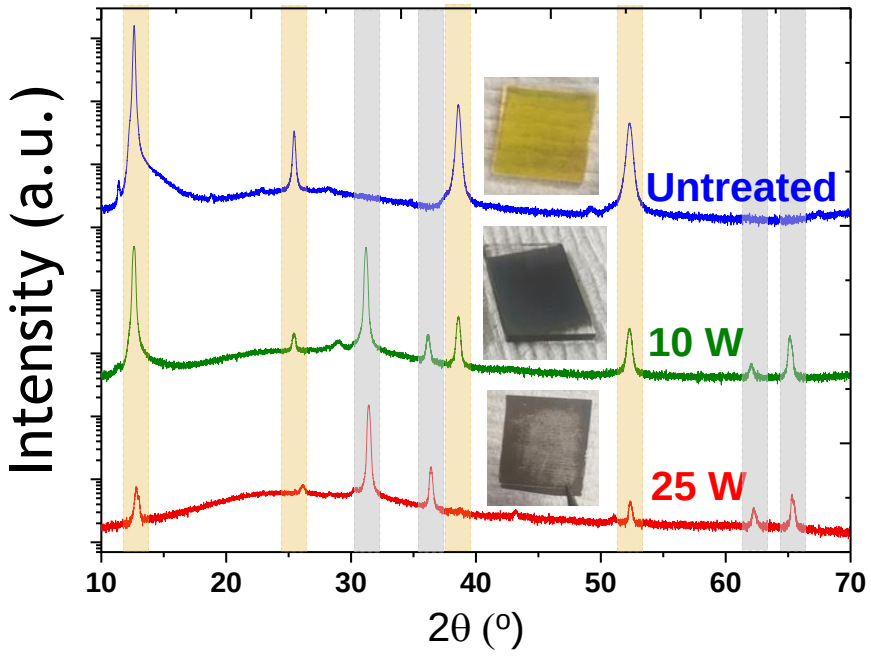

Figure 7-21: The XRD peaks of PECVD growth samples deposited at low chamber pressure (250 mtorr) and RF power of 10W (green) and 25W (red).

7.5 Summary

Successful growth of $CH_3NH_3PbI_3$ perovskite thin films by the PECVD process was discussed in this chapter. The films were grown starting from a prior deposition of PbI_2 thin films by the thermal evaporating that was discussed in Chapter 6. In order to form perovskite, PbI_2 thin films were exposed to the organic molecules in the plasma state that was formed by RF power via the PECVD technique. It was discovered that perovskite growth by such method was extremely sensitive to the deposition conditions.

As-deposited films were empirically optimised whereby each parameter (e.g. substrate temperature, RF power density, chamber pressure) was varied in turn, with the other held a constant. The RF frequency and electrode separation were remained a constant at 13.56 MHz and 3 cm respectively, as well as the gaseous flow rate remained at 10 sccm for methane gas and 20 sccm for ammonia gas. These resultant changes in the film properties were then examined using the characterisation techniques, described in chapter 5, to evaluate the effects of the growth process variables on the novel growth of $CH_3NH_3PbI_3$ films.

It was observed in the current study that a formation of the perovskite phase was more pronounced in the XRD analysis. The substrate temperature played a pivotal role in the physical and electrical properties of the film grown by PECVD. The conditions that yielded the best quality material achieved from this study were at a substrate temperature of 100 ℃ and under a low power density (22 mW/cm^2) and a high chamber pressure (1000 mtorr). However, the presence of a considerable amount of PbI_2 phase beside perovskite phase resulted in a great impact on the optoelectronic structure affecting the optical and electrical characteristics. In particular, this separation phase of residual (PbI_2) inorganic material in the resulted films prevented the outstanding properties of such perovskite material. The general view was that we did not reach the complete conversion of PbI_2 to perovskite phase, but this study presents the most comprehensive up to date on this topic, which takes us closer.

References

[1] H. Hsueh, H. Li, D. Chiang and S. Lee, "Effects of ammonia/methane mixtures on characteristics of plasma enhanced chemical vapor deposition n-type carbon films," *Journal of the electrochemical society*, vol 159, no 2, pp. D77-D83, 2011.

[2] E. Ermakova, A. Lis, M. Kosinova, Y. Rumyantsev, E. Maximovskii and V. Rakhlin, "Bis (trimethylsilyl) ethylamine: Synthesis, properties and its use as CVD precursor," *Physics procedia*, vol 46, pp. 209-218, 2013.

[3] F. L. Freire Jr, "Amorphous hydrogenated carbon-nitrogen films deposited by plasma-enhanced chemical vapor deposition," *Japanese journal of applied physics*, vol 36, no 7S, pp. 4886, 1997.

[4] D. Franceschini, F. Freire Jr, C. Achete and G. Mariotto, "Hard amorphous hydrogenated carbon-nitrogen films obtained by PECVD in methane-ammonia atmospheres," *Diamond and related materials*, vol 5, no 3-5, pp. 471-474, 1996.

[5] O. Amir and R. Kalish, "Properties of nitrogen-doped amorphous hydrogenated carbon films," *Journal of applied physics*, vol 70, no 9, pp. 4958-4962, 1991.

[6] L. Wojcik and A. Markowski, "Mass spectrometric study of ion/molecule reaction in methane and ammonia mixtures," *Vacuum*, vol 78, no 2-4, pp. 235-240, 2005.

[7] S.R. Droes, T.T. Kodas and M.J. Hampden-Smith, "Carbide, Nitride and Boride Materials Synthesis and Processing," in *Plasma-enhanced chemical vapor deposition (PECVD)*, Anonymous Springer, 1997, pp. 579- 579-603.

[8] H. Kersten, H. Deutsch, H. Steffen, G. Kroesen and R. Hippler, "The energy balance at substrate surfaces during plasma processing," *Vacuum*, vol 63, no 3, pp. 385-431, 2001.

[9] J. A. Thornton, "Influence of substrate temperature and deposition rate on structure of thick sputtered cu coatings," *Journal of vacuum science and technology*, vol 12, no 4, pp. 830-835, 1975.

[10] H. Winters, "Topics in Current Chemistry," in *Plasma chemistry III*, Anonymous Springer, 1980, pp. 69- 69-125.

[11] R. A. Marcus and O. Rice, "The kinetics of the recombination of methyl radicals and iodine atoms." *The journal of physical chemistry*, vol 55, no 6, pp. 894-908, 1951.

[12] C. Hopf, W. Jacob and A. Von Keudell, "Ion-induced surface activation, chemical sputtering, and hydrogen release during plasma-assisted hydrocarbon film growth," *Journal of applied physics*, vol 97, no 9, pp. 094904, 2005.

[13] F. Fu, L. Kranz, S. Yoon, J. Löckinger, T. Jäger, J. Perrenoud, T. Feurer, C. Gretener, S. Buecheler and A. N. Tiwari, "Controlled growth of PbI2 nanoplates for rapid preparation of CH3NH3PbI3 in planar perovskite solar cells," *Physica status solidi (a)*, vol 212, no 12, pp. 2708-2717, 2015.

[14] K. Jemli, H. Diab, F. Lédée, G. Trippé-Allard, D. Garrot, B. Geffroy, J. Lauret, P. Audebert and E. Deleporte, "Using low temperature photoluminescence spectroscopy to investigate CH3NH3PbI3 hybrid perovskite degradation," *Molecules*, vol 21, no 7, pp. 885, 2016.

[15] J. B. Patel, R. L. Milot, A. D. Wright, L. M. Herz and M. B. Johnston, "Formation dynamics of CH3NH3PbI3 perovskite following two-step layer deposition," *The journal of physical chemistry letters*, vol 7, no 1, pp. 96-102, 2015.

[16] H. Ko, J. Lee and N. Park, "15.76% efficiency perovskite solar cells prepared under high relative humidity: Importance of PbI 2 morphology in two-step deposition of CH 3 NH 3 PbI 3," *Journal of materials chemistry A*, vol 3, no 16, pp. 8808-8815, 2015.

[17] N. Ahn, D. Son, I. Jang, S. M. Kang, M. Choi and N. Park, "Highly reproducible perovskite solar cells with average efficiency of 18.3% and best efficiency of 19.7% fabricated via lewis base adduct of lead (II) iodide," *Journal of the american chemical society*, vol 137, no 27, pp. 8696-8699, 2015.

[18] E. W. Jones, P. J. Holliman, A. Connell, M. L. Davies, J. Baker, R. J. Hobbs, S. Ghosh, L. Furnell, R. Anthony and C. Pleydell-Pearce, "A novel dimethylformamide (DMF) free bar-cast method to deposit organolead perovskite thin films with improved stability," *Chemical communications*, vol 52, no 23, pp. 4301-4304, 2016.

[19] A. Dualeh, N. Tétreault, T. Moehl, P. Gao, M. K. Nazeeruddin and M. Grätzel, "Effect of annealing temperature on film morphology of organic–inorganic hybrid pervoskite solid-state solar cells," *Advanced functional materials*, vol 24, no 21, pp. 3250-3258, 2014.

[20] S. M. Jain, B. Philippe, E. M. Johansson, B. Park, H. Rensmo, T. Edvinsson and G. Boschloo, "Vapor phase conversion of PbI 2 to CH 3 NH 3 PbI 3: Spectroscopic evidence for formation of an intermediate phase," *Journal of materials chemistry A*, vol 4, no 7, pp. 2630-2642, 2016.

[21] X. Jia, Z. Hu, Y. Zhu, T. Weng, J. Wang, J. Zhang and Y. Zhu, "Facile synthesis of organic–inorganic hybrid perovskite CH3NH3PbI3 microcrystals," *Journal of alloys and compounds*, vol 725, pp. 270-274, 2017.

[22] A. M. Soufiani, Z. Yang, T. Young, A. Miyata, A. Surrente, A. Pascoe, K. Galkowski, M. Abdi-Jalebi, R. Brenes and J. Urban, "Impact of microstructure on the electron–hole interaction in lead halide perovskites," *Energy & environmental science*, vol 10, no 6, pp. 1358-1366, 2017.

[23] T. Oku, "Solar Cells-New Approaches and Reviews," in *Crystal structures of CH3NH3PbI3 and related perovskite compounds used for solar cells*, Anonymous InTech, 2015, .

[24] T. Baikie, Y. Fang, J. M. Kadro, M. Schreyer, F. Wei, S. G. Mhaisalkar, M. Graetzel and T. J. White, "Synthesis and crystal chemistry of the hybrid perovskite (CH 3 NH 3) PbI 3 for solid-state sensitised solar cell applications," *Journal of materials chemistry A*, vol 1, no 18, pp. 5628-5641, 2013.

[25] T. Meier, T. P. Gujar, A. Schönleber, S. Olthof, K. Meerholz, S. van Smaalen, F. Panzer, M. Thelakkat and A. Köhler, "Impact of excess PbI 2 on the structure and the temperature dependent optical properties of methylammonium lead iodide perovskites," *Journal of materials chemistry C*, vol 6, no 28, pp. 7512-7519, 2018.

[26] J. Burschka, N. Pellet, S. Moon, R. Humphry-Baker, P. Gao, M. K. Nazeeruddin and M. Grätzel, "Sequential deposition as a route to high-performance perovskite-sensitized solar cells," *Nature*, vol 499, no 7458, pp. 316, 2013.

[27] Y. H. Lee, J. Luo, R. Humphry-Baker, P. Gao, M. Grätzel and M. K. Nazeeruddin, "Unraveling the reasons for efficiency loss in perovskite solar cells," *Advanced functional materials,* vol 25, no 25, pp. 3925-3933, 2015.

[28] Q. Chen, H. Zhou, T. Song, S. Luo, Z. Hong, H. Duan, L. Dou, Y. Liu and Y. Yang, "Controllable self-induced passivation of hybrid lead iodide perovskites toward high performance solar cells," *Nano letters,* vol 14, no 7, pp. 4158-4163, 2014.

[29] S. Wang, W. Dong, X. Fang, Q. Zhang, S. Zhou, Z. Deng, R. Tao, J. Shao, R. Xia and C. Song, "Credible evidence for the passivation effect of remnant PbI 2 in CH 3 NH 3 PbI 3 films in improving the performance of perovskite solar cells," *Nanoscale,* vol 8, no 12, pp. 6600-6608, 2016.

[30] L. Zhang, Z. Jin, L. Zhang, M. Sui and K. Lu, "Superheating of confined pb thin films," *Physical review letters,* vol 85, no 7, pp. 1484, 2000.

[31] A. Ummadisingu and M. Grätzel, "Revealing the detailed path of sequential deposition for metal halide perovskite formation," *Science advances,* vol 4, no 2, pp. e1701402, 2018.

[32] H. A. Harms, N. Tétreault, N. Pellet, M. Bensimon and M. Grätzel, "Mesoscopic photosystems for solar light harvesting and conversion: Facile and reversible transformation of metal-halide perovskites," *Faraday discussions,* vol 176, pp. 251-269, 2015.

[33] A. Ummadisingu, L. Steier, J. Seo, T. Matsui, A. Abate, W. Tress and M. Grätzel, "The effect of illumination on the formation of metal halide perovskite films," *Nature,* vol 545, no 7653, pp. 208, 2017.

[34] T. J. Jacobsson, J. Correa-Baena, E. Halvani Anaraki, B. Philippe, S. D. Stranks, M. E. Bouduban, W. Tress, K. Schenk, J. Teuscher and J. Moser, "Unreacted PbI2 as a double-edged sword for enhancing the performance of perovskite solar cells," *Journal of the american chemical society,* vol 138, no 32, pp. 10331-10343, 2016.

[35] A. W. Sanches, M. A. da Silva, N. J. Cordeiro, A. Urbano and S. A. Lourenço, "Effect of intermediate phases on the optical properties of PbI 2-rich CH 3 NH 3 PbI 3 organic–inorganic hybrid perovskite," *Physical chemistry chemical physics,* vol 21, no 9, pp. 5253-5261, 2019.

[36] G. Sadoughi, D. E. Starr, E. Handick, S. D. Stranks, M. Gorgoi, R. G. Wilks, M. Bär and H. J. Snaith, "Observation and mediation of the presence of metallic lead in organic–inorganic perovskite films," *ACS applied materials & interfaces,* vol 7, no 24, pp. 13440-13444, 2015.

[37] A. S. Yerramilli, Y. Chen, D. Sanni, J. Asare, N. D. Theodore and T. Alford, "Impact of excess lead on the stability and photo-induced degradation of lead halide perovskite solar cells," *Organic electronics,* vol 59, pp. 107-112, 2018.

[38] H. Che, J. Huso, J. L. Morrison, D. Thapa, M. Huso, W. J. Yeh, M. Tarun, M. McCluskey and L. Bergman, "Optical properties of ZnO-alloyed nanocrystalline films," *Journal of nanomaterials,* vol 2012, pp. 7, 2012.

[39] M. Wang, E. J. Kim, S. Kim, J. S. Chung, I. Yoo, E. W. Shin, S. H. Hahn and C. Park, "Optical and structural properties of sol–gel prepared MgZnO alloy thin films," *Thin solid films,* vol 516, no 6, pp. 1124-1129, 2008.

[40] K. N. Manjunatha and S. Paul, "Investigation of optical properties of nickel oxide thin films deposited on different substrates," *Applied surface science,* vol 352, pp. 10-15, 2015.

[41] C. Lan, R. Dong, Z. Zhou, L. Shu, D. Li, S. Yip and J. C. Ho, "Large-Scale synthesis of freestanding Layer-Structured PbI2 and MAPbI3 nanosheets for High-Performance photodetection," *Advanced materials,* vol 29, no 39, pp. 1702759, 2017.

[42] T. Oku, "Solar Cells-New Approaches and Reviews," in *Crystal structures of CH3NH3PbI3 and related perovskite compounds used for solar cells,* Anonymous IntechOpen, 2015, .

[43] R.A. Street, *Hydrogenated amorphous silicon,* Cambridge university press, 2005.

[44] F. Fu, L. Kranz, S. Yoon, J. Löckinger, T. Jäger, J. Perrenoud, T. Feurer, C. Gretener, S. Buecheler and A. N. Tiwari, "Controlled growth of PbI2 nanoplates for rapid preparation of CH3NH3PbI3 in planar perovskite solar cells," *Physica status solidi (a),* vol 212, no 12, pp. 2708-2717, 2015.

[45] G. Grancini, S. Marras, M. Prato, C. Giannini, C. Quarti, F. De Angelis, M. De Bastiani, G. E. Eperon, H. J. Snaith and L. Manna, "The impact of the crystallization processes on the structural and optical properties of hybrid perovskite films for photovoltaics," *The journal of physical chemistry letters,* vol 5, no 21, pp. 3836-3842, 2014.

[46] M. Benlahsen and M. Therasse, "Spectroscopic investigations of the microstructure changes induced by substrate temperature in nitrogen-substituted amorphous carbon thin films," *Carbon,* vol 42, no 11, pp. 2255-2262, 2004.

[47] G. Lavareda, C. N. de Carvalho, A. Amaral, J. Conde, M. Vieira and V. Chu, "Properties of high growth rate amorphous silicon deposited by MC-RF-PECVD," *Vacuum,* vol 64, no 3-4, pp. 245-248, 2002.

Chapter 8 Atmospheric-Pressure Chemical Vapour Deposition (APCVD) of Perovskite material

8.1 Introduction

Perovskite materials have been deposited by various CVD methods, as discussed extensively in Chapter 2, in which a solid thin film is grown from the reaction of precursors that are in the gaseous state. The precursors in the gaseous state are supplied either from a gas source as is the case of PECVD process or by sublimation/vaporisation using solid/liquid precursors. This class of methods can be categorised based on the pressure range at which the process is carried out. Atmospheric-pressure chemical vapour deposition (APCVD) is a widespread and popular commercial technique used in the semiconductor industry to deposit thin films of materials in which their stoichiometry is precisely controlled along with the high growth rate and step coverage. However, this method is not widely used for the growth of perovskite material from a single-source liquid precursor, in which both organic (MAI) and inorganic (PbI_2) compounds of the deposited material are combined in one source. Moreover, in the published literature, the liquid-based source has been atomised by using a commercial nebuliser, resulting in the formation of an uncontrollable mist [1-3]. Therefore, it is necessary to design a delivery system that can be adjusted to obtain precise control over the growth in order to produce a functional thin film with almost defect-free.

In view of the importance of the typical CVD process that is preventing self-limiting chemical reactions, which is the case in the sequential-deposition whereas the reaction of gas-solid phase is limited by the properties of the underlying solid thin film (as it is seen from the PECVD growth method). In this case, MAI in the gas phase reacts with the pre-coated PbI_2 films, in which the conversion to perovskite from PbI_2 is achieved until the availability of PbI_2 [4-7]. The claim was made by the authors, as a CVD process, was lacking to qualify one of the tenets of the CVD - “an infinite source of precursors” to grow a film of an infinite thickness (However, in this research, thickness of a few micrometres or less was achieved). The pre-coated PbI_2 does not fit into the standard CVD deposition mechanism; the reactants land on the surface of substrate during the deposition and form a required layer. In a complete gas phase reaction of PbI_2 and MAI on the surface of substrates, a finite thickness can be realised easily with a conformal growth of the exact stoichiometry as it is presented in the single precursor [8]. So far, there are two reports concerning the growth of perovskite materials by employing the CVD growth via atomisation of a liquid precursor

[1,2]. Some important aspects related to this growth are presented (e.g. the effect of the distance between the substrate and upstream entry, the temperature gradient along the furnace, the actual substrate temperature). However, they do not report about the control methods used for the growth of material in order to control the number of species passing over the substrate and the residence time of the mist over the surface of the substrate that is required to form a film with minimal defects. These reports also used higher concentration with a faster growth rate at high temperature exceeding 200 ^{0}C, that may result in the formation of a thin film with high defect density (point, line or plane defects) and also undesirable stoichiometry; both these factors can result in the instability of the as-deposited material. In the current study, more attention was paid on the deposition process and the growth dynamics by controlling various parameters for eliminating aforementioned problems and thus paving the foundation of obtaining relatively stable perovskite thin films.

In a typical APCVD process, the substrate is exposed to one or more volatile precursors at atmospheric pressure. The compounds of the precursor are required to be delivered to a CVD reactor in a mist/vapour form containing droplets of a solvent with the compounds dissolved in. A major challenge of this method is an appropriate selection of an effective delivery system. There are numbers of critical factors or parameters that should be controlled during the formation of the mist/vapour in a steady-flow rate into the reactor such as droplet size, concentration of the solution, growth temperatures, molar concentration of precursor, substrates' surface, flow rate of a carrier gas, resonant frequency of the piezo transducer etc. In a nutshell, a CVD is a chemical process and all the thermodynamical parameters affect the growth process.

Herein, different deliveries' systems were used such as bubbler and in-house built piezoelectric transducer. The delivery systems were adjusted to meet their function, which was to sufficiently convert the solvent and the containing materials (PbI_2 and MAI) into a continuous streamline of proper size droplets by using two physical phenomenon; bubbles and piezoelectric vibrations to induce the droplet atomisation.

This chapter provides a description of the aforementioned systems, which was used for the formation of vapour/droplets and delivery, to examine:

- The deposition process of a thin film through a liquid precursor by APCVD.
- Two different physical mechanisms for the atomisation of liquid to form vapours.
- The factors that influence the generation of the vapours in both systems.
- The development of the method to determine the process parameters at which the droplet contains a desirable material.

8.2 APCVD Process

APCVD is an industrial technique to deposit thin films because it fulfils several important criteria; (1) a high growth rate, (2) high control of stoichiometry, (3) precise control over the thickness, (4) ability to produce thin film in large area, (5) no vacuum is required (reduce the cost and power consumption), (6) flexible to accommodate a wide range of substrates and (7) use of a wide range of materials [9,10]. It is important to note that the APCVD technique is not preferred for oxygen-sensitive materials over low-pressure CVD (LPCVD). However, if a higher quality material is obtained using APCVD, for example in our Perovskite (which is sensitive to oxygen and water vapours), LPCVD can further improve the quality of such material. It was attempted to prove the principle here in this work. The growth mechanisms of a desirable thin film prepared by the APCVD process consists several steps (**Figure 8-1**):

I. Mist formation: this is the key aspect as well as the first step in order to have an efficient atomisation of liquid feed, where the dissolved materials are evaporated along with the solvent or in other words – vapours of the solvent containing precursor materials which are required for the thin film deposition. Generally, the precursor mist can be generated by several techniques such as heating, bubbler, and ultrasonic humidifier/nebuliser. In fact, an energy that is transmitted from the delivery system to the liquid is required to break the liquid into droplets, causing atomisation. Therefore, it is critical to select the proper system depending on the precursor(s) properties. Ideally, the precursor with high volatility used to be readily volatile under temperature that is less than the temperature of its decomposition. As a consequence, a fine mist would be obtained to feed the CVD reactor where the deposition takes place on elevated substrate temperature.

II. Feed the reactor: the formed mist/vapour needs to be delivered to the reactor. Typically, a carrier gas (nitrogen, argon) is employed in order to transport the mist to the region of deposition through a bypass line, which can be accurately delivered with a mass flow controller (MFC) [11] or the use of flow-meter. The crucial step to deposit thin films is to guarantee the longer residence time (steady slow-flow rate) of the mist onto the substrate surface where possible reactions are occurred and prevented the effect of the hydrodynamics associated with the atomisation of the solvent at the hot substrate surface [10]. This means the morphology, possibly structure, of the deposited thin film will not be affected during the desorption of unwanted/desirable chemical species from the surface of growing film including the solvent (in our case DMF).

III. Precursor/substrate surface reaction: once the vapour, containing precursor materials, is passed over the hot substrate surface, undesirable species (solvents, the byproduct of the

reaction taking place at the surface of the substrate, etc.) has to be desorbed, which is typical CVD process (see Chapter 4). This thermal decomposition of the precursor on the substrate surface leads to the formation of a desired thin film.

However, the requirement of high volatility precursors is not always necessary, making this cost-effective and scale-up route that can be extended to the range of potential uses of various other compounds for a thin film deposition [12]. Therefore, a wide range of low volatility materials has been utilised by developing a variety of liquid delivery methods such as bubbler, ultrasonic nebuliser, and mesh nebuliser to feed the deposition reactants.

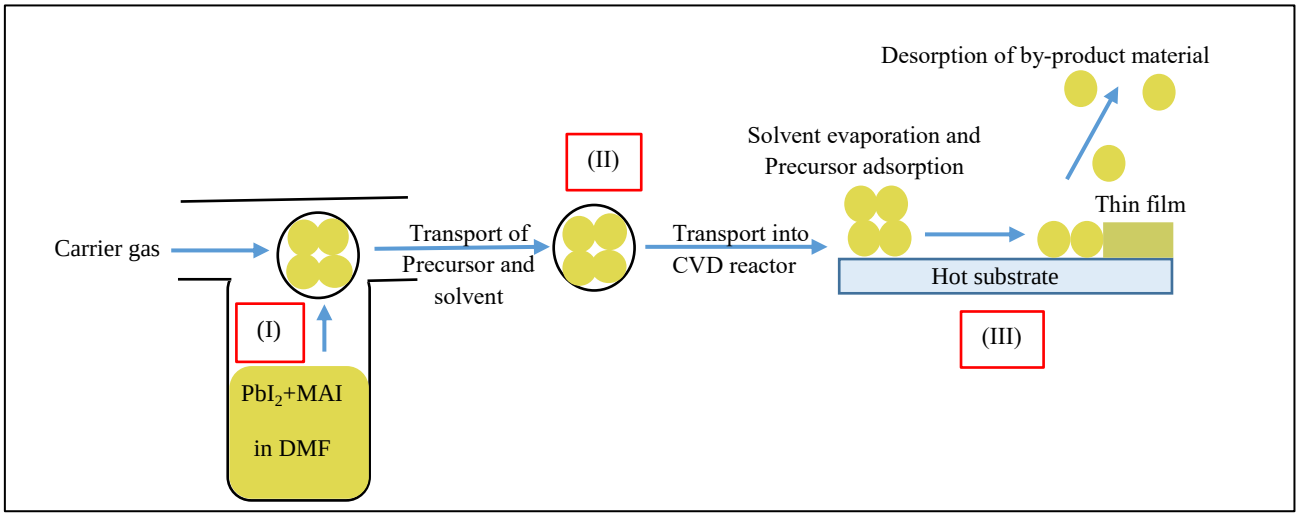

Figure 8-1: Schematic illustration of the process involved in one-step liquid-precursor CVD.

8.3 APCVD Based on Bubbler Delivery Unit

A bubbler technology is a well-known system in the field of vapour delivery. The first CVD growth was reported in 1969 by Manasevit in which the bubbler was employed as the delivery system of liquid precursors [13]. Typically, the system sufficiently converts the precursors, which their vapour pressure is moderate, into gas phase reactants [14].

The precursors (PbI_2 and MAI) with a molar ratio of 1:1 were dissolved in a DMF solvent and sonicated for 2 hours to be completely dissolved. The solution was fed into the bubbler, and the carrier gas (N_2) was passed through the solution to carry the vapours (possibly containing the required precursors). The gas, carrying vapours containing precursor materials, should be fully saturated when passing through the bubbler. To feed the reactor, the bubbler system was connected and equipped with the APCVD reactor through a quartz tube where the substrates were placed in. **Figure 8-2** shows the image of the APCVD system used in this work that involved glass bubbler with two necks; one was

connected with the carrier gas via a flow meter and the other (feed line) connected to the quartz tube of the APCVD reactor. Tubes were used for the connections that enable a carrier gas flowing to the solution and carrying the vapours into the quartz tube.

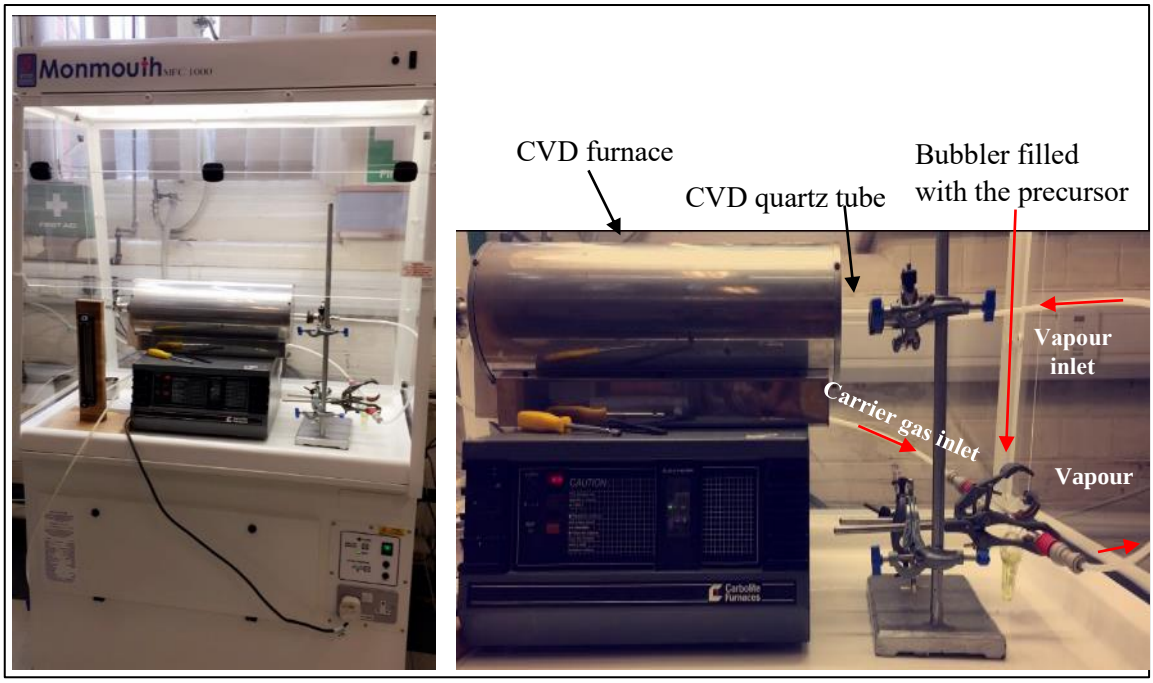

Figure 8-2: Images of APCVD system used in this work kept inside an insulated box to avoid precursor atoms vaporising out of system.

Using this system, the transformation of the formed vapour/mist onto the reactor was not successfully achieved. The vapour was condensed on the bubbler wall near the neck and in the connected tube between the bubbler and the CVD quartz tube. To overcome this difficulty, the bubbler was held at temperatures (50-200 °C), by immersing the bubbler in a hot silicon oil bath. The temperature was monitored by using thermocouple which was immersed in the oil. Such a method helped to increase the equilibrium vapour pressure within the bubbler; however, there was still a condensation of the vapour in the feed line. Therefore, a further adjustment was needed to prevent this condensation. In this stage, it became necessary to heat the feed lines, which was done by using a Halogen lamp.

Table 8-1 shows the parameters for the APCVD process considering all these setup. It was observed that the formed vapour was colourless, and a black powder was left behind in the bubbler as it can be seen in **Figure 8-3**. This black residue was confirmed that the solvent (DMF) was only delivered leaving behind the solute ($CH_3NH_3PbI_3$). In addition, it was proved that the solid precursors (PbI_2 and

MAI) have very low volatilities, so it was difficult to establish perovskite material by such delivery system.

Table 8-1: The CVD process parameters that used in the bubbler delivery system.

CVD parameters	
Flow rate of N_2 carrier gas	0.2 l/min
Molar ratio of PbI_2:MAI	1:1
Volume of precursor solution	4 ml
Substrate temperature	180 °C
Silicone oil temperature	150 °C
Feed-line temperature	30-33 °C
Deposition time	1h

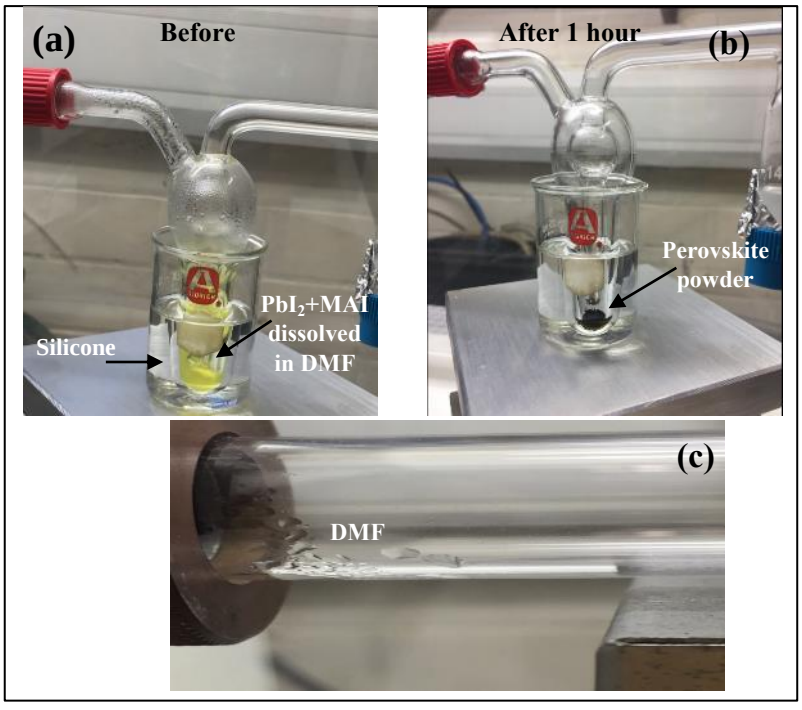

Figure 8-3: images of the precursor inside the bubbler before (a) and after (b) the CVD possessing and (c) shows the condensation of transformed vapour at the exhaust.

To understand this finding, it was worth to investigate the microscopic level of the dynamic governing dissolution of the solid material (PbI_2 and MAI) in DMF. Chemically, DMF is a solvent with a functional group containing oxygen which acts as O-donors [15]. Hence, it donates a free electron pair to Pb^{2+} ions via the hydrogen bonding interaction (Pb-O) [16]. This bonding enables dissociation of the PbI_6 octahedral frame of the perovskite material, which was formed initially when mixing the two powder sources (PbI_2 and MAI) before being dissolved in DMF (**Figure 8-4 (a)).** It consequently breaks up the compounds into ions (MA^+, Pb^{2+}, I^-) flouting in the solvent (DMF). Due to the potential energy of bonds holding the molecules together, atoms can vibrate/ move with respect to each other. This form of energy represents the total internal energy of the system in an equilibrium thermodynamic state. By introducing energy from an external source into the system such as heat (thermal energy) and/or bubble (mechanical energy), the state of equilibrium would be altered because the system is subjected to a change of temperature and pressure. As a result, the molecules and ions gain kinetic energy. According to the kinetic energy distribution of molecules (Maxwell-Boltzmann distribution), each molecule/ion gains certain kinetic energy, however, few molecules have exceedingly high kinetic energies. When the energy of molecule/ion is high enough to overcome the difference in chemical potentials between the two phases (liquid and gas), the liquid-gas transition occurs. This can be also explained in terms of Gibbs free energy (G) which can be expressed by the Clausius-Clapeyron equation:

$$Vapour\ pressure\ (P) \propto e^{-\Delta G/RT}$$

Since the DMF molecules and the existing ions have their translational kinetic energy (Gibbs free energy), only the molecules and ions with sufficient kinetic energy can overcome the kinetic barrier (potential energy wall ΔE, **Figure 8-4 (b))** for the phase transition and escape from the surface of liquid to enter the gas phase. At a critical temperature (T_c), the DMF with a higher volatility and relative low molecular weight (73.09 g/mole) can undergo a liquid-vapour transition after breaking the half of hydrogen bonds between the oxygen and lead. However, the MAI and PbI_2 compounds with a relative low volatility and higher molecular weights ((PbI_2: 461.01 g/mol, MAI: 158.97 g/mol)) do not have the lowest possible free energy, which prevents their transition into gaseous phase and thus they precipitate. Sequentially, a re-crystallisation of the black powder (initial solid powders source; $CH_3NH_3PbI_3$) was occurred which is its metastable phase **(Figure 8-3 (b)).** So, if sufficient energy is supplied to the solution, there is a possibility for the ions to evaporate, however, this was not explored any further. That was because the purpose of this work was to form the perovskite thin film by the APCVD process from a liquid source "not from the solid source", in which the solvent and the containing solid materials must reach the substrate and decompose on it. The deposition of perovskite thin film from a solid phase was extensively explored in literature (see chapter 2) [2, 3, 17, 18].

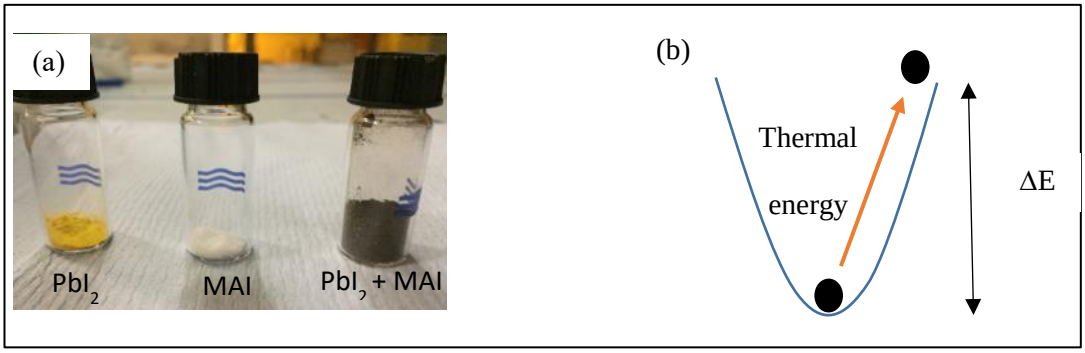

Figure 8-4: (a) shows the solid precursors of perovskite material (b) shows the depth of the potential energy wall and the thermal energy (or any source of energy) that the molecules and ions are needed for the phase transition, which is proportional to k_BT, where k_B is the Boltzmann's constant meaning that the phase transition depends on T.

It was desirable to find an alternative delivery system that had a different mechanism for an atomising process. The system needs to provide enough energy for atomising the liquid in the vapour form (fine mist), and avoiding the limitations associated with the bubbler system (dependent of thermal energy). The limitation was the variation in the temperature range for the solvent and the dissolved solid material, which was required to cause transference. The highly efficient alternative process for the liquid-vapour phase-change is examined in detail in the following section, which is based on the vibration induced-droplet generation from a liquid.

8.4 APCVD Process Based on Vibration Induced-Droplet Atomisation (VIDA)

Droplet ejection from liquid is a visible phenomenon that is seen in oceans and lakes and formed as a result of the breaking of the surface waves [19, 20]. These surface waves are formed when receiving a certain amount of energy from wind/gravity/heat driven flow that causes vibrations in the vertical oscillations of the liquid particles. Oscillation of these particles tears the peak of the surface wave from the liquid generating droplets (Faraday excitation) [21].

In this work, to generate droplets, oscillatory pressure disturbances were generated in the liquid that was placed in a contact with the piezoelectric transducer. These disturbances were propagated throughout the liquid causing instantaneous oscillations of the liquid molecules with the excitation frequency. A piezoelectric crystal was vibrated at a high frequency (1.7 MHz was used in this work), which was powered by a sinusoidal AC signal, producing the ultrasonic waves to counter the force of gravity and generate a continuous stream of vapours.

In order to produce perovskite thin films from a single-liquid precursor with a minimum defect density, using a single-step APCVD process, there were key processes in the preparative steps. A "T" joint was designed to host the piezoelectric disc and liquid precursor. The piezoelectric disc was placed at the bottom of the "T" joint and not allowed the electrical terminals being in a contact with the solution. These terminals were connected to the circuit to provide a required AC signal. Due to the corrosive properties of the solvent used (DMF), the "T" joint was fabricated from aluminium. The two necks of the "T" joint were connected to (1) the carrier gas flowmeter and to (2) the CVD reactor. The "T" joint hosing the piezoelectric disc is shown in **Figure 8-5**.

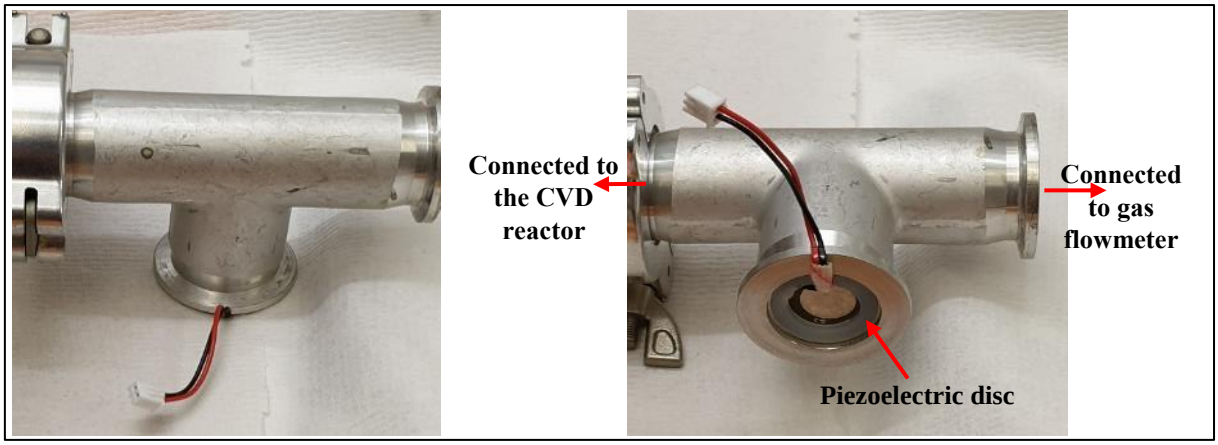

Figure 8-5: Photograph of the "T" joint holding the piezoelectric disc.

The growth was conducted in the same CVD reactor/furnace that was used in the process of the APCVD system using a bubbler. The substrates was held on an angled/ gradient stainless steel substrate-holder with a ledge angle of 7º (**Figure 8-6**), to ensure the streamline flow of precursor was equally passed over the substrate surface with carrying the same concentration of the reactant molecules, hence a uniform film from a composition point of view would be deposited. The CVD system was purged under N_2 gas with a constant flow rate at the required temperature and under atmospheric pressure, before carrying out any experiments to prevent the effect of humidity. Two equimolar solutions (0.01 M and 0.015 M) of PbI_2 (Sigma-Aldrich, 99.999%) and MAI (Solaronix) dissolved in 3 ml of N,N-dimethylformamide (DMF, Honeywell, ≥99.99995%) were used to validate the concentration effect. A range of temperatures (110 $^{\circ}$C- 250 $^{\circ}$C) and deposition time (10 minutes-40minutes) were used. A mist of water was successfully formed, which was flowed towards the hot wall CVD reactor using nitrogen gas as a carrier at a lower constant ratio of 1 L/min (**Figure 8-7**).

This experiment was carried out to access the working of the reactor before introducing any chemical, etc. A piezoelectric disc was used at a driving frequency of 1.7 MHz.

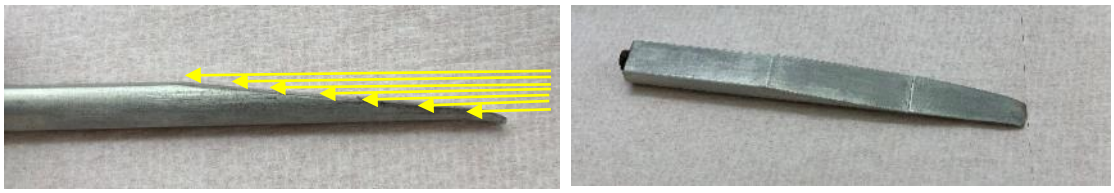

Figure 8-6: The substrate holder used in this work.

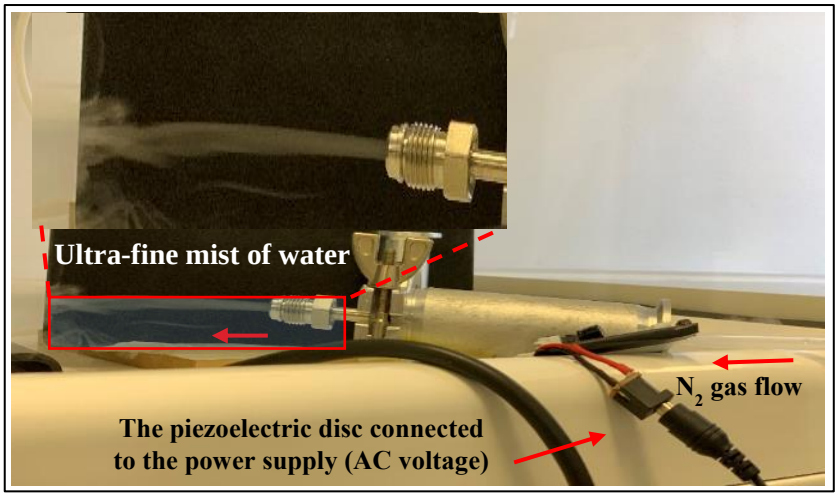

Figure 8-7: the formation of the ultra-fine mist by a piezoelectric transducer.

To validate the capability of this system for the generation of a mist of the perovskite precursor molecules (DMF, PbI_2 and MAI), a preliminary study was carried out at low temperature (<150 ºC). A pre-coated PbI_2 film was placed in the middle of the CVD reactor. The film changed to black colour as compared to the yellow colour from PbI2was found to be turned from yellow to black colour, which indicated that the mist was contained MAI molecules that was reacted with the PbI_2 forming the perovskite phase. **Figure 8-8** shows the optical properties of the PbI_2 films before and after the APCVD process. It can be clearly observed from the absorption spectra that the changing in the absorption onset which confirmed the formation of perovskite material after subjected to the APCVD process. In addition, the bandgap of the PbI_2 film obtained before the APCVD process was reduced into the optimal value of $MAPbI_3$ material (1.49 eV), which is in a good agreement with the literature [25]. It was indicated that the mist was contained the molecules of MAI beside to the solvent (DMF).

However, there was no confirmation yet that the PbI_2 molecules were also carried with the mist as the substrate was pre-coated with PbI_2. In order to monitor if the PbI_2 molecules were carried with the mist, an experiment was performed at high temperature (200-250 ºC) as it was already demonstrated from TGA analysis that the PbI_2 was stable up to 400 ℃. The yellowish film deposited on the substrates' surface is seen in **Figure 8-8 (c),** with the identical absorption spectral feature exhibited by PbI_2 film [22-24].

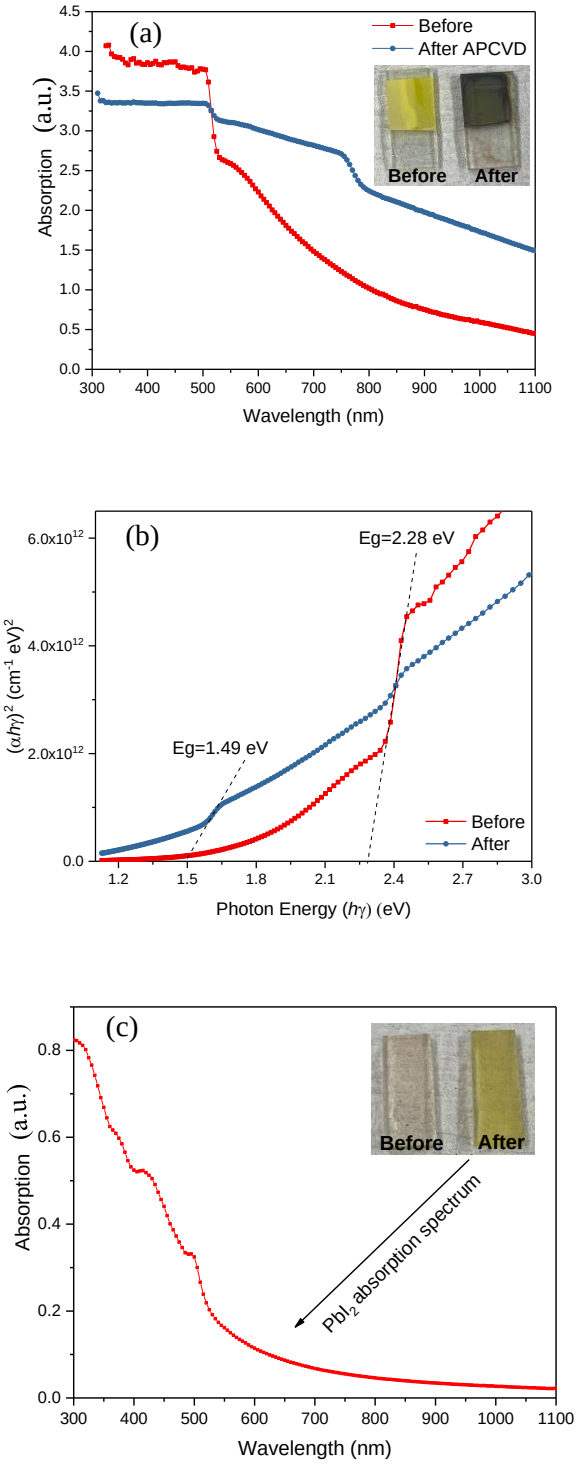

Figure 8-8: The absorption spectra of the PbI_2 thin films before and after treated by APCVD process (a) and the corresponding bandgap energy for both films (b), and the absorption spectrum of the PbI_2 film deposited by APCVD process (c).

It is well known that the substrate/growth temperature greatly influences the chemical reaction of the precursor (PbI_2 and MAI). Initially, the identical substrate/growth temperature obtained from the literature [1, 2], in which the experiments were conducted at high substrate temperatures (≥ 200 ºC). **Table 8-2** shows the parameters of the initial APCVD process. It was observed that the deposition of the film on the substrates (glass, Si, FTO and AZO coated glass) was not observed. Further increase in the concentration and duration of the deposition did not show any improvement (i.e. no deposition of the film). It could be due to the substrate temperatures were too high that could evaporate the deposited films if any, and vaporisation of the DMF carries both precursors since the boiling point of DMF was 158 ºC that was lower than the substrate temperature, during the cooling down of the system for 2h under N_2 flow. To examine this assumption, the substrate temperature was reduced to 120ºC.

Table 8-2: The initial CVD process parameters that used piezoelectric disc as a delivery system.

CVD conditions	
Solution concentrations	0.01 M and 0.015 M
N_2 flow rate	1 L/min
Deposition times	15-30 min
Substrate temperatures	200-250 ºC

In the following experiments, the substrate temperature was kept at 115±5 ºC. The parameters considered for the low-temperature experiments are shown in **Table 8-3**. These parameters were led to deposit a thin layer of $MAPbI_3$ on the heated substrate. To note, the piezoelectric disc according to our design was required to be fed with a certain amount of the liquid precursor which was ~ 15 ml, to effectively generate an ultra-fine mist for 40 minutes. There was also a certain residual amount of the used liquid precursor which was found after finishing the process. The remaining liquid precursor was re-used in the following experiment.

Table 8-3: The parameters that used in the low-temperature experiments.

CVD conditions	
Solution concentrations	0.01 M and 0.015 M
N_2 flow rate	1 L/min
Deposition time	36 min
Substrate temperatures	115±5ºC

According to the parameters shown in **Table 8-3**, a comparison between the films were formed from the two different concentrations as well as between the films were produced from the use of a fresh liquid precursor and the re-use precursor will be discussed.

Upon comparison between the fresh and reused liquid precursors, **Figure 8-9** presents the effect of the low concentration liquid precursor states on the structural and optical properties of the as-deposited films. The structural evolution of the $MAPbI_3$ perovskite was observed in both films besides the characteristic peaks of FTO [26-28]. The diffraction peaks were appeared at ~13.8º, 19.6º, 24.1º, 28º, 31.3º, 39.9º, and 42.5º which were shown that both films were exhibited a cubic structure [26, 27], This data indicated that the successful interaction of the PbI_2 and MAI molecules was taken place on the substrate surface resulting in a formation of $MAPbI_3$. It was worth to mention that this data was carried out after two weeks of continuous exposure in air. The research published on this topic where the quasi-stable lattice was reverted back from the initial cubic phase to a tetragonal phase or initially formed in a tetragonal phase [2, 3], this study was confirmed structural stability of the crystal lattice for an extended period of time. In addition, such an effect was clearly observed in the optical properties. **Figure 8-9 (b)** presents the transmittance spectra for both films. An absorption onset was observed in the fresh solution sample at ~ 800 nm corresponding to a bandgap of the perovskite which was matched the reported value [25].

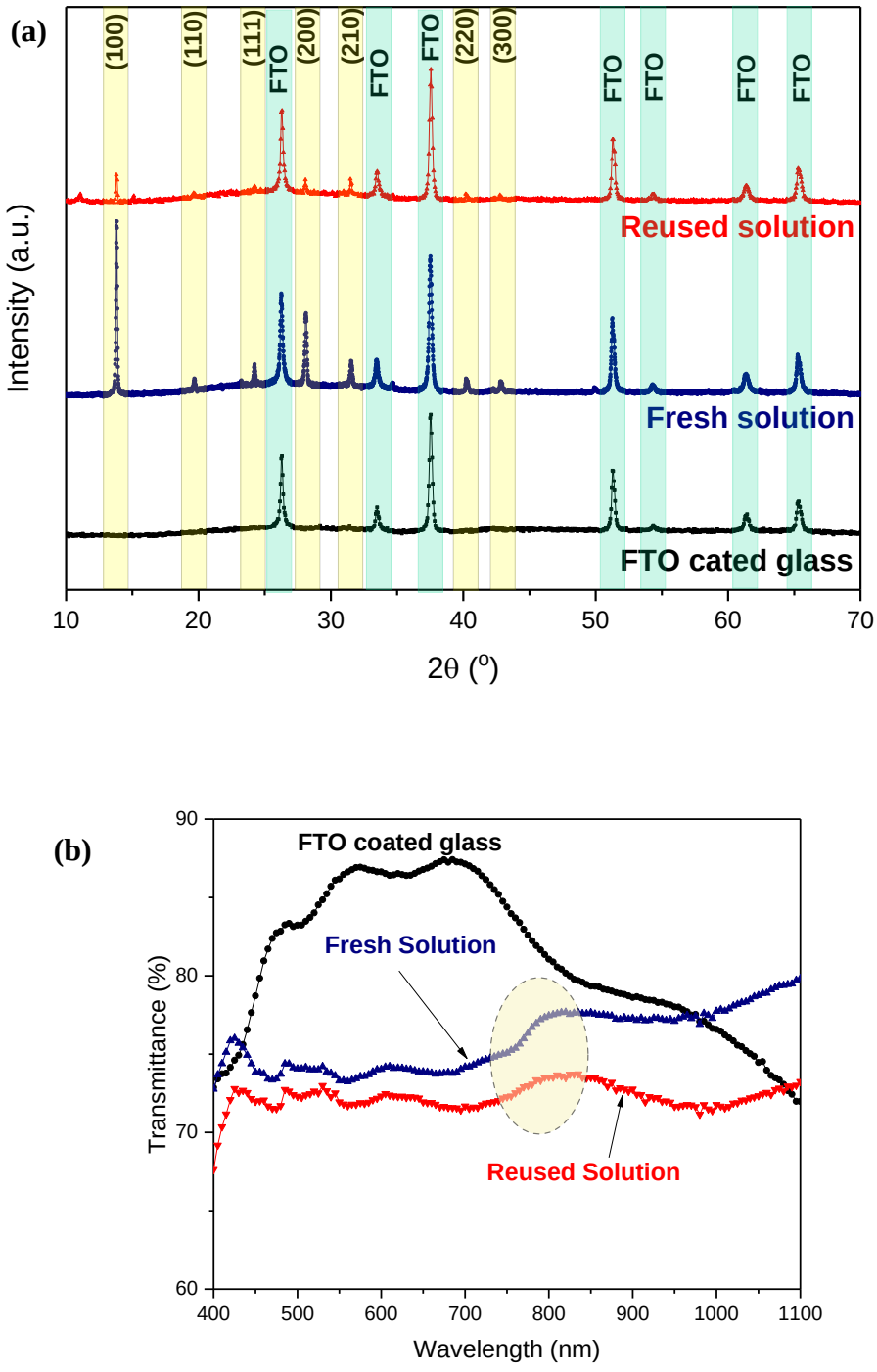

Figure 8-9: The effect of solution state (e.g. fresh and reused) on (a) The XRD pattern and on (b) transmittance spectra.

Comparing the perovskite x-ray diffraction peaks intensity with respect to the intensity of the reflected peaks from FTO crystal structure, the perovskite crystal lattice in the fresh sample was the dominant one, whereby the FTO crystal in the reused sample was more pronounced. It was because of a well-packed perovskite crystal lattice was formed in the fresh solution sample which could enhance the crystallinity of the material. In addition, there was an absence of the main absorption edge of perovskite material in the reused solution sample. These observations were most likely due to the fact that the crystallisation and growth of the perovskite crystals were critically affected by the reactance concentration [27]. As it was obvious that the molar concentration of molecules after being used previously was reduced. Therefore, all the following experiments were run with a fresh solution with known concentration to study the effect of other parameters. It was a clear indication of the effect of the concentration on the growth film which was further investigated to precisely understand the role of the concentration on the film properties.

Upon comparison of the effect of the precursor concentrations, **Figure 8-10** presents the effect of the precursor concentrations on the thin films colour which was formed during the APCVD process.

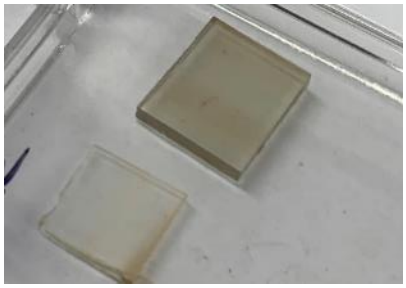

Lower concentration (0.01 M)

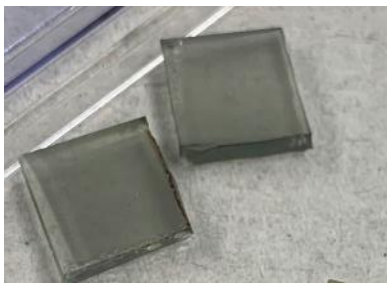

Higher concentration (0.015 M)

Figure 8-10: Photograph of the as-deposited thin films prepared at different precursor concentrations.

The change in colour of the films (**Figure 8-10**) was dependent on the concentration difference. It was clear that there were coated films with different colours. It was well known that the growth of perovskite material as evident by the grey colour of the film was appeared in the high concentration samples. For more investigation, structural properties of the as-deposited films on FTO coated glass substrates prepared at different concentrations were carried out. **Figure 8-11** shows the X-ray diffraction (XRD) patterns of the lower and higher concentrations samples and of the FTO coated

glass. The structural evolution of the perovskite ($MAPbI_3$) cubic structure was observed in the low concentration sample with a characteristic peaks of perovskite appears at ~13.8º, 19.6º, 24.1º, 27.9º, 31.3º, 39.9º, and 42.5º which were corresponding to (100), (110), (111), (200), (210), (220), and (300) diffraction planes of a cubic $CH_3NH_3PbI_3$ crystal [26, 27]. In addition, there were seven diffraction peaks were reflected from the FTO lattice plane at 26.4º, 33.5º, 37.5º, 51.3º, 54.5º, 61.5º, 65.3º [28]. However, splitting of the perovskite diffraction peak (~27.9º) which was observed in the higher concentration sample could be attributed to the phase transition from a cubic to a tetragonal crystallographic structure. That was indicated that the less species was passed over the surface of substrate leading to very slow growth, forming a strong and more stable structure.

The most of perovskite crystals tend to grow in a cubic structure, however, the instability of this structure due to the existence of a large structural defect density within the crystallographic lattice such as point, line or plane defects and/or grain boundaries [29, 31] , which causes a transition into a more stable structure at room temperature (e.g. tetragonal) [25]. This defect is usually formed in a very high deposition rate and/or high concentration of molecules in the gas stream, in which the molecules do not have an adequate amount of time to organise and bond with other atoms/molecules with minimal or no defects causing imperfect crystals. It is demonstrated that a stable in-situ cubic phase would be formed by using the lower concentration (0.01 M), whereas the higher concentration induced the phase transition into tetragonal. To note, this data was collected after storage for two weeks at an atmospheric condition. It is explained the phenomenon that to form a stable cubic structure with a low defect density, or ideally, zero defect density, the low concentration of reactants and very slow growth rate are some of the key parameters. Needless to say, this is the first study demonstrates or clarifies some of the riddles associated with the instability of perovskite materials.

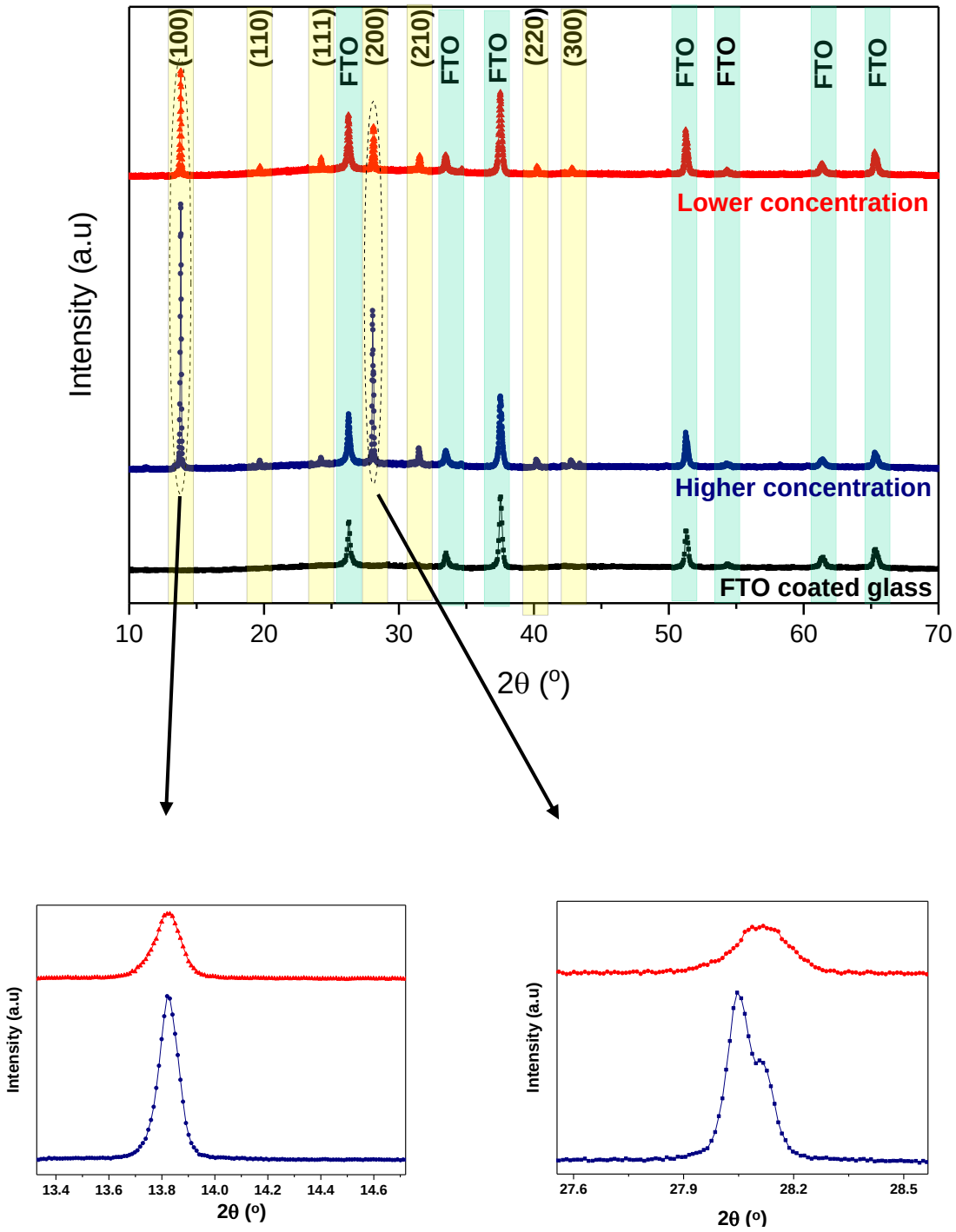

Figure 8-11: X-ray diffraction (XRD) patterns of as-prepared films at different precursor concentrations and of the FTO coated glass substrate (top graph) with magnification of the two main characteristic peaks of $MAPbI_2$ (bottom graphs).

The surface of the films prepared by the APCVD process using two different concentration solutions (0.01 M and 0.015 M) was examined via optical microscopy under three different magnifications (5x, 10x, 20x) (**Figure 8-12** and **Figure 8-13**). Thin film deposited at lower concentration exhibited ultra-smoother and more homogeneous surface compared to the thin film deposited with the use of higher concentration solution. It was indicated that when the streamline flow that contained a less number/density of molecules/species per unit volume arrived the substrate surface with very slow flow rate resulting in facilitating more time to form more stable bonding (chemisorbed reactions) and provide sufficient energy to atoms/molecules which rearranged themselves in a more stable structure [32]. The growth of defect free thin film, based on the aforementioned statement, was well established in atomic layer deposition (ALD) and molecular beam epitaxy (MBE).

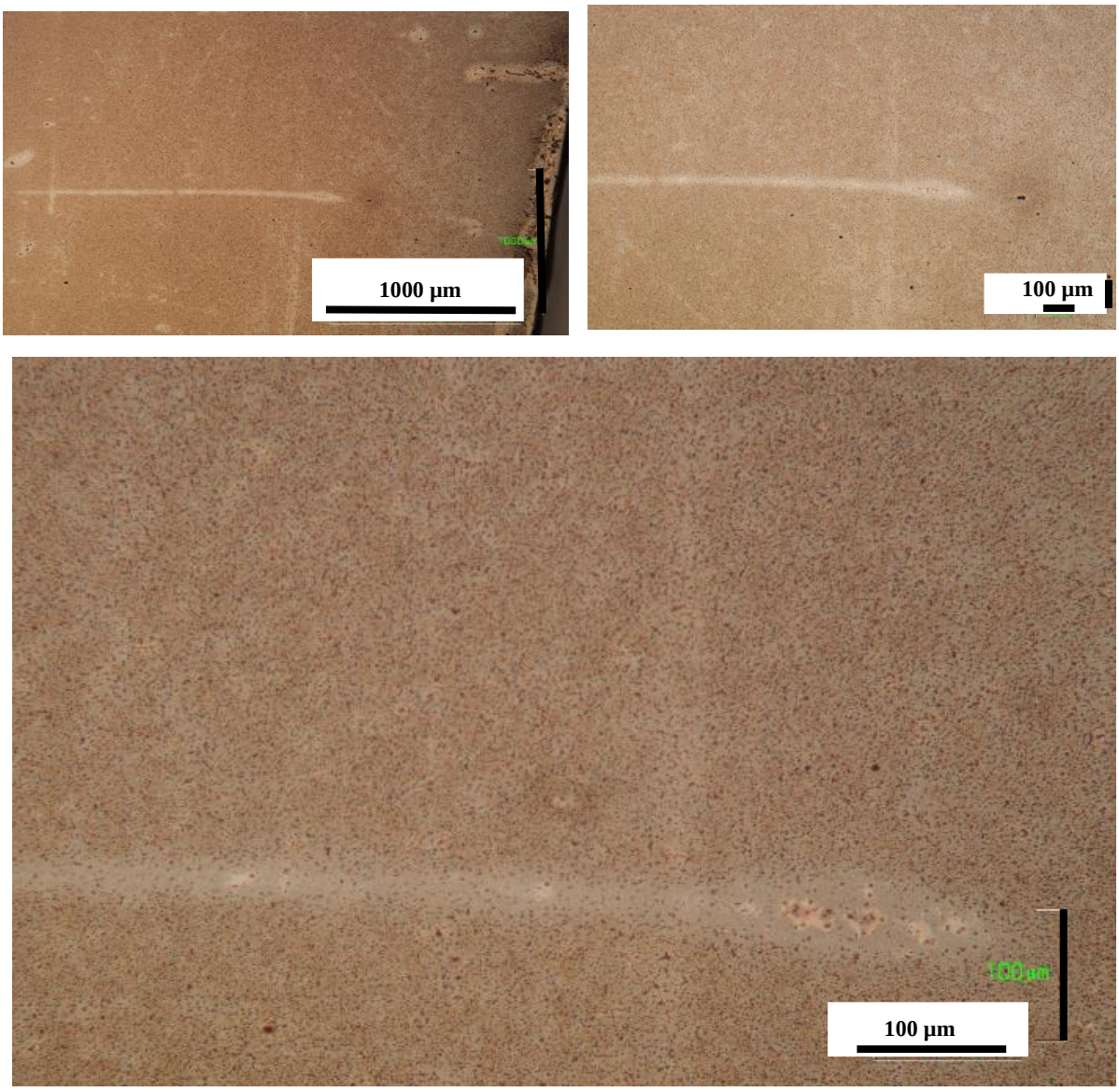

Figure 8-12: Optical microscopy images of the film deposited from a higher concentration precursor.

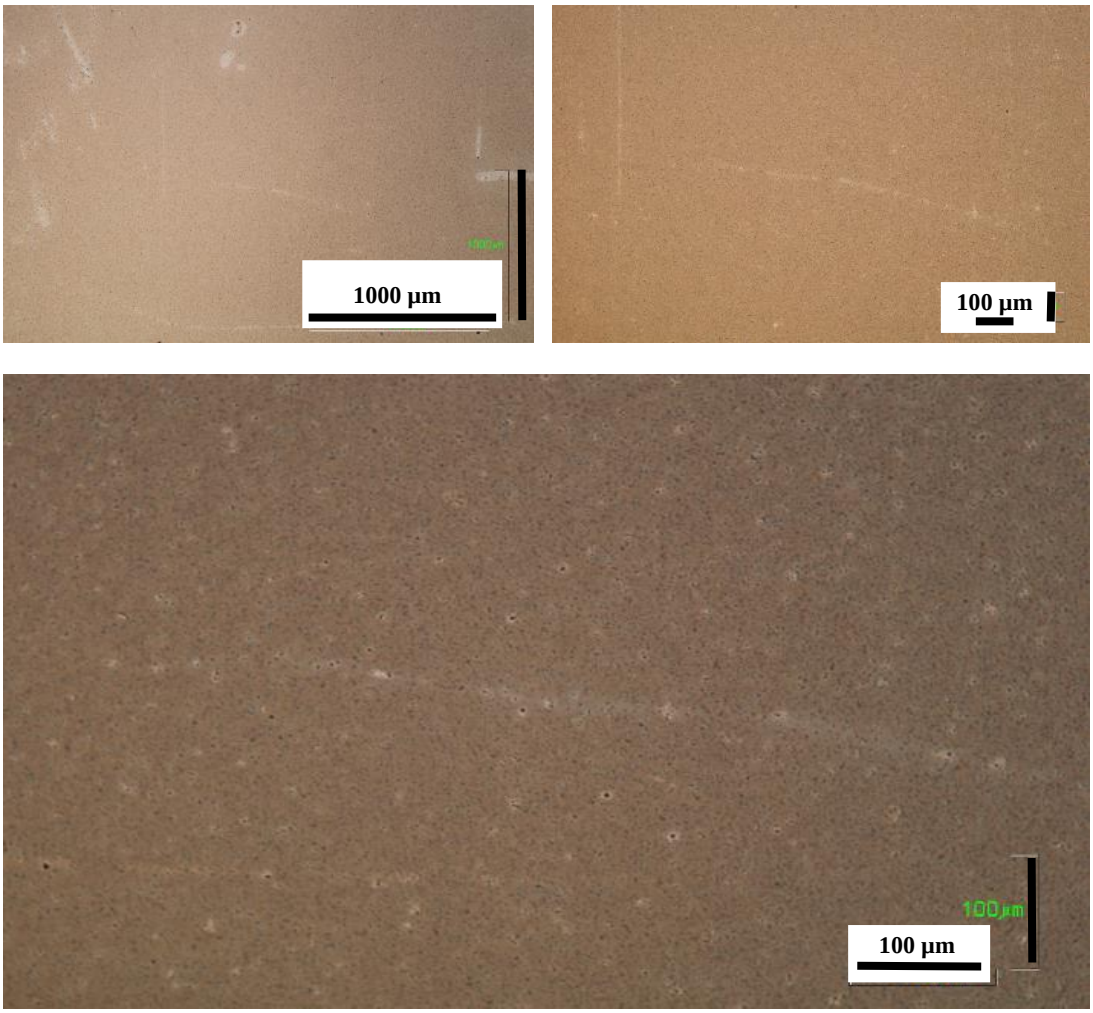

Figure 8-13: Optical microscopy images of the film deposited from a lower concentration precursor.

Upon investigation, the optical properties of the higher and lower concentration samples were studied by UV-Vis-IR spectroscopy. As samples were grown under the same parameters (deposition duration, amount of precursor, substrate temperature) shown in **Table 8-3**, the as-deposited sample at lower concentration solution could form a thinner layer compared to the sample deposited with the use of higher concentration solution. That was noticed in the strength of the sample absorbance which is depicted in **Figure 8-14 (a).** A higher concentration samples were shown a strong absorption edge at a wavelength of approximately 800 nm, corresponding to the bandgap of $MAPbI_3$ perovskite

(**Figure 8-14 (b**)), which is in a good agreement with the reported value of the bulk $MAPbI_3$ [1]. However, the low concentration sample did not show a clear peak, which could be attributed to an ultra-thin layer. Repeating a number of coating cycle can effectively increase the film thickness, which is the next scope of this study.

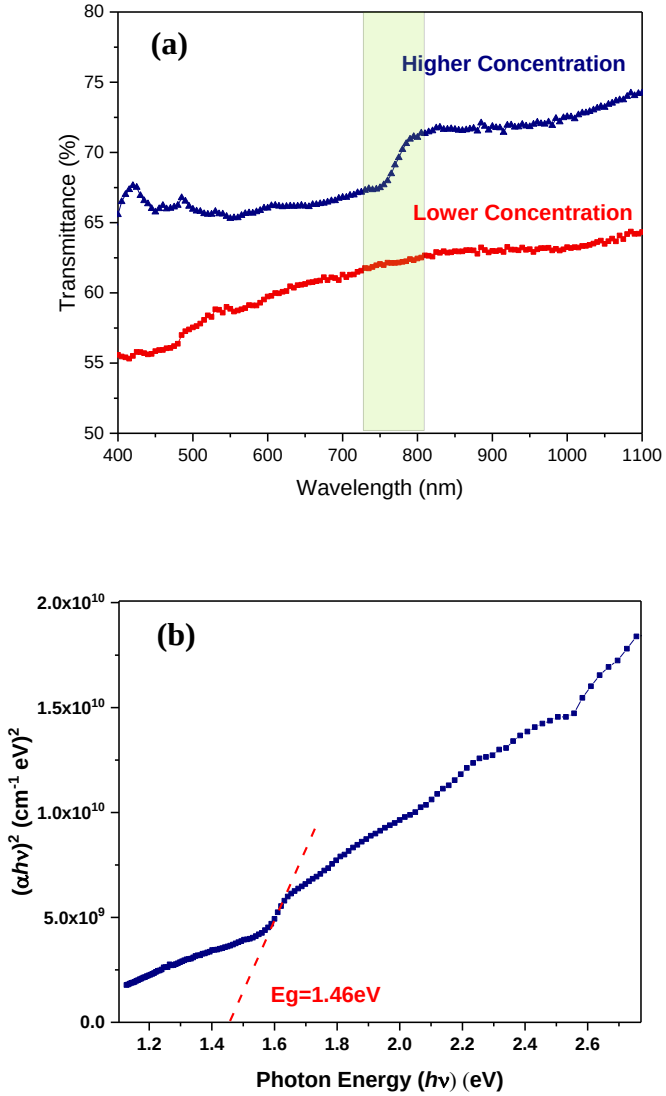

Figure 8-14: (a) The transmittance spectra of as-deposited films by APCVD process at different concentrations and (b) the plot of $(\alpha h\nu)^2$ versus hν for the film prepared at higher concentration precursor.

To investigate the structural cubic-phase stability of the low-concentration perovskite sample that was left in an ambient atmosphere without any care of storage, X-ray diffraction measurements of the

sample were recorded over a period of 70 days (1680 h) at room temperature as shown in **Figure 8-15**. Interestingly, the sample showed stability over 70 days based on the diffraction peaks symmetry. It can be noted that from this figure, no change in the XRD peaks or an appearance of new peaks. In addition, no shift in the peak positions were observed. It is confirmed that long-term cubic-phase stability at room temperature was investigated rather than the commonly pronounced cubic-to-tetragonal phase transition [1, 2].

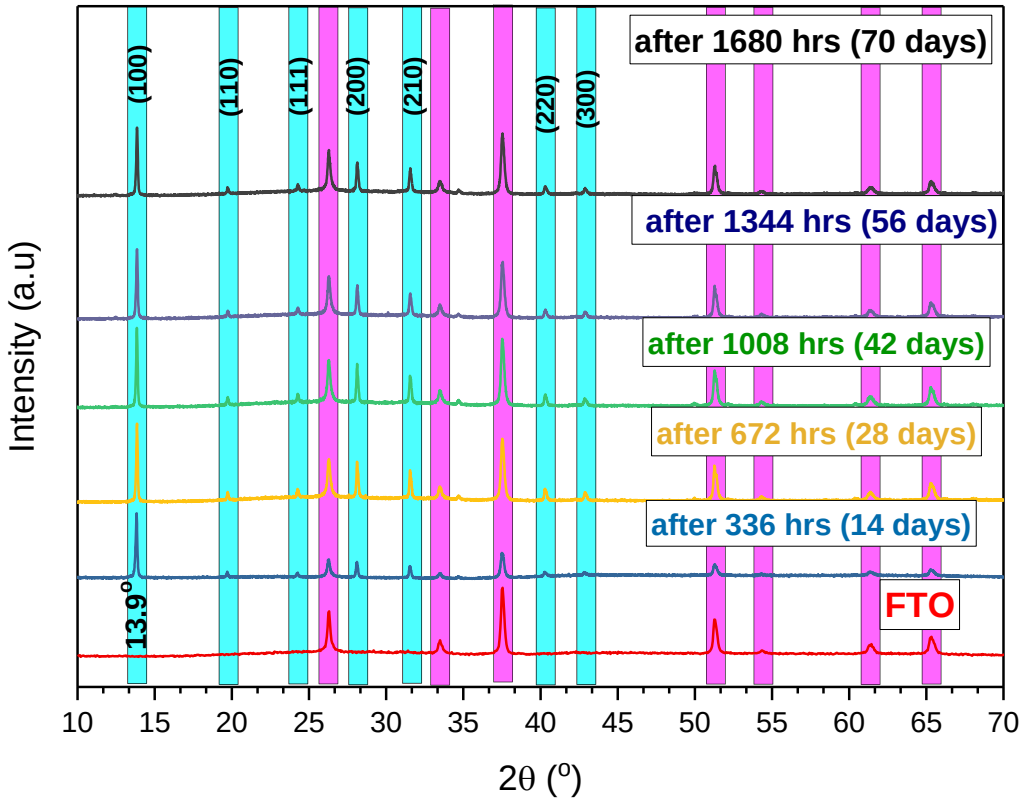

Figure 8-15: XRD patterns of cubic-phase perovskite material ($CH_3NH_3PbI_3$) deposited on FTO coated glass taken over a period of time indicating the stability of the cubic structural phase for the low-concentration sample stored in ambient atmosphere for more than two months.

In a nutshell, it can be concluded that having stability in the formed *in-situ* cubic crystal structure requires a formation of a compositionally uniform material with almost no defects via controlling the molecules arrangement within the lattice structure of crystal. This study approved that the APCVD deposition method, based on the proposed design (the piezoelectric transducer), is valuable for improving the phase stability of $MAPbI_3$.

To better appreciate the role of the APCVD films on the application perspective, this current work also demonstrated the use of such films in a photovoltaic application with FTO/c-TiO_2/$MAPbI_3$/Ag configuration. The schematic diagram of the solar cell structure is shown in **Figure 8-16**. These solar cells have been fabricated using an APCVD growth process of $MAPbI_3$ film on the top of a compact TiO_2 (c-TiO_2) that acts as an electron transport layer (ETL) and a hole blocking layer.

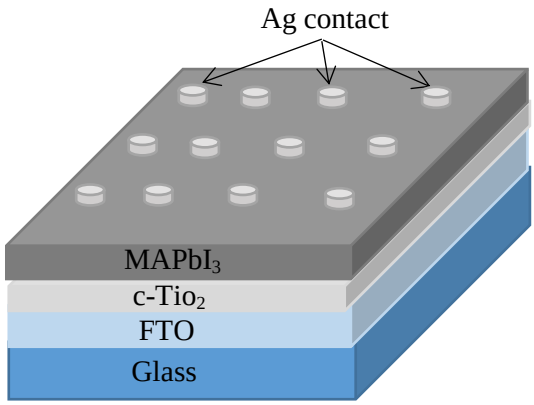

Figure 8.16: the schematic structure of the FTO/c-TiO2/$MAPbI_3$/Ag solar cell.

The *J-V* characteristics of the fabricated solar cell are shown in **Figure 8-17**. The inset graph in **Figure 8-17** showed the optical image of the solar cell under a test. The short circuit current density (J_{SC}) of the device was 0.0713 µA/cm^2 and the V_{OC} was 0.29 V. The parasitic resistance; shunt (R_{sh}) and series (R_s), is defined to be the inverse slope of I-V curve as can be seen in **Figure 8-18.** R_{sh} and R_s were found to be $1x10^{10}$ Ω and $0.4x10^{10}$ Ω, respectively. The possible reason, there may be other causes and require further investigation, of a high value of R_{sh} is the capping of TiO_2 surface by $MAPbI_3$, which may lead to a reduction of the shunt between c-TiO_2 and Ag and avoiding the unfavourable charge recombination [33]. However, the relatively low J_{SC} is likely due to high R_s that decreased the collection efficiency of the carrier at low net electric field across the device closer to V_{OC} [34]. As a result, the J_{SC} is reduced. A high value of R_s generally caused by the resistance of the absorber layer, contact resistance (between the absorber layer and the metal contact) and the resistance of the metal contacts (electrodes) that reduces the current flow [35]. To date, for the best of our knowledge, there has not been reported that a perovskite solar cell based on the film deposited by the aforementioned transducer integrated APCVD growth process. However, an optimisation of the film thickness and reduction of the R_s are required for achieving a high photocurrent density with high open circuit voltage to be such what have been reported in the literature (26 mA/cm^2 and 1.18 V). Nevertheless, it is worth mentioning that, this device was stable up to two months as tested and no special care was taken to store the device other than keeping it in the sample box.

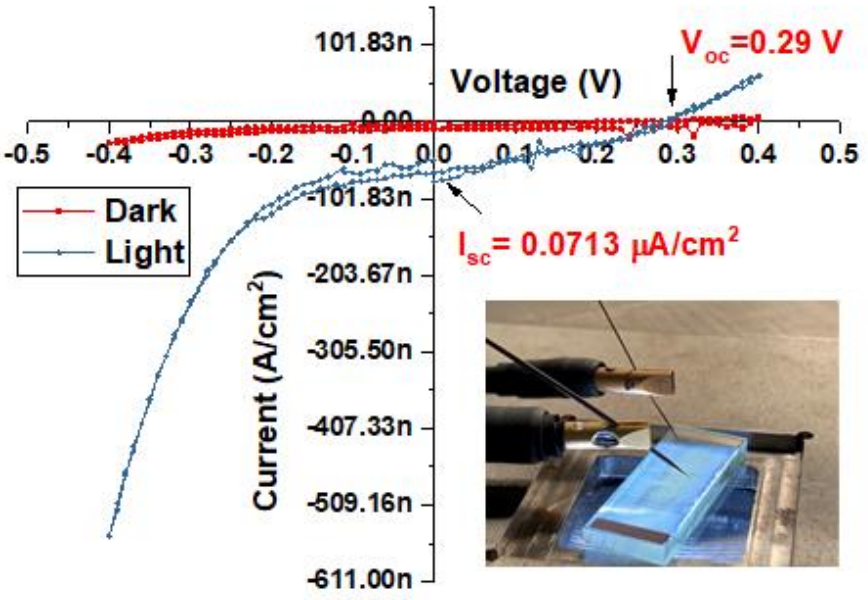

Figure 8-17: The J-V characteristic curve under dark and illumination conditions.

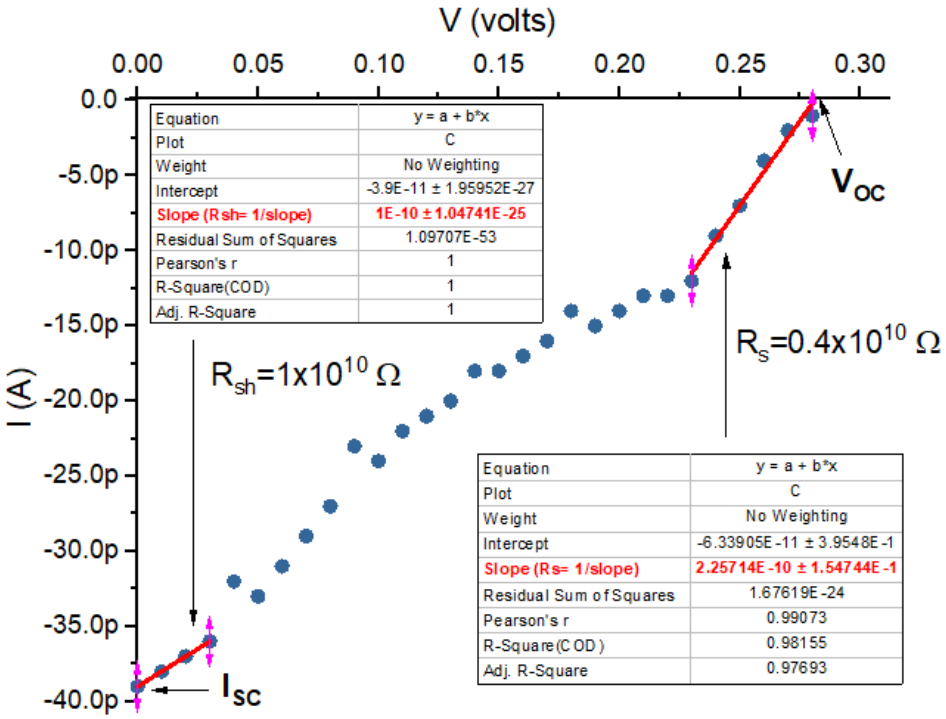

Figure 8.18: Illustrated *I-V* characteristic of $MAPbI_3$-based solar cells depicting the shunt resistance (R_{sh}) and series resistance (R_s).

8.5 Summary

In conclusion, methylammonium lead tri-iodide ($MAPbI_3$) perovskite films were successively deposited on FTO coated glass substrate by the atmospheric pressure chemical vapour deposition (APCVD)-VIDA. With this approach, it was substantiated that the potential for a deposition of an in-situ cubic structure that was stable at room temperature without taking care of storage for more than two weeks. The concentration of precursor was a key in this growth where the lower number of molecules passing over the substrate surface at a lower flow rate, the more stable crystals formed. The novelty of this research was to be able to fabricate for the first time a *stable in-situ cubic structure* at room temperature. Unlike most of the other researches have done in this topic where the quasi-stable lattice is reverted back to the tetragonal phase, this study was confirmed structural stability of the crystal lattice for an extended period of time. In addition to the low temperature fabrication conditions, this study was also successful in fabricating the solar cells using this method for the first time. This is a proof-of-concept that materials deposited using APCVD technique has a potential to use in the photovoltaic solar cell fabrication and further work is required to achieve the higher efficiency reported using other methods.

References

[1] D. Bhachu, D. Scanlon, E. Saban, H. Bronstein, I. Parkin, C. Carmalt and R. Palgrave, "Scalable route to CH 3 NH 3 PbI 3 perovskite thin films by aerosol assisted chemical vapour deposition," Journal of materials chemistry A, vol 3, no 17, pp. 9071-9073, 2015.

[2] M. Afzaal and H. M. Yates, "Growth patterns and properties of aerosol-assisted chemical vapor deposition of CH3NH3PbI3 films in a single step," Surface and coatings technology, vol 321, pp. 336-340, 2017.

[3] D. J. Lewis and P. O'Brien, "Ambient pressure aerosol-assisted chemical vapour deposition of (CH 3 NH 3) PbBr 3, an inorganic–organic perovskite important in photovoltaics," Chemical communications, vol 50, no 48, pp. 6319-6321, 2014.

[4] P. Luo, Z. Liu, W. Xia, C. Yuan, J. Cheng and Y. Lu, "Uniform, stable, and efficient planar-heterojunction perovskite solar cells by facile low-pressure chemical vapor deposition under fully open-air conditions," ACS applied materials & interfaces, vol 7, no 4, pp. 2708-2714, 2015.

[5] P. Luo, Z. Liu, W. Xia, C. Yuan, J. Cheng and Y. Lu, "A simple in situ tubular chemical vapor deposition processing of large-scale efficient perovskite solar cells and the research on their novel roll-over phenomenon in J–V curves," Journal of materials chemistry A, vol 3, no 23, pp. 12443-12451, 2015.

[6] M. R. Leyden, L. K. Ono, S. R. Raga, Y. Kato, S. Wang and Y. Qi, "High performance perovskite solar cells by hybrid chemical vapor deposition," Journal of materials chemistry A, vol 2, no 44, pp. 18742-18745, 2014.

[7] P. Shen, J. Chen, Y. Chiang, M. Li, T. Guo and P. Chen, "Low-Pressure hybrid chemical vapor growth for efficient perovskite solar cells and Large-Area module," Advanced materials interfaces, vol 3, no 8, pp. 1500849, 2016.

[8] M. J. Powell, D. B. Potter, R. L. Wilson, J. A. Darr, I. P. Parkin and C. J. Carmalt, "Scaling aerosol assisted chemical vapour deposition: Exploring the relationship between growth rate and film properties," Materials & design, vol 129, pp. 116-124, 2017.

[9] A. Jayal, F. Badurdeen, O. Dillon Jr and I. Jawahir, "Sustainable manufacturing: Modeling and optimization challenges at the product, process and system levels," CIRP journal of manufacturing science and technology, vol 2, no 3, pp. 144-152, 2010.

[10] M. J. Powell and C. J. Carmalt, "Aerosols: A sustainable route to functional materials," Chemistry–A european journal, vol 23, no 62, pp. 15543-15552, 2017.

[11] S.P. Krumdieck, "Chemical Vapour Deposition," in CVD reactors and delivery system technology, Anonymous 2008, pp. 37- 37-92.

[12] P. Marchand, I. A. Hassan, I. P. Parkin and C. J. Carmalt, "Aerosol-assisted delivery of precursors for chemical vapour deposition: Expanding the scope of CVD for materials fabrication," Dalton transactions, vol 42, no 26, pp. 9406-9422, 2013.

[13] H. Manasevit and W. I. Simpson, "The use of Metal-Organics in the preparation of semiconductor materials I. epitaxial Gallium-V compounds," Journal of the electrochemical society, vol 116, no 12, pp. 1725-1732, 1969.

[14] V. Astié, C. Millon, J. Decams and A. Bartasyte, "Chemical Vapor Deposition for Nanotechnology," in Direct liquid injection chemical vapor deposition, Anonymous IntechOpen, 2018, .

[15] M. L. Petrus, J. Schlipf, C. Li, T. P. Gujar, N. Giesbrecht, P. Müller-Buschbaum, M. Thelakkat, T. Bein, S. Hüttner and P. Docampo, "Capturing the sun: A review of the challenges and perspectives of perovskite solar cells," Advanced energy materials, vol 7, no 16, pp. 1700264, 2017.

[16] B. J. Kim, D. H. Kim, S. L. Kwon, S. Y. Park, Z. Li, K. Zhu and H. S. Jung, "Selective dissolution of halide perovskites as a step towards recycling solar cells," Nature communications, vol 7, pp. 11735, 2016.

[17] K. F. Jensen and D. Graves, "Modeling and analysis of low pressure CVD reactors," Journal of the electrochemical society, vol 130, no 9, pp. 1950-1957, 1983.

[18] P. Luo, Z. Liu, W. Xia, C. Yuan, J. Cheng and Y. Lu, "A simple in situ tubular chemical vapor deposition processing of large-scale efficient perovskite solar cells and the research on their novel roll-over phenomenon in J–V curves," Journal of materials chemistry A, vol 3, no 23, pp. 12443-12451, 2015.

[19] D. H. Peregrine, "Breaking waves on beaches," Annual review of fluid mechanics, vol 15, no 1, pp. 149-178, 1983.

[20] C. L. Goodridge, W. T. Shi, H. Hentschel and D. P. Lathrop, "Viscous effects in droplet-ejecting capillary waves," Physical review E, vol 56, no 1, pp. 472, 1997.

[21] I. Kemerchou, F. Rogti, B. Benhaoua, N. Lakhdar, A. Hima, O. Benhaoua and A. Khechekhouche, "Processing temperature effect on optical and morphological parameters of organic perovskite CH3NH3PbI3 prepared using spray pyrolysis method," 2019.

[22] H. Agrawal, A. Vedeshwar and V.K. Saraswat, , "Growth and characterization of PbI2 thin films by vacuum thermal evaporation," In Journal of nano research, 2013, pp. 1-6.

[23] D. Bhavsar and K. Saraf, "Optical properties of lead iodide between 0.4946 and 6.185 eV," Journal of materials science: Materials in electronics, vol 14, no 4, pp. 195-198, 2003.

[24] S. I. Mohammed, Y. Al-Douri, U. Hashim, N. Ahmed and R. Al-Gaashani, "Structural and optical properties of PbI2 nanostructures obtained using the thermal evaporation method," Canadian journal of physics, vol 91, no 10, pp. 826-832, 2013.

[25] T. Baikie, Y. Fang, J. M. Kadro, M. Schreyer, F. Wei, S. G. Mhaisalkar, M. Graetzel and T. J. White, "Synthesis and crystal chemistry of the hybrid perovskite (CH 3 NH 3) PbI 3 for solid-state sensitised solar cell applications," Journal of materials chemistry A, vol 1, no 18, pp. 5628-5641, 2013.

[26] Y. Dang, Y. Liu, Y. Sun, D. Yuan, X. Liu, W. Lu, G. Liu, H. Xia and X. Tao, "Bulk crystal growth of hybrid perovskite material CH 3 NH 3 PbI 3," CrystEngComm, vol 17, no 3, pp. 665-670, 2015.

[27] N. Ahn, S. M. Kang, J. Lee, M. Choi and N. Park, "Thermodynamic regulation of CH 3 NH 3 PbI 3 crystal growth and its effect on photovoltaic performance of perovskite solar cells," Journal of materials chemistry A, vol 3, no 39, pp. 19901-19906, 2015.

[28] K. Lee and S. Lu, "Porous FTO thin layers created with a facile one-step sn 4 -based anodic deposition process and their potential applications in ion sensing," Journal of materials chemistry, vol 22, no 32, pp. 16259-16268, 2012.

[29] V. V. Brus, F. Lang, J. Bundesmann, S. Seidel, A. Denker, B. Rech, G. Landi, H. C. Neitzert, J. Rappich and N. H. Nickel, "Defect dynamics in proton irradiated CH3NH3PbI3 perovskite solar cells," Advanced electronic materials, vol 3, no 2, pp. 1600438, 2017.

[30] M. L. Agiorgousis, Y. Sun, H. Zeng and S. Zhang, "Strong covalency-induced recombination centers in perovskite solar cell material CH3NH3PbI3," Journal of the american chemical society, vol 136, no 41, pp. 14570-14575, 2014.

[31] J. S. Park, S. Kim, Z. Xie and A. Walsh, "Point defect engineering in thin-film solar cells," Nature reviews materials, pp. 1, 2018.

[32] S. Seo, S. Jeong, H. Park, H. Shin and N. Park, "Atomic layer deposition for efficient and stable perovskite solar cells," Chemical communications, vol 55, no 17, pp. 2403-2416, 2019.

[33] P. Qin, S. Tanaka, S. Ito, N. Tetreault, K. Manabe, H. Nishino, M. K. Nazeeruddin and M. Grätzel " Inorganic hole conductor-based lead halide perovskite solar cells with 12.4% conversion efficiency," nature cummunication, vol 5, no 3834, 2014.

[34] P. Schulz, J. O. Tiepelt, J. A. Christians, I. Levine, E. Edri, E. M. Sanehira, G. Hodes, D. Cahen, and A. Kahn "High-Work-Function Molybdenum Oxide Hole Extraction Contacts in Hybrid Organic−Inorganic Perovskite Solar Cells," ACS applied materials & interfaces, vol 8, 31491-31499, 2016.

[35] J. Xue, S. Uchida, B. P. Rand and S. R. Forrest, "4.2% efficient organic photovoltaic cells with low series resistances," Applied physics letters, vol 84, pp. 3013, 2004.

Chapter 9 Conclusion and Future Scope

The aim of this research work was to develop novel methods for the deposition of perovskite thin films that are scalable and industry-accepted techniques such as RF-PECVD and APCVD. Along with the scalable process, this work also aimed at producing films that are defect free, with focusing to make materials with ATM (Atom to Matter) process. In such a process it is always required to deposit films or grow any material with the control of a precursor with one atom resolution. Such a process is similar to ALD where materials are obtained with the least defect in the films. As the obtained perovskite material ($CH_3NH_3PbI_3$) has a significant contribution to the understanding of stability issues reported in the next generation photovoltaics that has incorporated into perovskite materials over the last recent years.

Currently, in the published literature, the most perovskite films are deposited by spin coating, doctor blade, wire wound, inkjet printing, thermal evaporation, dip coating, and CVD. However, in most of these processes, it is difficult to control over the amount of a precursor that is applied, as a lot of material is squirted/printed/dropped/pushed not providing an adequate amount of time for the atoms and/or molecules to organise and bond with other atoms with minimal or no defects. Additionally, few of these processes will require a further annealing process to improve the crystallinity and minimise the defects. Is it really required to add more steps (process, etc) to obtain a film with larger defects by using such processes? Hence, if it is designed a single step process to obtain a film with minimal defect density and might result in the most stable material will be an ideal step toward the commercialisation of the perovskite solar cells.

In this research study, the first proof-of-concept was demonstrated to obtain perovskite films that were a tetragonal crystal structure in a RF-PECVD process, which that is not reported till date. This achievement is encouraging as RF-PECVD process is fully scalable and already available technology in the industries. This research was also demonstrated the stable film for more than two months kept in normal atmosphere conditions with the use of an ultrasonic transducer crystal to control the size of the precursor droplets that were suspended in the N_2 streamlines. These droplets interacted with the surface of the substrate that was kept at elevated temperature, where additional thermal energy was gained by the reactants and further led towards more controlled growth/deposition of the film. In this work, high stable cubic phase of perovskite thin films was obtained by APCVD method. It is believed that the deposition performed in the non-vacuum with controlled amount of the precursor molar

concentration at adequate time available for these atoms will lead to the stable growth with proper arrangement of atoms that are extremely stable.

9.1 Main Outcomes of this Research Study

Deposition of perovskite films by the RF-PECVD process was shown several barriers which were discussed in detail through the thesis. Thoroughly, the supporting arguments and potential reasons where required to provide more understating and justification for the observations that were seen in this work. An initial PbI_2 layer was deposited by spin coating and thermal evaporation processes Where the film thickness was fixed Conversion of the PbI_2 films into perovskite was observed, however, on some occasions, it was partial and/or not converted due to unfavourable deposition parameters. A number of interesting findings were reported in this thesis, which in themselves might be a primary study for several researchers to contribute to the improvement of the shortfalls for not being able to fabricate a solar cell.

Through the structural and morphological examinations of the PbI_2 films, it was observed from XRD that both techniques were formed c-oriented films. Increased crystallite size with less macrostrain was observed in the evaporated films. The smoothness of the films was investigated by SEM and AFM. The densely packed crystal growth in the spin-coated films was observed, while the decrease in the density and the presence of an interferon void were additionally observed in the evaporated films. This might further induce the intercalation of the organic compound into the lattice to form perovskite after RF-PECVD process.

With an aid of XRD, the effect of RF-PECVD deposition parameters on the material compositional and structural change was studied. Varying the substrate temperature was found to greatly affect the perovskite phase formation. At lower temperatures < 100 ºC, the reaction commenced with an increase in PbI_2 crystallinity. At 100^{o}C, the main characteristic peaks of the tetragonal $CH_3NH_3PbI_3$ crystals were observed. Apart from the perovskite, PbI_2 crystalline phase was observed in the collected data, which suggests that the perovskite material was successfully grown with a residual amount of an unreacted PbI_2. However, at temperature > 100 ºC, the peaks corresponding to the perovskite were not present and the presence of diffraction peaks that correspond to metallic Pb was observed. The effect of the variation of the RF power on the microstructure of films was found to be significant. At RF power of 25 W, ions present in the plasma gained more energy that increased their flux towards the substrate surface, which caused the removal of iodine atoms leaving behind metallic lead (Pb) atoms. While the lower RF power (10 W) resulted in the diffusion of the appropriate ions into the PbI_2 films with successful formation of perovskite. The lower deposition pressure (250 and 500 mtorr), on the other hand, resulted in no perovskite growth, whereas the growth was observed for the sample with

PbI_2 film exposed to ammonia and methane plasma at 1000 mtorr. However, extensive further optimisation is required to obtain perovskite material.

Through the optical and electrical measurements, it was observed that the electronic structure of (PbI_6) cage was likely to have the main contribution to the excitonic properties of $CH_3NH_3PbI_3$. Although the presence of perovskite diffraction peaks was shown in the XRD data, the predominant absence of the optical absorption onset of the perovskite material was observed in the film that was grown at different deposition parameters. A higher photo-responsivity was observed for those films that were embedded PbI_2 and perovskite phase. Meanwhile, the metallic nature of the films was observed in the films grown at high RF power > 10 W and lower pressure < 1000 mbar as depicted in the XRD. Similar observation reflected on the electrical characteristics of the films by showing a conductive I-V behaviour in both dark and light conditions.

In the RF-PECVD process that was reported here, two step deposition processes were used. However, in any CVD process, both the precursors are supposed to available infinitely and hence the obtained film will have better stoichiometry. Considering the cost with the use of a scalable process that any industrial technique would prefer, in this work, a modified non-vacuum CVD system was used to deposit perovskite films at atmospheric pressure, hence the name APCVD.

By using APCVD approach, it was established that the precursor presented in the bubbler should be heated to provide adequate energy to the molecules/atoms. However, the instability of MAI and PbI_2 at the elevated temperature posed several problems in the deposition of perovskite films. This was due to the volatile nature of these molecules/atoms that were difficult to be vaporised in a right stoichiometric ratio, as the molecular mass of these components is different. It was observed that DMF was initially carried away by the gas owing to its higher volatility and lower molecular mass (73.09 g/mol) leaving behind PbI_2 and MAI in the bubbler due to the relatively low volatility and higher molecular mass (PbI_2: 461.01 g/mol, MAI: 158.97 g/mol). Later, it was realised that the different molecular mass of each component presented in the solution led to an improper transport of the solute and solvent at the same time. This means a sequential transport of the DMF, MAI and PbI_2 was corresponding to its molecular mass with the available energy. Therefore, an alternative approach to carry DMF, PbI_2 and MAI simultaneously was used. By using a piezoelectric transducer atomisation, it was possible to generate a reproducible and reliable mist that comprised both (MAI and PbI_2) contents in the liquid precursor. The mist was carried to a hot substrate that was maintained at 115 ± 5 ºC with a lower flow rate of the gas containing the mist. The growth of the perovskite films was controlled based on the concentration of the precursor and the temperature. The lower concentration of the molecules passing over the substrate enhanced the crystallographic stability, where the *in-situ* cubic structure was achieved. With the use of this novel design of the reactor specifically for the deposition of perovskite

films; excellent stability of these films at room temperature without taking care of storage for more than two months in an open atmosphere was achieved, providing an alternative approach to obtain the stable perovskite film. This study was indicated that the lower number of molecules passing over the substrate surface at a lower flow rate provided an adequate amount of time for the atoms to find a stable atom pair and form a stronger bond that in turn will lead to more stable as-grown thin film. The additional contribution of this research was to be able to grow an *in-situ* stable perovskite thin film with a cubic structure, such films did not degrade and convert to other crystal structures as reported in plentiful papers. Other researchers working in this study area have used a higher concentration of the precursor ($\geq$ 1 M) that resulted in the quasi-stable lattice; conversion of the as-grown cubic structure into the tetragonal structure after a week when storing in a dry box. However, this study was demonstrated a structural (cubic) stability of the crystal lattice for an extended period of time kept in normal atmospheric conditions where other researches failed to demonstrate. In addition to the low temperature and lower concentration of the precursor used for the fabrication of a novel design of the reactor to grow films with the bottom-up approach (i.e. Atom by atom or molecules), this study was successful in fabricating proof-of-concept solar cells using this method for the first time.

9.2 Recommendations for Future Research Work

In this research, the new unexplored methods for growing perovskite material were demonstrated. Initial experiments were demonstrated the ability for synthesising the perovskite material by using an RF-PECVD process. Despite some of the promising results, there is still needed for further optimisation in order to completely convert the PbI_2 into perovskite phase that has to be explored in the near future by varying the deposition parameters. As a result, it opens up a new avenue to explore this growth method. Additionally, it is important to find and/or develop a new gas that acts as a source of iodine and lead, which can be used with ammonia and methane, hence there will be the availability of the infinite source of the precursor as required for any CVD process. In addition, the growth mechanism proposed is required to be validated with the in-situ experimental methods that would support the theoretical calculations and observations with the use of methods like Secondary Ion Mass Spectrometry (SIMS), Optical emission spectroscopy (OEM) and Inductively Coupled Plasma Optical Emission Spectroscopy (ICPOES).

There are few other areas in this research study that can be further explored by optimising the material. For instance, studying the effect of the thickness of PbI_2 film on the perovskite formation can result in a significant improvement in the understanding of growth and conversion of PbI_2 into perovskite. In addition, only three parameters (temperature, RF power, chamber pressure) were used in a limited framework in this research study, which leaves a greater opportunity to expand on the study of these parameters in greater details by conducting a greater number of experiments, not just with individual

parameters but also focusing on the inter dependency of the individual parameters with each other. For example, the temperature range between 50 $^{\circ}$C and 150 $^{\circ}$C was studied and optimised at the deposition duration of 60 min. It would be interesting to explore the effects of duration of the RF-PECVD process at a certain temperature. More RF-PECVD parameters such as flow rate of the gas, pre-treatment, duration, prior plasma treatment and post H-plasma treatment could also be explored. Further analysis of these deposited films and their growth optimisation can be directed/encouraged towards the fabrication of photovoltaic cells, which is the key to the future work.

Several promising results and conclusions were drawn from the novel design of APCVD process, which are required to be explored in-depth to understand the governing principles with the *in-situ* experiments to strengthen the theoretical conclusion, especially to the growth dynamics. More research on the atomisation of the solution with the use of piezoelectric disc by altering the resonant frequency and the thickness of the disc has to be explored. The detrimental analysis of the droplet diameter and its distribution (possible Gaussian distribution that provides mean diameter and standard deviation) produced during the deposition process, by using an appropriate measuring system, would be helpful for more controlled deposition of uniform thin films. An investigation into the dependency of the generated droplet on the resonant frequency of the used piezoelectric disc would also add to the knowledge of its effect on the properties of deposited films. We have just touched the tip of the iceberg in this research area; however, there are lots of unexplored possibilities that can be extended to deposition of other materials for various applications.